

University of Alberta

Electrically Conductive Metal Nanowire Polymer Nanocomposites

by

Xiaoxiong Luo

A thesis submitted to the Faculty of Graduate Studies and Research
in partial fulfillment of the requirements for the degree of

Doctor of Philosophy

in

Chemical Engineering

Department of Chemical and Materials Engineering

©Xiaoxiong Luo

Spring 2013

Edmonton, Alberta

Permission is hereby granted to the University of Alberta Libraries to reproduce single copies of this thesis and to lend or sell such copies for private, scholarly or scientific research purposes only. Where the thesis is converted to, or otherwise made available in digital form, the University of Alberta will advise potential users of the thesis of these terms.

The author reserves all other publication and other rights in association with the copyright in the thesis and, except as herein before provided, neither the thesis nor any substantial portion thereof may be printed or otherwise reproduced in any material form whatsoever without the author's prior written permission.

Abstract

This thesis investigates electrically conductive polymer nanocomposites formulated with metal nanowires for electrostatic discharge and electromagnetic interference shielding.

Copper nanowires (CuNWs) of an average length of 1.98 μm and diameter of 25 ± 4 nm were synthesized. The oxidation reaction of the CuNWs in air can be divided into two stages at weight of 111.2% on TGA curves. The isoconversional activation energies determined by Starink method were used to fit the different master plots. Johnson-Mehl-Avrami (JMA) equation gave the best fit. The surface atoms of the CuNWs are the sites for the random nucleation and the crystallite strain in the CuNWs is the driving force for the growth of nuclei mechanism during the oxidation process.

To improve the anti-oxidation properties of the CuNWs, silver was coated onto the surface of the CuNWs in Ag-amine solution. The prepared silver coated CuNWs (AgCuNWs) with silver content of 66.52 wt. %, diameter of 28–33 nm exhibited improved anti-oxidation behavior. The electrical resistivity of the AgCuNW/low density polyethylene (LDPE) nanocomposites is lower than that of the CuNW/LDPE nanocomposites with the same volume percentage of fillers.

The nanocomposites formulated with CuNWs and polyethylenes (PEs) were compared to study the different interaction between the CuNWs and the different types of PE matrices. The electrical conductivity of the different PE matrices

filled with the same concentrations of CuNWs correlated well with the level of the CuNW dispersion. The intermolecular force and entanglement resulting from the different macromolecular structures such as molecular weight and branching played an important role in the dispersion, electrical properties and rheological behaviour of the CuNW/PE nanocomposites.

Ferromagnetic polycrystalline nickel nanowires (NiNWs) were synthesized with uniform diameter of ca. 38 nm and an average length of 2.68 μm . The NiNW linear low density polyethylene (LLDPE) nanocomposites exhibited electrical percolation threshold at NiNW volume fraction of 0.005. The power law fitting results imply that the electrical conductivity of the NiNW/LLDPE nanocomposites mainly originated from the contact among individual nanowires.

Acknowledgement

First of all, I would like to express my sincere gratitude to my both supervisors Dr. Jingli Luo and Dr. Uttandaraman Sundararaj in acknowledgement of all their encouragement, guidance, inspiration, advice, contributions and friendship during these years. This PhD project would not be possible without the help and support from my both supervisors. At the same time, I am grateful to my supervisory committee member Dr. Dongyang Li.

I would like to appreciate the orientation and training by Dr. Xianzhu Fu and Dr. Adrien Vincent when I just arrived in Canada. I wish to acknowledge the help, advice and instruction from Dr. Bin Lin and Dr. Yun Bai the former members of polymer processing group. My special thanks would be given to Dr. Genaro A. Gelves, who trained me to synthesize copper nanowires, helped to arrange the tests, revised part of my papers, and discussed various academic issues with me. I would like to thank the other group members Dr. Kambiz Chizari, Dr. Hesam Ghasemi, Ms. Fatima Nia roodsari, Ms. Maryam Khajehpour, Ms. Yan Li, Ms. Ivonne Otero, Mr. Mohammad Arjmand, Mr. Ali Sarvi, Mr. Soheil Sadeghi and Mr. Alireza Zehtabeyazdi for the aid, discussion, teamwork, friendship and fun.

I want to thank the department of chemical and materials engineering at University of Alberta for giving me the opportunity of coming here and providing the excellent courses, good learning environment and knowledgeable

mentors. I also appreciate the office and labs provided by the department of chemical and petroleum engineering at University of Calgary.

We thank the Xerox Foundation and Natural Science and Engineering Research Council of Canada (NSERC) for the funding. We would like to thank Nova Chemical, Ticona, ExxonMobil, Dow Chemical Corporate for the generous donation of polymers. We thank Mr. Weixiang Dong for microtoming the nanocomposites, Dr. Tobias Fürstenhaupt for collecting the TEM images and Dr. Michael Schoel for SEM imaging. The imaging facilities provided by Microscopy and Imaging Facility (MIF) of University of Calgary are acknowledged too.

Finally, I would like to thank my dear wife Cui Yang for her tolerance, and accompanying me of this journey.

Table of Contents

| | |
|--|-----------|
| Chapter 1 Introduction..... | 1 |
| 1.1. Application of nanowires..... | 1 |
| 1.2. Synthesis of metal nanowires..... | 3 |
| 1.3. Porous aluminum oxide templates..... | 10 |
| 1.4. Applications of electrically conductive polymer nanocomposites..... | 16 |
| 1.5. From polymers to electrically conductive polymer nanocomposites | 18 |
| 1.6. Factors influencing the electrical conductivity or percolation threshold .. | 22 |
| <i>1.6.1. The influence of conductive fillers.....</i> | <i>22</i> |
| <i>1.6.2. The influence of polymer matrix.....</i> | <i>24</i> |
| <i>1.6.3. The influence of the mixing process.....</i> | <i>25</i> |
| 1.7. Motivation and overview of this project..... | 26 |
| 1.8. References..... | 30 |
| | |
| Chapter 2 Bench Scale Synthesis and Characterization of High Aspect Ratio Copper Nanowires with Anodic Porous Aluminum Oxide Template | 46 |
| 2.1. Introduction | 46 |
| 2.2. Experimental | 49 |
| <i>2.2.1. Preparation of anodic porous aluminum oxide template</i> | <i>49</i> |
| <i>2.2.2. AC electrodeposition of copper into the anodic PAO template.....</i> | <i>54</i> |
| <i>2.2.3. Liberation of copper nanowires from PAO templates.....</i> | <i>56</i> |
| <i>2.2.4. Determination of CuNWs yield with PAO templates anodized for different hours.....</i> | <i>59</i> |
| <i>2.2.5. Determination the length distribution of CuNWs</i> | <i>59</i> |
| <i>2.2.6. SEM and TEM characterization</i> | <i>60</i> |

| | |
|--|----|
| 2.2.7. XRD and XPS characterization | 61 |
| 2.3. Results and Discussion..... | 61 |
| 2.3.1. Surface morphological evolvement from aluminum plate to PAO template..... | 61 |
| 2.3.2. AC electrodeposition of copper into anodic PAO template..... | 64 |
| 2.3.3. Effect of the second anodization period on the yield..... | 66 |
| 2.3.4. Length distribution of the CuNWs | 69 |
| 2.3.5. Morphology and aspect ratio of the CuNWs | 71 |
| 2.3.6. Crystal structure and composition of the CuNWs | 75 |
| 2.4. Conclusions | 81 |
| 2.5. References..... | 82 |

Chapter 3 Oxidation Kinetics of Copper Nanowires Synthesized by AC Electrodeposition of Copper into Porous Aluminum Oxide Templates 87

| | |
|--|-----|
| 3.1. Introduction | 87 |
| 3.2. Experimental | 90 |
| 3.2.1. Preparation of CuNW dry powder..... | 90 |
| 3.2.2. Morphology characterization of the CuNWs..... | 90 |
| 3.2.3. Thermogravimetric analysis (TGA) of the CuNW powder | 91 |
| 3.2.4. XRD characterization | 93 |
| 3.3. Results and discussion | 93 |
| 3.3.1. CuNWs before oxidation..... | 93 |
| 3.3.2. Two stages oxidation of the CuNW powder..... | 97 |
| 3.3.3. Determination of activation energy by Kissinger method and isoconversional methods..... | 103 |
| 3.3.4. Determination of reaction kinetics | 108 |
| 3.4. Conclusions | 115 |
| 3.5. References..... | 116 |

Chapter 4 Silver Coated Copper Nanowires with Improved Anti-oxidation Property as Conductive Fillers in Low Density Polyethylene and Polystyrene..... 121

| | |
|---|------------|
| 4.1. Introduction | 121 |
| 4.2. Experimental | 123 |
| 4.2.1. <i>Synthesis of AgCuNWs.....</i> | <i>123</i> |
| 4.2.2. <i>Length distribution of the nanowires.....</i> | <i>125</i> |
| 4.2.3. <i>Preparation of NW/LDPE nanocomposites by hot solution mixing method.....</i> | <i>125</i> |
| 4.2.4. <i>Preparation of NW/PS nanocomposites by MSMP method.....</i> | <i>127</i> |
| 4.2.5. <i>Characterization of NWs, NW/LDPE and NW/PS nanocomposites</i> | <i>127</i> |
| 4.3. Results and discussion | 132 |
| 4.3.1. <i>Morphology and composition of the CuNWs and AgCuNWs</i> | <i>132</i> |
| 4.3.2. <i>Length distribution of the CuNWs and AgCuNWs.....</i> | <i>136</i> |
| 4.3.3. <i>Anti-oxidation behavior of the CuNWs and AgCuNWs</i> | <i>136</i> |
| 4.3.4. <i>Electrical resistivity of NW/LDPE nanocomposites, dispersion and composition of NWs in LDPE matrix.....</i> | <i>141</i> |
| 4.3.5. <i>The Effect of NWs on the crystallinity of the LDPE matrices.....</i> | <i>146</i> |
| 4.3.6. <i>Fragmentation of the AgCuNWs in PS matrices</i> | <i>148</i> |
| 4.4. Conclusions | 152 |
| 4.5. References..... | 153 |

Chapter 5 Effect of Macromolecular Structure on Electrical and Rheological Properties in Copper Nanowire Polyethylene Nanocomposites: Effect of Molecular Weight and Branching..... 159

| | |
|--|------------|
| 5.1. Introduction | 159 |
| 5.2. Experimental | 162 |
| 5.2.1. <i>Preparation of CuNW/CH₃OH dispersion.....</i> | <i>162</i> |
| 5.2.2. <i>DSC characterization of the PEs.....</i> | <i>163</i> |

| | |
|--|-----|
| 5.2.3. Preparation of CuNW/PE nanocomposites | 163 |
| 5.2.4. Morphological characterization of the CuNW/PE nanocomposites | 167 |
| 5.2.5. Electrical and rheological characterization of the CuNW/PE nanocomposites..... | 168 |
| 5.3. Results and discussion | 169 |
| 5.3.1. Electrical conductivity of the CuNW/PE nanocomposites..... | 169 |
| 5.3.2. Melt rheology of CuNW/PE nanocomposites at 200 °C..... | 171 |
| 5.3.3. Morphology of CuNW/PE nanocomposites | 190 |
| 5.3.4. Effect of macromolecular structures on filler dispersion, electrical and rheological properties | 195 |
| 5.4. Conclusions | 202 |
| 5.5. References..... | 203 |

Chapter 6 Scalable AC Electrosynthesis and Characterization of High Aspect Ratio Polycrystalline Nickel Nanowires 208

| | |
|--|-----|
| 6.1. Introduction | 208 |
| 6.2. Experimental | 211 |
| 6.2.1. Preparation of anodic PAO templates..... | 211 |
| 6.2.2. AC electrodeposition of Ni into the PAO templates and the liberation of the deposited NiNWs..... | 212 |
| 6.2.3. Preparation of NiNW/LLDPE nanocomposites..... | 214 |
| 6.2.4. SEM characterization of the aluminum plates, the liberated NiNWs and the NiNW/LLDPE nanocomposites..... | 214 |
| 6.2.5. TEM/EDX/SAED characterization of the liberated NiNWs and the NiNW/LLDPE nanocomposites | 215 |
| 6.2.6. XRD and XPS characterization of the NiNW powder | 215 |
| 6.2.7. TGA of the NiNW powder | 216 |
| 6.2.8. Ferromagnetic properties of the NiNW powder | 216 |
| 6.2.9. Electrical characterization of the NiNW/LLDPE nanocomposites . | 217 |
| 6.3. Results and discussion | 217 |

| | |
|--|------------|
| 6.3.1. Surface morphology evolvement of the aluminum plate during the anodization in oxalic acid solution..... | 217 |
| 6.3.2. Morphology and aspect ratio of the liberated NiNWs..... | 219 |
| 6.3.3. Chemistry and crystal structure of liberated NiNWs..... | 222 |
| 6.3.4. TGA of the NiNW powder..... | 229 |
| 6.3.5. Ferromagnetic properties of the NiNW powder..... | 231 |
| 6.3.6. Electrical resistivity of the NiNW/LLDPE nanocomposites and the dispersion of NiNWs..... | 234 |
| 6.4. Conclusions..... | 240 |
| 6.5. References..... | 242 |
| Chapter 7 General Discussion and Future Work | 245 |
| 7.1. General discussion..... | 245 |
| 7.2. Future work..... | 253 |
| 7.2.1. Enhancing dispersion of CuNWs in polymer matrix by melt mixing..... | 253 |
| 7.2.2. Quantitation of the structure-property relationships in CuNW/LLDPE nanocomposites..... | 255 |
| 7.2.3. Evaluation of the EMI shielding and mechanical properties of the NiNW/PE nanocomposites..... | 256 |
| 7.2.4. Polymer nanocomposites of hybrid conductive nanofillers..... | 256 |
| 7.3. References..... | 257 |

List of Tables:

| | |
|--|-----|
| Table 1-1. A summary on the size, properties, and uses of nano-sized fillers [89]. | 20 |
| Table 2-1. Composition of the solution for AC electrodeposition of copper. | 54 |
| Table 2-2. The d-spacings of the corresponding planes of fcc copper determined by MDI Jade 5.0 from the XRD pattern..... | 77 |
| Table 2-3. Chemical shifts of Cu ₂ O and CuO referenced to metal copper [19]. | 79 |
| Table 3-1. Activation energies Reported for Copper Oxidation [7]..... | 89 |
| Table 3-2. Algebraic expressions for the $f(\alpha)$ and $g(\alpha)$ functions for the most common mechanisms in solid reactions [22]..... | 111 |
| Table 4-1. The quantitative element content of the AgCuNWs determined from the EDX spectra. | 135 |
| Table 5-1. The details of the four types of PEs used as polymer matrices | 164 |
| Table 6-1. The electrical conductivity relative to copper (σ_r), relative magnetic permeability (μ_r) and the product of both ($\sigma_r\mu_r$) of selected metals and alloys [4]. | 209 |
| Table 6-2. The typical conditions to obtain self-ordered pores of different dimensions in polyprotic acids [6]. | 210 |
| Table 6-3. The AC electrodeposition conditions and solution composition. ... | 213 |
| Table 6-4. The d-spacings of the corresponding planes of fcc metal nickel determined from the SAED and XRD patterns..... | 225 |
| Table 6-5. The X-ray photoelectron binding energies (eV) of metal nickel and its oxides [9]..... | 229 |

List of Figures:

Figure 1-1. The structure of the O^{2-} / Al^{3+} deficit barrier layer that makes it function like a diode..... 7

Figure 1-2. The schematic illustration of the procedures to prepared PAO membrane for DC electrodeposition and AC electrodeposition. 8

Figure 1-3. The illustration of the ideal structure of the anodic PAO template. Reproduced with permission of ECS–The Electrochemical Society. “Conditions for fabrication of ideally ordered anodic porous alumina using pretextured Al” J. Electrochem. Soc. 2001; 148 (4): B152–B156. Copyright 2001. 10

Figure 1-4. A schematic flow chart represents the two-step anodization process for improved self-ordering of the pores in the anodic PAO template..... 12

Figure 1-5. The schematic illustration of the ion distribution and the movement direction within the barrier layer during the film growth (OXx- representing acid anion). 14

Figure 1-6. The SEM image of the highly ordered domain of a PAO template anodized in oxalic acid solution..... 15

Figure 1-7. The surface resistivity ranges of different materials and applications 17

Figure 2-1. Schematic illustrations of the six different approaches used to produce 1D nanostructures. (A) dictation by the anisotropic crystallographic structure of a solid, (B) confinement by a liquid droplet, (C) template assisted synthesis, (D) kinetic control with surfactant as a capping agent, (E) self-assembly of 0D nanostructures, (F) size reduction of 1D microstructure.

Reproduced with permission from “One-dimensional nanostructures: synthesis, characterization and applications” Adv. Mater. 2003; 15 (5): 353. Copyright 2003, Wiley-VCH. 47

Figure 2-2. The photographs of the plexiglass anodization tank: (a) the front view showing the setup overview and (b) the top view showing the configuration of electrodes and the electrical connection. The aluminum plates connected to the positive terminal with red alligator clips, the stainless steel plates connected to the negative terminal with black ones..... 51

Figure 2-3. The photograph of the front panel of the Mastech HY5020EX DC power supply for anodization..... 52

Figure 2-4. The stepwise anodization voltage decrease during barrier layer thinning at the end of the second anodization..... 53

Figure 2-5. The schematic illustration of the AC electrodeposition setup..... 55

Figure 2-6. The continuous sine voltage produced by a Kepco BOP 20–50 Mg power supply for the AC electrodeposition of copper into the anodic PAO template..... 56

Figure 2-7. The flow chart representing the process of the CuNWs synthesis by AC electrodeposition of copper into PAO template. 58

Figure 2-8. The surface morphological development from the aluminum plate to the PAO template: (a, b) acetone and NaOH (aq.) cleaned bare aluminum plate before anodization, (c, d) after anodized in 0.3 mol/L H₂SO₄ for 2 h, (e, f) after etched in a solution of 0.1 mol/L H₂CrO₄ and 0.3 mol/L H₃PO₄ under 60 °C for 30 min, (g, h) after anodized in 0.3 mol/L H₂SO₄ for 8 h..... 63

| | |
|--|----|
| Figure 2-9. The (a) low magnification and (b) high magnification SEM images showing the surface morphology of the PAO template electrically deposited with copper..... | 66 |
| Figure 2-10. CuNW yield with different second anodization periods. | 67 |
| Figure 2-11. The length distribution of the CuNWs synthesized with the PAO templates with the second anodization for 8 h, liberated with 1 mol/L NaOH solution and ultrasonicated for 1 h. (a) One of the SEM images used for measuring the lengths of individual CuNWs, (b) the statistical results of the CuNWs length distribution. | 71 |
| Figure 2-12. The SEM images of the CuNWs after liberation and 1 h ultrasonication. (a) The low magnification image of the area with few CuNWs, (b) the high magnification image of the area with concentrated CuNWs..... | 73 |
| Figure 2-13. The (a) low magnification and (b) high magnification TEM images of the CuNWs after liberation and 1 h ultrasonication. | 74 |
| Figure 2-14. The EDX spectra of the CuNWs on an aluminum stub collected with the SEM EDX analyzer..... | 75 |
| Figure 2-15. The XRD pattern of the CuNW powder..... | 76 |
| Figure 2-16. The X-ray photoelectron spectra of the CuNW powder. (a) The surveys, (b) the high resolution XP spectra of the Cu 2P peak and (c) the high resolution XP spectra of the Cu LMM peak. | 79 |
| Figure 3-1. The photographs of (a) the TA Q500 TGA and (b) the furnace configuration and gas flow route. | 92 |

| | |
|--|-----|
| Figure 3-2. The (a, b) SEM and (c) TEM images of the CuNWs before oxidation. | 95 |
| Figure 3-3. The XRD patterns of the CuNW powder before oxidation, after stage 1 and after stage 2. | 96 |
| Figure 3-4. The TGA plot of the CuNW powder before oxidation reduced in H ₂ | 97 |
| Figure 3-5. The TGA curves of the CuNW powder oxidized at different heating rates. | 98 |
| Figure 3-6. The DTG curves of the CuNW powder oxidized at different heating rates. | 99 |
| Figure 3-7. The (a, c) SEM and (b, d) TEM images of the CuNWs oxidized (a, b) after stage 1 and (c, d) after stage 2. | 102 |
| Figure 3-8. The Arrhenius plots based on Kissinger Equation for stage 1 and stage 2. | 104 |
| Figure 3-9. The activation energies for stage 1 determined by the different model free isoconversional equations. | 106 |
| Figure 3-10. The activation energies for Stage 2 determined by the different model free isoconversional equations. | 107 |
| Figure 3-11. Kinetic model fitting for the CuNW powder oxidation using JMA equation in Table 3–2 with different <i>m</i> values. | 113 |
| Figure 4-1. The flow chart representing the process of the AgCuNW synthesis by chemical plating method. | 125 |

| | |
|---|-----|
| Figure 4-2. The photographs of the (a) Loresta GP resistivity meter, (b) ESP four-pin probe and (c) Keithley 6517A electrometer (right) with an 8009 test fixture (left)..... | 131 |
| Figure 4-3. The (a, b) secondary SEM images and (c, d) TEM images of the (a, c) CuNWs and (b, d) AgCuNWs..... | 133 |
| Figure 4-4. The EDX spectra of the CuNWs and AgCuNWs..... | 135 |
| Figure 4-5. The length distribution of the AgCuNWs. | 136 |
| Figure 4-6. The XRD patterns of the CuNWs and AgCuNWs. | 138 |
| Figure 4-7. The temperature-dependent TGA curves of the CuNWs and AgCuNWs using 100 mL/min air as purge gas at 10 °C/min heating rate. | 139 |
| Figure 4-8. The time-dependent TGA curves of the CuNWs and AgCuNWs using 100 mL/min air as purge gas at 250 °C. | 140 |
| Figure 4-9. The volume electrical resistivity of the CuNW/LDPE and AgCuNW/LDPE nanocomposites as a function of the volume concentration of the NWs..... | 142 |
| Figure 4-10. The (a, b) backscattered SEM images of the freeze fractures and (c, d, e, f) TEM images of the ultramicrotomed section of the LDPE nanocomposites, containing 1 vol. % of either the (a, c, e) CuNWs or the (b, d, f) AgCuNWs. The (c, d) TEM images show the areas with less concentrated NWs in the nanocomposites. And the (e, f) TEM images show the concentrated NWs in the nanocomposites with alignments. | 144 |
| Figure 4-11. The XRD patterns of the reference neat LDPE and the compression molded CuNW/LDPE and AgCuNW/LDPE nanocomposites. | 146 |

| | |
|--|-----|
| Figure 4-12. The effect of the NW concentration on the crystallinity of the LDPE matrices in the CuNW/LDPE and AgCuNW/LDPE nanocomposites... | 148 |
| Figure 4-13. The volume electrical resistivity of the CuNW/PS and AgCuNW/PS nanocomposites as a function of the volume concentration of the NWs. | 149 |
| Figure 4-14. The backscattered SEM images of the freeze fractures of the AgCuNW/PS nanocomposites, containing 4.0 vol. % of the AgCuNWs, (a) before the compression molding, (b) after the compression molding and (c) after the removal of the PS matrices from the molded samples. | 151 |
| Figure 5-1. The DSC analyses of the four types of PEs used as polymer matrices. | 165 |
| Figure 5-2. The flow chart illustrating the experimental process for the CuNW/PE nanocomposite preparation and characterization..... | 167 |
| Figure 5-3. The electrical conductivity of the four types of PE nanocomposites with different concentrations of CuNWs. | 170 |
| Figure 5-4. Complex viscosity (η^*) as a function of frequency at 200 °C for the (a) CuNW/UHMWPE, (b) CuNW/HDPE, (c) CuNW/LDPE and (d) CuNW/LLDPE nanocomposites..... | 175 |
| Figure 5-5. Storage Modulus (G') as a function of frequency at 200 °C for the (a) CuNW/UHMWPE, (b) CuNW/HDPE, (c) CuNW/LDPE and (d) CuNW/LLDPE nanocomposites..... | 178 |

| | |
|---|-----|
| Figure 5-6. Phase angle (δ) as a function of the absolute value of the complex modulus (van Gorp Palmen plot) at 200 °C for the (a) CuNW/UHMWPE, (b) CuNW/HDPE, (c) CuNW/LDPE and (d) CuNW/LLDPE nanocomposites..... | 183 |
| Figure 5-7. Storage modulus (G') versus loss modulus (G'') at 200 °C for the (a) CuNW/UHMWPE, (b) CuNW/HDPE, (c) CuNW/LDPE and (d) CuNW/LLDPE nanocomposites..... | 187 |
| Figure 5-8. The (a) complex viscosity (η^*) and (b) storage modulus (G') at 200 °C and 1 rad/s for the CuNW/PE nanocomposites as functions of the CuNW concentration..... | 189 |
| Figure 5-9. The low (left) and high (right) magnification backscattered SEM images of the freeze-fractured (a, b) UHMWPE, (c, d) HDPE, (e, f) LDPE and (g, h) LLDPE nanocomposites containing 1.0 vol. % CuNWs..... | 192 |
| Figure 5-10. The low (left) and high (right) magnification TEM images of the (a, b) UHMWPE, (c, d) HDPE, (e, f) LDPE and (g, h) LLDPE nanocomposites containing 1.0 vol. % CuNWs. | 195 |
| Figure 5-11. The schematic illustration of CuNW dispersion, the (a, c, e, g) rheological percolation threshold at 200 °C and (b, c, d, f) electrical percolation threshold for the (a, b) CuNW/UHMWPE, (c) CuNW/HDPE, (d, e) CuNW/LDPE and (f, g) CuNW/LLDPE nanocomposites. I represents the networks between the polymer chains (poly-poly networks), II stands for the networks between the polymer chain and the individual CuNWs/CuNW agglomerates (poly-NW networks), III presents the networks formed among the individual CuNWs/CuNW agglomerates (NW-NW networks). II poly-NW | |

| | |
|--|-----|
| network is absent in d, e, f and g because the branches on the chains of LDPE and LLDPE hinder its formation. The CuNW concentration in the nanocomposites increases from left to right. | 201 |
| Figure 6-1. The photograph of the anodization setup in a double-walled, chilled cylindrical glass container..... | 212 |
| Figure 6-2. Surface morphology development of the aluminum plate during the anodization: (a, b) after anodized in 0.3 mol/L oxalic acid for 2 h, (c, d) after etched in the solution of 0.1 mol/L H ₂ CrO ₄ and 0.3 mol/L H ₃ PO ₄ under 60 °C for 30 min, (e, f) after anodized in 0.3 mol/L oxalic acid for 8 h. | 218 |
| Figure 6-3. The (a) low magnification and (b) high magnification (b) SEM images of the liberated NiNWs..... | 220 |
| Figure 6-4. The (a) SEM image with well-dispersed NiNWs used for length distribution determination and the (b) length distribution of the NiNWs..... | 221 |
| Figure 6-5. The low magnification (a) and high magnification (b) TEM images of liberated NiNWs. | 222 |
| Figure 6-6. The EDX spectra of the NiNW powder collected with TEM. | 223 |
| Figure 6-7. The SAED pattern of the NiNW powder collected with TEM. | 224 |
| Figure 6-8. The XRD pattern of the NiNW powder. | 225 |
| Figure 6-9. The X-ray photoelectron spectra of the NiNW powder. (a) The surveys, (b) the high resolution XP spectra of O 1S peak and (c) the high resolution XP spectra of Ni 2P _{3/2} peak..... | 228 |
| Figure 6-10. The TGA plot of the NiNW powder heated up to 600 °C at 10 °C/min rate in air. | 230 |

| | |
|---|-----|
| Figure 6-11. The TGA plot of the NiNW powder heated up to 800 °C at 10 °C/min rate in 4% H ₂ | 231 |
| Figure 6-12. The photographs of (a) the NiNWs staying on the bottom in methanol and (b) the NiNWs attracted to one side of the vial by a bar permanent magnet..... | 232 |
| Figure 6-13. The TGA plot for the determination of the Curie temperature and ferromagnetism reversibility of the NiNW powder. | 234 |
| Figure 6-14. (a) The electrical conductivity of the NiNW/LLDPE nanocomposites as a function of the volume fraction of the NiNWs, and (b) the linear fitting of the data to the power law for the electrical conductivity with percolation threshold $\phi_c = 0.005$ | 237 |
| Figure 6-15. The (a, b) backscattered SEM images of the freeze fractures and (c, d) TEM images of the ultramicrotomed section of the NiNW/LLDPE nanocomposites, containing 1 vol. % of NiNWs. | 240 |

Abbreviations:

| | |
|--------|---|
| PAO | porous aluminum oxide |
| CuNW | copper nanowire |
| PNC | polymer nanocomposite |
| AgNW | silver nanowire |
| ESD | electrostatic dissipative |
| EMI | electromagnetic interference |
| ECPNC | electrically conductive polymer nanocomposite |
| VGCNF | vapor grown carbon nanofibers |
| CNT | carbon nanotube |
| PS | polystyrene |
| PE | polyethylene |
| NiNW | nickel nanowire |
| AgCuNW | silver coated copper nanowire |
| UHMWPE | ultra high molecular weight polyethylene |
| HDPE | high density polyethylene |
| LDPE | low density polyethylene |

LLDPE linear low density polyethylene

MSMP miscible solvent mixing and precipitation

Nomenclature:

| | |
|----------|--------------------------------------|
| t_{bl} | thickness of the barrier layer |
| V_a | anodization voltage |
| R_c | contact resistance |
| ρ_T | bulk resistivity |
| E | Young's Modulus |
| ν | Poisson's ratio |
| F | elastic force |
| r | protrusion radius |
| W_i | initial weight percentage |
| W_f | final weight percentage |
| $W(T)$ | weight percentage at temperature T |
| A | Arrhenius frequency factor |
| E_a | activation energy |
| α | conversion ratio |
| β | heating rate |
| R | gas constant |

| | |
|----------|----------------------------------|
| ρ_v | volume resistivity |
| R_v | volume resistance |
| T_C | Curie temperature |
| σ | electrical conductivity |
| ϕ | volume fraction |
| ϕ_c | electrical percolation threshold |

Chapter 1

Introduction

In this thesis, the synthesis of metal nanowires by AC electrodeposition of metal into porous aluminum oxide (PAO) templates, coating of silver onto copper nanowires (CuNWs) to improve anti-oxidation behavior, and the electrical and rheological properties of metal nanowires polymer nanocomposites (PNCs) are presented. This chapter introduces the general background related to this research including the fabrication of PAO template, the synthesis and application of metal nanowires and metal nanowire/polymer nanocomposites, and the electrical conduction mechanism. Finally, the motivations and the structure of this thesis are presented at the end of this chapter.

1.1. Application of nanowires

Nanowires are conductive nanofibers with a solid core and have diameter less than 100 nm. They have a variety of potential applications due to their unique electrical, optical, magnetic and chemical properties [1–8]. The electrical properties of nanowires have been intensively studied. The high electrical conductivity and extremely small size make them very promising candidates in nanoelectronics application [9–11]. Many researchers have demonstrated the application of nanowires made of various materials in transistors [12–15]. The

thermoelectric properties of the nanowires made of a variety of materials such as bismuth alloys [15–18] and skutterudites [19, 20] have been widely studied; some of these nanowires and their composites showed superconducting properties [21–23].

Another field that can be greatly impacted by the application of nanowires is sensing. Electromagnetic field enhancement at the tip of metal nanowires provides feasibility to use them for chemical sensing by measuring the changes in the electrical or physical properties of the nanowires in the presence of the target analyte [24]. Nanowire sensors have been developed based on the electrical resistivity response of Ag, Au and Pt nanowires to chemical species to detect amines [25], ammonia [26], and hydrogen [27], respectively. Other gases such as oxygen [28] and NO₂ [29] have also been detected by nanowire sensors at very low concentrations. Nanowire sensors to detect the presence of ultraviolet light [30] or low-density lipoprotein cholesterol [31], and the changes in pH [32] have also been developed. The sensitivity of nanowire sensors may be improved by selective doping or surface modifications that enhance their affinity for certain substances [33].

Many efforts have been made to investigate the optical properties of nanowires and nanowire arrays such as the infrared absorption of bismuth nanowires [34] and the green light emission from ZnSe nanowires [35]. Nanowire laser [36, 37] can be created by using nanoribbons (nanowires with rectangular cross sections) as waveguides. Silver nanowires (AgNWs) have been

demonstrated to produce a substance that exhibits a negative index of the refraction-like properties in the near-infrared [38].

Some researchers also attempted to use metal nanowires for plasmonics applications [39]. Ni-Au nanorods of 100 nm in diameter internalized into cells were attempted to deliver genes directly into the nucleus [40]. Au nanorods can strongly absorb the near-infrared radiation and cause local temperature increase, which can be utilized to kill cancer cells in cell cultures [41]. Our group is working on the application of PNCs with low concentrations of metal nanowires for electrostatic dissipative (ESD), antistatic and electromagnetic interference (EMI) shielding [42, 43]. Ferromagnetic nanowires are even more interesting in that they have the possible application as ultra-high-density magnetic data storage devices [44, 45]. The advantages of ferromagnetic nanowires filled PNCs for EMI shielding application are that the shielding effect by absorption mechanism can be significantly improved due to their relatively higher magnetic permeability [46] and the distribution of the ferromagnetic nanowires in polymer matrices can be localized as desired by manipulating the magnetic field so as to achieve maximum EMI shielding with minimum amount of nanowires.

1.2. Synthesis of metal nanowires

Silver nanowires (AgNWs) of 0.4 nm in diameter and approximately 750 nm in length are the smallest nanowires synthesized by the electro-/photochemical redox reaction in an ambient aqueous phase inside the pores of the self-assembled calyx(4)hydroquinone nanotube array template [47]. Metal nanowires

from 10 to 100 nm in diameter have attracted the interest of most researchers. One of the most common methods for metal nanowire synthesis is template assisted synthesis, in which the metal nanowires are grown within another nanometer-scale structure. Vapor or liquid phases can be introduced into, and solidified within, the nanometer-scale structured templates through the electro-/chemical reaction or the cooling process.

Electrochemical deposition is the most commonly used template growth method. Anodic PAO is the most frequently used template because it is relatively inert and easy to control the size, shape, and distribution of its pores [48, 49]. Polymer membranes by ion-track-etching can also be used as the template substrate [50–52]. Metal nanowires can also be synthesized by coating or filling nanotubes and other nanometer-scale fibers [47, 53–56]. The template substrate can then be etched away after deposition, leaving only metal nanowires behind.

The first attempt to synthesize Sn, In and Zn nanowires with hard porous templates was reported by Possin in 1970 [57]. Nanowires of 40–70 nm in diameter and up to 15 μm in length were synthesized by DC electrodeposition of metals into porous mica membranes that were coated with a metallic contact layer on one side prior to electrodeposition. The preparation of the porous mica membranes by acid etching of the tracks produced in mica by highly charged nuclear particles was first reported by Price and Walker in 1962 [58, 59]. Willaims and Giordano [60] improved Possin's method to synthesize Au nanowires as small as 80 \AA in diameter using the track-etched mica membranes.

Martin and Penner first prepared the track-etched porous polymeric membranes [61]. Martin later introduced PAO template to synthesize several 1D nanostructures: conductive polymer, semiconductor and metal nanowires [62]. Goad et al [63] further developed the synthesis of metal nanowires with PAO templates by AC electrodeposition.

After preparation of PAO templates, DC or AC current will be applied to the templates immersed in proper deposition solution to electrodeposit metals into the pores. The well-developed method of DC electrodeposition of metals into template pores can control the crystallinity and the precise modulation of composition along the length of the synthesized metal nanowires [64–68].

The alumina membranes commercially available for filtration application can also be used for DC electrodeposition to synthesize metal nanowires. However, the alumina membranes contain poorly ordered pores with varying diameter, which results in a wide distribution of diameters of the nanowires synthesized with the commercial alumina membranes as templates. Monodisperse nanostructures can be synthesized with the self-ordered PAO templates by DC electrodeposition. However, direct DC electrodeposition of metals into the PAO templates grown on Al substrate is hindered by the capacitance of the barrier layer between the bottom of the pores and the Al substrate, whose structure and mechanism of growth will be interpreted in Section 1.3. Due to the existence of the barrier layer, high voltage is required to tunnel electrons through and uniform deposition is difficult to achieve because of the increase of pH at the cathodic side that dissolves the barrier layer partially [69].

Therefore, several procedures are involved in the DC electrodeposition of metals into PAO templates. First, the PAO membrane must be detached from the Al substrate by dissolution in HgCl_2 or CuCl aqueous solution; and the pores have to be opened by removal of the barrier layer with H_3PO_4 etching [70, 71]. An electrically conductive layer of Au or Ag can then be sputtered or electrodeposited on one side of the PAO membrane, which can subsequently be used for DC electrodeposition. After DC electrodeposition, the sputtered electrically conductive layer can be dissolved in HNO_3 , and the PAO template can be removed by NaOH solution to liberate the metal nanowires [72].

Although the capacitance of the barrier layer of the PAO template adversely affects direct DC electrodeposition, the rectification property of the barrier layer makes it possible to electrodeposit metal into the nano-pores by AC current [73–77]. Aluminum oxide is a semiconductor material with high electrical resistivity. In the barrier layer of aluminum oxide, there are O^{2-} deficit at the interface between the barrier layer and the Al substrate, and Al^{3+} deficit in its lattice at the interface between the barrier layer and the electrolyte, which make the barrier layer act like a couple of N and P semiconductor that rectifies current like a diode [78]. Figure 1–1 represents the structure of the $\text{O}^{2-} / \text{Al}^{3+}$ deficit barrier layer that makes it function like a diode.

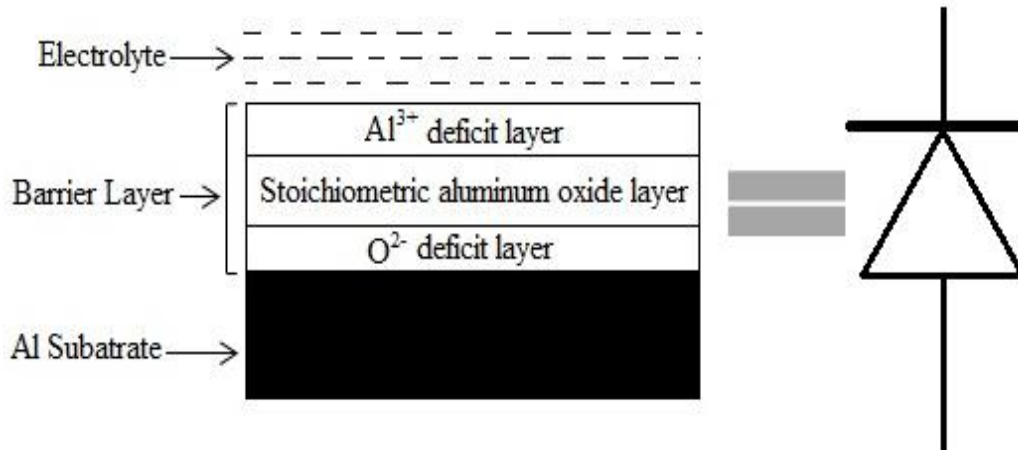


Figure 1-1. The structure of the O²⁻ / Al³⁺ deficit barrier layer that makes it function like a diode.

Although the barrier layer can function as a diode under AC electrodeposition, high AC voltage may still be required to tunnel electrons through the high resistivity barrier layer. This is even more crucial for the PAO templates anodized in oxalic acid or phosphoric acid solution, in which aluminum plates typically are anodized under DC 25 V or 195 V respectively.

However, the thickness of the barrier layer t_{bl} is proportional to the anodization voltage V_a , under which the aluminum plate is anodized. This relationship [79] can be expressed as:

$$t_{bl} = V_a \cdot 1.2 \text{ nm/V} \quad (1-1)$$

The property of this thickness of the barrier layer to the anodization voltage is a very useful relationship facilitates the thinning of the barrier layer, by turning down the anodization voltage at the end of anodization, to obtain certain thickness that is suitable for AC electrodeposition. It also ensures that the

template has adequate mechanical strength to hold the PAO template on the aluminum substrate. The appropriate voltage to meet both requirements is around 9 V [73]. The schematic illustration of the procedure used to prepare PAO membrane for DC electrodeposition and AC electrodeposition is presented in Figure 1-2.

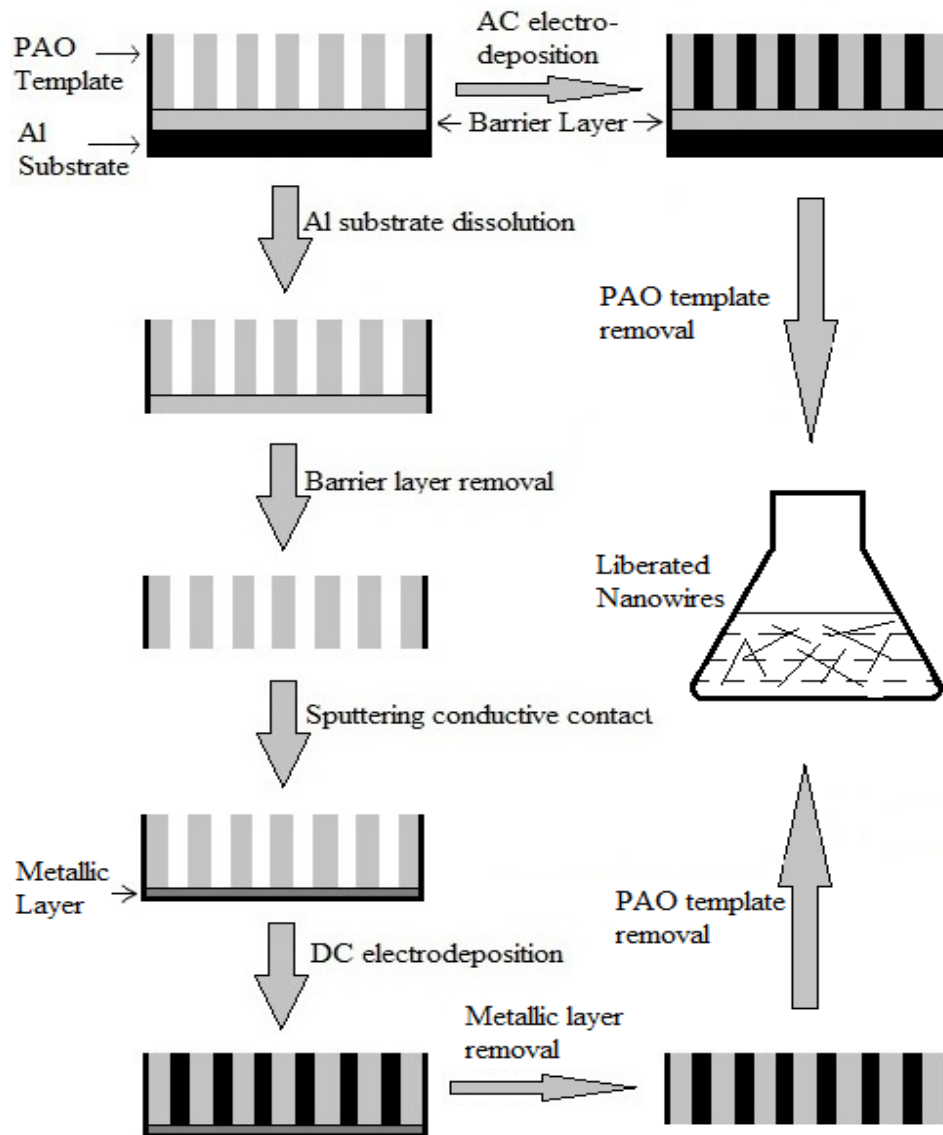


Figure 1-2. The schematic illustration of the procedures to prepared PAO membrane for DC electrodeposition and AC electrodeposition.

As shown in Figure 1–2, it requires six steps to get liberated nanowires from the anodized PAO templates by DC electrodeposition, but only two steps by AC electrodeposition. In addition, AC electrodeposition can use both faces of the aluminum plate as templates, and the plates can be reused after liberation until it becomes too thin to handle, which can dramatically bring down the unit cost of the nanowires by saving on the cost of the expensive high purity aluminum plates. Moreover, the PAO attached on aluminum substrate for AC electrodeposition has sufficient mechanical strength to facilitate the multi-step handling. In general, it is much easier and less infrastructure intensive to synthesize metal nanowires by AC electrodeposition than by DC electrodeposition. These are the main reasons we have used AC electrodeposition in this work.

Other efforts have been made on DC electrodeposition of metals into the PAO template attached on aluminum substrate directly. Gösele et al [80] synthesized monodisperse silver nanowire of 30 μm or more in length with a diameter monodispersity of about $\pm 2\%$ by direct DC electrodeposition of silver into the PAO template after thinning the barrier layer to ~ 1 nm by slowly reducing the anodization voltage to 1 V at the end of anodization. Zhou and co-workers [81] reported the fabrication of nickel nanorod arrays by DC electrodeposition without detaching the PAO template from the aluminum substrate by progressively turning down the anodization voltage from 40 V to 2V at the rate of 2 V/min at the end of anodization in 0.3 mol/L oxalic acid aqueous solution. We also tried a similar approach to prepare metal nanowires. Unfortunately, the

barrier layer became too thin to have adequate mechanical strength to hold the PAO template on the aluminum substrate when the final anodization voltage was decreased below 4 V, which in turn made it difficult to achieve uniform deposition.

1.3. Porous aluminum oxide templates

Porous aluminum oxide (PAO) templates have attracted more and more interest for the synthesis of 1D nanostructures. The structure and the growth mechanism of the PAO templates will be discussed in this section. The ideal geometry of the anodic PAO template with high aspect ratio of fine tunnels like a close-packed array of hexagonal cells each with a pore located in the center exhibits a honeycomb-like structure as shown in Figure 1-3.

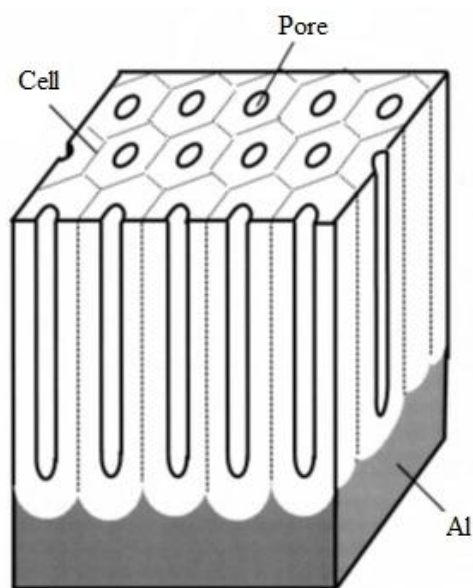


Figure 1-3. The illustration of the ideal structure of the anodic PAO template. Reproduced with permission of ECS–The Electrochemical Society. “Conditions

for fabrication of ideally ordered anodic porous alumina using pretextured Al” J. Electrochem. Soc. 2001; 148 (4): B152–B156. Copyright 2001.

Masuda et al [82–84] reported the hexagonally ordered array of the nanopores in the anodic PAO template by anodization of aluminum plate in oxalic acid or sulfuric acid solution. It was found that the self-ordering of the pores can be achieved by the prolonged anodization under specific conditions. Masuda and coworkers [84] later reported a two-step anodization process to improve the self-ordering of the pores in the anodic PAO template by selectively removing the PAO formed after the first step anodization that provides a structured aluminum surface facilitating the self-ordering of the pores during the second anodization. A schematic flow chart represents the two-step anodization process for improved self-ordering of the pores in the anodic PAO template is shown in Figure 1–4.

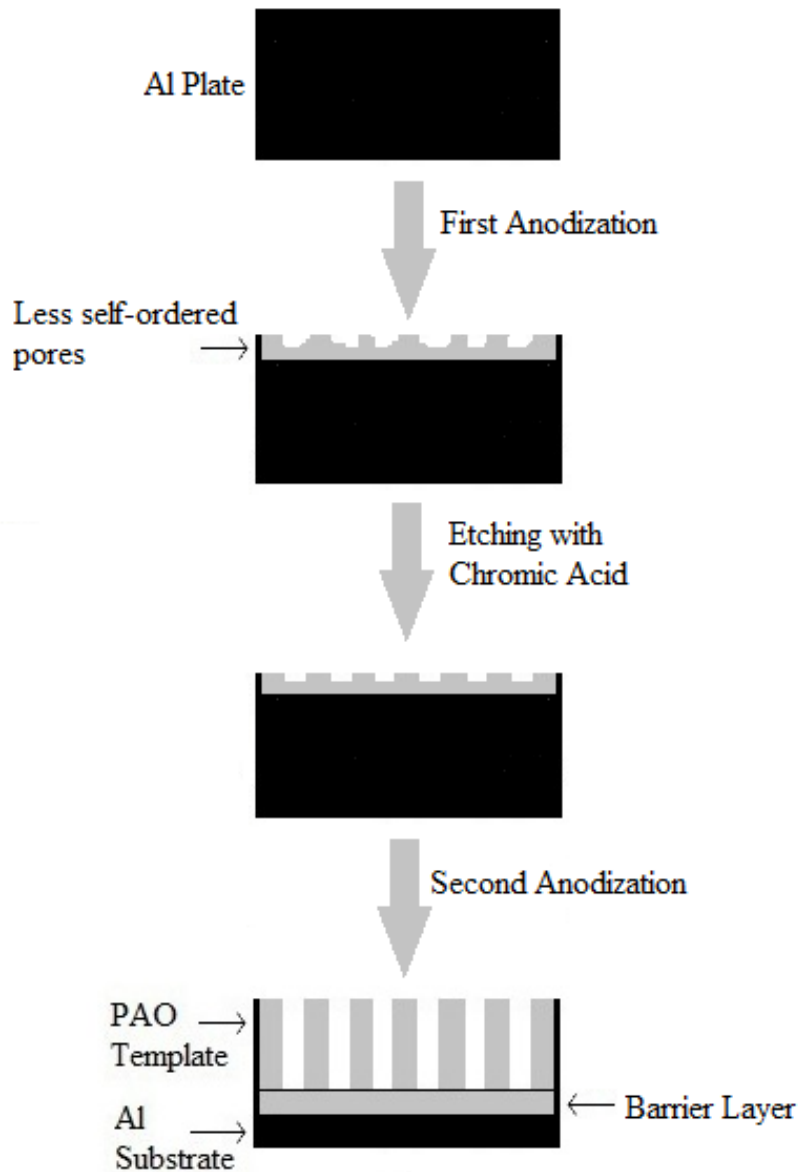


Figure 1-4. A schematic flow chart represents the two-step anodization process for improved self-ordering of the pores in the anodic PAO template.

Several models have been suggested to interpret the growth and formation mechanism of the anodic PAO templates. One of the most widely accepted

models was developed by O'Sullivan and Wood [79]. It was suggested that the pore initiation in the anodic film of the aluminum plate under constant current density occurs by the merging of the thickening oxide regions at neighboring locations, which is supposed to depend on the substructure of the substrate as well as the subsequent current density into the residual thin regions. The oxide dissolution can be significantly accelerated by the electrical field, which leads to the deepening of the pores due to the higher electrical field at the bottom of the pores than at the surface. Moreover, the heat produced by the electrical current and the dissolution process also plays an important role in the pore growth in that it is easier for the heat to accumulate to increase the local temperature at the bottom of pores which in turn accelerates the oxide dissolution at the bottom of the pores. The pores grow to keep their diameter in proportion to the applied voltage when approaching steady state. Under steady state, the barrier layer thickness, cell diameter and pore diameter are all proportionate to the applied voltage. The steady state is determined by the equilibrium between the oxide growth at the interface of Al/oxide and the electrical field enhanced oxide dissolution at the interface of oxide/electrolyte. This steady state equilibrium initiates the diffusion of Al^{3+} through the barrier layer to the oxide/electrolyte interface before it is dissolved into the acidic solution as well as the diffusion of O^{2-} through the barrier layer to the Al/oxide interface contributing to the oxide growth. Moreover, the authors also mentioned that there was evidence suggesting that some of the migrating anions are OH^- , besides O^{2-} or oxoanions from the acid. In addition, there was supposed to be a concentration gradient of

OH^- and oxoanions through the barrier layer with enrichment towards the outer surface as well as a reverse distribution for cations. Figure 1–5 schematically illustrates the ion distribution and the movement direction within the barrier layer during the film growth.

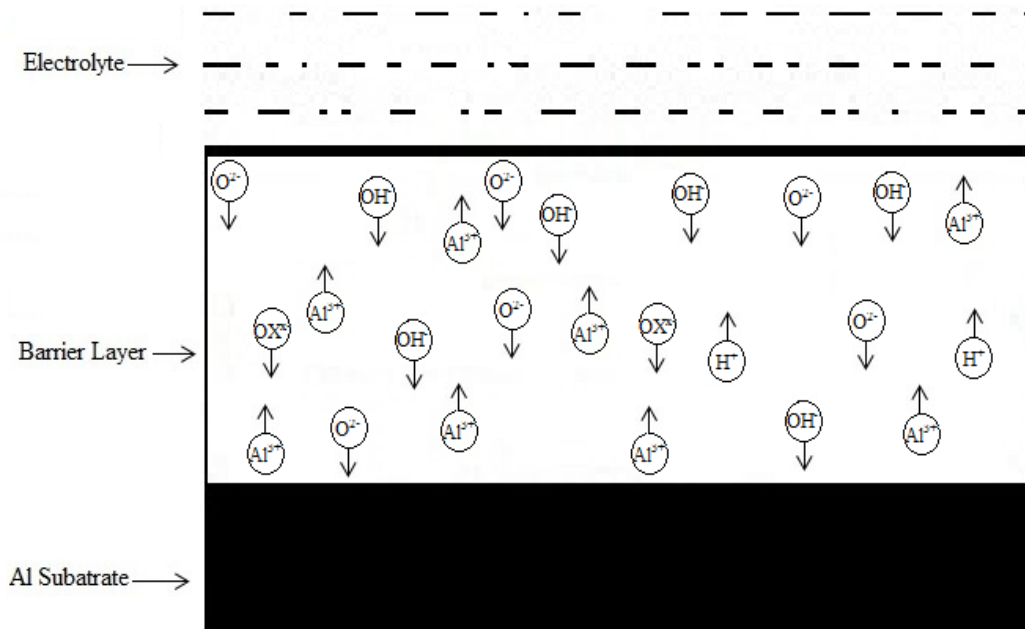


Figure 1-5. The schematic illustration of the ion distribution and the movement direction within the barrier layer during the film growth (OX^{x-} representing acid anion).

Gösele et al [83] described the mechanism of the formation of the self-organised hexagonal pore arrays in the anodic aluminum oxide. By anodizing the high purity aluminum plates in oxalic acid or sulfuric acid as electrolyte, it was found that the optimal conditions for the self-ordering of the pores occurred

when the anodization voltage corresponded to a moderate expansion of the aluminum during the oxidation, whereas no self-ordered domains can be observed when the aluminum volume contracted or expanded dramatically during the oxidation. Therefore, it was suggested that the mechanical stress associated with the expansion of the aluminum during the formation of oxide caused repulsive forces between the neighboring pores during the oxidation process leading to the formation of the self-organized hexagonal pore arrays. Figure 1-6 shows the SEM image of the highly ordered domain of a PAO template anodized in oxalic acid solution.

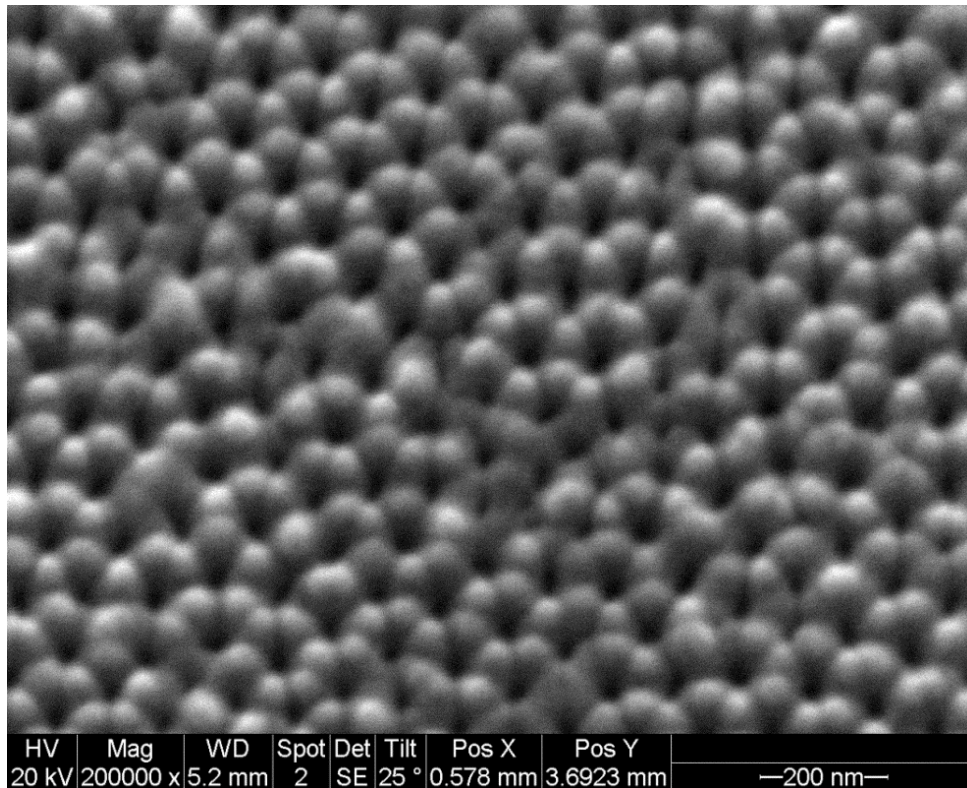


Figure 1-6. The SEM image of the highly ordered domain of a PAO template anodized in oxalic acid solution.

1.4. Applications of electrically conductive polymer nanocomposites

PNCs are among the most promising class of new materials because they are light weight, flexible, low cost, anti-corrosive, and have good processability and mechanical properties. Most polymers are electrical insulators and are used for a variety of insulating applications in industry. However, the inherent electrical insulation means polymers tend to hold the electrostatic charges, and allow the electromagnetic frequency interference (EMI) to travel through without loss

Engineers have begun to explore the design freedom and economic benefits of electrically conductive polymer nanocomposites (ECPNCs) in industrial and business applications for ESD and EMI shielding. Recently, ECPNCs have become the alternative materials to replace metals for the internals in electric components or as wrappers to protect the sensitive electric devices from the adverse effects of electrostatic charges or from the effect of the incoming EMI or to reduce the undesirable emission of EMI.

ESD is the transfer of electrostatic charges between bodies at different potentials induced by the direct contact of the electrostatic fields. ESD problems can destroy or damage sensitive electronic components, alter magnetic media, or trigger explosions or fires in inflammable environments. EMI is the radiated or conducted energy that impairs the performance of circuits or sensitive electronic devices. EMI can interfere with the operation of electric appliances, ruin data in large-scale computer systems, lead to inaccurate readings and output in aircraft guidance systems, and interrupt the functioning of precision medical devices

such as pacemakers. The economic loss to industry from the ESD and EMI shielding problems comprises billions of dollars each year [86].

The main objective of ESD is to limit the possible impact of ESD from the triboelectric charge generation, direct discharge, and electrostatic fields. The main objective of EMI shielding is to prevent the passage of the incoming or outgoing electromagnetic waves. EMI shielding works by reflection, absorption, or by transferring the electromagnetic radiation to ground.

The surface resistivity of the ECPNCs defines their applications. For ESD application, the desired surface resistivity ranges from $10^6 \Omega/\text{sq.}$ to $10^9 \Omega/\text{sq.}$; while the materials for effective EMI shielding should have a surface resistivity less than $10 \Omega/\text{sq.}$ [87]. Figure 1–7 shows the surface resistivity ranges of different materials and applications.

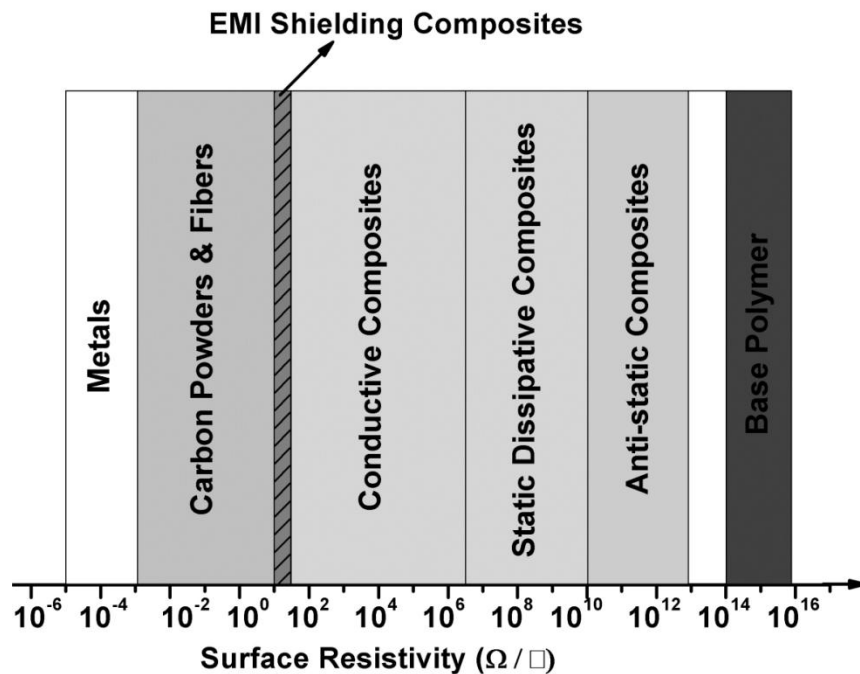


Figure 1-7. The surface resistivity ranges of different materials and applications.

ESD is required in computer chips and circuit board carriers for the shipping of electronic equipment as well as in the parts with relative motions between dissimilar materials such as conveyor belts, weaving machine arms and vehicle tires. Some working facilities like clean-rooms, integrated device workshops, etc also require ESD. In these demanding areas, the clothes, shoes, gloves, floor mats and carpets must be made of ESD materials. Explosion-proofing applications such as those in fuel production, storage and transportation systems and the chemical industry are rapidly growing markets for ESD. The largest market for EMI shielding is housings for machines or electronic components, which are either high EMI emitters or are particularly sensitive to incoming EMI. EMI shielding can be used within a wide variety of products such as: GPS devices, defense and military facility housings, precise analytical instruments, aerospace shuttles and components, airliner and helicopter components, personal computers, laptops and mobile phone housings, automotive components and medical device housings.

1.5. From polymers to electrically conductive polymer nanocomposites

The way to permanently endow insulative polymers with ESD and/or EMI shielding properties is to fill the matrices with specific conductive fillers to increase electrical conductivity. The conductive fillers comprise carbon black, carbon fibers, carbon nanofibers, carbon nanotubes, metallic powders/flakes/fibers, metal nanowires and intrinsically conductive polymers.

The conductivity of the polymer composites is determined by the polymer matrix, the conductive filler and the processing technique.

The price difference between the fillers and the polymer matrix and the desired composite properties determine the type and loading of fillers. Typically, conductive fillers are more expensive than the polymer matrix, so the goal is to minimize loading. On the practical point of view, filler selection depends on many considerations such as cost, availability, wettability and compatibility with the polymer matrix, effect on polymer rheology characteristics, physical properties, thermal stability, chemical resistivity, abrasiveness or wear, toxicity and recyclability [88]. The final application needs govern which factors are more important and which ones are less important. PNCs are polymers filled with small quantities of nano-sized particles. The nano-sized fillers are more attractive than the micron fillers in that the larger surface area of the nano-sized particles can have better interaction with the polymer matrix to improve the synergetic effect that provides the value-added properties not present in either the fillers or the polymer matrix. Moreover, the required dosage of the nano-sized fillers to achieve desirable properties is much less than that of the micron size fillers, which can significantly enable greater retention of the inherent processability and the mechanical properties of the polymer matrix. A summary on the size, properties, and uses of the nano-sized fillers is listed in Table 1–1 [89]. Some of the nano-sized fillers have been investigated to prepare ECPNCs for ESD and/or EMI shielding.

Table 1-1. A summary on the size, properties, and uses of nano-sized fillers [89].

| Nano-sized Fillers | Approx. Shape | Smallest Dimension (nm) | Aspect Ratio | Elastic Modulus (Mpa) | Electrical Conductivity (S/m) | Thermal Conductivity (W/m·K) | Commercial Uses |
|-------------------------------------|---------------|-------------------------|--------------|-----------------------|--------------------------------------|------------------------------|---|
| VGCNF | rod | 50–100 | 50–200 | 500 | 700–1,000 | 10–20 | hoses, aerospace, adhesives, ESD/EMI shielding, |
| MWCNT | rod | 5–50 | 100–10,000 | 1,000 | 500–10,000 | 100–1,000 | ESD/EMI shielding, sporting, automotive |
| SWCNT | rod | 0.6–1.8 | 1,000–10,000 | 1,500 | 1,000–10,000 | 1,000 | filters, ESD/EMI shielding |
| Nanoclay | plate | 1–10 | 50–1,000 | 200–250 | ... | 1–10 | automotive, packaging, sporting, aerospace |
| Nano-TiO ₂ | sphere | 10–40 | ~1 | 230,000 | 10 ⁻¹¹ –10 ⁻¹² | 12 | Photocatalysis, gas sensors, paint |
| Nano-Al ₂ O ₃ | sphere | 300 | ~1 | 50 | 10 ⁻¹⁴ | 20–30 | seal rings, furnace liner tubes, gas laser tubes, wear pads |
| Metal nanowires | wire | 5–100 | 50–500 | ... | 10 ⁶ –10 ⁸ | 400 | ESD/EMI shielding, adhesives, packaging |

Vapor grown carbon nanofibers (VGCNFs) as high aspect ratio conductive nano-sized fillers for PNCs have been evaluated. Zhang et al. [90] found that the EMI SE of the 3 mm thickness of polyesterpolyol filled with 6.7 wt. % VGCNFs was 35 dB and 60 dB for EM frequencies of 26 GHz and 75 GHz respectively and the EMI SE improved with increased thickness of the shielding nanocomposite. Lee et al. [91] reported that the EMI SE of 30 μm thick VGCNF/PVA film was lower than that of a film filled with carbon black of similar thickness, but the EMI SE of the VGCNF/PVA film increased significantly after heat treatment of the VGCNF. The application of VGCNFs as conductive fillers is limited by their poor tensile strength, leading to reduced aspect ratio during the mixing process.

Carbon nanotubes (CNTs) exhibit superior properties over other types of carbon fibers. Rao M. et al. [92] have drawn the structures of the single-walled carbon nanotube (SWCNT) and the multi-walled carbon nanotube (MWCNT). CNT/polymer nanocomposites have been widely investigated in the past years. The most attractive characteristic of CNTs as fillers in PNCs is the extremely low volume percolation threshold fraction (5.2×10^{-5} [93] in CNT/epoxy nanocomposites) due to their high aspect ratio and specific surface area as well as the tendency to be arranged in PNCs randomly to form electrically conductive networks [94]. Their tensile strength is almost 100 times higher than that of premium carbon fibers [95], which helps maintain their high aspect ratio during the mixing process. At the same time, CNTs are usually available in very entangled bundles, which results in serious handling and dispersion problems

during the preparation of PNCs [96]. And their price is also prohibitive (about \$375/g for unpurified nanotubes to about \$2000/g for purified ones) that limits its commercial availability [97].

Gelves et al. [98] prepared copper nanowires (CuNWs) and silver nanowires (AgNWs) of ca. 25 nm in diameter and 5–10 μm in length by electrodeposition in PAO templates. The CuNW/PS and AgNW/PS nanocomposites were prepared by solution processing, and the electrical percolation thresholds for the CuNW/PS and AgNW/PS nanocomposites were 0.50 vol. % and 0.63 vol. %, respectively [43]. Lin et al. [99] reported that there was copper oxide formed in the CuNW/PS nanocomposite prepared by melt mixing. The copper oxide layer on the surface of the CuNWs increases electrical resistivity dramatically, so the formation of copper oxide should be mitigated to ensure good conductivity of the PNCs filled with CuNWs.

1.6. Factors influencing the electrical conductivity or percolation threshold

1.6.1. The influence of conductive fillers

The types, concentration, geometry and morphology of conductive fillers are supposed to impact the overall electrical conductivity of PNCs significantly. For the highly conductive fillers, the contact resistance between fillers is the dominant contribution to the overall resistivity of PNCs [100]. Strumpler et al. [100] deduced equation (1–2) for the contact resistance between two fillers:

$$R_c = \frac{1}{2} \rho_T \left(\frac{2}{3} \frac{E}{1 - \nu^2} \right)^{\frac{1}{3}} F^{-\frac{1}{3}} r^{-\frac{1}{3}} \quad (1 - 2)$$

where, R_c is the contact resistance between the two fillers in contact, ρ_T is the bulk resistivity of the filler material, E is Young's Modulus, ν is Poisson's ratio, F is the elastic force between the grains and r is the protrusion radius.

According to equation (1-2), the contact resistance decreases with increasing protrusion radius. Usually, the protrusion radius increases with the particle size, so larger filler particles should lead to lower overall resistivity of PNCs. From equation (1-2), the contact resistance increases with increasing Young's modulus. In other words, the material with lower Young's modulus is easier to deform under stress. Thus when in contact, the fillers with lower Young's modulus can attain larger contact area by the deformation caused by the contact stress. The larger contact area, in turn, results in the lower contact resistance. Therefore, the metallic fillers with lower Young's modulus and better ductility contact each other over a larger area than the ceramic and carbon fillers which are very hard and thus, they contact each other at point-like areas.

The aspect ratio of fillers is another important factor that influences the electrical conductivity of PNCs. The fillers with higher aspect ratio can reduce the percolation threshold concentration significantly.

1.6.2. The influence of polymer matrix

Miyasaka et al. [101] reported that the electrical percolation threshold of PNCs is related to the polarity of the polymer matrix: the higher polarity of the polymer matrix, the higher the electrical percolation threshold concentration of the carbon particles. However, the opposite relationship was also observed by Sau et al. [102] in the ethylene-propylenediene monomer rubber (EPDM)/acrylonitrile butadiene rubber (NBR)/their blends and acetylene black systems.

The electrical percolation threshold also depends on the viscosity of the polymer matrix in the mixing process. The percolation threshold concentration increases with the increasing viscosity. Part of the reason is that it is more difficult to disperse the fillers homogeneously when the polymer matrix viscosity is higher. In addition, fillers in polymer matrices with higher viscosity are subjected to more severe degradation in the mixing process, which results in lower aspect ratio.

Crystallinity of the polymer matrix can influence the distribution of the conductive fillers. For instance, carbon black aggregates tend to concentrate in the amorphous region in the semi-crystalline polymers leading to lower electrical percolation threshold concentration.

Gubbels et al. [103] successfully decreased the electrical percolation threshold concentration of carbon blacks by selectively distributing the carbon black aggregates in one phase of the multiphase polymers or in the interface of

the multiphase polymers. Al-Saleh and Sundararaj [104] selectively localized the carbon black aggregates at the immiscible interface of polypropylene/polystyrene (PP/PS) blend by introducing styrene-butadiene-styrene (SBS) tri-block copolymer to the blend, which increased the composite conductivity significantly in the (60/40) and (70/30) PP/PS blends upon the addition of 5 vol. % SBS.

In summary, some information has been reported in the literature regarding the influence of the polymer matrix on the electrical percolation threshold, conductivity or EMI SE of the composites. However, these relationships are not precise due to the interaction between factors and the complexity of the polymer matrix itself.

1.6.3. The influence of the mixing process

The mixing process is instrumental to disperse the conductive fillers in the polymer matrix homogeneously, while the adverse effect of mixing, i.e. the reduction of the aspect ratio of the fillers due to breakage of filler particles should also be considered. Prolonging the mixing time can lead to better dispersion of the fillers, but since the fillers are also subjected to the shearing force for longer time there can be a negative effect on the electrical conductivity of the composites. Andrews et al. [96] studied the impact of mixing time on the length of MWCNTs by TEM analysis and showed that the length of MWCNTs decreased with the prolonged mixing time. Regarding the metallic fillers, longer

mixing time may also result in a thicker oxide layer on the surface which will dramatically increase the contact resistance.

Martin et al. [105] compared the resistivity of the high abrasion furnace (HAF) black filled polymer nanocomposites formed under different mixing temperature and found that the resistivity increased when increasing the mixing temperature was increased from 120 °C to 190 °C when the mixing was done open to air, while the relationship between the mixing temperature and the resistivity reversed if the mixing process was under nitrogen atmosphere. For metallic fillers, the higher mixing temperature in air may accelerate the oxide growth on the surface leading to the higher resistivity of the composites.

1.7. Motivation and overview of this project

In ESD and EMI shielding application, ECPNCs are better alternatives for surface coatings. All the surface coating operations are secondary to molding, and almost all these operations need surface pre-treatments to ensure the cleanliness so as to achieve desirable bonding between the conductive coating and the housings, which complicates the production process and results in additional cost. Unfortunately, it is still extremely difficult (or impossible) to apply coatings on the surface of some substrate materials such as polytetrafluoroethylene and polyolefins, even if the substrate surface has been completely cleaned and free of silicone mold release agents and other contaminants.

Surface coating can only produce a conductive layer of limited thickness on the housing. It has long been observed that until the conductive layer is thicker than the skin depth, there is almost no change in the attenuation of electrical fields that are also the fields for most electric devices [106]. Moreover, the performance of the thin conductive film is very poor in the shielding against low frequency magnetic fields [107]. Limitations may exist for the individual coating technology. For instance, vacuum metallization operation depends on the geometry of parts, and requires a basecoat for good adhesion and a topcoat to protect the conductive layer from flaking in humid environment [108]. Both the flame spraying and the metal arc spraying process may generate metal dusts and produce non-uniform films [108]. Electroplating requires the acid solution etching pre-treatment involves the toxic electroplating solution, and is highly energy-consuming [107]. Cathode sputtering can only be applied on the heat resistant substrates.

ECPNCs for ESD and EMI shielding work in a fundamentally different way from surface coatings. The conductivity of ECPNCs is in the wall of the enclosure rather than only on the surface. In this sense, there is no direct relationship between the shielding effect and the surface resistivity of the ECPNCs. On the contrary, it is the volume resistivity of the ECPNCs that determines their shielding effectiveness. Because of this volume effect, the practical shielding effect of the conductive polymer composite also depends on the wall thickness, the distribution and dispersion of the conductive fillers in the matrix and the overall conductive level of the filler.

ECPNCs show significant advantages over surface coating. The ESD and EMI shielding is an integrated part of the components made of ECPNCs, so there is no problem with delamination or scratching, which are the potential issues for surface coatings. ECPNC components are completed after molding or extrusion without additional coating process that can help reduce scrap rate and cost. Components made of ECPNCs do not require spraying or coating masks which results in lower setup expense and higher productivity. ECPNCs can be developed as inclusions in almost all polymer materials. They can be used in complex component designs with ESD or EMI shielding requirement where the cost of masking could be very high or prohibitive. They are more homogeneous than surface coating and thus less troublesome in thermal expansion, and can perform much more stable as moving mechanical components.

The nano-sized conductive fillers that can be used with the polymer matrix to formulate ECPNCs consist of carbon based materials, metallic materials and intrinsically conductive polymers. The morphology of the conductive nano-sized fillers includes powders, flakes, fibers, wires, nanotubes, nanowires, etc.

Regarding the materials of the conductive fillers, metals are more electrically conductive than others. Therefore, the ECPNCs formulated with the metallic nano-sized fillers could have better ESD/EMI shielding effect and lower percolation threshold concentration. On the other hand, most of the metals are more ductile than carbon, so the metallic fillers tend to bend rather than break under the shear flow that can help keep the initial aspect ratio of the fibrous

fillers. The most promising candidates among the metallic fillers are copper and nickel due to their high ductility, formability, strength, and electrical conductivity along with relatively low cost. The ECPNCs formulated with the ferromagnetic nickel fillers can be expected to achieve better EMI shielding effect by adsorption mechanism than those formulated with the non-ferromagnetic electrically conductive fillers due to the high magnetic permeability of the nickel fillers [109].

The nano-sized conductive fillers with higher interfacial area can improve the physical properties of the polymer matrix much more than the micron-sized fillers used in conventional polymer composites. The nano-sized fillers usually aggregate during the mixing process to be arranged in chains to form a kind of tree-like structures, which can shift the percolation threshold to the lower filler concentration. Otherwise, the percolation threshold can be significantly reduced by higher aspect ratio like fiber or wire shape fillers that can facilitate the form of the electrically conductive networks.

Based on the discussion above, CuNWs and nickel nanowires (NiNWs) are among the choices as fillers to formulate the ECPNCs for the ESD and EMI shielding application with a relatively lower filler concentration so as to keep the original processability and physical properties of the matrix polymer.

This thesis is organized in seven chapters. The first chapter is an introduction of relevant background information for the whole dissertation. The second chapter reports the synthesis of CuNWs by AC electrodeposition of copper into

anodic PAO templates. Oxidation kinetics of CuNWs in air is studied in the third chapter so as to understand their long term performance and durability. The fourth chapter reports the synthesis of silver coated copper nanowire (AgCuNWs) via chemical plating method and the evaluation of ECPNCs using AgCuNWs as fillers. The fifth chapter evaluates the effect of macromolecular structure on the electrical and rheological properties of the CuNW/polyethylene nanocomposites. The sixth chapter reports the synthesis and characterization of the ferromagnetic NiNWs as well as the evaluation of the electrical properties of the NiNWs/polyethylene nanocomposites. The conclusions and future work are summarized in the seventh chapter.

1.8. References

- [1] Nicewarner-Pena SR, Freeman RG, Reiss BD, He L, Pena DJ, Walton ID, Cromer R, Keating CD, Natan MJ. Submicrometer Metallic Barcodes. *Science* 2001; 294 (5540): 137–141.

- [2] Wang JG, Tian ML, Kumar N, Mallouk TE. Controllable Template Synthesis of Superconducting Zn Nanowires with Different Microstructures by Electrochemical Deposition. *Nano. Lett.* 2005; 5 (7): 1247–1253.

- [3] Francois MH, Luc P, Sebastien M. Fabrication and physical properties of Pb/Cu multilayered superconducting nanowires. *Appl. Phys. Lett.* 2005; 86 (15): 152510–152510–3.

- [4] Wang JG, Tian ML, Mallouk TE, Chan MHW. Microstructure and Interdiffusion of Template-Synthesized Au/Sn/Au Junction Nanowires. *Nano. Lett.* 2004; 4 (7): 1313–1318.
- [5] Salem AK, Hung CF, Kim TW, Wu TC, Searson PC, Leong KW. Multi-component nanorods for vaccination applications. *Nanotech.* 2005; 16 (4): 484–487.
- [6] Keating CD, Natan MJ. Striped Metal Nanowires as Building Blocks and Optical Tags. *Adv. Mater.* 2003; 15 (5): 451–454.
- [7] Gravier L, Serrano-Guisan S, Ansermet JP. Spin-dependent Peltier effect in Co/Cu multilayer nanowires. *J. Appl. Phys.* 2005; 97 (10): 10C501.
- [8] Paxton WF, Kistler KC, Olmeda CC, Sen A, St. Angelo SK, Cao YY, Mallouk TE, Lammert PE, Crespi VH. Catalytic Nanomotors: Autonomous Movement of Striped Nanorods. *J. Am. Chem. Soc.* 2004; 126 (41): 13424–13431.
- [9] Cui Y, Lieber, CM. Functional nanoscale electronic devices assembled using silicon nanowire building blocks. *Science* 2001; 291 (5505): 851–853.
- [10] Ferry DK. Nanowires in Nanoelectronics. *Science* 2008; 319 (5863): 579–580.
- [11] Tseng GY, Ellenbogen JC. Toward Nanocomputers. *Science* 2001; 294 (5545): 1293–1294.

- [12] Wang DW, Wang Q, Javey A, Tu R, Dai HJ, Kim H, McIntyre PC, Krishnamohan T, Saraswat KC. Germanium nanowire field-effect transistors with SiO₂ and high- κ HfO₂ gate dielectrics. *Appl. Phys. Lett.* 2003; 83 (12): 2432–2434.
- [13] Duan XF, Niu CM, Sahi V, Chen J, Parce JW, Empedocles S, Jay L, Goldman JL. High-performance thin-film transistors using semiconductor nanowires and nanoribbons. *Nature* 2003; 425: 274–278.
- [14] Chen J, Klaumunzer S, Lux-Steiner MC, Konenkamp R. Vertical nanowire transistors with low leakage current. *Appl. Phys. Lett.* 2004; 85 (8): 1401–1403.
- [15] Kang D, Park W. Change in electrical characteristics of gallium phosphide nanowire transistors under different environments. 2004; 4th IEEE Conference on Nanotechnology.
- [16] Huber T, Constant P, Celestine K. Magnetoresistance and thermopower of ultrafine bismuth nanowire arrays. 2001; 20th International Conference on Thermoelectronics.
- [17] Lin YM, Rabin O, Cronin SB, Ying JY, Dresselhaus MS. Experimental investigation of thermoelectric properties of Bi_{1-x}Sb_x nanowire arrays. 2002; 21st International Conference on Thermoelectronics.
- [18] Li DY, Prieto AL, Wu YY, Martin-Gonzalez MS, Stacy A, Sands T, Gronsky R, Yang PD; Majumdar A. Measurements of Bi₂Te₃ nanowire thermal

conductivity and Seebeck coefficient. 2002; 21st International Conference on Thermoelectronics.

[19] Wang JY, Liu H, Hu XB, Jiang HD, Zhao SR, Li Q, Boughton RI, Jiang MH. Progress in skutterudite-based thermoelectric materials. 2001; 20th International Conference on Thermoelectronics.

[20] Hu XB, Liu H, Wang JY, Jiang HD, Zhao SR, Zhang DM, Gu MY; Jiang MH. Synthesis and growth mechanism of $\text{NaFe}_4\text{P}_{12}$ nanowires. 2001; 20th International Conference on Thermoelectronics.

[21] Michotte S, Matefi-Tempfli S, Piraux L. Current-voltage characteristics of Pb and Sn granular superconducting nanowires. *Appl. Phys. Lett.* 2003; 82 (23): 4119–4121.

[22] de Horne F, Piraux L, Michotte S. Fabrication and physical properties of Pb/Cu multilayers superconducting nanowires. *Appl. Phys. Lett.* 2005; 86: 152510–1.

[23] Tian ML, Wang JG, Snyder J, Kurtz J, Liu Y, Schiffer P, Mallouk TE, Chan MHW. Synthesis and characterization of superconducting singlecrystal Sn nanowires. *Appl. Phys. Lett.* 2003; 83 (8): 1620–1622.

[24] Jeong DH, Zhang YX, Moskovits M. Polarized Surface Enhanced Raman Scattering from Aligned Silver Nanowire Rafts. *J. Phys. Chem. B* 2004; 108 (34) 12724–12728.

[25] Murray BJ, Newberg JT, Walter EC, Li Q, Hemminger JC, Penner RM. Reversible resistance modulation in mesoscopic silver wires induced by exposure to amine vapor. *Anal. Chem.* 2005; 77 (16): 5205–5214.

[26] Li CZ, He HX, Bogozzi A, Bunch JS, Tao NJ. Molecular detection based on conductance quantization of nanowires. *J. Appl. Phys. Lett.* 2000; 76 (10): 1333–1335.

[27] Favier F, Walter EC, Zach M, Benter T, Penner RM. Hydrogen Sensors and Switches from Electrodeposited Palladium Mesowire Arrays. *Science* 2001; 293 (5538): 2227–2231.

[28] Li QH, Liang YX, Wan Q, Wang TH. Oxygen sensing characteristics of individual ZnO nanowire transistors. 2004; *Appl. Phys. Lett.* 85; (26): 6389–6391.

[29] Zhang DH, Li C, Liu XL, Han S, Tang T, Zhou CW. Gas sensing properties of single-crystalline indium oxide nanowires. 2003; 3rd IEEE Conference on Nanotechnology.

[30] Kind H, Yan H, Messer B, Law M, Yang P. Nanowire ultraviolet photodetectors and optical switches. *Adv. Mater.* 2002; 14 (2): 158–160.

[31] Li C, Zhang DH, Lei B, Zhou CW. Detection of biomolecules using In_2O_3 nanowires. 2003; 3rd IEEE Conference on Nanotechnology

- [32] Cui Y, Wei Q, Park H, Lieber C. Nanowire nanosensors for highly sensitive and selective detection of biological and chemical species. *Science* 2001; 293 (5533): 1289–1292.
- [33] Zhang DH, Li C, Liu XL. Doping dependent NH₃ sensing of indium oxide nanowires. *Appl. Phys. Lett.* 2003; 83 (9): 1845–1847.
- [34] Black MR, Lin YM, Cronin SB, Rabin O, Dresselhaus MS. Infrared absorption in bismuth nanowires resulting from quantum confinement. *Phys. Rev. B* 2002; 65: 195417-1.
- [35] Xiang B, Zhang HZ, Li GH, Yang FH, Su FH, Wang RM, Xu J, Lu GW, Sun XC, Zhao Q, Yu DP. Green-light-emitting ZnSe nanowires fabricated via vapor phase growth. *Appl. Phys. Lett.* 2003; 82 (19): 3330–3332.
- [36] Johnson JC, Choi HJ, Knutsen KP, Schaller RD, Yang PD, Saykally RJ. Single gallium nitride nanowire lasers. *Nat. Mater.* 2002; 1, 106–110.
- [37] Kong YC, Yu DP, Zhang B, Fang W, Feng SQ. Ultraviolet-emitting ZnO nanowires synthesized by a physical vapor deposition approach. *Appl. Phys. Lett.* 2001; 78 (4), 407–409.
- [38] Hu XH, Chan CT. Photonic crystals with silver nanowires as a nearinfrared superlens. *Appl. Phys. Lett.* 2004; 85 (9): 1520–1522.

- [39] Maier SA, Atwater HA. Plasmonics: Localization and guiding of electromagnetic energy in metal/dielectric structures. *J. Appl. Phys.* 2005; 98 (1): 011101.
- [40] Salem AK, Searson PC, Leong KW. Multifunctional nanorods for gene delivery. *Nat. Mater.* 2003; 2 (10): 668–671.
- [41] Huang XH, El-Sayed IH, Qian W, El-Sayed MA. Cancer cell imaging and photothermal therapy in the near-Infrared region by using gold nanorods. *J. Am. Chem. Soc.* 2006; 128 (6): 2115–2120.
- [42] Gelves GA, Sundararaj U, Haber JA. Electrostatically dissipative polystyrene nanocomposites containing copper nanowires. *Macromol. Rapid Commun.* 2005, 26: 1677–1681.
- [43] Gelves GA, Lin B, Sundararaj U, Haber JA. Low electrical percolation threshold of silver and copper nanowires in polystyrene composites. *Adv. Funct. Mater.* 2006; 16: 2423–2430.
- [44] Tsuya N, Saito Y, Nakamura H, Hayano S, Furugohri A, Ohta K, Wakui Y, Tokushima T. A perpendicular magnetic recording medium by alumite. *J. Magn. Mater.* 1986; 54–57 (3): 1681–1682.
- [45] Kawai S, Ishiguro I. Recording characteristics of anodic oxide films on aluminum containing electrodeposited ferromagnetic metals and alloys. *J. Electrochem. Soc.* 1976; 123 (7): 1047–1051.

- [46] Chung DDL. Materials for electromagnetic interference shielding. *J. Mater. Eng. Perform.* 2000; 9 (3): 350–354.
- [47] Hong BH, Bae SC, Lee CW, Jeong S, Kim KS. Ultrathin single-crystalline silver nanowire arrays formed in an ambient solution phase. *Science* 2001; 294 (5541): 348–351.
- [48] Black MR, Lin YM, Cronin SB, Rabin O, Dresselhaus MS. Infrared absorption of bismuth nanowires resulting from quantum confinement. *Phys. Rev. B* 2002; 65 (19): 195417.
- [49] Nielsch K, Wehrspohn RB, Barthel J, Kirschner J, Gösele U, Fischer SF, Kronmüller H. Hexagonally ordered 100 nm period nickel nanowire arrays. *Appl. Phys. Lett.* 2001; 79 (9): 1360–1362.
- [50] Molares MET, Hühberger EM, Schaefflein C, Blick RH, Neumann R, Trautmann C. Electrical characterization of electrochemically grown single copper nanowires. *Appl. Phys. Lett.* 2003; 82 (13): 2139–2141.
- [51] Yu SF, Li NC, Wharton J, Martin CR. Nano wheat fields prepared by plasma-etching gold nanowire-containing membranes. *Nano Lett.* 2003; 3 (6): 815–818.
- [52] Tian ML, Wang JG, Snyder J, Kurtz J, Liu Y, Schiffer P, Mallouk TE, Chan MHW. Synthesis and characterization of superconducting singlecrystal Sn nanowires. *Appl. Phys. Lett.* 2003; 83 (8): 1620–1622.

- [53] Kumzerov Y. Transport properties of nanostructures within porous materials. 2002; 21st International Conference on Thermoelectronics.
- [54] Wu HP, Wu XJ, Ge MY, Zhang GQ, Wang YW, Jiang JZ. Properties investigation on isotropical conductive adhesives filled with silver coated carbon nanotubes. *Compos. Sci. Technol.* 2007; 67: 1182–1186.
- [55] Garcí'a-Vidal FJ, Pitarke JM, Pendry JB. Silver-filled carbon nanotubes used as spectroscopic enhancers. *Phys. Rev. B* 1998; 58 (11): 6783–6786.
- [56] Kalenczuk RJ, Borowiak-Palen E, Ruemmeli MH, Gemming T. Synthesis and characterization of silver filler single-wall carbon nanotubes. *Rev. Adv. Mater. Sci.* 2006; 12: 78–83.
- [57] Possin GE. A Method for Forming Very Small Diameter Wires. *Rev. Sci. Instrum.* 1970; 41 (5): 772–774.
- [58] Fleisher RL, Price PB, Walker RM. Method of forming fine holes of near atomic dimensions. *Rev. Sci. Instrum.* 1963; 34 (5): 510–512.
- [59] Price PB, Walker RM. Chemical Etching of Charged-Particle Tracks in Solids. *J. Appl. Phys.* 1962; 33 (12): 3407–3412.
- [60] Willaims WD, Giordano N. Fabrication of 80 Å metal wires. *Rev. Sci. Instrum.* 1984; 55 (3): 410–412.
- [61] Penner RM, Martin CR. Controlling the morphology of electronically conductive polymers. *J. Electrochem. Soc.* 1986; 133 (10): 2206–2207.

[62] Martin CR. Nanomaterials: a membrane-based synthetic approach. *Science* 1994; 266 (5193): 1961–1966.

[63] Goad DGW, Moskovits M. Colloidal metal in aluminum-oxide. *J. Appl. Phys.* 1978; 49 (5): 2929–2934.

[64] Tian ML, Wang JG, Kurtz J, Mallouk TE, Chan MHW. Electrochemical growth of single-crystal metal nanowires via a two-dimensional nucleation and growth mechanism. *Nano Lett.* 2003; 3 (7): 919–923.

[65] Wang JG, Tian ML, Mallouk TE, Chan MHW. Microtwinning in template-synthesized single-crystal metal nanowires. *J. Phys. Chem. B* 2004; 108 (3): 841–845.

[66] Pan H, Liu BH, Yi JB, Poh C, Lim S, Ding J, Feng YP, Huan HA, Lin JY. Growth of single-crystalline Ni and Co nanowires via electrochemical deposition and their magnetic properties. *J. Phys. Chem. B* 2005; 109 (8): 3094–3098.

[67] Salem AK, Chen M, Hayden J, Leong KW, Searson PC. Directed assembly of multisegment Au/Pt/Au nanowires. *Nano Lett.* 2004; 4 (6): 1163–1165.

[68] Salem AK, Chao J, Leong KW, Searson PC. Receptor-mediated self-assembly of multi-component magnetic nanowires. *Adv. Mater.* 2004; 16 (3): 268–271.

- [69] Nielsch K, Müller F, Li AP, Gösele U. Uniform Nickel Deposition into Ordered Alumina Pores by Pulsed Electrodeposition. *Adv. Mater.* 2000; 12 (8): 582–586.
- [70] Zhang XY, Zhang LD, Lei Y, Zhao LX, Mao TQ. Fabrication and characterization of highly ordered Au nanowire arrays. *J. Mater. Chem.* 2001; 11: 1732–1734.
- [71] Shingubara S. Fabrication of nanomaterials using porous alumina templates. *J. Nanopart. Res.* 2003; 5(1–2): 17–30.
- [72] Martin BR, Dermody DJ, Reiss BD, Fang MM, Lyon LA, Natan MJ, Mallouk TE. Orthogonal self-assembly on colloidal gold-platinum nanorods. *Adv. Mater.* 1999; 11 (12) 1021–1025.
- [73] Sauer G, Brehm G, Schneider S, Nielsch K, Wehrspohn RB, Choi J, Hofmeister H, Göselem U. Highly ordered monocrystalline silver nanowire arrays. *J. Appl. Phys.* 2002; 91 (5): 3243–3247.
- [74] D. AlMawlawi, N. Coombs, and M. Moskovits. Magnetic properties of Fe deposited into anodic aluminum oxide pores as a function of particle size. *J. Appl. Phys.* 1991; 70 (8): 4421–4425.
- [75] Preston CK, Moskovits M. Optical characterization of anodic aluminum oxide films containing electrochemically deposited metal particles. 1. Gold in phosphoric acid anodic aluminum oxide films. *J. Phys. Chem.* 1993; 97 (32): 8495–8503.

[76] Davydov DN, Sattari PA, AlMawlawi, Osika DA, Haslett TL, Moskovits M. Field emitters based on porous aluminum oxide templates. *J. Appl. Phys.* 1999; 86 (7): 3983–3987.

[77] Yin AJ, Li J, Jian W, Bennett AJ, Xu JM. Fabrication of highly ordered metallic nanowire arrays by electrodeposition. *Appl. Phys. Lett.* 2001; 79 (7): 1039–1041.

[78] Saedi A, Ghorbani M. Electrodeposition of Ni–Fe–Co alloy nanowire in modified AAO template. *Mater. Chem. Phys.* 2005; 91: 417–423.

[79] O'Sullivan JP, Wood GC. The morphology and mechanism of formation of porous anodic films on aluminium. *Proc. R. Soc. London, Ser. A* 1970; 317 (1531): 511–543.

[80] Choi J, Sauer G, Nielsch K, Wehrspohn RB, Gösele U. Hexagonally arranged monodisperse silver nanowires with adjustable diameter and high aspect ratio. *Chem. Mater.* 2003; 15 (3): 776–779.

[81] Zhou ZF, Zhou YC, Pan Y, Wang XG. Growth of the nickel nanorod arrays fabricated using electrochemical deposition on anodized Al templates. *Mater. Lett.* 2008; 62: 3419–3421.

[82] Masuda H, Fukuda K. Ordered metal nanohole arrays made by a two-step replication of honeycomb structures of anodic alumina. *Science* 1995; 268 (5216): 1466–1468.

[83] Masuda H, Hasegawa F, Ono S. Self-ordering of cell arrangement of anodic porous alumina formed in sulfuric acid solution. *J. Electrochem. Soc.* 1997; 144 (5): L127–L130.

[84] Masuda H, Yada K, Osaka A. Self-ordering of cell configuration of anodic porous alumina with large-size pores in phosphoric acid solution. *Jpn. J. Appl. Phys. part 2* 1998; 37 (11A): L1340–L1342.

[85] Jessensky O, Müller F, Gösele U. Self-organized formation of hexagonal pore arrays in anodic alumina. *Appl. Phys. Lett.* 1998; 72 (10): 1173–1175.

[86] Rupprecht, L. *Conductive polymers and plastics in industrial applications.* 1999; Society of Plastics Engineers.

[87] Al-Saleh M, Sundararaj U. A review of vapor grown carbon nanofiber/polymer conductive composites. *Carbon.* 2009; 47 (1): 2–22.

[88] Shenoy AV. *Rheology of Filled Polymer Systems.* Springer-Verlag, 1999.

[89] Winey KI, Vaia RA. Polymer nanocomposites. *MRS Bull.* 2007; 32: 314–322.

[90] Zhang CS, Ni QQ, Fu SY, Kurashiki K. Electromagnetic interference shielding effect of nanocomposites with carbon nanotube and shape memory polymer. *Compos. Sci. Technol.* 2007; 67 (14): 2973–2980.

[91] Lee BO, Woo WJ, Kim MS. EMI shielding effectiveness of carbon nanofiber filled poly(vinyl alcohol) coating materials. *Macromol. Mater. Eng.* 2001; 286 (2): 114–118.

[92] Rao M, Andrews R, Derbyshire F. *Energieia*; 1998; 9: 1.

[93] Bryning MB, Islam MF, Kikkawa JM, Yodh AG. Very low conductivity threshold in bulk isotropic single-walled carbon nanotube–epoxy composites. *Adv. Mater.* 2005; 17 (9): 1186–1191.

[94] Haggemueller R, Gommans HH, Rinzler AG, Fischer JE, Winey KI. Aligned single-wall carbon nanotubes in composites by melt processing methods. *Chem. Phys. Lett.* 2000; 330 (3–4): 219–225.

[95] Cooper CA, Ravich D, Lips D, Mayer J, Wagner HD. Distribution and alignment of carbon nanotubes and nanofibrils in a polymer matrix. *Comp. Sci. Technol.* 2002; 62 (7–8): 1105–1112.

[96] Andrews R, Jacques D, Minot M, Rantell T, Fabrication of carbon multiwall nanotube/polymer composites by shear mixing. *Macromol. Mater. Eng.* 2002; 287: 395–403.

[97] Al-Saleh MH. Nanostructured conductive polymeric materials. University of Alberta. 2008.

[98] Gelves GA, Murakami ZTM, Krantz MJ, Haber JA. Multigram synthesis of copper nanowires using ac electrodeposition into porous aluminium oxide templates. *J. Mater. Chem.* 2006; 16: 3075–3083.

[99] Lin B, Gelves GA, Haber JA, Pötschke P, Sundararaj U. Electrical, Morphological and rheological study of melt-mixed polystyrene/copper nanowire nanocomposites. *Macromol. Mater. Eng.* 2008; 293: 631–640.

[100] Strumpler RS, Glatz-Reichenbach J. Conducting Polymer Composites. *J. Electrocer.* 1999; 3 (4): 329–346.

[101] Miyasaka K, Watanabe K, Jojima E, Aida H, Sumita M, Ishikawa K. Electrical conductivity of carbon-polymer composites as a function of carbon content. *J. Mater. Sci.* 1982; 17: 1610–1616.

[102] Sau KP, Chaki TK, Khastgir D. Carbon fibre filled conductive composites based on nitrile rubber (NBR), ethylene propylene diene rubber (EPDM) and their blend. *Polym.* 1998; 39 (25): 6461–6471.

[103] Gubbels F, Jerome R, Teyssie Ph, Vanlathem E, Deltour R, Calderone A, Parente V, Breads JL. Selective localization of carbon black in immiscible polymer blends: a useful tool to design electrical conductive composites. *Macromol.* 1994; 27 (7): 1972–1974.

[104] Al-Saleh MH, Sundararaj U. Nanostructured carbon black filled polypropylene/polystyrene blends containing styrene–butadiene–styrene

copolymer: Influence of morphology on electrical resistivity. *Europ. Polym. J.* 2008; 44 (7): 1931–1939.

[105] Martin BJA, Parkinson D. Milling procedure its effect on physical properties. *Rubber Chem. Technol.* 1995; 28: 261–277.

[106] Huang JC. EMI shielding plastics: A review. *Adv. Polym. Technol.* 1995; 14 (2): 137–150.

[107] White DRJ, Mardiguian M. *Electromagnetic Shielding*. 1988; Interference Control Technologies Inc., Gainesville, VA.

[108] Margolis JM, *Conductive Polymers and Plastics*. 1989; Chapman and Hall, New York.

[109] Chung DDL, *Materials for electromagnetic interference shielding*. *J. Mater. Eng. Perf.*, 2000, 9 (3): 350–354.

Chapter 2

Bench Scale Synthesis and Characterization of High Aspect Ratio Copper Nanowires with Anodic Porous Aluminum Oxide Template

2.1. Introduction

1D nanostructures can be defined as having at least one dimension below 100 nm, which have attracted intensive research interest due to their unique and fascinating properties and applications superior to their bulk counterparts [1–3]. The ability to produce such 1D nanostructures is essential to much of the advanced science and technology. Simultaneous control over morphology, dimension and uniformity is the most important in developing synthetic methods to produce 1D nanostructures. The synthesis and characterization of 1D nanostructures: nanowires, nanorods, nanobelts, and nanotubes have been frequently reported in the past decades, and were summarized in a review paper [4]. Figure 2–1 shows the schematic illustrations of the six different approaches used to produce 1D nanostructures: A) dictation by the anisotropic crystallographic structure of a solid, B) confinement by a liquid droplet, C) template assisted synthesis, D) kinetic control with surfactant as a capping agent, E) self-assembly of 0D nanostructures, F) size reduction of 1D microstructure [4].

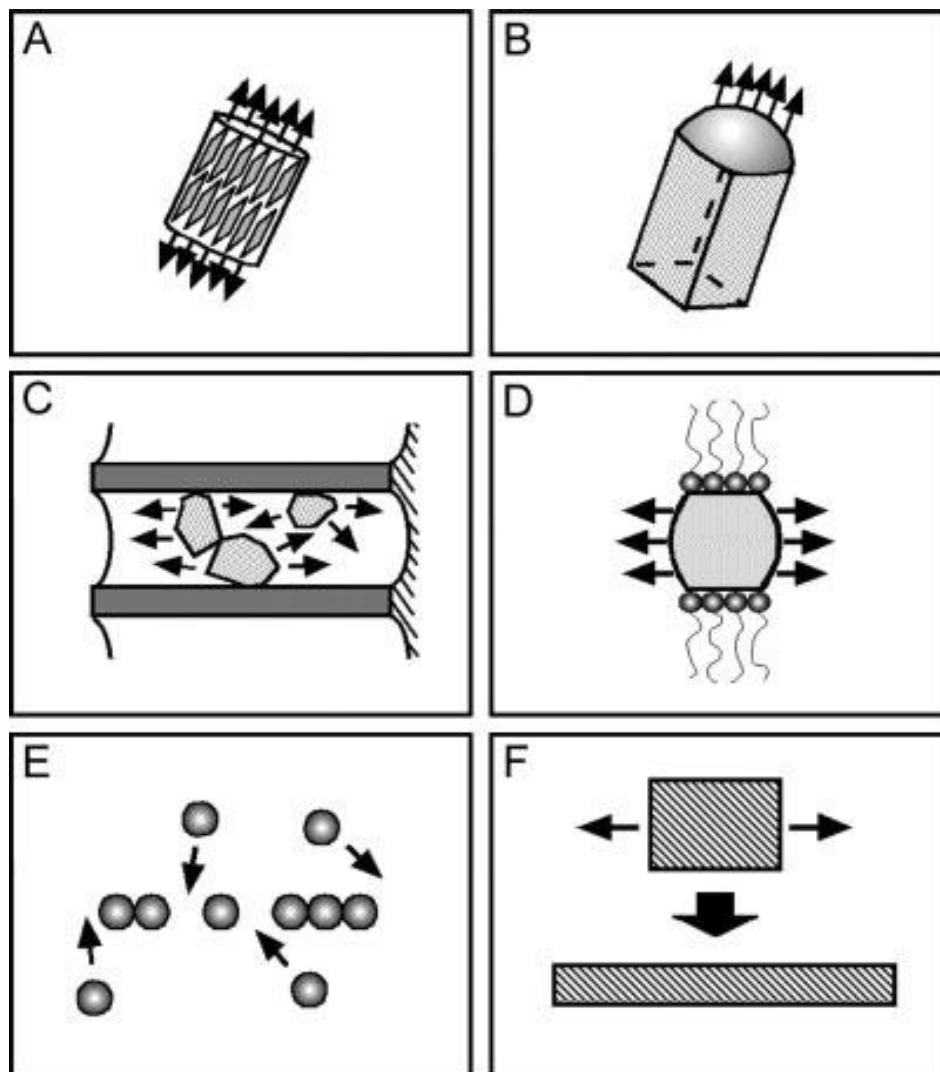


Figure 2-1. Schematic illustrations of the six different approaches used to produce 1D nanostructures. (A) dictation by the anisotropic crystallographic structure of a solid, (B) confinement by a liquid droplet, (C) template assisted synthesis, (D) kinetic control with surfactant as a capping agent, (E) self-assembly of 0D nanostructures, (F) size reduction of 1D microstructure. Reproduced with permission from “One-dimensional nanostructures: synthesis, characterization and applications” Adv. Mater. 2003; 15 (5): 353. Copyright 2003, Wiley-VCH.

Template-assisted synthesis of 1D nanostructures is a straightforward method, in which the template simply functions like a mold within which materials can be generated and shaped into nanostructures conforming to the morphology of the template. The post-synthesis treatment that removes the template by chemical process makes it possible to obtain pure 1D nanostructures. It is widely accepted that the template-assisted synthesis of 1D nanostructures is a simply, high-through-put and cost effective approach.

The production of 1D nanostructures such as CuNWs by using anodic PAO as the mask or matrix structure can significantly reduce the cost compared to the technologies based on the traditional methods like nanoscaling using electron beam lithography [5]. To use such an anodic PAO template for the synthesis of new 1D nanostructures, the pores should be filled with one or more desired materials by chemical vapor deposition (CVD), physical vapor deposition (PVD) or electrodeposition. Electrodeposition can be applied to synthesize the electrically conducting or semiconducting 1D nanostructures, by which the growth direction of the nanowires is in contrast to other deposition methods like CVD and PVD in that the growth of nanowires in electrodeposition starts at the pore tips and continues in the pore direction from the pore bottom to the pore opening [6].

AC electrodeposition has been reported to synthesize metal nanowires in anodic PAO template for years [4, 7–11]. However, the relationship between the electrodeposition parameters and the structure of the barrier layer during AC

electrodeposition is not fully understood up to now. Thus, AC electrodeposition method is primarily developed on the experimental basis. The microstructure and properties of the synthesized 1D nanostructures depend on the deposition solution composition, temperature, and parameters of the AC wave: voltage, frequency, wave form, etc.

In this chapter, a scalable approach to synthesize CuNWs by AC electrodeposition of copper into anodic PAO template is presented in bench scale. The liberated CuNWs can be utilized as fillers in polymer matrices to formulate ECPNCs for ESD and EMI shielding application.

2.2. Experimental

2.2.1. Preparation of anodic porous aluminum oxide template

To prepare the anodic PAO template for the synthesis of CuNWs by AC electrodeposition, Aluminum plates of 1 mm thick (99.99+%, Alfa Aesar) were cut into 10 cm × 25 cm pieces and cleaned with acetone. The rectangular aluminum pieces were immersed in 1 mol/L NaOH aqueous solution for 10 min to remove the oxide layer on the surface completely.

An anodization tank of 0.75 inch plexiglass wall with an approximate maximum volume of 32 L as shown in Figure 2–2a was filled with 28 L 0.3 mol/L H₂SO₄ aqueous solution as electrolyte for the anodization, which was circulating with a pump via the aqueous glycol cooling fluid of a chiller to control the temperature of the electrolyte between 0~4 °C.

Subsequently, 10 bare high purity aluminum plates as anodes were vertically inserted into the slots of the anodization tank one by one. 11 stainless steel plates of the same size as cathodes were also placed into the slots of the anodization tank alternating with and parallel to the aluminum plates with inter-electrode distance of 2.0 cm. And it was the stainless steel plates at both ends of the electrode array as shown in Figure 2–2b. The electrical contact was made by using an alligator clip to connect the top of each electrode to the terminals of a Mastech HY5020EX DC power supply: aluminum plates connected to the positive terminal with red alligator clips, stainless steel plates connected to the negative terminal with black ones. The front image of the Mastech HY5020EX DC power supply is shown in Figure 2–3.

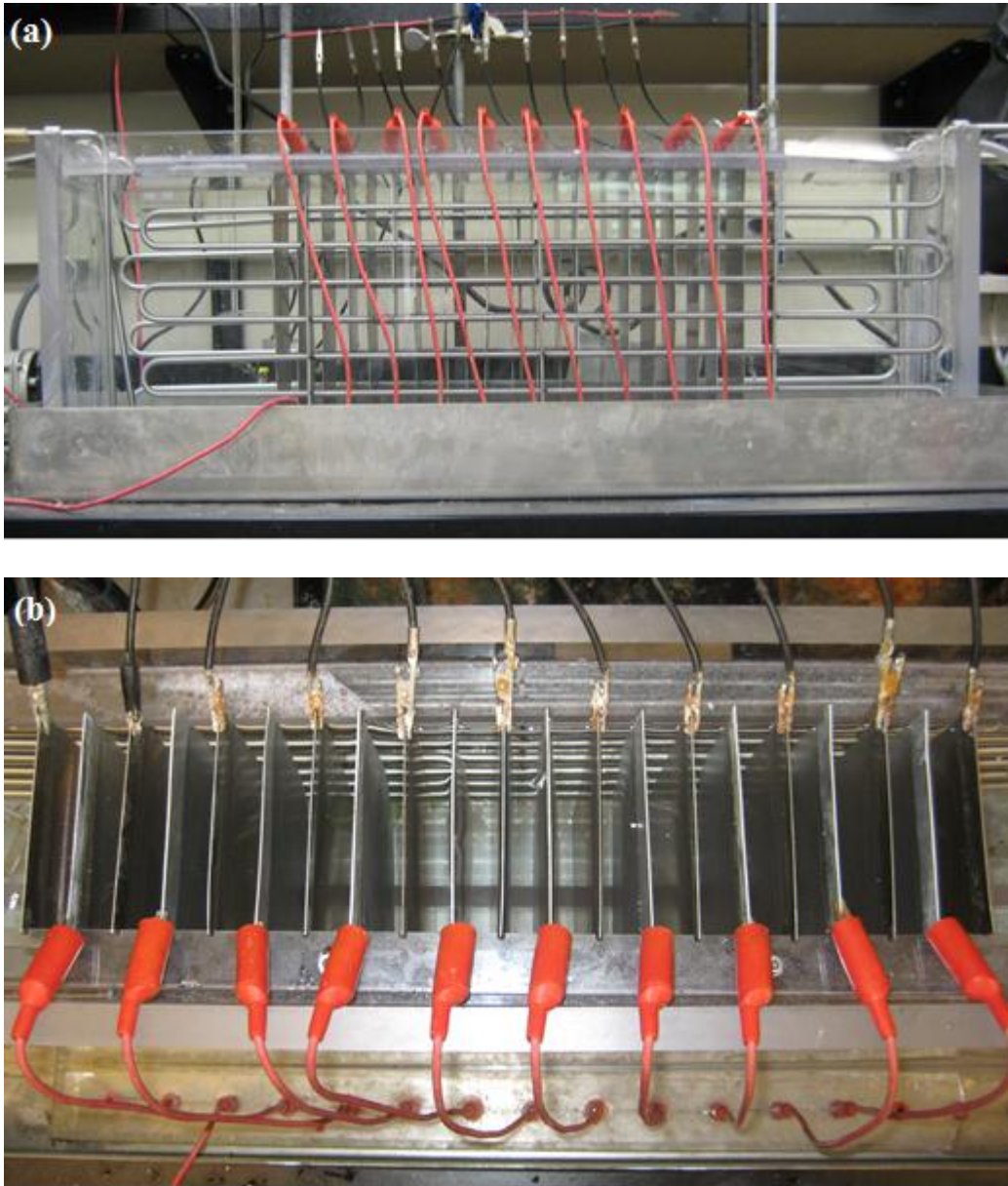


Figure 2-2. The photographs of the plexiglass anodization tank: (a) the front view showing the setup overview and (b) the top view showing the configuration of electrodes and the electrical connection. The aluminum plates connected to the positive terminal with red alligator clips, the stainless steel plates connected to the negative terminal with black ones.

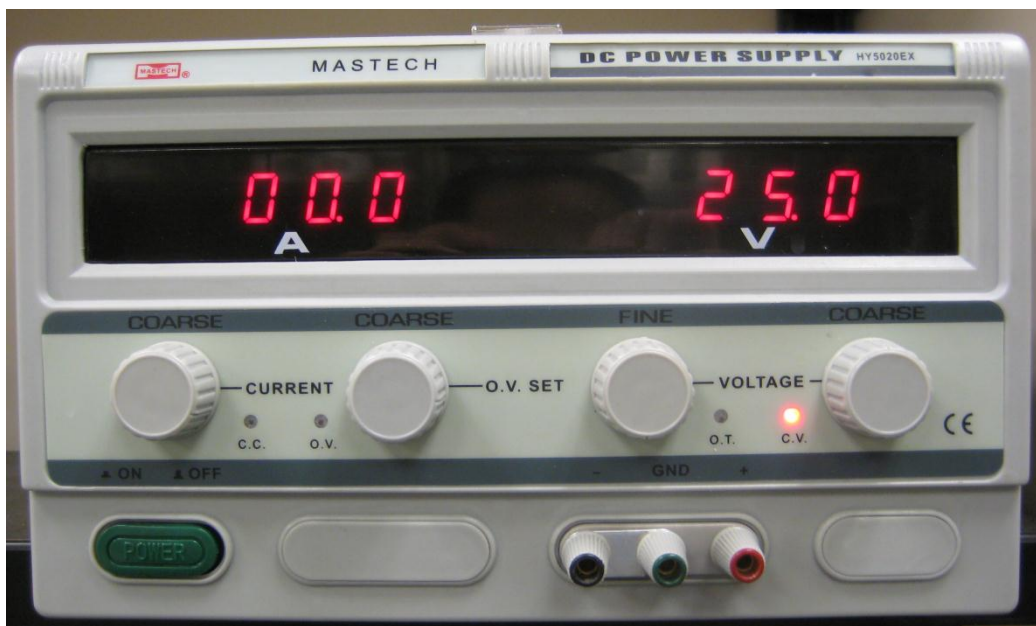


Figure 2-3. The photograph of the front panel of the Mastech HY5020EX DC power supply for anodization.

The bare aluminum plates were anodized with Masuda's two-step process [12, 13]. The bare aluminum plates were first anodized under 25 V DC at 0~4 °C for 2 h. As described in Chapter 1, to dissolve the initially formed PAO film and improve the self-organization of the formed pores, the anodized aluminum plates were etched in a solution of 0.1 mol/L H_2CrO_4 and 0.3 mol/L H_3PO_4 at 60 °C for 30 min. H_2CrO_4 of 0.1 mol/L was prepared by dissolution of CrO_3 (99.8%, J. T. Baker) in deionized water. The etched aluminum plates were fully rinsed with deionized water to remove the chemical residual. Immediately following the etching and rinse, the aluminum plates were placed into the original H_2SO_4 solution and anodized for another 8 h under identical conditions. At the end of the second anodization, the DC voltage was decreased from 25 V to 9 V within

10 minutes and held for 5 min at 9 V to thin the alumina barrier layer at the bottom of the PAO layer. The stepwise decrease of anodization voltage at the end of the second anodization is shown in Figure 2-4. After the second anodization, the aluminum plates were rinsed and dried completely with air flow.

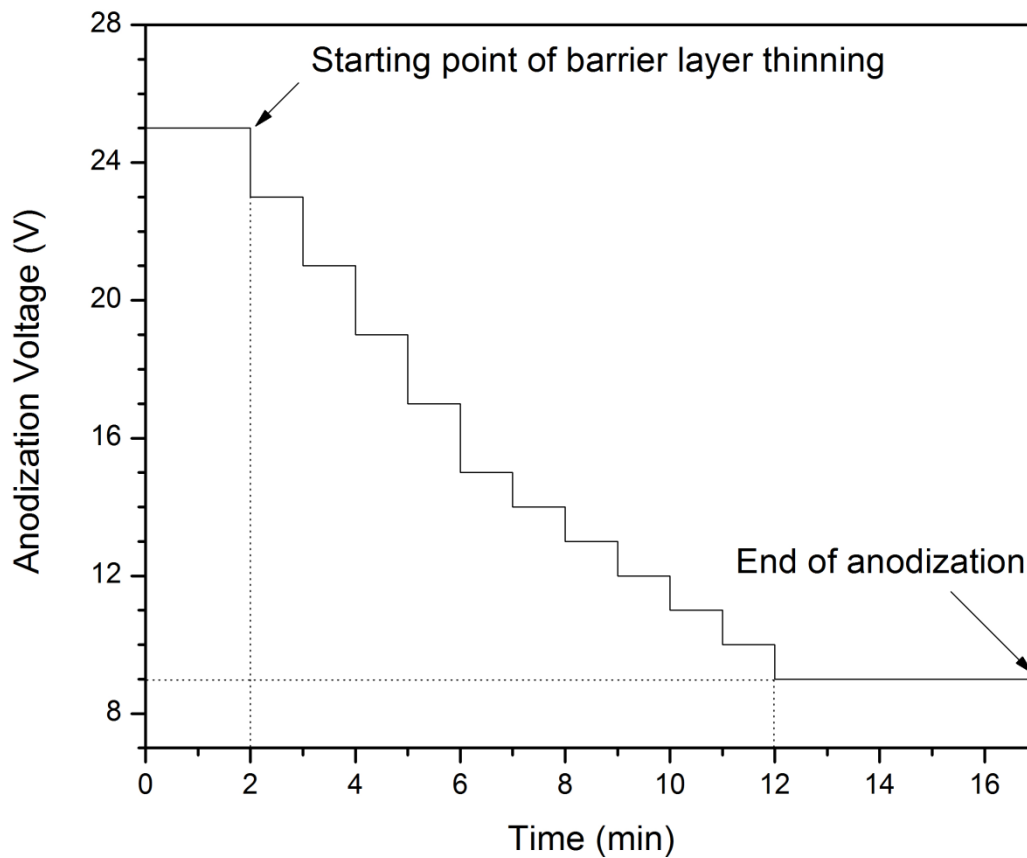


Figure 2-4. The stepwise anodization voltage decrease during barrier layer thinning at the end of the second anodization.

2.2.2. AC electrodeposition of copper into the anodic PAO template

The anodized aluminum plates were coated with nail polish on the edges to prevent the preferential deposition of copper on the edges. Individual plate was vertically immersed into the electrodeposition solution of 4 L in a beaker. The composition of the electrodeposition solution is listed in Table 2-1.

Table 2-1. Composition of the solution for AC electrodeposition of copper.

| | Concentration |
|--|---------------|
| CuSO ₄ ·5H ₂ O (99%, Alfa Aesar) | 0.5 mol/L |
| H ₃ BO ₃ (99.5% min., EMD Millipore) | 0.285 mol/L |

Two copper plates (99.999%, Alfa Aesar) were used as counter-electrodes immersed in the electrodeposition solution parallel to the aluminum plate in order to deposit copper into the template on both faces. The aluminum plate and the copper plates were connected to either of the terminals of a Kepco BOP 20–50 MG AC power supply. The schematic illustration of the AC electrodeposition setup is shown in Figure 2-5.

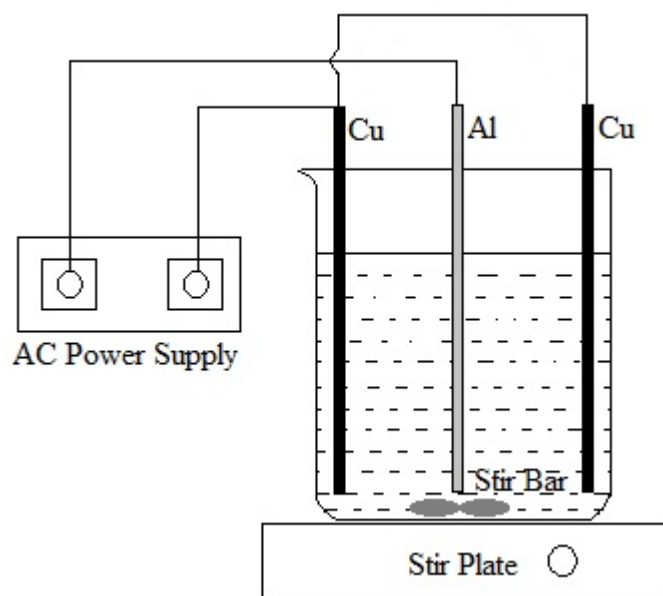


Figure 2-5. The schematic illustration of the AC electrodeposition setup.

The aluminum plate was immersed in the electrodeposition solution for 5 min, and then a 200 Hz continuous sine AC of $10 V_{\text{rms}}$ was supplied to start the electrodeposition of copper into the pores of the PAO template for 10.5 min. The continuous AC wave for the electrodeposition is shown in Figure 2–6. After the 10.5 min AC electrodeposition of copper, both faces of the aluminum plate were covered with the copper deposition, which turned the surface of aluminum plate from shiny bright to dark black or yellow brown (if electrodeposited for prolonged period). The aluminum plate with copper deposition was then fully rinsed with deionized water and dried with air flow ready for the liberation of CuNWs from the PAO template.

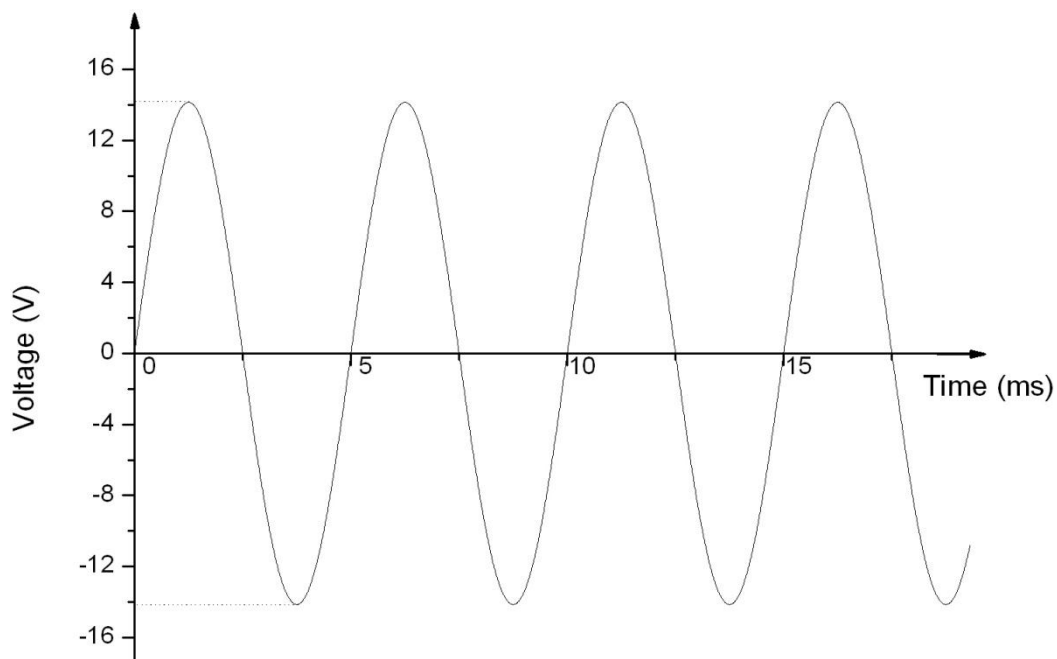


Figure 2-6. The continuous sine voltage produced by a Kepco BOP 20–50 Mg power supply for the AC electrodeposition of copper into the anodic PAO template.

2.2.3. Liberation of copper nanowires from PAO templates

The aluminum plates with CuNWs deposition were immersed into 0.6 mol/L H_3PO_4 aqueous solution for 5 min under room temperature, followed by rubbing the surface with a Kimwipe to remove the bulk copper deposition on the surface. The color of the aluminum plates with CuNWs deposition will change from yellow with bulk copper deposition on the surface to dark black without bulk copper deposition on the surface.

After the removal of bulk copper deposition, the aluminum plates with

CuNWs were immersed into 1 mol/L NaOH aqueous solution for 10 min under room temperature to dissolve the aluminum oxide template so as to liberate the CuNWs. The liberated CuNWs appeared large mass floating on the surface of the NaOH solution, which can be collected with a spatula and put into a flask with methanol to clean under vigorous stirring. The mixture of CuNWs and methanol was then filtered with a nylon membrane (Whatman, 0.45 μm pore size), rinsed twice with methanol, and transferred into 250 mL methanol to ultrasonicate for 1 h in a sonication bath. The ultrasonic treatment consisted of 135 W average power and 38.5–40.5 kHz frequency applied for 5 min periods with a 5-min rest period between sonications. The CuNWs dispersed in methanol can then be used for characterization directly or filtered with a nylon membrane (Whatman, 0.45 μm pore size) and dried out in a vacuum oven to get dry powder. The flow chart representing the process of the CuNWs synthesis by AC electrodeposition of copper into PAO template is shown in Figure 2–7.

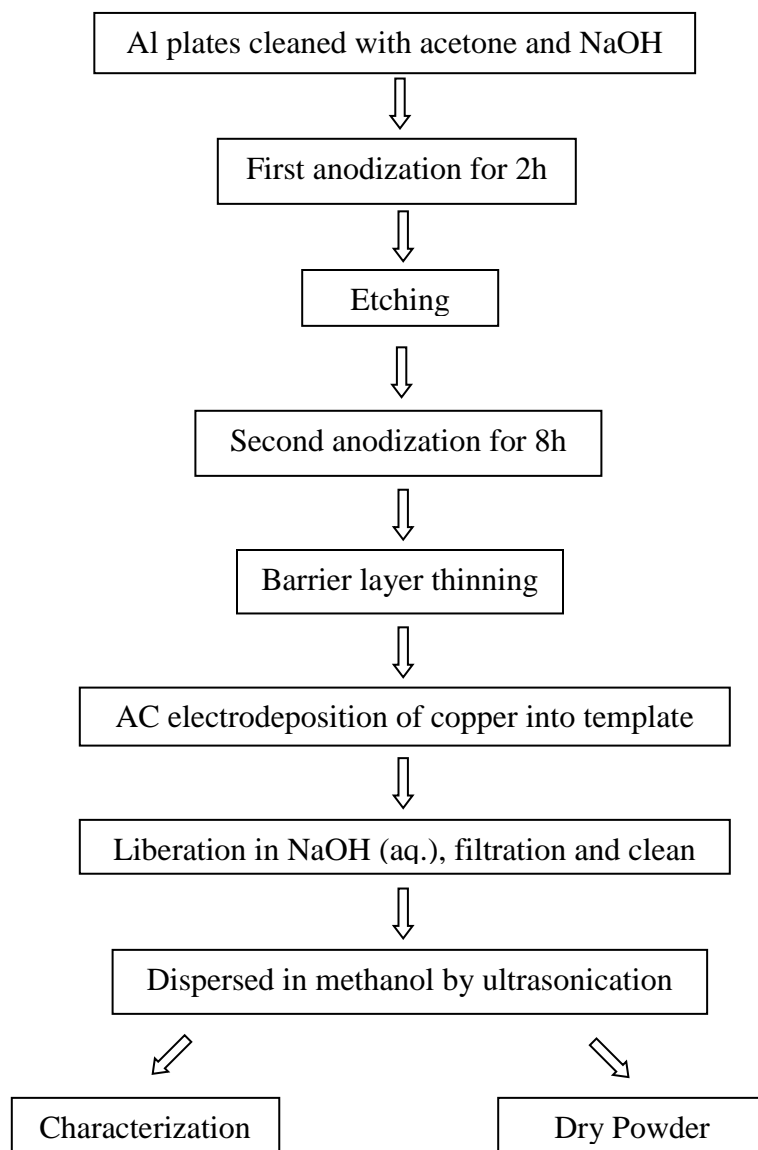


Figure 2-7. The flow chart representing the process of the CuNWs synthesis by AC electrodeposition of copper into PAO template.

2.2.4. Determination of CuNWs yield with PAO templates anodized for different hours

The process of the first anodization and etching was carried out as described in Section 2.2.1 with the aluminum plates of 10 cm × 25 cm. Subsequently, the aluminum plates were anodized for the second time for different periods: 2 h, 4 h, 6 h, 8 h, 10 h and 12 h, respectively. After the second anodization, the barrier layer thinning, AC electrodeposition and CuNWs liberation were finished as described in the previous sections of this chapter.

The CuNWs liberated from 2 PAO templates with the same second anodization hours were collected, cleaned, filtered, dried and weighed separately to determine the yield.

2.2.5. Determination the length distribution of CuNWs

The CuNWs was synthesized with the anodic PAO template with the second anodization for 8 h. The length distribution of the CuNWs dispersed in methanol was determined from the SEM images of a 22 mm × 22 mm cover glass (0.16–0.19 mm thick, Fisherbrand) with well-dispersed CuNWs, which was prepared beforehand by spin casting of a drop of CuNW/CH₃OH dispersion at 3000 rpm on the glass cover for 1 min with a Laurell WS-200-4T2 spin coater. The lengths of over 1000 individual CuNWs were measured with ImageJ 1.44p software (National Institute of Health, USA).

2.2.6. SEM and TEM characterization

Scanning electron microscope (SEM) images of the aluminum plates before and after anodization were collected after coating the plates with gold and palladium by cathode sputtering in argon atmosphere.

To prepare the CuNW samples for SEM imaging, a piece of 22 mm × 22 mm cover glass (0.16–0.19 mm thick, Fisherbrand) was fastened to the sample stage center of a Laurell WS-200-4T2 spin coater. Two drops of CuNW/CH₃OH dispersion were dropped onto the cover glass spinning at around 3000 rev/min. After 1 min spinning, the cover glass was stuck onto an Al stub with double-sided adhesive carbon tape. The assembly of the cover glass and the Al tub was coated with Au and Pd by cathode sputtering in argon atmosphere before the SEM imaging. All the SEM images in this chapter were collected using a Philips XL30 scanning electron microscope equipped with an energy dispersive X-ray (EDX) analyzer under 20 kV accelerating voltage.

The samples for transmission electron microscope (TEM) imaging were prepared by dropping the very dilute CuNW/CH₃OH dispersion onto a holey carbon coated nickel TEM grid. All the TEM images in this chapter were collected with a Tecnai F20 field emission gun TEM under 200 kV accelerating voltage.

2.2.7. XRD and XPS characterization

The X-ray diffraction (XRD) pattern of the CuNW powder was collected by an Ultima III Multi Purpose Diffraction System with Cu K α radiation operating at 40 kV and 44 mA. The CuNW powder was prepared by drying the CuNWs/CH₃OH dispersion in a vacuum oven at room temperature and kept the CuNW powder in liquid nitrogen before test.

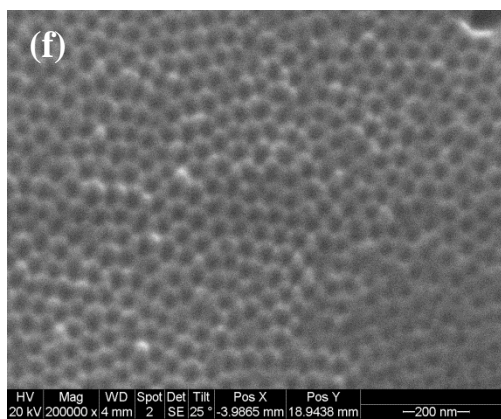
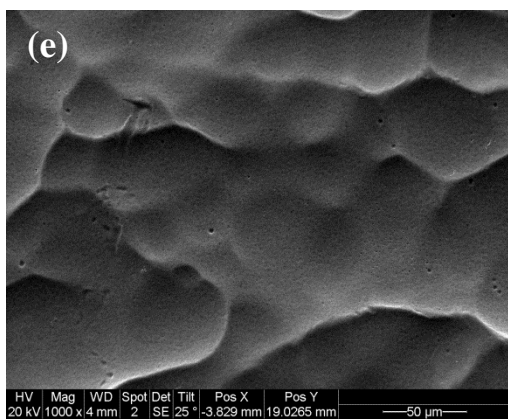
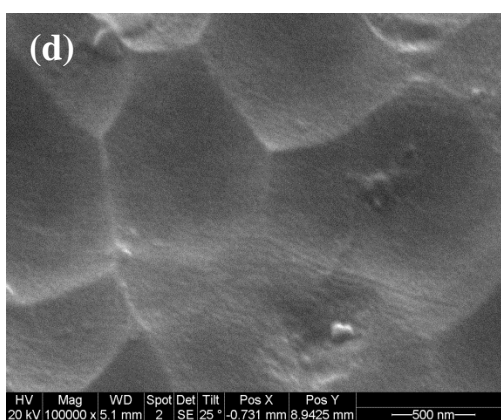
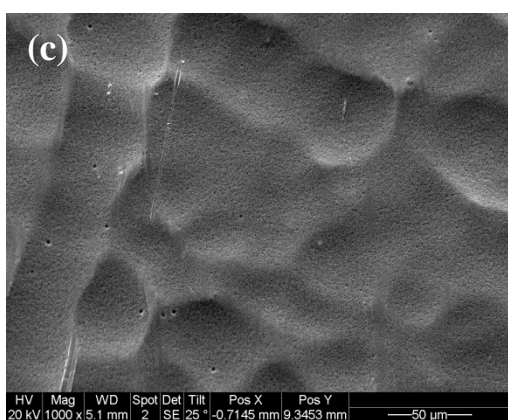
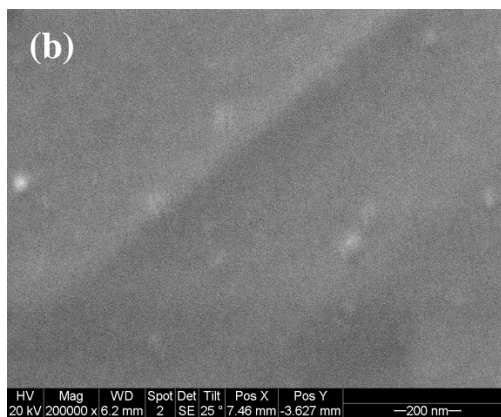
The X-ray photoelectron spectra (XPS) were collected with a PHI VersaProbe 5000-XPS spectrometer with the K α X-rays from an Al source operating at 25 mV. The base pressure of the XPS spectrometer was around 8×10^{-8} Pa. The CuNW sample for XPS characterization was prepared by sticking the CuNW powder onto an aluminum stub with double-sided carbon tape.

2.3. Results and Discussion

2.3.1. Surface morphological evolution from aluminum plate to PAO template

The surface morphological evolution from the aluminum plate to the PAO template is shown in Figure 2–8. Figures 2–8a and b show the surface morphology of the bare aluminum plate after fully cleaned with acetone and 1 mol/L NaOH aqueous solution. White spots in the images were dusts on the surface. The bare aluminum plate surface was mostly smooth with a few straight ridges before anodization.

Chapter 2. Bench Scale Synthesis and Characterization of High Aspect Ratio Copper Nanowires with Anodic Porous Aluminum Oxide Template



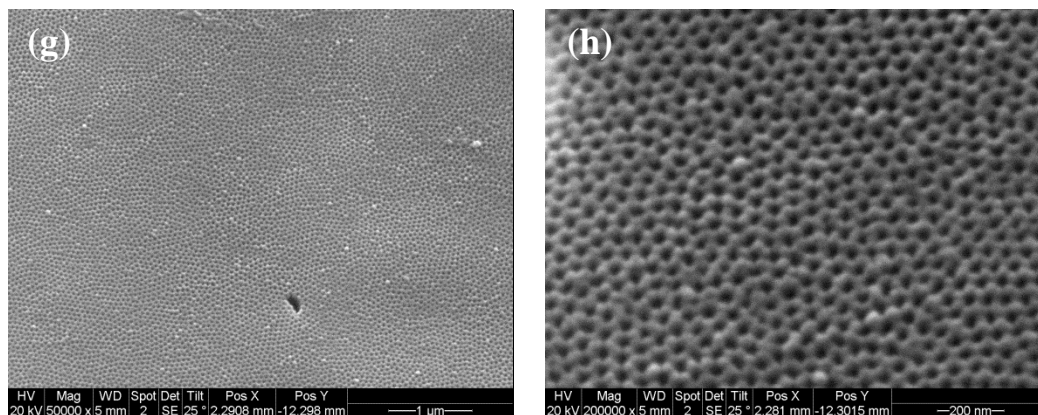


Figure 2-8. The surface morphological development from the aluminum plate to the PAO template: (a, b) acetone and NaOH (aq.) cleaned bare aluminum plate before anodization, (c, d) after anodized in 0.3 mol/L H_2SO_4 for 2 h, (e, f) after etched in a solution of 0.1 mol/L H_2CrO_4 and 0.3 mol/L H_3PO_4 under 60 °C for 30 min, (g, h) after anodized in 0.3 mol/L H_2SO_4 for 8 h.

Figures 2–8c and d reveal the surface morphology of the aluminum plate after 2 h anodization in 0.3 mol/L H_2SO_4 solution. Some shallow concaves of 35~60 μm in diameter can be observed in both images. A few pores were visible in the left image. It seems that there was a layer of loose floccule covering the surface, which can be attributed to the aluminum oxide formed during the first 2 h anodization.

Figures 2–8e and f are the SEM images of the aluminum plate etched in the solution of 0.1 mol/L H_2CrO_4 and 0.3 mol/L H_3PO_4 under 60 °C for 30 min. The surface looked clearer and cleaner in Figure 2–8e than that in Figure 2–8c,

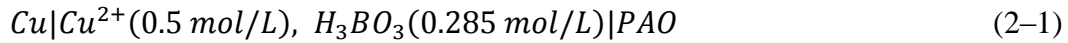
which indicates that the etching process can remove the surface aluminum oxide formed during the first 2 h anodization. Moreover, the pattern of the self-organized pores can be well observed in Figure 2–8f. By comparison of Figure 2–8d with Figure 2–8f, it seems that removal of the surface aluminum oxide improved the self-organization of the pores formed during the first 2 h anodization.

The surface morphology of the aluminum plate after the second 8 h anodization and the barrier layer thinning at the end of the second anodization is shown in Figures 2–8g and h. The self-organization of the pores was further improved by the second 8 h anodization. And the pores also looked deeper and more regular after the second anodization, which was ready for AC electrodeposition.

2.3.2. AC electrodeposition of copper into anodic PAO template

As described in Section 1.2, the barrier layer at the bottom of the pores functions like a diode with a p-n junction that allows the electrical current to pass preferentially in the cathodic direction. Therefore, the copper deposition can be generated in the PAO pores when the stronger sine AC electrical current is directed from the aluminum substrate to the electrolyte, and the electrically deposited copper will be partially dissolved to Cu^{2+} when the weaker sine AC electrical current is in the opposite direction, which results in some copper deposition left in the PAO pores during a full cycle of the sine AC voltage. At

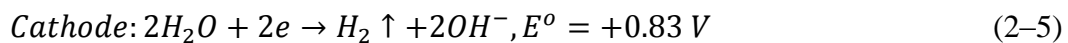
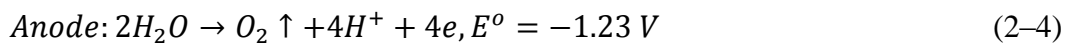
the same time, anodic reactions will also take place on the counter copper electrodes to allow the current flow and keep the electroneutrality. The electrochemical cell representing the AC electrodeposition of copper into the anodic PAO template is expressed in Equation 2–1.



And the half reactions along with respective standard electrode potentials at 25 °C vs. NHE in the aqueous solution are expressed in Equation 2–2 and Equation 2–3.



At the same time, side reactions can also take place on the electrodes to produce H₂ and O₂ bubbles, which hinder the uniform deposition of copper into the PAO pores.



With copper plates as counter electrodes, Equation 2–3 is the most favorable cathodic reaction that produces copper deposition into the PAO pores accompanying the most favorable anodic reaction expressed in Equation 2–2. H₃BO₃ acts as a PH buffer to stabilize the PH value of the electrodeposition solution.

The SEM images of the surface morphology of the PAO templates electrically deposited with copper are shown in Figure 2–9. In both images, the large shallow concaves from the aluminum substrate were clearly visible. But no unfilled pores can be observed even in the high magnification image, which indicates the high uniformity of the AC electrodeposition process.

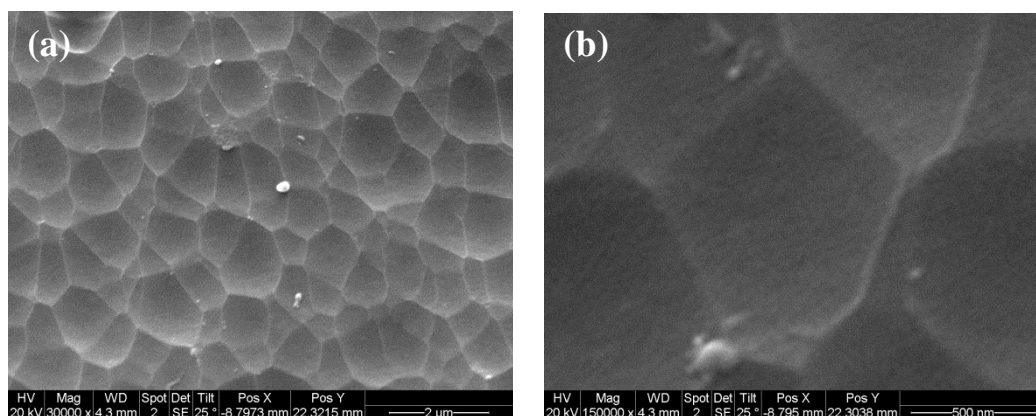


Figure 2-9. The (a) low magnification and (b) high magnification SEM images showing the surface morphology of the PAO template electrically deposited with copper.

2.3.3. Effect of the second anodization period on the yield

The CuNW yield with different second anodization period (2 h, 4 h, 6 h, 8 h, 10 h and 12 h) is shown in Figure 2–10. Two aluminum plates of 10 cm × 25 cm for each second anodization time were used to measure the CuNW yield per unit effective area that is the area of the aluminum plate covered with black CuNW deposition after the AC electrodeposition for 10.5 min.

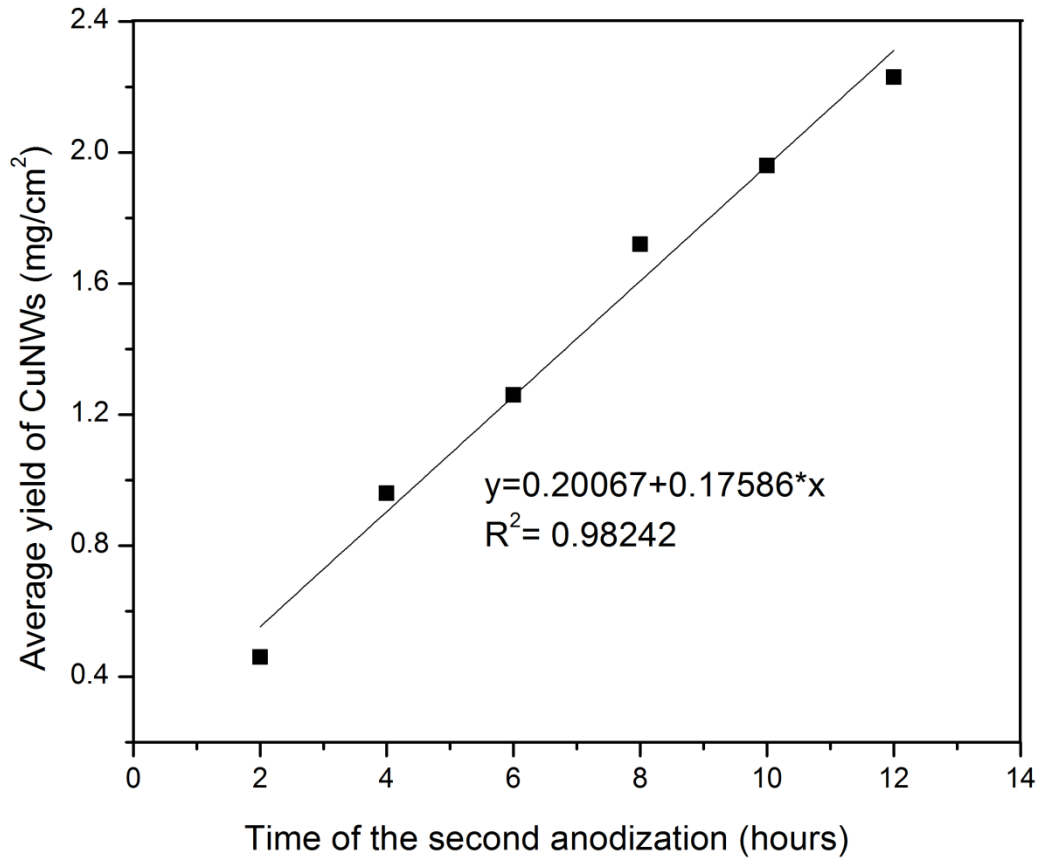


Figure 2-10. CuNW yields with different second anodization periods.

The converted CuNWs yields were 0.46 mg/cm^2 , 0.96 mg/cm^2 , 1.26 mg/cm^2 , 1.72 mg/cm^2 , 1.96 mg/cm^2 and 2.23 mg/cm^2 for the second anodization periods of 2 h, 4 h, 6 h, 8 h, 10 h and 12 h, respectively. The relationship between the CuNW yield and the second anodization period was highly linear with correlation coefficient $R^2 = 0.9824$. This linear relationship can be utilized to predict the CuNW yield of different second anodization period.

The CuNW yields increased almost linearly with the prolonged second anodization periods hints that the pore depth of the anodic PAO template grew in proportion to the anodization time.

Gerein and Haber [14] have studied the percentage of pore-filling vs. depth under the initial sample surface of the anodic PAO template after the AC electrodeposition with sine wave or square wave voltages and found that the pore-filling percentage increased with the depth under the initial sample surface nearly linearly.

In this case of CuNW yield at different second anodization period, the deeper pore was formed by the longer anodization time. Moreover, the deeper pore requires longer time of AC electrodeposition to fill it with copper deposition as much as possible. Both the longer walls of the pores and the longer electrodeposition time increased the probability of pore-blocking by non-conductive substance. Therefore, the longer second anodization period tends to decrease the pore-filling percentage in the electrodeposition process.

Although the CuNW yield increased with the prolonged second anodization period, it is not a good idea to prolong the second anodization period unlimitedly. The time consumption in the liberation process increased with the prolonged second anodization period. It took around 5~8 min to liberate the CuNWs from the PAO templates anodized for 2 h, 4 h, 6 h and 8 h, but took 10~15 min to liberate the CuNWs from the PAO templates anodized for 10 h and 12 h. The CuNWs deposited in the PAO templates anodized for over 14 h cannot be fully

liberated even after 30 min, and it was very difficult to clean the aluminum plates after the liberation, which hindered the recycling of the expensive high purity aluminum plates. Another problem for the PAO template anodized for over 14 h is that the barrier layer was not robust enough to hold the PAO template with copper deposition and the PAO layer automatically peeled off from the aluminum substrate during the post-deposition processes: rinse and air dry. In addition, some insoluble junks were mixed up in the liberated CuNWs in the case of anodization of the PAO template for over 12 h. Therefore, the second anodization for 8 h is a good choice to yield more CuNWs while avoid the adverse effects.

2.3.4. Length distribution of the CuNWs

Length distribution of the CuNWs synthesized with PAO templates with the second anodization for 8 h, liberated with 1 mol/L NaOH solution and ultrasonicated for 1 h as described in Section 2.2.5 is shown in Figure 2–11b. One of the SEM images used for measuring the lengths of individual CuNWs is shown in Figure 2–11a.

According to the statistical results in different length intervals, the CuNWs of length less than 0.5 μm and over 7 μm accounted for 14.8% and 1.0% respectively in the total number of CuNWs. 17.7% CuNWs with length fell between 0.5 μm and 1.0 μm . 32.0% of CuNWs were between 1 μm and 2 μm in length. Around 20.0% of CuNWs were between 2 μm and 3 μm in length. The

Chapter 2. Bench Scale Synthesis and Characterization of High Aspect Ratio Copper Nanowires with Anodic Porous Aluminum Oxide Template

CuNWs of length between 3 μm and 7 μm accounted for 14.7% in the total number.

Regarding the accumulative statistical results, 64.4% of CuNWs were less than 2 μm in length. The CuNWs of length less than 4 μm accounted for 90.9% in the total number. And 97.1% of CuNWs were less than 2 μm in length.

Based on the lengths of over 1000 individual CuNWs measured with ImageJ 1.44p, The determined average length of the CuNWs synthesized with the PAO templates with the second anodization for 8 h, liberated with 1 mol/L NaOH solution and ultrasonicated for 1 h was 1.98 μm .



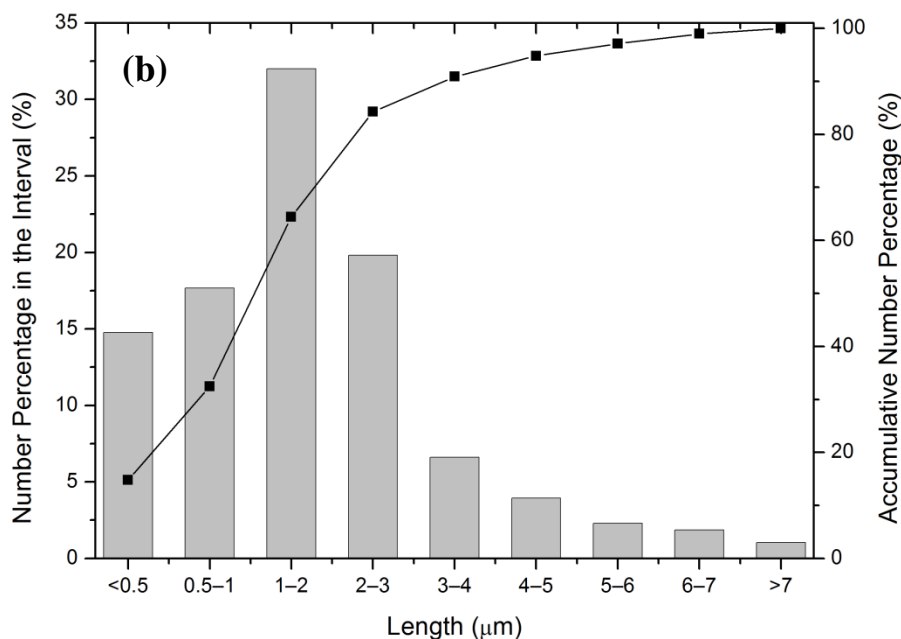


Figure 2-11. The length distribution of the CuNWs synthesized with the PAO templates with the second anodization for 8 h, liberated with 1 mol/L NaOH solution and ultrasonicated for 1 h. (a) One of the SEM images used for measuring the lengths of individual CuNWs, (b) the statistical results of the CuNWs length distribution.

2.3.5. Morphology and aspect ratio of the CuNWs

The SEM images of the CuNWs after liberation and 1 h ultrasonication are shown in Figure 2–12. Most of the CuNWs in the low magnification image existing as individual nanowires indicated good dispersion of the CuNWs after 1 h ultrasonication. Some of the CuNWs aggregated to form nanowire agglomerates with bigger diameter in the high magnification image, which can

be attributed to the high surface energy of the CuNWs. The CuNWs in both SEM images showed regular wire-shape and smooth surface.

Figure 2–13 shows the TEM images of the CuNWs after liberation and 1 h ultrasonication. The low magnification image showed the CuNW agglomerate from the CuNW/methanol dispersion. Most of the individual nanowires in the image were aligned in the length direction, which way can minimize the surface area of the CuNW agglomerate to meet the minimal surface Gibbs free energy. The single CuNW shown in the high magnification image revealed the smooth surface with some fluctuation in diameter.

The diameter of individual CuNWs determined from the high magnification TEM images was 25 ± 4 nm. The average aspect ratio of the CuNWs after liberation and 1 h ultrasonication was 80 based on the average length $1.98 \mu\text{m}$ determined in Section 2.3.4 divided by the average diameter of 25 nm.

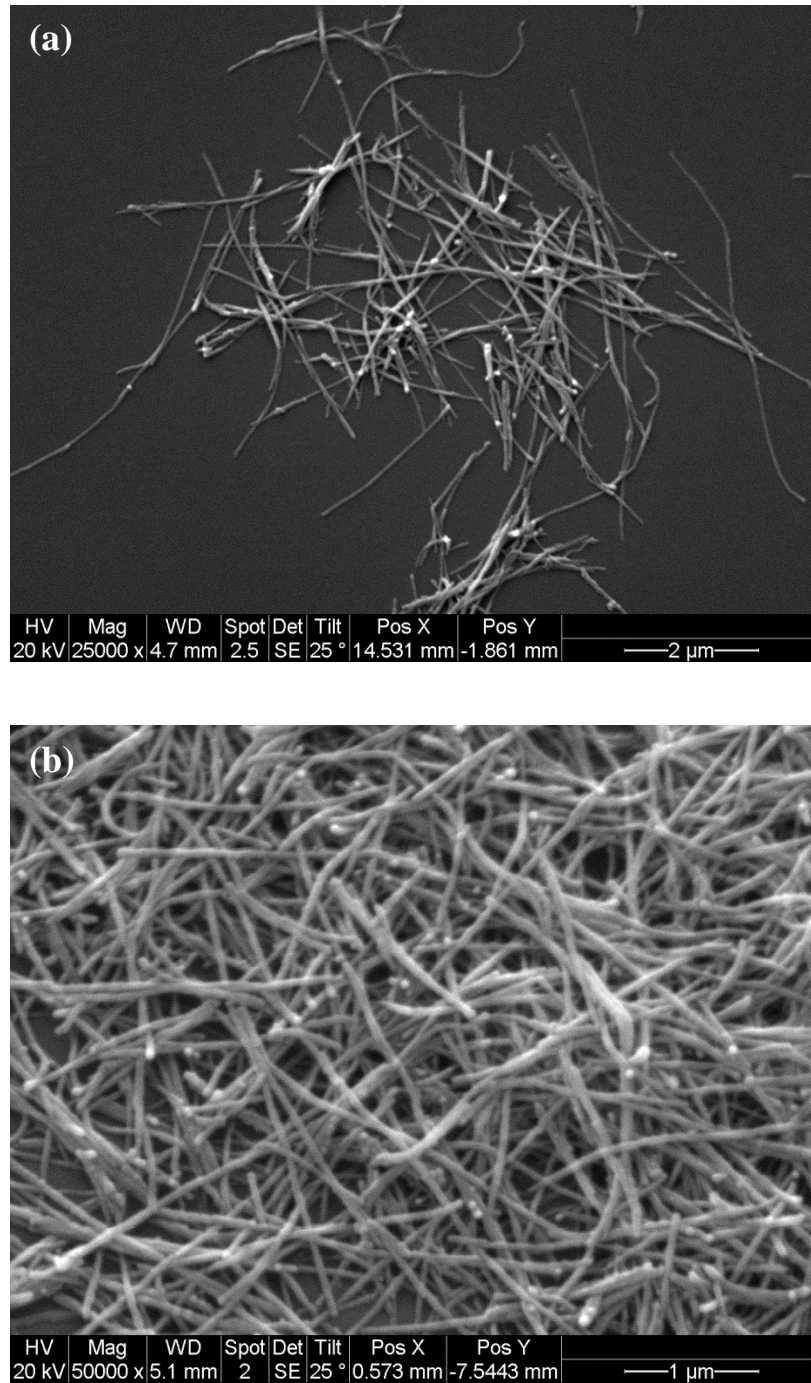


Figure 2-12. The SEM images of the CuNWs after liberation and 1 h ultrasonication. (a) The low magnification image of the area with few CuNWs, (b) the high magnification image of the area with concentrated CuNWs.

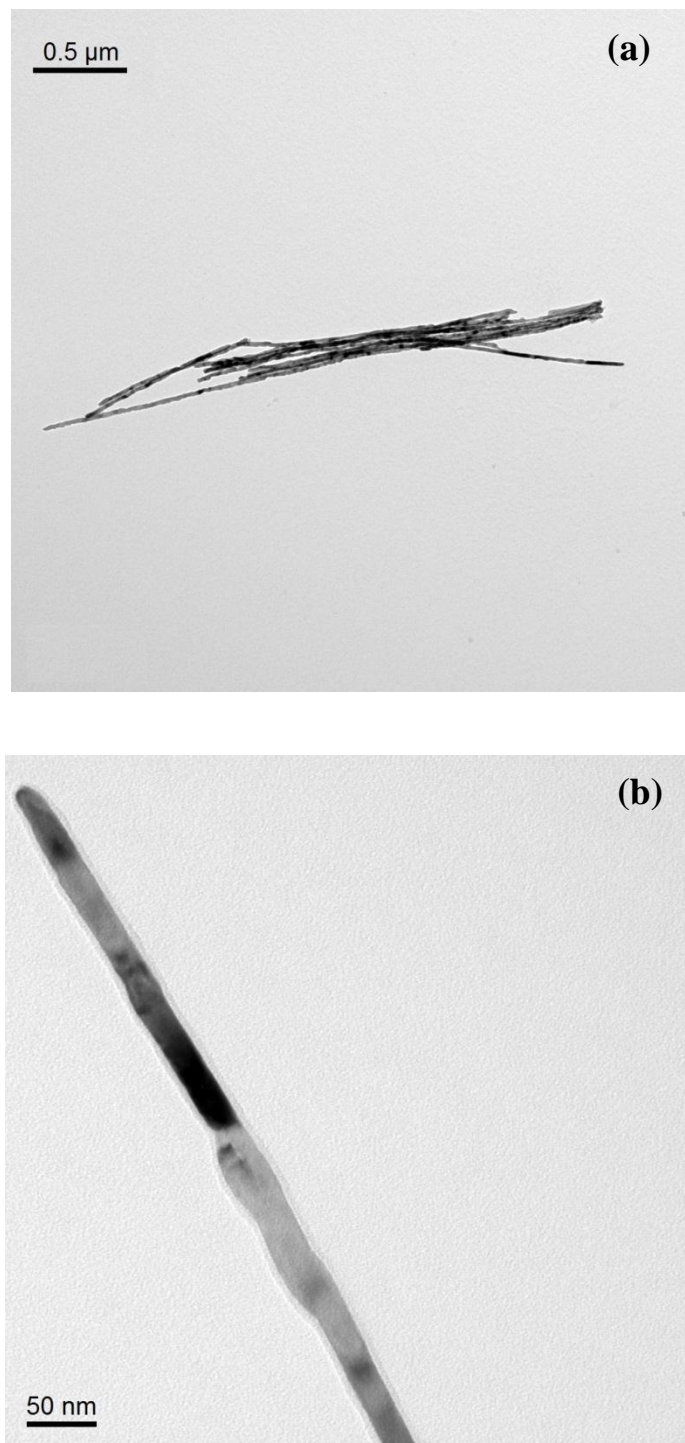


Figure 2-13. The (a) low magnification and (b) high magnification TEM images of the CuNWs after liberation and 1 h ultrasonication.

2.3.6. Crystal structure and composition of the CuNWs

Figure 2–14 shows the EDX spectra of the CuNW powder on an aluminum stub collected with the SEM EDX analyzer. The Al peak in the EDX spectra was from the aluminum stub. The peaks appearing at 0.93 keV, 8.09 keV and 8.94 keV were the CuL, CuK α , and CuK β lines respectively [15–18], which confirmed the copper element in the synthesized nanowires.

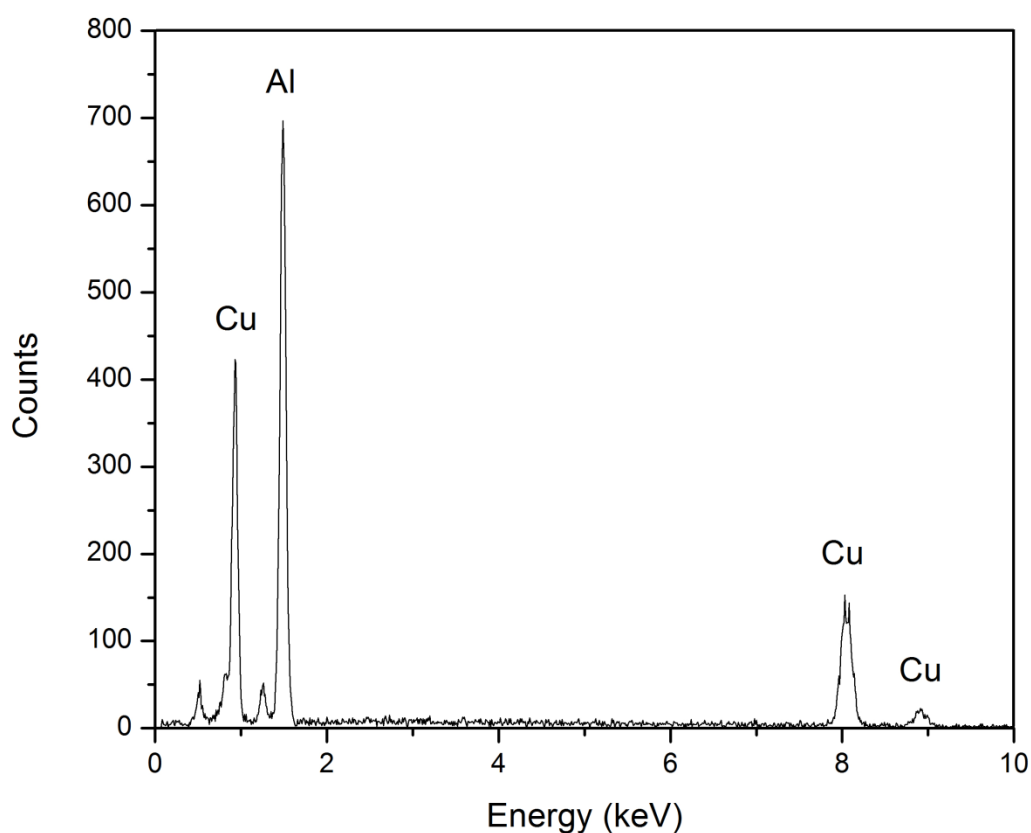


Figure 2-14. The EDX spectra of the CuNWs on an aluminum stub collected with the SEM EDX analyzer.

The XRD pattern of the CuNW powder is shown in Figure 2–15. The three sharp peaks of the fcc copper can be clearly identified at two theta of 43.32, 50.45 and 74.12 corresponding to the planes of (111), (200) and (220), respectively (PDF# 04-0836) as labeled in Figure 2–15. The d-spacings of the corresponding planes of fcc copper determined by MDI Jade 5.0 from the XRD pattern are shown in Table 2–2. The small peaks of Cu_2O can also be identified in the XRD pattern. The highest peak of Cu_2O at two theta of 37.1 corresponds to the (110) plane of the cubic Cu_2O (PDF# 35-109). CuO was not found in the XRD pattern.

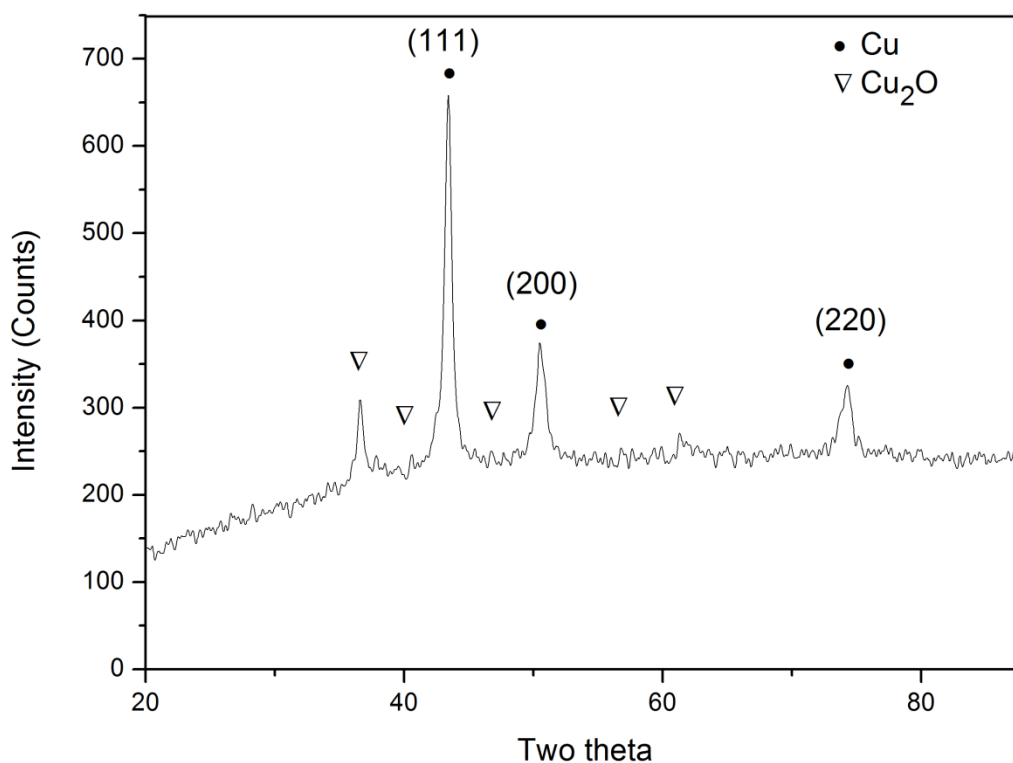


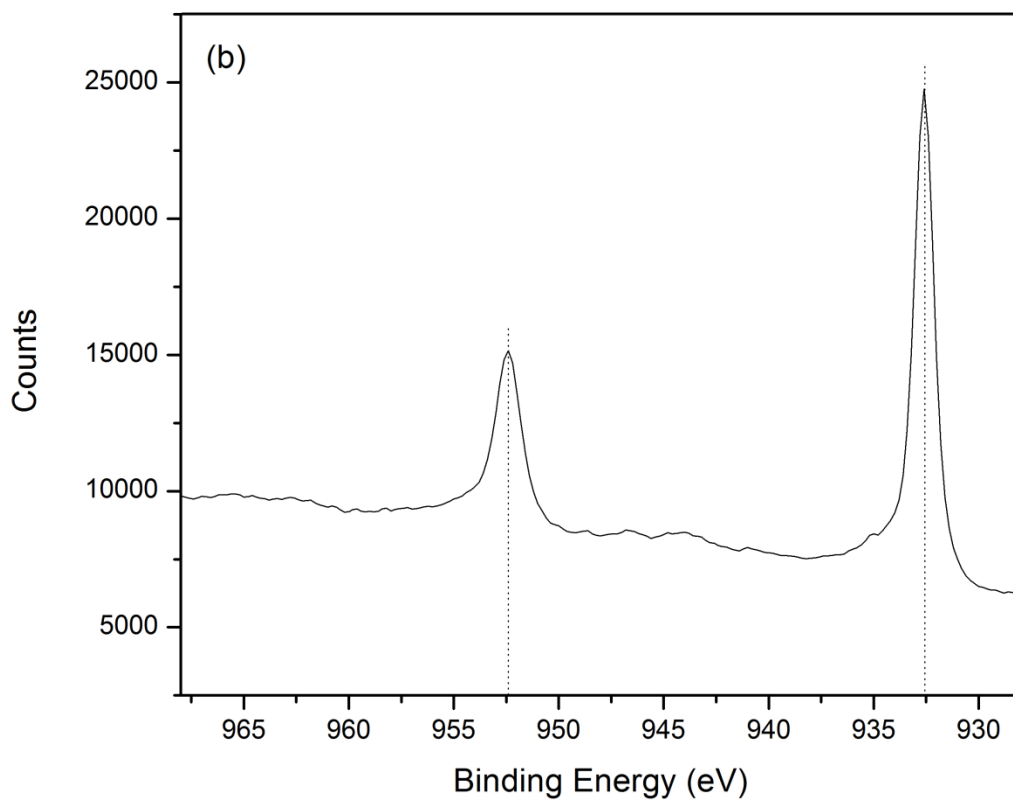
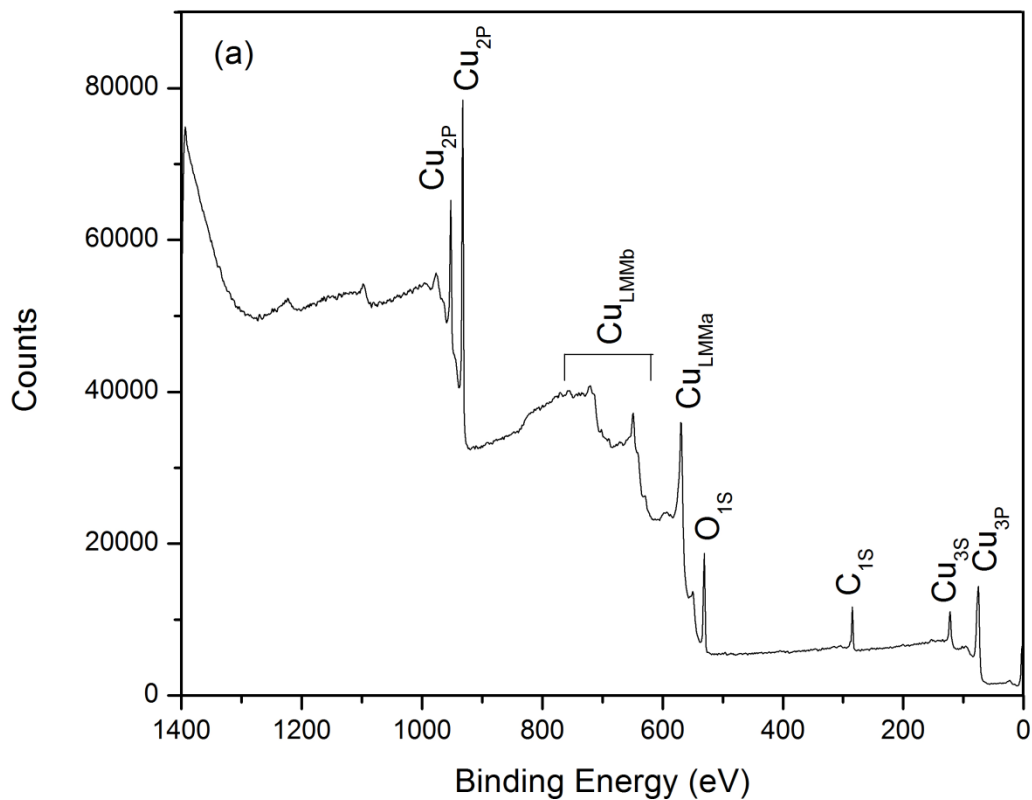
Figure 2-15. The XRD pattern of the CuNW powder.

Table 2-2. The d-spacings of the corresponding planes of fcc copper determined by MDI Jade 5.0 from the XRD pattern.

| (hkl) | d (Å) | Two theta |
|-------|--------|-----------|
| (111) | 2.0871 | 43.32 |
| (200) | 1.8075 | 50.45 |
| (220) | 1.2781 | 74.12 |

Figure 2–16 shows the X-ray photoelectron spectra of the CuNW powder. The survey spectra, high resolution spectra of the Cu 2P peak and Cu LMM peak are shown in Figures 2–16a, b and c, respectively. Table 2–3 shows the chemical shifts of Cu₂O and CuO referenced to metal copper in XP spectra, which can help to identify the different Cu species in the XP spectra.

The peaks of Cu, O and C can be identified from the survey spectra. The O peaks may originate from the oxide species in the sample or the O₂ absorbed on the surface. The C signals can be attributed to the carbon tape used to stick the CuNW powder on the aluminum stub. The survey spectra showed that the CuNW powder was pretty clean with no impurity above the detection limit of the XPS.



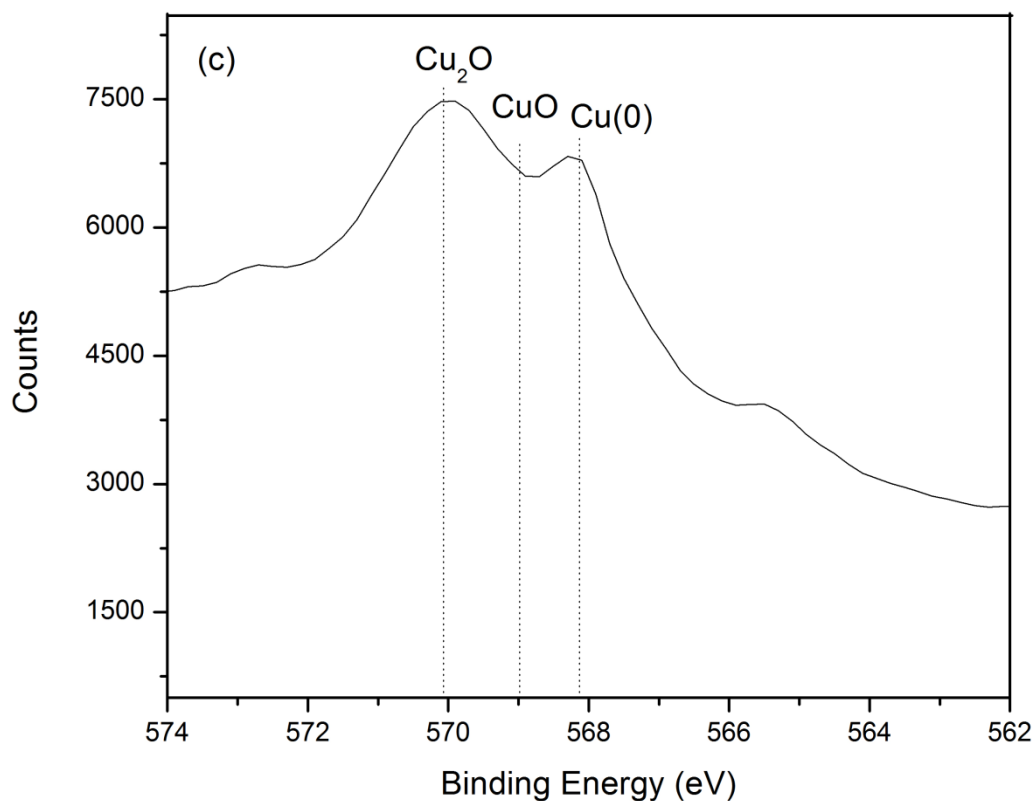


Figure 2-16. The X-ray photoelectron spectra of the CuNW powder. (a) The surveys, (b) the high resolution XP spectra of the Cu 2P peak and (c) the high resolution XP spectra of the Cu LMM peak.

Table 2-3. Chemical shifts of Cu₂O and CuO referenced to metal copper [19].

| Species | Cu 2P peak | Cu LMM peak |
|-------------------|------------|-------------|
| Cu | 0 | 0 |
| Cu ₂ O | 0.1 | 2.3 |
| CuO | 1.2 | 1.0 |

The chemical shifts of Cu_2O and CuO from metal Cu are 0.1 eV and 1.2 eV respectively in Cu 2P XP spectra, which means that the Cu 2P spectra can be readily used to identify CuO from metal Cu , but cannot be used to identify Cu_2O from metal Cu [20] because of the chemical shifts 0.1 eV is within the error limit of the instrument [19]. In Figure 2–16b, the Cu $2\text{P}_{1/2}$ and Cu $2\text{P}_{2/3}$ were detected at 952.4 eV and 932.5 eV respectively, which can be attributed to either metal Cu or Cu_2O , or both [19, 21] in the sample. Moreover, the chemical shifts of the Cu 2P spectra in Figure 2–16b from metal Cu were far less than 1.2 eV indicating the absence of CuO whose main peak in Cu $2\text{P}_{2/3}$ spectra should appear at 933.6 eV [22].

Another distinct way to identify CuO species in Cu 2P XP spectra is the shake-up satellite peaks, which are the characteristic of materials with an open d^9 shell [23–25]. The divalent state copper in CuO has a d^9 configuration in the ground state, while Cu_2O is supposed to have an essentially full 3d shell [25, 26]. Therefore, the shake-up satellite feature of CuO can be utilized to identify the species in the CuNW powder sample [27–29]. The shake-up satellite peaks of CuO should appear at ~945 eV and ~965 eV for the Cu $2\text{P}_{3/2}$ and Cu $2\text{P}_{1/2}$ core levels, respectively [28]. That no obvious shake-up satellite peaks can be observed from the Cu 2P XP spectra in Figure 2–16b indicated the absence of CuO species in the CuNW powder.

The chemical shifts of both CuO and Cu_2O in Cu LMM spectra are ≥ 1.0 eV, which means that the three common species metal Cu , CuO and Cu_2O can be

readily identified in Cu LMM spectra [30, 31]. The peaks of metal Cu and Cu₂O can be clearly distinguished in Figure 2–16c, which appeared at the binding energies of 568.1 eV and 570.1 eV, respectively. However, The CuO peak cannot be observed in the Cu LMM spectra, which indicated the absence of CuO species in the CuNW powder. This result is consistent with the result from the Cu 2P XP spectra as well as the result from the XRD pattern.

2.4. Conclusions

PAO templates were prepared by Masuda's two-step process by the anodization of high purity aluminum plates in 0.3 mol/L H₂SO₄ aqueous solution with 25 V DC under 0~4 °C. The barrier layer was thinned by the stepwise decrease of the DC voltage at the end of the second anodization process from 25 V to 9 V.

A 200 Hz continuous sine AC of 10 V_{rms} was applied to deposit copper into the pores of the PAO template for 10.5 min. The yield of CuNWs per unit area of the PAO template was proportional to the hours of the second anodization. The CuNWs liberated and ultrasonicated had an average length of 1.98 μm. The diameter of the CuNWs measured in TEM images was 25 ± 4 nm. Therefore, the average aspect ratio of the CuNWs was around 80.

The EDX spectra confirmed the Cu element in the CuNWs. Both metal Cu and Cu₂O can be identified in the XRD pattern of the CuNW powder. The

composition of the CuNW powder was also verified by the X-ray photoelectron spectra.

2.5. References

- [1] Alivisatos AP, Barbara PF, Castleman AW, Chang J, Dixon DA, Klein ML, McLendon GL, Miller JS, Ratner MA, Rosky PJ, Stupp SJ, Thompson ME. From molecules to materials: current trends and future directions. *Adv. Mater.* 1998, 10 (16): 1297–1336.
- [2] Ozin GA. Nanochemistry: synthesis in diminishing dimensions. *Adv. Mater.* 1992; 4 (10): 612–649.
- [3] Thiaville A, Miltat J. Small Is Beautiful. *Science* 1999; 284 (5422): 1939–1940.
- [4] Xia YN, Yang PD, Sun YG, Wu YY, Mayers B, Gates B, Yin YD, Kim F, Yan YQ. One-dimensional nanostructures: synthesis, characterization and applications. *Adv. Mater.* 2003; 15 (5) 353–389.
- [5] Routkevitch D, Tager AA, Haruyama J, Almawlawi D, Moskovits M, Xu JM. Nonlithographic nano-wire arrays: fabrication, physics, and device applications. *IEEE Trans. Electron Devices* 1996; 147 (10): 1646–1658.

- [6] Nielsch K, Müller F, Li AP, Gösele U. Uniform nickel deposition into ordered alumina pores by pulsed electrodeposition. *Adv. Mater.* 2000; 12 (8): 582–586.
- [7] Possin GE. A Method for Forming Very Small Diameter Wires. *Rev. Sci. Instrum.* 1970; 41 (5): 772–774.
- [8] Fleisher RL, Price PB, Walker RM. Method of forming fine holes of near atomic dimensions. *Rev. Sci. Instrum.* 1963; 34 (5): 510–512.
- [9] Price PB, Walker RM. Chemical Etching of Charged-Particle Tracks in Solids. *J. Appl. Phys.* 1962; 33 (12): 3407–3412.
- [10] Murphy CJ, Gole AM, Hunyadi SE, Orendorff CJ. One-dimensional colloidal gold and silver nanostructures. *Inorg. Chem.* 2006; 45 (19): 7544–7554.
- [11] Kline TR, Tian ML, Wang JG, Sen A, Chan MWH, Mallouk TE. Template-grown metal nanowires. *Inorg. Chem.* 2006; 45 (19): 7555–7565.
- [12] Masuda H, Hasegawa F, Ono S. Self-ordering of cell arrangement of anodic porous alumina formed in sulfuric acid solution. *J. Electrochem. Soc.* 1997; 144 (5): L127–L130.
- [13] Masuda H, Satoh M. Fabrication of gold nanodot array using anodic porous alumina as an evaporation mask. *Jpn. J. Appl. Phys.* 1996; 35: L126–L129.

- [14] Gerein NJ, Haber JA. Effect of ac electrodeposition conditions on the growth of high aspect ratio copper nanowires in porous aluminum oxide templates. *J. Phys. Chem. B* 2005; 109 (37): 17372–17385.
- [15] Ang LM, Hor TSA, Xu GQ, Tung CH, Zhao SP, Wang JLS. Decoration of activated carbon nanotubes with copper and nickel. *Carbon* 2000; 38: 363–372.
- [16] Xu C, Wu G, Liu Z, Wu D, Meek TT, Han Q. Preparation of copper nanoparticles on carbon nanotubes by electroless plating method. *Mater. Res. Bull.* 2004; 39: 1499–1505.
- [17] Gonzalez-Chavez C, D’Haen J, Vangronsveld J, Dodd JC. Copper sorption and accumulation by the extraradical mycelium of different *Glomus* spp. (arbuscular mycorrhizal fungi) isolated from the same polluted soil. *Plant Soil* 2002; 240: 287–297.
- [18] Bourdillon AJ, Self PG, Stobbs WM. Crystallographic orientation effects in energy dispersive X-ray analysis. *Philos. Mag. A.* 1981; 44 (6): 1335–1350.
- [19] Larson PE. X-ray induced photoelectron and Auger spectra of Cu, CuO, Cu₂O, and Cu₂S thin films. *J. Electron Spectrosc. Relat. Phenom.* 1974; 4: 213–218.
- [20] Speckmann HD, Haupt S, Strehblow HH. A quantitative surface analytical study of electrochemically-formed copper oxides by XPS and X-Ray-induced Auger spectroscopy. *Surf. Interface Anal.* 1988; 11: 148–155.

- [21] Yin M, Wu CK, Lou YB, Burda C, Koberstein T, Zhu Y, O'Brien S. Copper oxide nanocrystals. *J. Am. Chem. Soc.* 2005; 127: 9506–9511.
- [22] Lin B, Gelves GA, Haber JA, Pötschke P, Sundararaj U. Electrical, morphological and rheological study of melt-mixed polystyrene/copper nanowire nanocomposites. *Macromol. Mater. Eng.* 2008; 293: 631–640.
- [23] Rosencwaig A, Wertheim GK, Guggenheim HJ. Origins of satellites on inner-shell photoelectron spectra. *Phys. Rev. Lett.* 1971; 27 (8): 479–481.
- [24] Laibinis PE, Whitesides GM. Self-assembled monolayers of n-alkanethiolates on copper are barrier films that protect the metal against oxidation by air. *J. Am. Chem. Soc.* 1992; 114 (23): 9022–9028.
- [25] Ghijsen J, Tjeng LH, van Elp J, Eskes H, Westerink J, Sawatzky GA, Czyzyk MT. Electronic structure of Cu₂O and CuO. *Phys. Rev. B* 1998; 38 (16): 11322–11330.
- [26] Chawla SK, Sankarraman N, Payer JH. Diagnostic spectra for XPS analysis of Cu–O–S–H compounds. *J. Elec. Spectrosc. Relat. Phenom.* 1992; 61 (1): 1–18.
- [27] Gelves GA, Lin B, U Sundararaj U, Haber JA. Electrical and rheological percolation of polymer nanocomposites prepared with functionalized copper nanowires. *Nanotechnology* 2008; 19: 215712 (12pp).

[28] Chusuei CC, Brookshier MA, Goodman DW. Correlation of Relative X-ray Photoelectron Spectroscopy Shake-up Intensity with CuO Particle Size. *Langmuir* 1999; 15 (8): 2806–2808.

[29] Wu CK, Yin M, O'Brien, Koberstein JT. Quantitative analysis of copper oxide nanoparticle composition and structure by X-ray photoelectron spectroscopy. *Chem. Mater.* 2008; 18: 6054–6058.

[30] Gelves GA, Lin B, Haber JA, Sundararaj U. Enhancing Dispersion of Copper Nanowires in Melt-Mixed Polystyrene Composites. *J. Polym. Sci. Pol. Phys.* 2008; 46: 2064–2078.

[31] McIntyre NS, Cook MG. X-ray photoelectron studies on some oxides and hydroxides of cobalt, nickel, and copper. *Anal. Chem.* 1975; 47 (13), 2208–2213.

Chapter 3

Oxidation Kinetics of Copper Nanowires Synthesized by AC

Electrodeposition of Copper into Porous Aluminum Oxide Templates

3.1. Introduction

CuNWs with one dimensional nanostructure have potential applications in many fields such as electronics, optoelectronics and photonics [1–3] due to their high electrical and thermal conductivity. The specific properties of CuNWs make them excellent candidates for nanofillers in multi-functional polymer nanocomposites. AC electrodeposition of copper into anodized porous aluminum oxide templates is one of the most efficient methods to produce CuNWs [4].

CuNWs of diameters less than 100 nm have much higher surface area, and thus are subject to much higher oxidation rate than bulk copper due to the crystallite strain and more surface area. It is very important to study the oxidation kinetics of CuNWs to know their corrosion mechanism and activity loss so as to understand their long term performance and durability.

The oxidation kinetics of bulk copper have been extensively studied. The conclusion has been reached that the oxidation rate increases with temperature while O_2 partial pressure makes no difference on the rate when it is above the equilibrium potential for Cu/CuO [5]. Regarding the oxidation kinetics, parabolic law has been reported most frequently, while logarithmic and inverse-logarithmic laws were also observed at low temperatures as well as cubic law at

moderate temperatures 600 °C to 850 °C [6]. The reported activation energies of bulk copper oxidation in air/O₂ between 300 °C and 1050 °C vary from 39 kJ/mol to 223 kJ/mol [7] as shown in Table 3–1.

Although the kinetics and mechanism of bulk copper oxidation are widely studied and well understood, very little is known about the nanoscale copper particles like CuNWs. In this study, the oxidation kinetics of CuNWs synthesized by AC electrodeposition of Cu into PAO templates was studied. The activation energies were determined by different model-free methods, and the oxidation mechanism was determined by fitting the results with different models.

Table 3-1. Activation energies Reported for Copper Oxidation [7]

| Type of Copper | Atmosphere (1 atm) | Temperature (°C) | Activation Energy (kJ/mol) | References |
|-----------------|-----------------------|------------------|----------------------------|------------|
| Spectrally Pure | Air | 900~1,050 | 140 | [8] |
| OFHC | Air | 300~500 | 39 | [9] |
| | | 600~900 | 123 | |
| OFHC | O ₂ | 700~1,000 | 132 | [5] |
| 99.995 pct | Air | 900~1,050 | 159 | [10] |
| 99.999 pct | O ₂ or air | 750~1,040 | 172 | [11] |
| | | 450~750 | 84 | |
| | | 350~450 | 223 | |
| — | Air | 750~1,000 | 146 | [12] |
| 99.999 pct | O ₂ | 660~937 | 179 | [13] |
| OFHC | O ₂ | 300~550 | 84 | [14] |
| | | 550~900 | 158 | |

3.2. Experimental

3.2.1. Preparation of CuNW dry powder

CuNWs were synthesized by AC electrodeposition of copper into the anodic PAO template. The details of the synthesis and liberation were described in Chapter 2. The CuNWs prepared by this method after 1 h ultrasonication in methanol have diameter of 25 ± 4 nm and an average length ca. 2 μ m. The CuNW/CH₃OH dispersion was then filtered with a nylon membrane (Osmonics Inc.) with pore size 0.45 μ m. The sludge after filtration was dried in a vacuum oven under room temperature and -25 inHg vacuum for 3 h. The vacuum oven was flushed with N₂ for three times at the beginning of the drying process. After drying, the cake was grounded slightly in a mortar to make a uniform fine powder. The fine powder of CuNWs was then immediately stored in liquid nitrogen.

3.2.2. Morphology characterization of the CuNWs

The SEM images of the CuNW dry powder before and after oxidation were collected using a Philips XL30 scanning electron microscope. The dry powder before and after oxidation was stuck onto carbon tape stuck on an aluminum stub. All these samples were coated with gold prior to SEM imaging.

The TEM images were collected with a Tecnai F20 field emission gun transmission electron microscope under 200 kV accelerating voltage. A very dilute CuNW/CH₃OH dispersion (before oxidation) was dropped onto a holey

carbon coated nickel TEM grid. The CuNWs powder after oxidation was dispersed into methanol by 30 min ultrasonication and then dropped onto a holey carbon coated nickel TEM grid for TEM observation.

3.2.3. Thermogravimetric analysis (TGA) of the CuNW powder

All the TGA data and plots were collected with a TA Q500 TGA instrument, and all the TGA tests were carried out within 10 min after the CuNW powder was taken out of liquid nitrogen. The oxygen content in the CuNW powder before oxidation was determined from the TGA curve acquired with 60 mL/min 4% H₂ balance N₂ (Praxair) as purge gas and 40 mL/min N₂ (Praxair) as balance gas at heating rate 20 °C/min from room temperature to 800 °C. The photographs of the TA Q500 TGA, the furnace configuration and gas flow route are shown in Figure 3–1.

The oxidation TGA curves were obtained with 60 mL/min air (Praxair) as purge gas and 40 mL/min N₂ (Praxair) as balance gas at different heating rates from room temperature to 500 °C. The sample of the CuNW powder for each oxidation experiment was controlled between 3~5 mg and distributed evenly in the platinum pan to minimize the temperature gradient inside the sample and facilitate the release of the oxidation heat quickly.

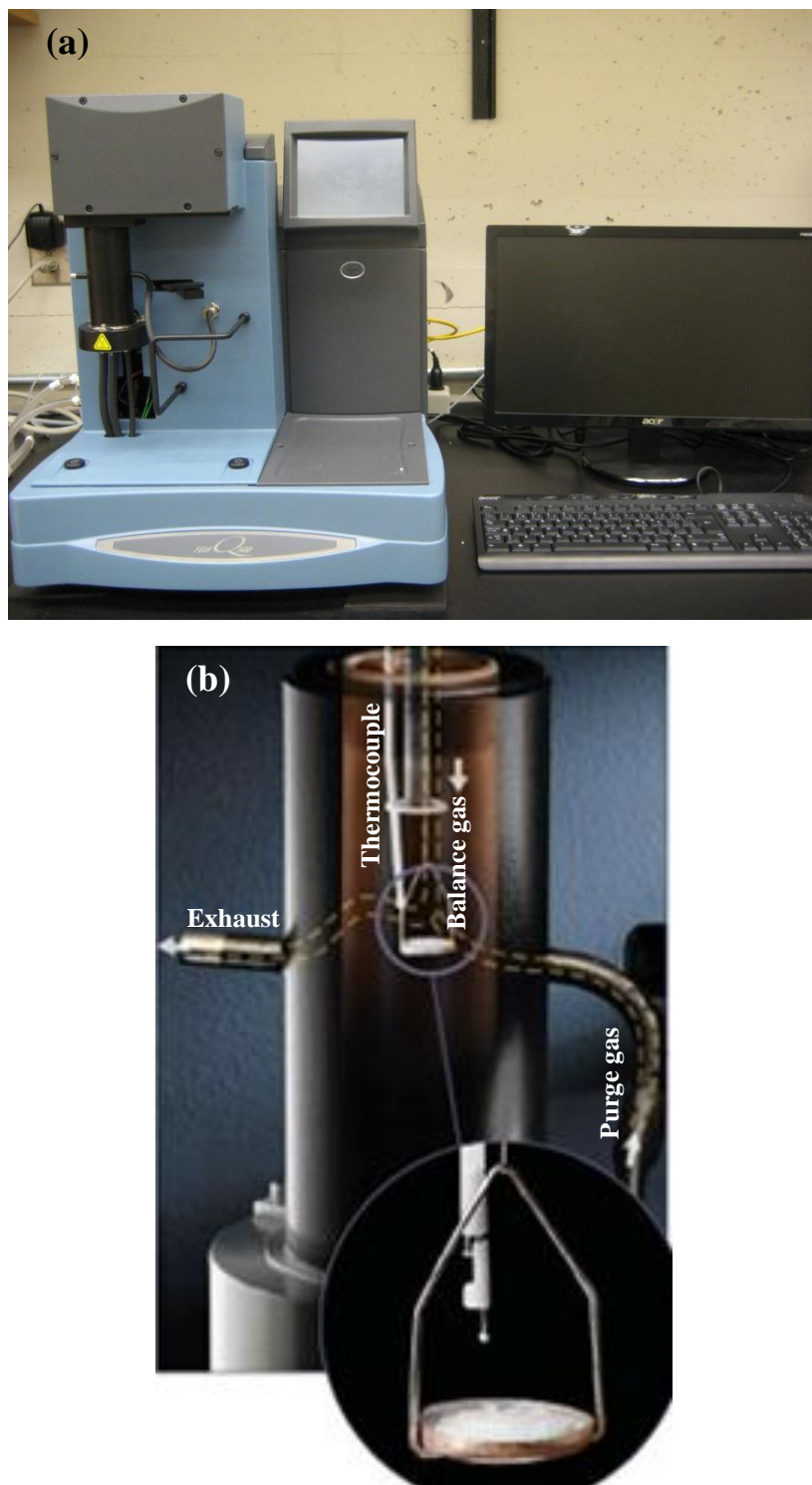


Figure 3-1. The photographs of (a) the TA Q500 TGA and (b) the furnace configuration and gas flow route.

3.2.4. XRD characterization

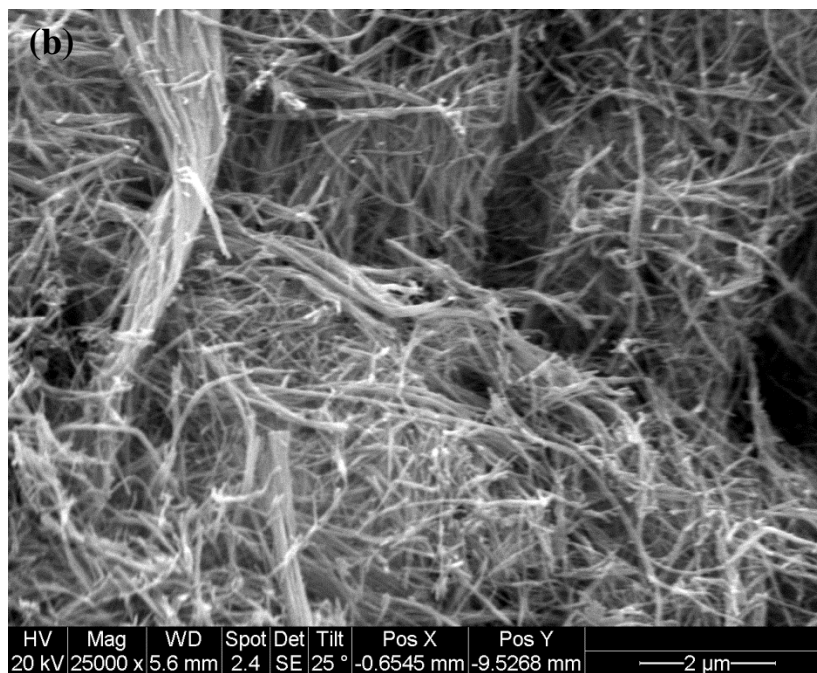
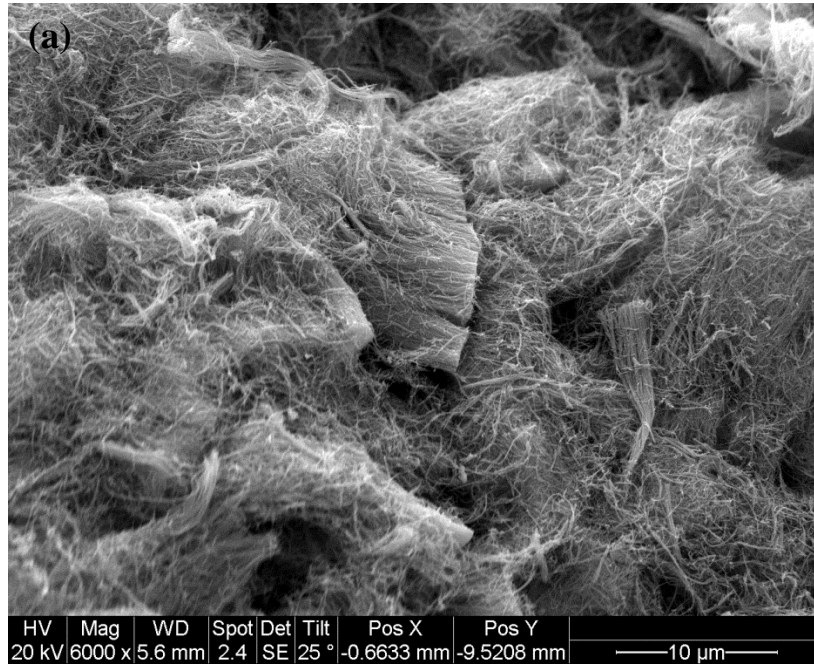
The XRD patterns were obtained with an Ultima III Multi Purpose Diffraction System with Cu K α radiation operating at 40 kV and 44 mA.

The CuNW powder taken out of liquid nitrogen was immediately used to collect the XRD pattern before oxidation. The CuNW powder heated to 175 °C at 9 °C/min rate with 60 mL/min air as purge gas and 40 mL/min N₂ as balance gas in the TGA instrument was used to collect the XRD pattern of CuNWs after Stage 1. The CuNW powder heated to 350 °C at 9 °C/min rate with 60 mL/min air as purge gas and 40 mL/min N₂ as balance gas in the TGA was used to collect the XRD pattern of CuNWs after Stage 2.

3.3. Results and discussion

3.3.1. CuNWs before oxidation

The SEM and TEM images of the CuNW powder before oxidation are shown in Figure 3–2. Figure 3–2a shows the low magnification SEM image, Figure 3–2b shows the high magnification image; and Figure 3–2c shows the TEM image of the CuNWs before oxidation. In the SEM images, most of the CuNWs in the dry powder are seen to exist as single wires; however, some CuNWs in bundles merged into nanowire agglomerates with larger diameter. The diameter of the individual CuNWs in the TEM image was 25 ± 4 nm, which is consistent with the value reported by Gelves et al [8].



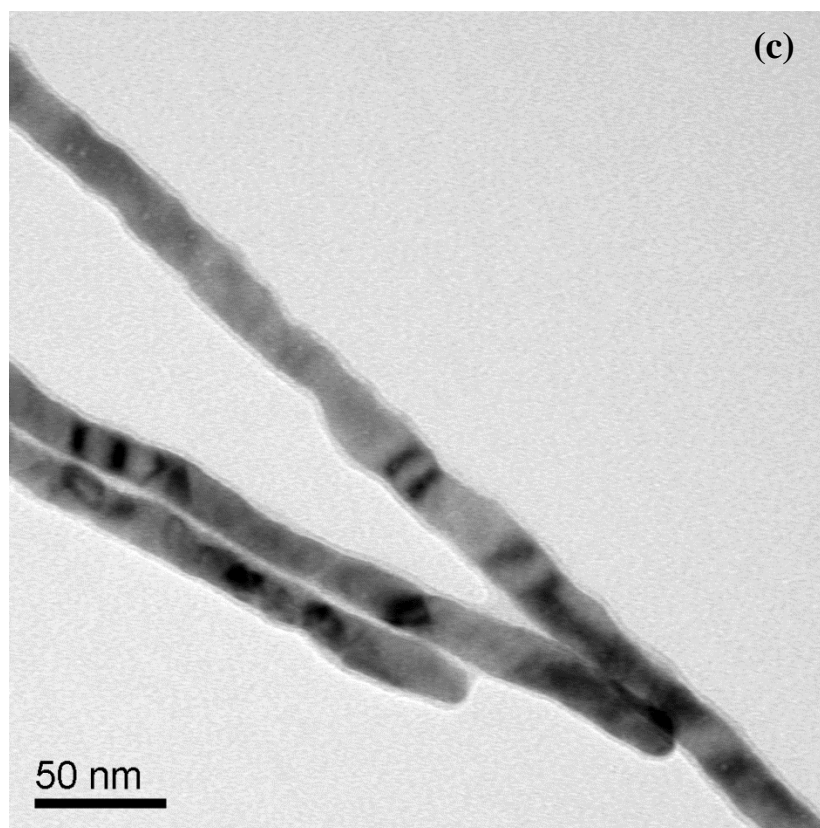


Figure 3-2. The (a, b) SEM and (c) TEM images of the CuNWs before oxidation.

All the XRD patterns of the CuNW powder before and after oxidation are shown in Figure 3–3. The Composition of the CuNW powder before oxidation included metallic Cu and Cu_2O . After oxidation, only Cu_2O and CuO were detected by XRD. In the TGA plot shown in Figure 3–4, the CuNW dry powder before oxidation reduced in H_2 at $600\text{ }^\circ\text{C}$ had weight loss of 3.0%, which can be attributed to the O content in the sample. Combining the XRD pattern of CuNW powder before oxidation with the TGA plot collected during the reduction in H_2 , it can be calculated that the CuNW dry powder before oxidation comprised 26.8

wt. % Cu_2O and 73.2 wt. % Cu.

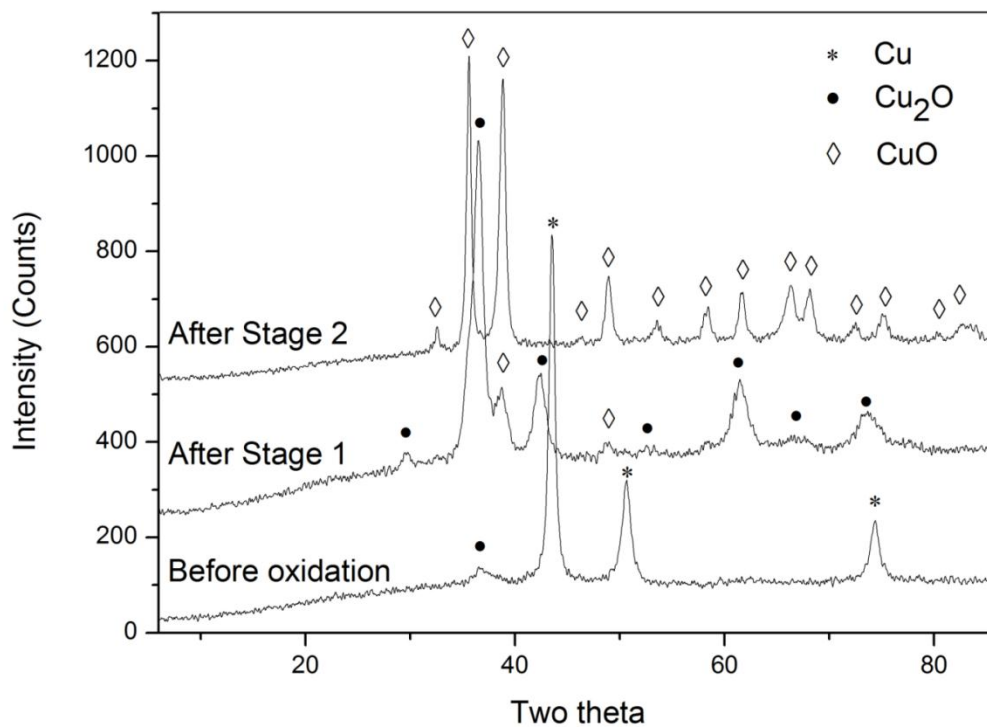


Figure 3-3. The XRD patterns of the CuNW powder before oxidation, after stage 1 and after stage 2.

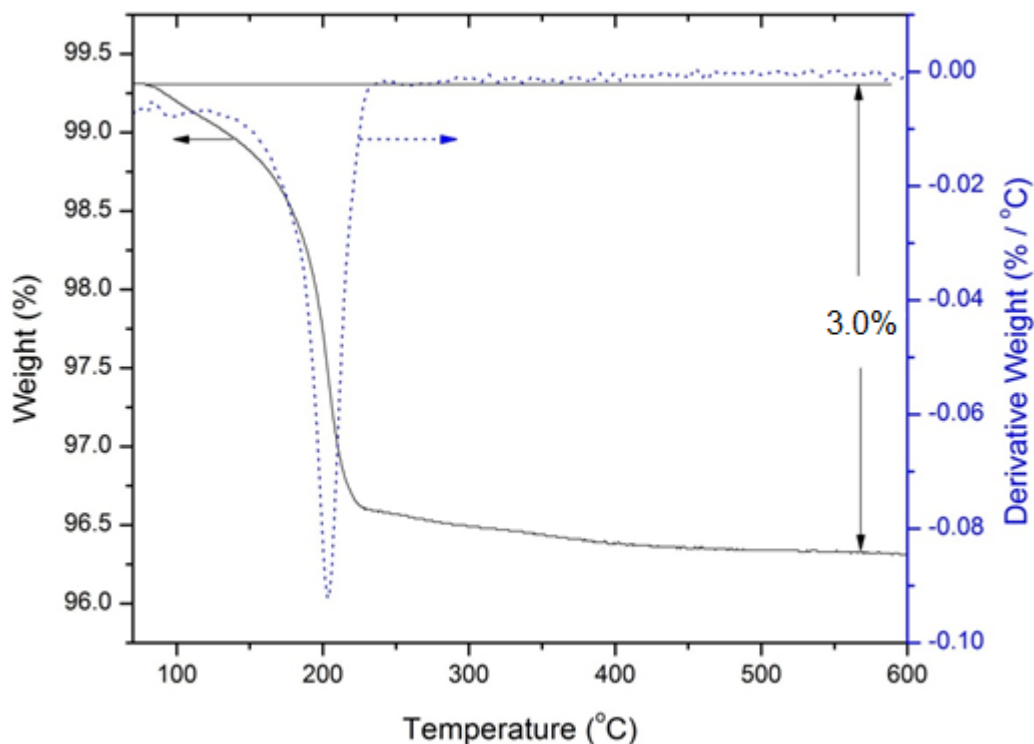


Figure 3-4. The TGA plot of the CuNW powder before oxidation reduced in H_2 .

3.3.2. Two stages oxidation of the CuNW powder

Figure 3-5 and Figure 3-6 illustrate the TGA and differential thermogravimetric (DTG) curves of different heating rates during oxidation, respectively. Both the TGA and the DTG curves in similar patterns shifted to higher temperature at higher heating rate. And the peak maximums of the DTG curves also shifted to higher temperature at higher heating rate.

By observing the TGA and the DTG curves, the oxidation reaction of the CuNW powder can be divided into two different stages. On the TGA curves, there is a plateau at around 175 °C connecting the two different stages: the stage

1 with higher weight gain rate took place at temperature lower than 175 °C, and the stage 2 with lower weight gain rate took place at temperature higher than 175 °C. In addition, there are two peaks on each DTG curve, which also indicates the two-stage oxidation of the CuNW powder. Based on the DTG curves, the oxidation reaction of the CuNW powder was divided into two stages at 172 °C on the TGA curve of 9 K/min heating rate which corresponds to the weight of 111.2 % as indicated by the horizontal dash line on the TGA plots in Figure 3–5.

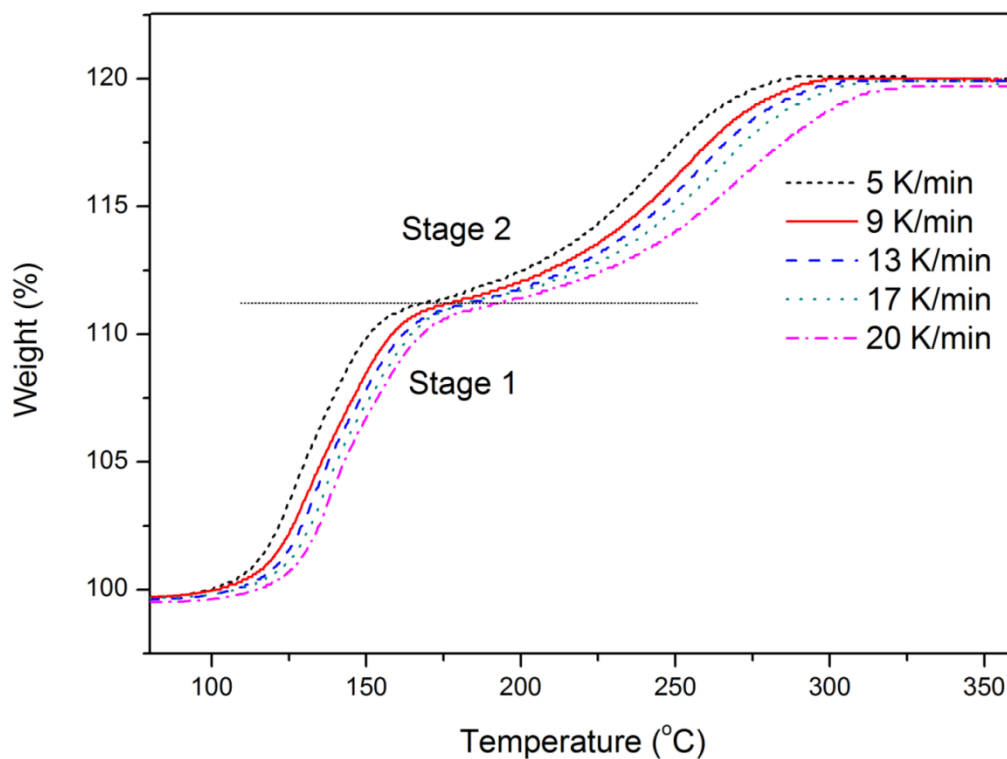


Figure 3-5. The TGA curves of the CuNW powder oxidized at different heating rates.

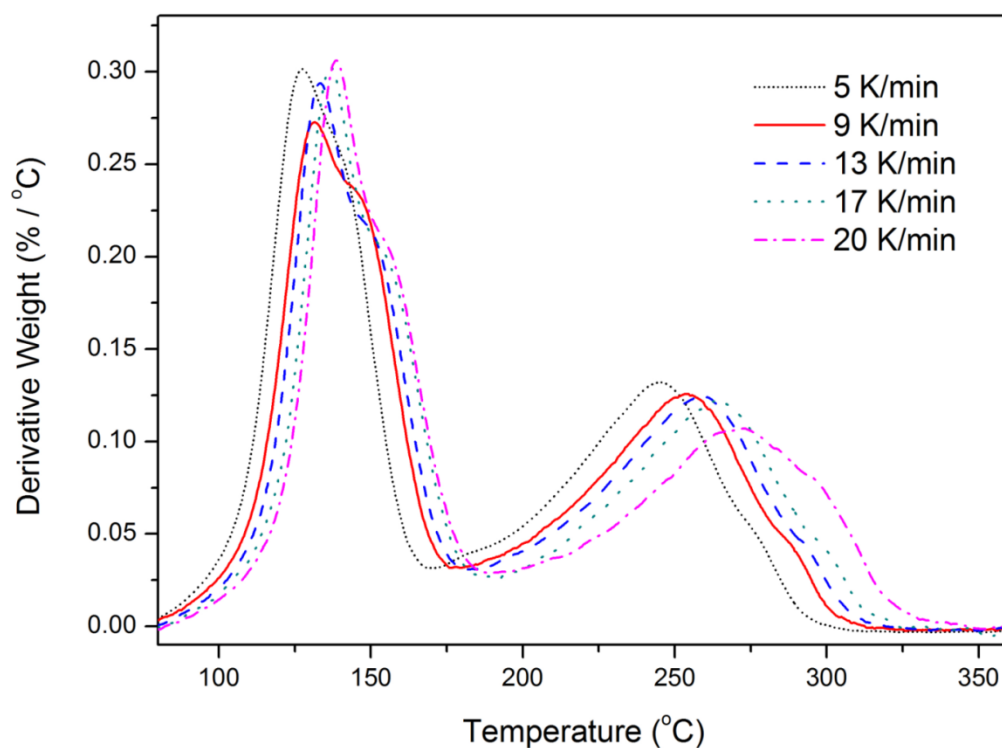


Figure 3-6. The DTG curves of the CuNW powder oxidized at different heating rates.

The composition of the oxidized CuNW powder after stage 1 and stage 2 was identified by XRD as shown in Figure 3–3. The oxidized CuNW powder after stage 1 comprised Cu_2O and CuO , and the oxidized CuNW powder after stage 2 consisted of CuO only.

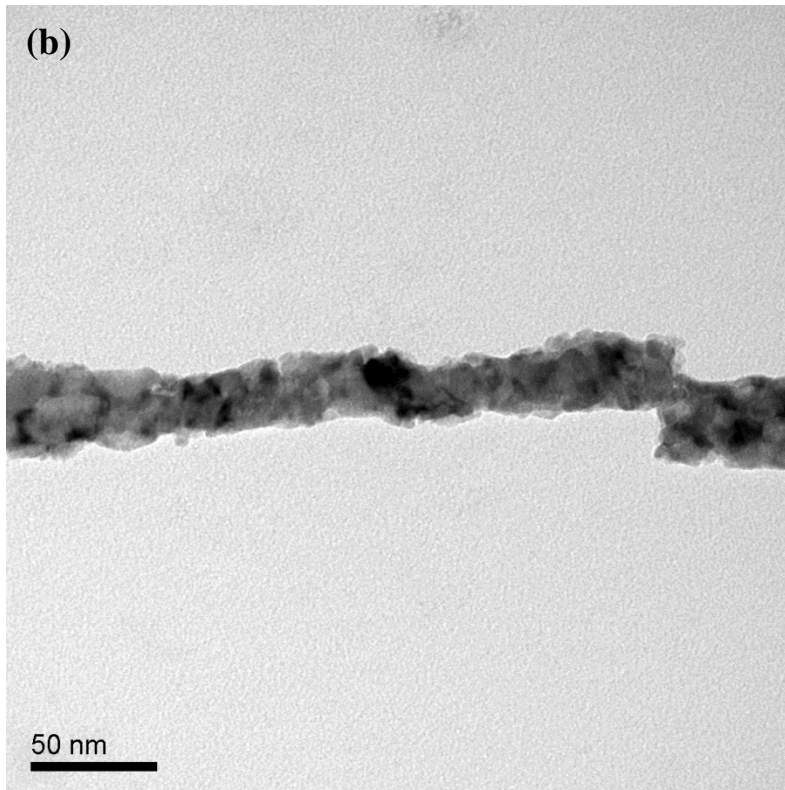
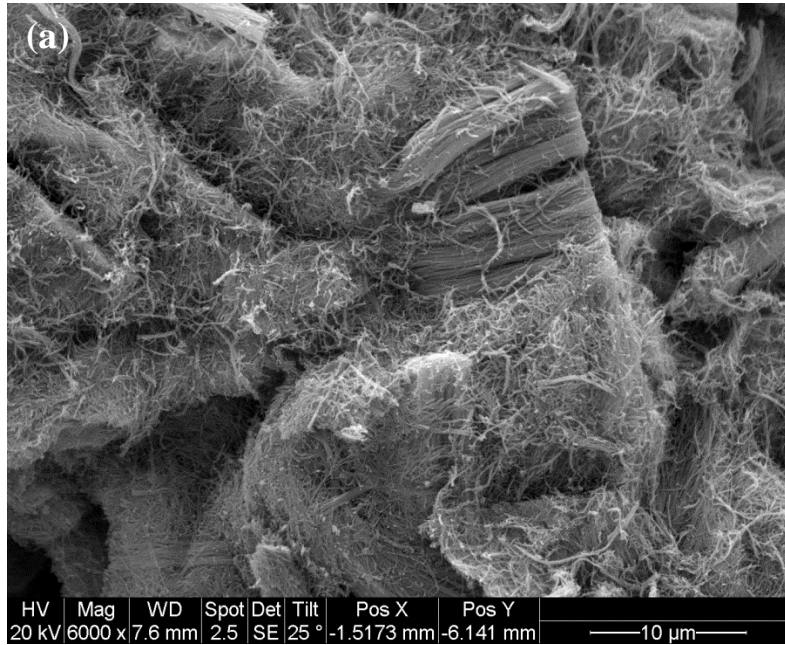
Based on the composition of the CuNW powder before oxidation, the final weight gain of the CuNW powder after stage 2 should be 19.9% if both the Cu and the Cu_2O in the initial CuNW powder were converted to CuO stoichiometrically. On the TGA plot, the final weight gain of the CuNW powder

after stage 2 was around 20.0% based on the lowest weight point on the plot, which is slightly higher than the theoretical value of 19.9%. Conversion ratio α at given temperature was determined from TGA data by the assumption of stoichiometric reaction with 19.9% final weight gain:

$$\alpha(T) = \frac{W(T) - W_i}{W_f - W_i} \quad (3-1)$$

Where W_i is the initial weight percentage of the sample, W_f is the final weight percentage of the sample. $W(T)$ is the weight percentage of the sample at temperature T . For stage 1, W_i is 99.7%, the lowest weight percentage point on the TGA plot, W_f is 111.2%. For stage 2, W_i is 111.2%, W_f is 119.9%.

The SEM and TEM images of the CuNWs after oxidation are shown in Figures 3–7 (a, c) and (c, d), respectively. Figures 3–7a and b are the images after stage 1 oxidation and Figures 3–7c and d are the images after stage 2 oxidation. The oxidation process made no difference on the SEM images. However, The CuNWs after stage 1 became loose and rough with diameter 25 ± 6 nm in the TEM image. The CuNWs after stage 2 looked dense and smooth with larger diameter of 32 ± 6 nm which could result from the merge of two or more individual CuNWs into one during the oxidation.



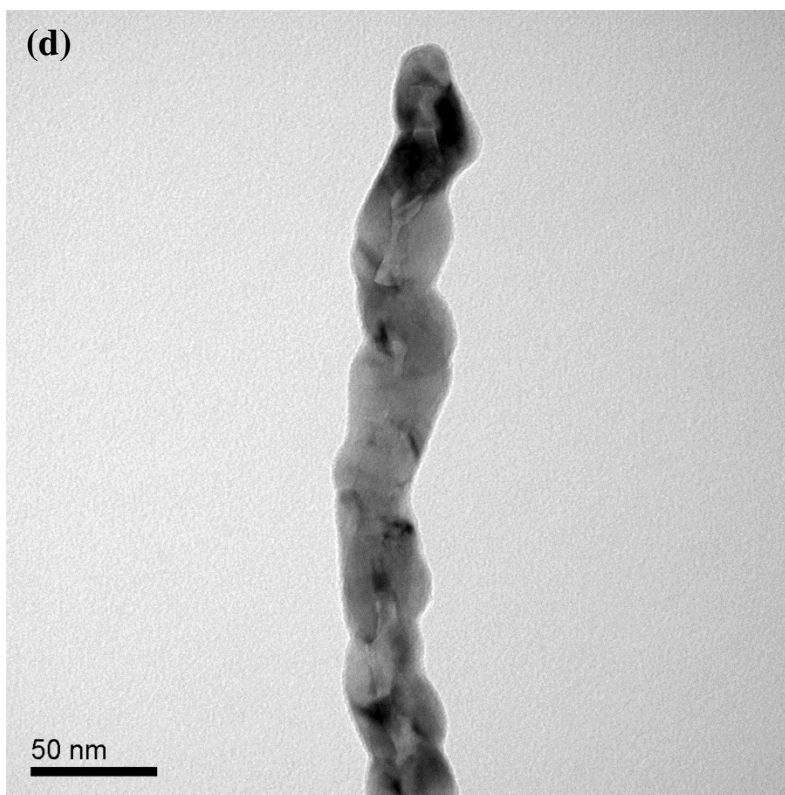
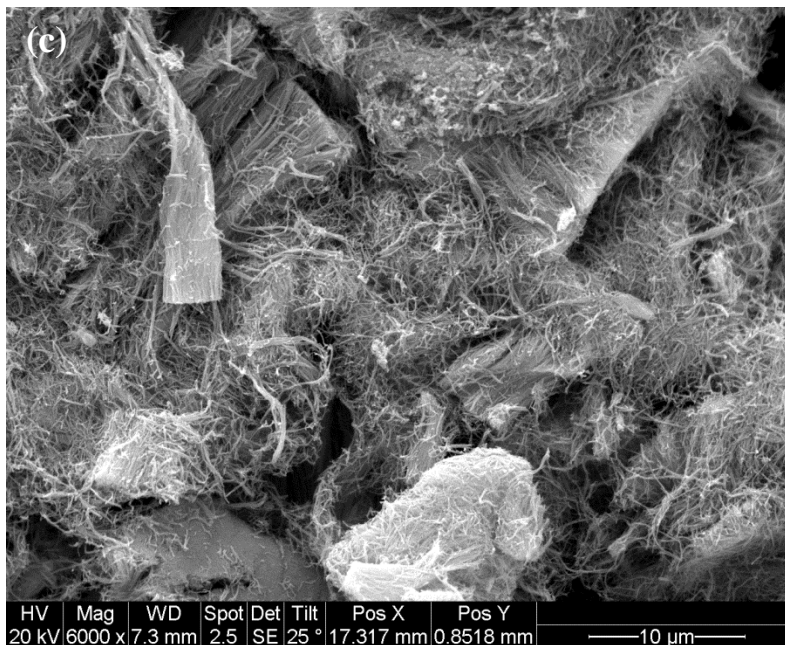


Figure 3-7. The (a, c) SEM and (b, d) TEM images of the CuNWs oxidized (a, b) after stage 1 and (c, d) after stage 2.

3.3.3. Determination of activation energy by Kissinger method and isoconversional methods

Unlike the well-known bulk copper oxidation, little is known about the mechanism of the CuNW powder oxidation. It is necessary to use model-free methods to determine the activation energy.

Kissinger method [15] involving no assumption of the reaction mechanism can be used to determine the activation energy with a single value. Kissinger equation is:

$$\ln\left(\frac{\beta}{T_{max}^2}\right) = \ln\frac{AR}{E_a} - \frac{E_a}{RT_{max}} \quad (3-2)$$

Where A is the Arrhenius frequency factor, T_{max} is the temperature of the peak maximum on the DTG plot. The activation energy E_a can be determined from the slope of the plot of $\ln\left(\frac{\beta}{T_{max}^2}\right)$ against $1/T_{max}$. The Arrhenius plots based on Kissinger equation for stage 1 and stage 2 are shown in Figure 3–8. The activation energies determined by Kissinger method were 163.5 kJ/mol (1.69 eV) for stage 1 and 109.6 kJ/mol (1.14 eV) for stage 2.

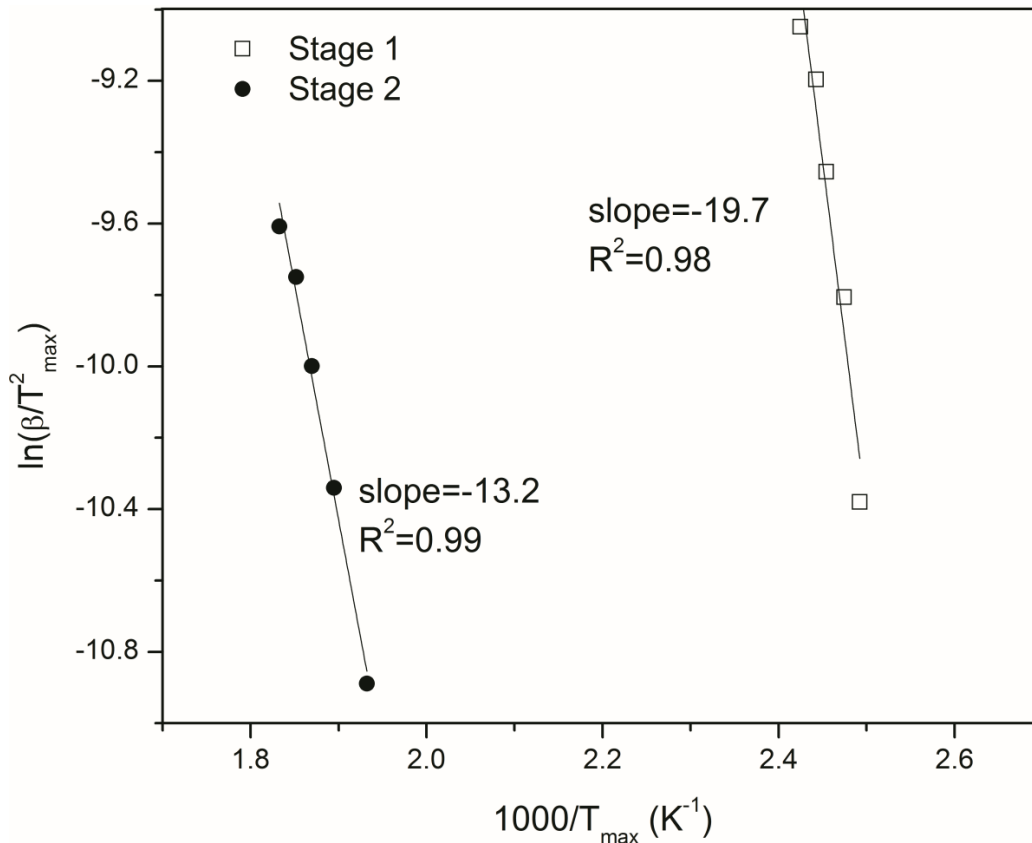


Figure 3-8. The Arrhenius plots based on Kissinger Equation for stage 1 and stage 2.

Model-free isoconversional methods are based on the assumption that the reaction rate at a certain conversion is only a function of temperature and the reaction model is independent of temperature and heating rate. These models make it possible to determine the activation energy without determination of the reaction mechanism and reaction order. The common isoconversional methods to study solid state reactions are listed as below:

Flynn-Wall-Osawa (FWO) equation in differential form [16]

$$\frac{d \ln \beta}{d(1/T)} = -\frac{1.052 E_a}{R} \quad (3-3)$$

Starink equation [17]

$$\ln \frac{\beta}{T^{1.8}} = C - \frac{B E_a}{RT} \quad (3-4)$$

Kissinger-Akahira-Sunose (KAS) equation [18]

$$\ln \frac{\beta}{T^2} = \ln \frac{A}{E_a g(\alpha)} - \frac{E_a}{RT} \quad (3-5)$$

Friedman differential equation [19]

$$\ln \left(\beta \frac{d\alpha}{dT} \right) = \ln [A f(\alpha)] - \frac{E_a}{RT} \quad (3-6)$$

Boswell Equation [20]

$$\ln \frac{\beta}{T} = C - \frac{E_a}{RT} \quad (3-7)$$

Where C is a constant, $B = 1.0070 - 1.2 \times 10^{-5} \times E_a$ (when E_a in kJ/mol), β is the heating rate, A is the Arrhenius frequency factor, $g(\alpha)$ is the mechanism function, $f(\alpha)$ is the differential mechanism function, E_a is the activation energy, R is gas constant, T is absolute temperature.

The activation energies determined with above five methods were plotted against each conversion ratio α for both stages in Figure 3-9 and Figure 3-10, respectively. The activation energies were between 1.0 eV and 1.7 eV for stage 1 and between 0.87 eV and 1.15 eV for stage 2. The activation energies of stage 1

dropped at the beginning of the oxidation reaction and then increased to their maximum at around 50% conversion. The higher activation energy at the beginning of stage 1 could result from the influence of the Cu_2O in the CuNW powder before oxidation, which covered the surface of the CuNWs leading to the enhanced stability. The activation energies of stage 2 were much lower than those of stage 1. The activation energies of stage 2 increased slightly at the beginning, and then dropped to the minimum at the end of the oxidation reaction.

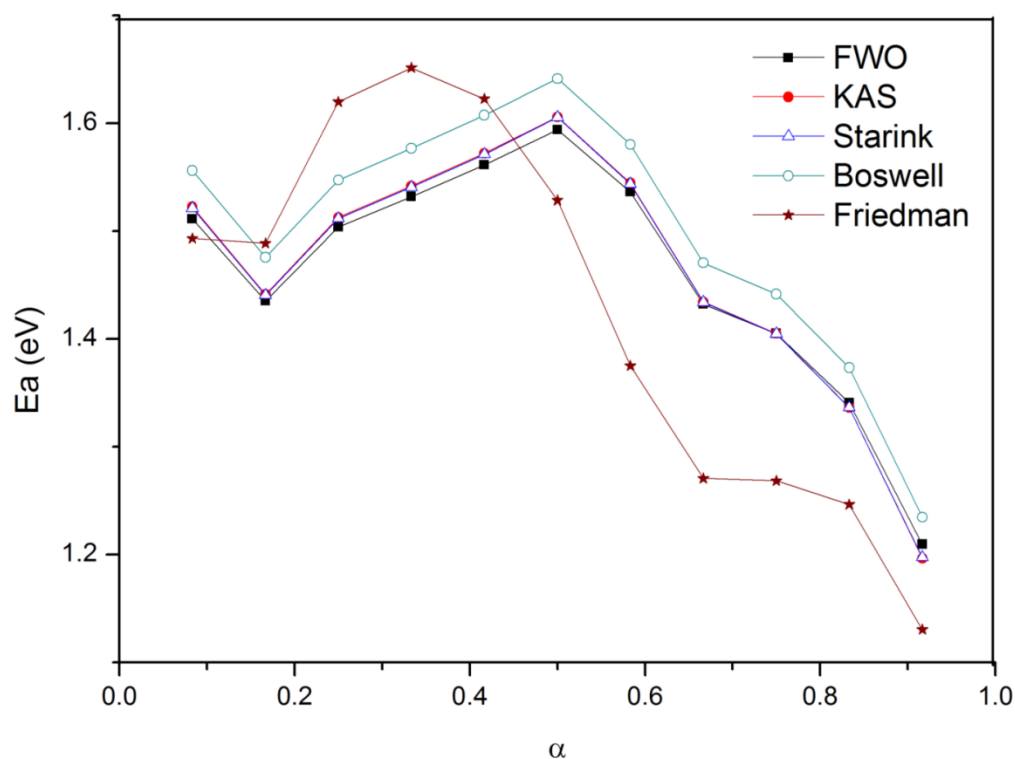


Figure 3-9. The activation energies for stage 1 determined by the different model free isoconversional equations.

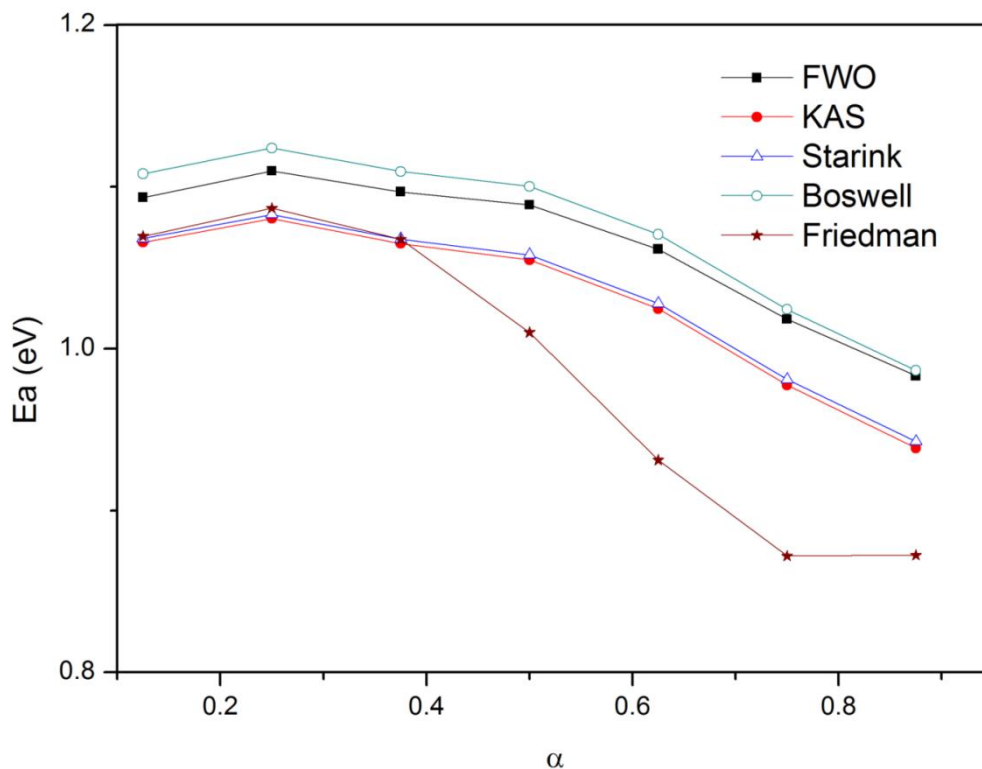


Figure 3-10. The activation energies for Stage 2 determined by the different model free isoconversional equations.

Theoretically, the activation energy with a fixed value should be held for the homogeneous reactions in which all the reactant molecules are identical and unaffected by the formation of the product as the reaction proceeds. However, the activation energies of CuNW powder oxidation in this study fluctuated as the oxidation reaction proceeds indicating that the reactant CuNW powder were undergoing the reactivity change because of the formation of crystal defect, i.e. the change of intracrystalline strain and the process of particle disintegration [21]. Moreover, the reactivity of the individual nanowires in the original CuNWs also

changed significantly during the oxidation reaction—this may result from the particle size evolvement, change in the boundary faces of different indices exposed, and crystal imperfections and damages [21] as indicated in the TEM images in Figure 3–2 and Figure 3–7. Therefore, it is reasonable that the activation energy of the CuNW powder oxidation may not be constant as the oxidation reaction proceeded, and variable activation energies should be used to determine the oxidation kinetics. Among the activation energies determined by different methods, Kissinger and Boswell methods obtained higher values, the values by Friedman method exhibited the maximum fluctuation, and Starink and KAS methods obtained very similar values that fell among the values determined by other methods.

3.3.4. Determination of reaction kinetics

Based on the generalized kinetic equations, Gotor et al [22] deduced the relationship between the experimental kinetic data and the theoretical mechanism function. The rate of a solid reaction can be expressed in the general law:

$$\frac{d\alpha}{dt} = A \cdot \exp\left(-\frac{E_a}{RT}\right) \cdot f(\alpha) \quad (3-8)$$

Where, t is the reaction time. The kinetics rate equation at infinite temperature can be derived by defining the generalized time θ [23–25] as:

$$\theta = \int_0^t \exp\left(-\frac{E_a}{RT}\right) dt \quad (3-9)$$

Where, θ stands for the reaction time taken to reach a particular α at infinite temperature. The differentiation of equation 3–9 results in

$$\frac{d\theta}{dt} = \exp\left(-\frac{E_a}{RT}\right) \quad (3-10)$$

Dividing equation 3–8 by equation 3–10, the following expression can be obtained:

$$\frac{d\alpha}{d\theta} = A \cdot f(\alpha) \quad (3-11)$$

Or

$$\frac{d\alpha}{d\theta} = \frac{d\alpha}{dt} \exp\left(\frac{E_a}{RT}\right) \quad (3-12)$$

Selecting a reference point at $\alpha = 0.5$, equation 3–13 can be easily derived from equation 3–11.

$$\frac{d\alpha/d\theta}{(d\alpha/d\theta)_{\alpha=0.5}} = \frac{f(\alpha)}{f(0.5)} \quad (3-13)$$

According to equation 3–12,

$$\frac{d\alpha/d\theta}{(d\alpha/d\theta)_{\alpha=0.5}} = \frac{(d\alpha/dT)_{\alpha} \exp(E_a/RT)}{(d\alpha/dT)_{\alpha=0.5} \exp(E_a/RT)_{0.5}} \quad (3-14)$$

Combining equation 3–13 and equation 3–14, the relationship between the experimental kinetic data and the theoretical mechanism function $f(\alpha)$ can be expressed as:

$$\frac{f(\alpha)}{f(0.5)} = \frac{(d\alpha/dT)_\alpha \exp(E_a/RT)}{(d\alpha/dT)_{\alpha 0.5} \exp(E_a/RT)_{0.5}} \quad (3-15)$$

This expression of the conventional master plot method can be utilized to study the oxidation kinetics of the CuNW powder.

The left side of equation 3–15 can be plotted with the individual differential mechanism function $f(\alpha)$ (listed in Table 3–2) against the conversion ratio α . The right side of equation 3–15 is plotted using the variable activation energies determined by Starink method.

Chapter 3. Oxidation Kinetics of Copper Nanowires Synthesized by AC Electrodeposition of Copper into Porous Aluminum Oxide Templates

Table 3-2. Algebraic expressions for the $f(\alpha)$ and $g(\alpha)$ functions for the most common mechanisms in solid reactions [22]

| Mechanism | Symbol | $f(\alpha)$ | $g(\alpha)$ |
|---|--------|---|---|
| Phase boundary controlled reaction (contracting area) | $R2$ | $(1 - \alpha)^{1/2}$ | $2[1 - (1 - \alpha)^{1/2}]$ |
| Phase boundary controlled reaction (contracting volume) | $R3$ | $(1 - \alpha)^{2/3}$ | $3[1 - (1 - \alpha)^{1/3}]$ |
| Unimolecular decay law | $F1$ | $1 - \alpha$ | $-\ln(1 - \alpha)$ |
| Random nucleation and growth of nuclei (Johnson-Mehl-Avrami equation) | Am | $m(1 - \alpha)[- \ln(1 - \alpha)]^{1-1/m}$ | $[- \ln(1 - \alpha)]^{1/m}$ |
| Two-dimensional diffusion | $D2$ | $1/[- \ln(1 - \alpha)]$ | $(1 - \alpha) \ln(1 - \alpha) + \alpha$ |
| Three-dimensional diffusion (Jander Equation) | $D3$ | $\frac{3(1 - \alpha)^{2/3}}{2(1 - \alpha)^{1/3}}$ | $[1 - (1 - \alpha)^{1/3}]^2$ |
| Three-dimensional diffusion (Ginstein-Brounshtein Equation) | $D4$ | $\frac{3}{2[(1 - \alpha)^{-1/3} - 1]}$ | $\left(1 - \frac{2\alpha}{3}\right) - (1 - \alpha)^{2/3}$ |

The master plots of Johnson-Mehl-Avrami (JMA) equation in Table 3–2 with different m values and the experiment points are shown in Figure 3–11. JMA equation gave the best fit among all equations in Table 3–2. JMA equation with $m = 2$ presented the best fit for $\alpha < 0.5$ at stage 1, while $m = 3$ had the best fit for $\alpha > 0.5$ at stage 1 and $m = 4$ exhibited the best fit for stage 2. Based on the fitting results, it can be concluded that random nucleation and growth of nuclei were the mechanism for the CuNW oxidation in both stages. The deviation of the experimental data from the theoretical function may result from two reasons. One the one hand, it is not easy to determine the value of $d\alpha/dT$ accurately due to its high sensitivity to the baseline stability [17]; on the other hand, the pre-existing oxide Cu_2O in CuNW powder before oxidation interfered with the ideal random nucleation and growth of nuclei mechanism. J. C. Yang et al [26, 27] reported the dominant process was oxygen surface diffusion for transport and nucleation [27] as well as oxygen surface diffusion plus direct impingement mechanism [28] for the initial growth of Cu_2O on the single crystal Cu(001) thin films. In addition, Johnson-Mehl-Avrami-Kolmogorov (JMAK) surface theory, which suggests that the nucleation and coalescence of thin films result from surface processes, was applied to describe the nucleation and coalescence growth of Cu_2O [26]. In this study, the diameter of the CuNWs was only 25 ± 4 nm, which means a large number of atoms distributed on the surface of CuNWs and the high crystallite strain caused by the high gradient of the surface curvature. The surface atoms and crystallite strain in the CuNWs should account for the random nucleation and growth of nuclei mechanism in oxidation.

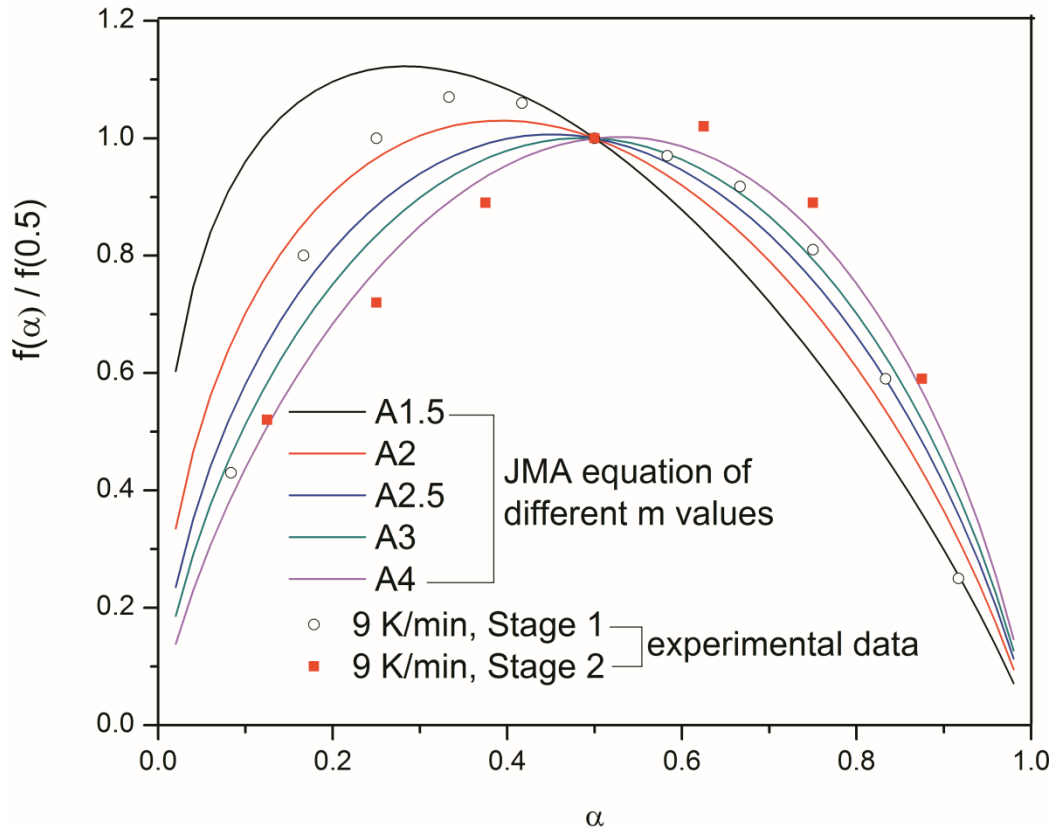


Figure 3-11. Kinetic model fitting for the CuNW powder oxidation using JMA equation in Table 3–2 with different m values.

The oxidation TGA curves in Figure 3–5 exhibit typical sigmoidal shapes for both stages, which indicate random nucleation and growth of nuclei mechanism for the oxidation of CuNWs. Moreover, the morphological evolution of CuNWs during oxidation is shown in Figure 3–2 and Figure 3–7, which is consistent with the mechanism of random nucleation and growth of nuclei. The CuNWs have smooth surface before oxidation. Due to the random nucleation of CuO over the parent phase of Cu_2O , the oxidized CuNWs after Stage 1 become loose and

rough (See Figures 3–2c and 3–7b). Near the end of Stage 2, the oxidation rate decreases as the untransformed Cu_2O phase becomes less and less so that new CuO nuclei cannot form; and the CuO nuclei already existing continue to grow and begin to touch each other to form larger grains and boundaries that terminate the growth of CuO nuclei. This results in the dense smooth surface of the oxidized CuNWs after Stage 2 (see Figures 3–7b and 3–7d) and the merging of two or more individual CuNWs into one.

Regarding the oxidation of bulk copper under ambient oxygen pressures, the parabolic rate law was the one most frequently observed at intermediate temperature between 300 °C and 1050 °C [7, 29]. The cubic law was reported at moderate temperatures 600 °C to 850 °C [6, 30]. At temperature below 300 °C, logarithmic and inverse-logarithmic laws were observed [6, 30]. Two major mechanisms for the Cu_2O and/or CuO scale growth during the oxidation of bulk copper were proposed: the diffusion of copper ions from the metal to the oxide-oxygen interface driven by concentration gradient, and tunnelling electrons coming up against the surface electric field [6]. However, the oxidation of CuNWs in this study does not obey any law reported for the oxidation of bulk copper. Instead, the oxidation of CuNWs follows the JMA equation which means oxidation occurs by random nucleation and growth of nuclei driven by surface processes.

3.4. Conclusions

The CuNWs synthesized for oxidation kinetics study had diameter 25 ± 4 nm with smooth surface. The composition of the CuNW dry powder before oxidation comprised Cu and Cu_2O as identified by XRD with 3.0% oxygen content, which is equivalent to 73.2 wt. % metal Cu and 26.8 wt. % Cu_2O .

Based on the TGA and DTG plots of different heating rates, the oxidation reaction of the CuNW powder should be divided into two stages at the weight of 111.2%. The oxidized CuNWs after stage 1 became loose and rough with diameter of 25 ± 6 nm; and the composition identified by XRD consisted of Cu_2O and CuO. The oxidized CuNWs after stage 2 looked dense and smooth with larger diameter of 32 ± 6 nm, which could result from the merging of two or more individual CuNWs into one during the oxidation; and the composition identified by XRD comprised CuO only.

The activation energies of both stages were determined by Kissinger method and other five isoconversional methods. The activation energies of stage 2 were much lower than those of stage 1. Among the activation energies determined by different methods, Kissinger and Boswell methods obtained higher values, the values by Friedman method exhibited the maximum fluctuation, and Starink and KAS methods obtained very similar values that fell among the values determined by other methods.

The activation energies determined by Starink method were used to fit the different master plots. JMA equation gave the best fit among all the equations.

JMA equation with $m = 2$ presented the best fit for $\alpha < 0.5$ at stage 1, while $m = 3$ gave the best fit for $\alpha > 0.5$ at stage 1 and $m = 4$ exhibited the best fit for stage 2. The surface atoms were the sites for the random nucleation and the crystallite strain in CuNWs was the driving force for the growth of nuclei mechanism during the oxidation process.

3.5. References

- [1] Mohl M, Pusztai P, Kukovecz A, Konya Z, Kukkola J, Kordas K, Vajtai R, Ajayan PM. Low-temperature large-scale synthesis and electrical testing of ultralong copper nanowires. *Langmuir* 2010; 26 (21): 16496–16502.
- [2] Duan JL, Liu J, Yao HJ, Mo D, Hou MD, Suna YM, Chen YF, Zhang L. Controlled synthesis and diameter-dependent optical properties of Cu nanowire arrays. *Mater. Sci. Eng. B-Solid* 2008; 147: 57–62.
- [3] Shi Y, Li H, Chen LQ, Huang XJ. Obtaining ultra-long copper nanowires via a hydrothermal process. *Sci. Technol. Adv. Mater.* 2005; 6: 761–765.
- [4] Zhou ZF, Zhou YC, Pan Y, Wang XG. Growth of the nickel nanorod arrays fabricated using electrochemical deposition on anodized Al templates. *Mater. Lett.* 2008; 62: 3419–3421.
- [5] Bridges DW, Baur JP, Baur GS, Fassell WM. Oxidation of copper to Cu_2O and CuO (600 °–1000 °C and 0.026–20.4 atm oxygen). *J. Electrochem. Soc.* 1956; 103: 475–478.

- [6] Gao W, Gong H, He J, Thomas A, Chan L, Li S. Oxidation behaviour of Cu thin films on Si wafer at 175–400 °C. *Mater. Lett.* 2001; 51: 78–84.
- [7] Zhu YF, Mimura K, Lim JW, Isshiki M, Jiang Q. Brief review of oxidation kinetics of copper at 350 °C to 1050 °C. *Metall. Mater. Trans. A* 2006; 37A: 1231–1237.
- [8] Mrowec S, Stoklosa A. Oxidation of copper at high temperatures. *Oxid. Metal.* 1971; 3 (3): 291–311.
- [9] Tylecote RF. The oxidation of copper at 350 °–900 ° in air. *J. Inst. Metals* 1950–51; 78: 327–350.
- [10] Czerski L, Mrowec S, Werber T. The influence of nickel on the kinetics of oxidation of copper at high temperatures. *Roczniki Chem.* 1964; 38: 643–654.
- [11] Park JH Natesan K. Oxidation of copper and electronic transport in copper oxides. *Oxid. Metal.* 1993; 39 (5–6): 411–435.
- [12] Kofstad P. Oxidation of metals: determination of activation energies. *Nature* 1957; 179: 1362–1363.
- [13] Sartell JA Li CH. The oxidation of high-purity copper-nickel alloys. *Trans. Am. Soc. Metall.* 1962; 55: 158–162.
- [14] Valensi G. Pittsburgh International Conference on Surface Reactions. Corrosion Publ. Co., Pittsburgh 1948; 156–159.

- [15] Kissinger HE. Reaction kinetics in differential thermal analysis. *Anal. Chem.* 1957; 29: 1702–1706.
- [16] Flynn JH, Wall LA. A quick, direct method for the determination of activation energy from thermogravimetric data. *J. Polymer Sci. B Polymer Lett.* 1966; 4 (5): 323–328.
- [17] Starink MJ. A new method for the derivation of activation energies from experiments performed at constant heating rate. *Thermochim. Acta.* 1996; 288 (1–2): 97–104.
- [18] Robinson PP, Arun V, Manju S, Aniz CU, Yusuff KKM. Oxidation kinetics of nickel nano crystallites obtained by controlled thermolysis of diaquabis(ethylenediamine)nickel(II) nitrate. *J. Therm. Anal. Calorim.* 2010; 100 (2): 733–740.
- [19] Friedman HL. New methods for evaluating kinetic parameters from thermal analysis data. *J. Polymer Sci. B Polymer Lett.* 1969; 7 (1): 41–46.
- [20] Boswell PG. On the calculation of activation energies using a modified Kissinger method. *J. Thermal. Acta.*, 1980; 18 (2): 353–358.
- [21] Song P, Wen D, Guo ZX, Korakianitis T. Oxidation investigation of nickel nanoparticles. *Phys. Chem. Chem. Phys.* 2008; 10: 5057–5065.

- [22] Gotor FJ, Criado JM, Malek J, Koga N. Kinetic Analysis of Solid-State Reactions: The Universality of Master Plots for Analyzing Isothermal and Nonisothermal Experiments. *J. Phys. Chem. A* 2000; 104 (46): 10777–10782.
- [23] Ozawa T. A new method of analyzing thermogravimetric data. *Bull. Chem. Soc. Jpn.* 1965; 38 (11): 1881–1886.
- [24] Ozawa T. Kinetic analysis of derivative curves in thermal analysis. *J. Therm. Anal.* 1970; 2 (3): 301–324.
- [25] Ozawa T. Non-isothermal kinetics and generalized time. *Thermochim. Acta* 1986; 100 (1): 109–118.
- [26] Yang JC, Bharadwaj MD, Zhou G, Tropia L. Surface Kinetics of Copper Oxidation Investigated by In Situ Ultra-high Vacuum Transmission Electron Microscopy. *Microsc. Microanal.*, 2001; 7 (6): 486–493.
- [27] Yang JC, Yeadon M, Kolasa B, Gibson JM. The homogeneous nucleation mechanism of Cu_2O on $\text{Cu}(001)$. *Scripta Mater.*, 1998; 8: 1237–1242.
- [28] Yang JC, Yeadon M, Kolasa B, Gibson JM. Oxygen surface diffusion in three-dimensional Cu_2O growth on $\text{Cu}(001)$ thin films. *Appl. Phys. Lett.* 1997; 70 (26): 3522–3524.
- [29] Y. Zhu, K. Mimura and M. Isshiki: Oxidation mechanism of copper at 623–1073 K. *Mater. Trans.* 43, 2173 (2002) .

[30] A. Yabuki and S. Tanaka: Oxidation behavior of copper nanoparticles at low temperature. Mater. Res. Bull. 46, 2323 (2011).

Chapter 4

Silver Coated Copper Nanowires with Improved Anti-oxidation Property as Conductive Fillers in Low Density Polyethylene and Polystyrene

4.1. Introduction

High aspect ratio metallic nanowires are attractive due to their unique properties and a variety of applications in electronics, optoelectronics, photonics, magnetics, genetic engineering and chemical sensors [1–5]. CuNWs have been frequently studied because of their excellent electrical and thermal conductivity [5].

Conductive polymer composites show significant advantages over surface coatings in ESD and EMI shielding [6]. Polymer nanocomposites are made of polymers filled with nanoparticles that have at least one dimension less than 100 nm. Conductive polymer composites with nanoparticle fillers exhibit advantages over those with micron-sized fillers in lighter weight, better processability, etc [7]. Both the low density polyethylene (LDPE) and polystyrene (PS) are thermoplastic polymers made from petroleum. The good processability, non-toxicity, low temperature stability and the excellent resistance to chemicals make LDPE an important plastic material in the worldwide market, despite competition from more and more new polymers. PS is widely used around the world with annual consumption of billions kilograms.

Our group has studied the electrically conductive CuNW polymer nanocomposites and AgNW polymer nanocomposites for ESD and EMI shielding [8, 9]. If copper particles are used as the electrically conductive fillers in polymer composites, the oxidation of copper results in the formation of an electrically insulative and non-self-protective layer of CuO and Cu₂O on the surface [10–12]. That increases the contact resistance between filler particles and thus the electrical resistivity of the composites. Metallic coatings are usually applied on various fillers for conductive polymer composites to reduce the cost and density. Bulk fillers such as high aspect ratio glass fibers, mica, carbon nanotubes and carbon fibers were coated with copper, silver, nickel, etc [13–16]. Silver is more resistant to oxidation than copper; and its electrical resistivity, $1.6 \times 10^{-6} \Omega \cdot \text{cm}$, is also lower than copper's resistivity, $1.7 \times 10^{-6} \Omega \cdot \text{cm}$ [8]. In addition, silver oxide is also much more electrically conductive [17] than copper oxides. Lin and Chiu [18] reported that the silver coating prevents the copper powder from oxidation at temperatures lower than 175 °C. However, there is still no report on the application of AgCuNWs as fillers in conductive polymer nanocomposites.

Because both copper and silver are more conductive than carbon, the CuNW/LDPE and AgCuNW/LDPE nanocomposites should exhibit higher electrical conductivity than the CNT/LDPE nanocomposites at high filler concentration (> 1.0 vol. %). In addition, the CuNW/LDPE and AgCuNW/LDPE nanocomposites are expected to provide higher EMI shielding for the X-band (8.2~12.4 GHz) electromagnetic radiation at filler concentration greater than 1.0

vol. % [19].

In this study, the CuNWs synthesized by AC electrodeposition of copper into PAO templates were coated with silver to improve their anti-oxidation property. The electrical resistivity of the AgCuNW/LDPE and AgCuNW/PS nanocomposites prepared by hot solution mixing and miscible solvent mixing and precipitation (MSMP) methods was evaluated and compared with that of the CuNW/LDPE and CuNW/PS nanocomposites, respectively.

4.2. Experimental

4.2.1. Synthesis of AgCuNWs

The CuNWs were synthesized by AC electrodeposition of copper into the anodic PAO template. The details of the synthesis and liberation were described in Chapter 2. The CuNWs synthesized by this method after 1 h ultrasonication in methanol had diameters of 25 ± 4 nm and an average length of ca. 2 μ m. After complete cleaning, the CuNWs for silver coating were dispersed into deionized water with one drop of 0.2 mol/L sodium dodecyl sulfate (SDS) and ultrasonicated for a period of 1 h in a sonication bath. The ultrasonic treatment consisted of 135 W average power and 38.5–40.5 kHz frequency applied for 5 min periods with a 5-min rest period between sonications. For CuNWs/LDPE nanocomposites, the CuNWs were dispersed in acetone beforehand with one drop of polyethylene glycol (PEG 200, Alfa Aesar) and subject to 30 min ultrasonication treatment.

AgCuNWs were prepared by chemical plating method. First, stoichiometrically excess AgNO_3 (+99%, Sigma Aldrich) was weighed and dissolved in distilled water to prepare 30 g/L AgNO_3 solution. To prepare Ag-amine reagent, ammonium hydroxide (NH_4OH , 28~30%, BDH) aqueous solution was added into the AgNO_3 solution drop by drop under vigorous stirring until all yellow precipitate disappeared and the solution became clear.

The Ag-amine reagent solution was then added drop by drop into the CuNW dispersion of deionized water under vigorous stirring. After 30 min mixing, the mixture was filtered. The AgCuNWs on the filter paper were then transferred into acetone with one drop of PEG 200 and dispersed via ultrasonic treatment for 30 min. Then, the nanowires were filtered and rinsed with deionized water for three times and with acetone for two times. The flow chart representing the process of the AgCuNW synthesis by chemical plating method is shown in Figure 4-1.

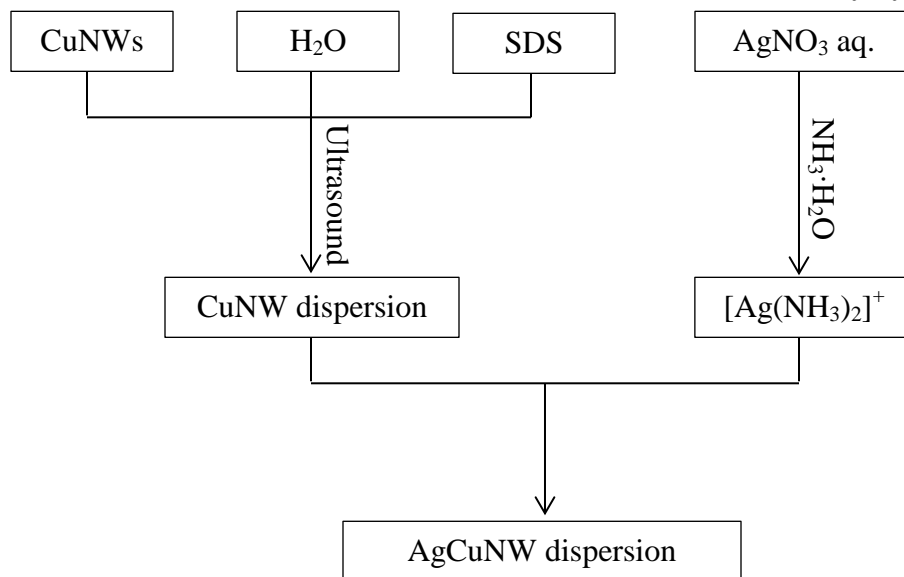


Figure 4-1. The flow chart representing the process of the AgCuNW synthesis by chemical plating method.

4.2.2. Length distribution of the nanowires

The length distribution of the nanowires (NWs) dispersed in acetone was determined from the SEM images of well-dispersed nanowires as described in Section 2.2.5.

4.2.3. Preparation of NW/LDPE nanocomposites by hot solution mixing method

The bulk densities of copper 8.96 g/cm³, silver 10.49 g/cm³ and LDPE 0.92 g/cm³ were used to calculate the volume percentages of NWs in the LDPE nanocomposites. The average density of the AgCuNWs was determined using the EDX quantitative element content listed in Table 4-1.

The LDPE (LA-0219-A, Nova Chemicals) composites with nanowires were prepared by adding the nanowire dispersion into 100 °C 3.5 wt. % LDPE hot solution in xylene (+98.5%, Alfa Aesar) under vigorous stirring. After an additional 5 min mixing at around 100 °C, the hot mixture of the LDPE and nanowires were poured into an evaporating dish to evaporate the solvent in a fume hood under ambient conditions for 24 h, and then dried in a vacuum oven under 40 °C for 6 h.

The NW/LDPE nanocomposites were prepared by hot solution mixing method. The NWs were well dispersed in acetone to form NW/acetone dispersion. When the NWs dispersed in acetone were added to the LDPE/xylene solution held at 100 °C, the acetone on the surface of the NWs decreased the surface energy of the nanowires and improved the dispersion of the NWs in the LDPE/xylene solution. However, the boiling point (57 °C) of acetone is much lower than the temperature of the LDPE/xylene solution, resulting in the rapid evaporation of the acetone from the mixture. After 5 min of mixing at around 100 °C, acetone was completely removed, and the NWs were dispersed in the mixture.

The completely dried NW/LDPE nanocomposites were cut into tiny pieces around 1–5 mm² and then added to a mold in a compression molding machine at 250 °C and 138 MPa for 30 min. The stainless steel mold dimensions were 0.21 mm thickness, 42.0 mm length and 25.0 mm width and PTFE sheets were used as release films between the mold and the top/bottom stainless steel plates. As a

reference, the neat LDPE samples from Nova Chemicals were first dissolved in xylene at 100 °C and then dried and hot pressed under the same processing conditions of the NW/LDPE nanocomposites.

4.2.4. Preparation of NW/PS nanocomposites by MSMP method

Polystyrene (Styron 666D, M_w 200,000 g/mol, T_g 100 °C, MFI 7.5 and density 1.04 g/cm³) was provided by the Dow Chemical Company. Both the CuNW/PS and the AgCuNW/PS nanocomposites were prepared by the MSMP method [20]. 3.0 g PS was added into 100 mL CH₂Cl₂ to prepare the solution under vigorous stirring. The CuNW/CH₃OH suspension measured by volume according to the calculation was added into the PS/CH₂Cl₂ solution under ultrasonication. The mixture after complete precipitation was placed in an evaporation dish for 24 h in a fume hood to evaporate the solvent completely. The dry NW/PS nanocomposite powder was then compression molded under the identical conditions as the NW/LDPE nanocomposites.

4.2.5. Characterization of NWs, NW/LDPE and NW/PS nanocomposites

The SEM images and EDX spectra were collected using a Philips XL30 scanning electron microscope. The NW dispersion in acetone was dropped onto an aluminum stub to dry out under ambient conditions. The nanowires on the aluminum stub were coated with gold to improve the electrical conductivity prior to imaging. Secondary images of the NWs were collected. The NW/LDPE and

NW/PS nanocomposites were fractured in liquid nitrogen and coated with gold and palladium to collect the backscattered images. The AgCuNW/PS nanocomposites after compression molding were dissolved in CH_2Cl_2 to remove PS, then dropped onto an aluminum stub and coated with gold and palladium to collect the backscattered images.

The TEM images were collected with a Tecnai F20 transmission electron microscope under 200 kV accelerating voltage. Dilute NW dispersion in acetone was dropped onto a holey carbon coated nickel TEM grid. The NW/LDPE nanocomposite samples were ultramicrotomed under $-130\text{ }^\circ\text{C}$ to obtain cross sections with thickness about 100 nm. The ultramicrotomed section was transferred onto a copper TEM grid for observation.

XRD patterns of the NWs and the NW/LDPE nanocomposites were collected by an Ultima III Multi Purpose Diffraction System with $\text{Cu K}\alpha$ radiation operating at 40 kV and 44 mA. The NW samples were prepared by drying the NW/acetone dispersion in a vacuum oven under room temperature. The dry NWs were then pulverized in a mortar and stored in a vial full of nitrogen for XRD test.

TGA data were obtained with a Perkin Elmer Pyris 1 TGA instrument. To determine temperature dependence, the pulverized dry nanowires samples were heated from room temperature to $800\text{ }^\circ\text{C}$ at heating rate of $10\text{ }^\circ\text{C}/\text{min}$ using $100\text{ mL}/\text{min}$ air as purge gas. The time-dependent TGA data were obtained by programming the temperature to step to $250\text{ }^\circ\text{C}$ and the TGA was kept isothermal for 25 min using $100\text{ mL}/\text{min}$ air as purge gas.

Differential scanning calorimetry (DSC) analyses were carried out with a TA DSC Q100 instrument with 50 mL/min N₂ (Praxair) as purge gas at heating rate of 20 °C/min. The DSC data were analyzed with Universal Analysis 2000 software (TA Instruments, Waters LLC) to determine the heats of fusion of the NW/LDPE nanocomposites. The heat of fusion of 100% crystalline PE used for the crystallinity calculation is 293 J/g [21]. The weight of the NW percent was deducted from the total weight of the nanocomposites to calculate the crystallinity of the LDPE matrices.

The electrical resistivity of the NW/LDPE and NW/PS nanocomposites was measured by two different instruments. For the nanocomposites with resistivity lower than 10⁴ Ω·m, a Loresta GP resistivity meter (MCP-T610 model, Mitsubishi Chemical Co., Japan) connected to an ESP four-pin probe (MCP-TP08P model, Mitsubishi Chemical Co., Japan) with inter-pin distance of 5 mm and pin diameter of 2 mm was used in order to minimize the impact of the contact resistance according to ASTM 257-75 standards. For the nanocomposites with higher resistivity, the electrical resistance measurements were performed using a Keithley 6517A electrometer connected to an 8009 test fixture with Keithley 6524 high resistance measurement software conforming to ASTM D991-89 standards. Alternating voltages between 10 V and -10 V or 100 V and -100 V were applied to the samples to reduce the inherent background current and improve the accuracy. The measured volume resistance R_v was converted to resistivity ρ_v by the equation:

$$\rho_v = R_v \cdot \frac{A}{t} \quad (4-1)$$

Where, t is the thickness, and A is the effective area of the tested samples. The tested sample was mounted at the center of the electrodes of the fixture with a PTFE sheet to cover the other area of the electrodes not covered by the sample in order to avoid the direct contact between the top and bottom electrodes. The samples for electrical measurements were thoroughly rinsed with methanol beforehand to remove the oily residue on the surface. Each sample was measured four times to determine the average electrical resistivity. The photographs of the Loresta GP resistivity meter, the ESP four-pin probe and (c) the Keithley 6517A electrometer with an 8009 test fixture are shown in Figure 4–2.





Figure 4-2. The photographs of the (a) Loresta GP resistivity meter, (b) ESP four-pin probe and (c) Keithley 6517A electrometer (right) with an 8009 test fixture (left).

4.3. Results and discussion

4.3.1. Morphology and composition of the CuNWs and AgCuNWs

The SEM and TEM images of the CuNWs and AgCuNWs are shown in Figure 4–3. We observed that both the CuNWs and AgCuNWs tended to aggregate to form bundles instead of single NWs when they were added to acetone. This can be attributed to the high surface energy of the NWs. The high surface energy also makes the NWs more susceptible to oxidation when exposed to air than bulk metal. The surface of CuNWs was quite smooth, while AgCuNWs exhibited rough surface due to the uneven deposition of silver onto the surface of the CuNWs. The diameter of the CuNWs in the TEM images was 23–26 nm, and that of the AgCuNWs was 28–33 nm.

Therefore, the diameter of the AgCuNWs increased 5–7 nm due to the larger atomic radius of silver and the stoichiometric ratio of the substitution reaction in which one copper atom can be substituted with two silver atoms.

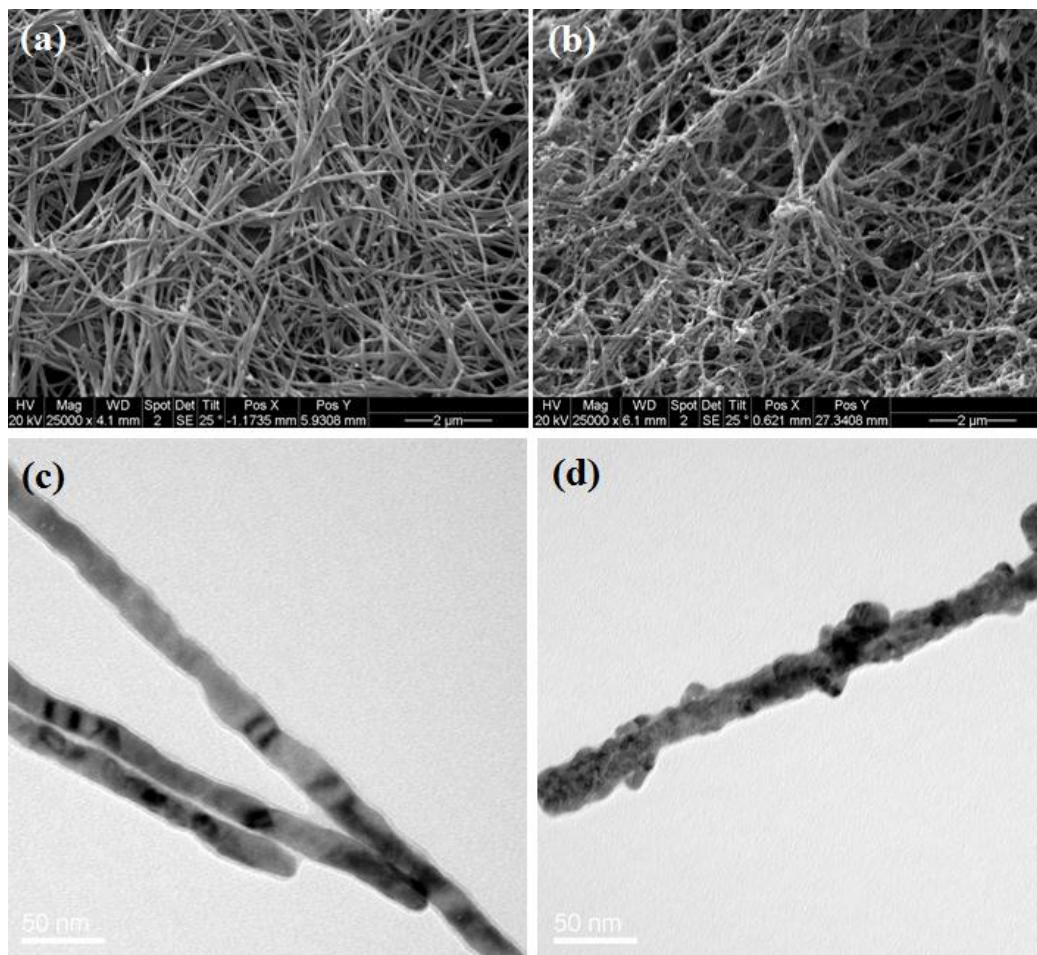
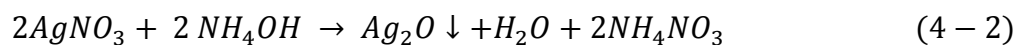
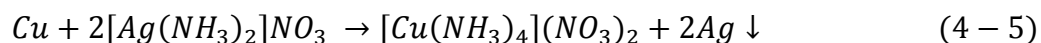


Figure 4-3. The (a, b) secondary SEM images and (c, d) TEM images of the (a, c) CuNWs and (b, d) AgCuNWs.

The reactions involved in this chemical plating process are illustrated in equations (4-2) to (4-5) as follows [22]:





The formation of $[\text{Ag}(\text{NH}_3)_2]^+$ is described in equation (4-4). The substitution of copper with silver is given in equation (4-5). During the redox reaction, the $[\text{Ag}(\text{NH}_3)_2]^+$ was consumed to produce silver deposition and the copper atoms on the surface of the CuNWs can be expected to form an ammino complex $[\text{Cu}(\text{NH}_3)_4]^{2+}$. H.T. Hai [23] et al. studied the electroless plating of silver on the copper powder of particle size 2–40 μm . They reported that the pre-existent oxide and the hydroxide formed by hydrolysis on the surface of the copper particles led to the uneven distribution of the silver nuclei and a decrease in the number of the nuclei on the surface of the copper particles at the early stage of the displacement reaction, which in turn resulted in the uneven deposition of silver on the surface of the copper particles.

Figure 4-4 and Table 4-1 show the results of the EDX characterization carried out to obtain a quantitative composition of the AgCuNWs. The weight and atomic percentages of Ag in the AgCuNWs accounted for 66.52% and 53.92%, respectively. It can be determined that around 37% Cu atoms were substituted by the Ag atoms. The high content of Ag in the AgCuNWs can cover the overall surface of the CuNWs to achieve the desired anti-oxidation property.

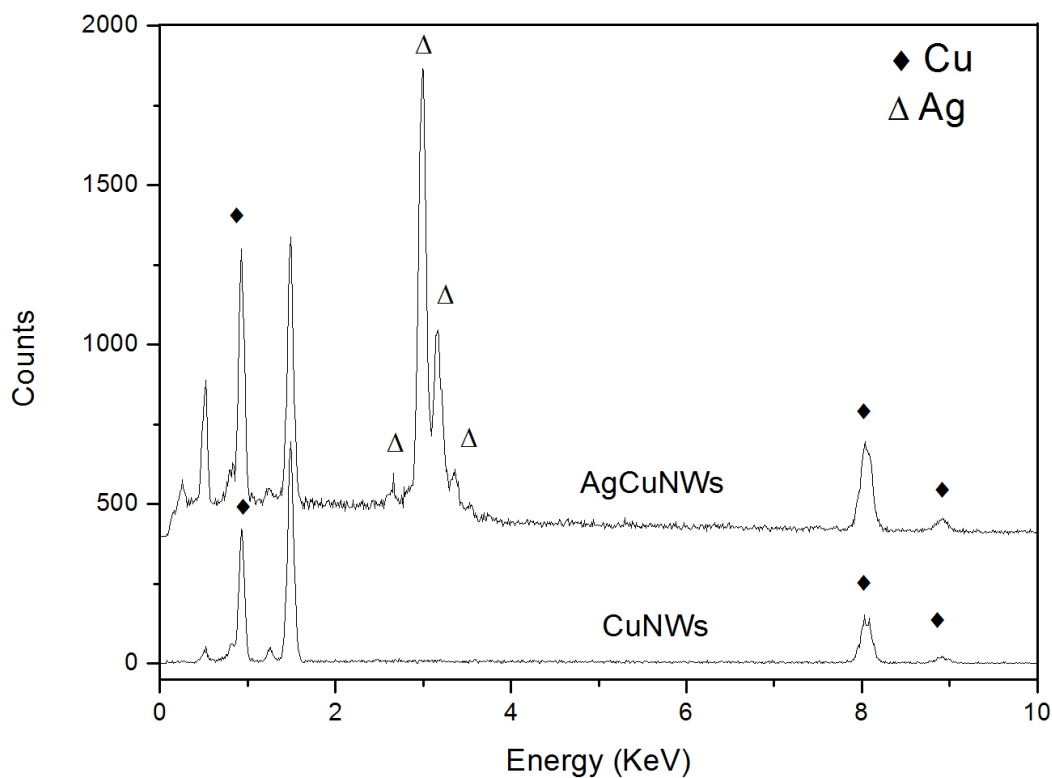


Figure 4-4. The EDX spectra of the CuNWs and AgCuNWs.

Table 4-1. The quantitative element content of the AgCuNWs determined from the EDX spectra.

| Element | Wt. % | At. % | K-ratio |
|---------|-------|-------|---------|
| Cu | 33.48 | 46.08 | 0.3409 |
| Ag | 66.52 | 53.92 | 0.6197 |

4.3.2. Length distribution of the CuNWs and AgCuNWs

Figures 4–5 shows the length distribution of the AgCuNWs. The length distribution of the CuNWs is shown in Figure 2–11. The length of over 84% of the NWs ranged from 0.5 to 7 μm . The NWs of length between 1–2 μm accounted for 32.0% and 32.1% for both the CuNWs and AgCuNWs. The NWs of length $< 3 \mu\text{m}$ comprised up to 84.3% and 84.6% for the CuNWs and AgCuNWs, respectively. The determined average length was ca. 1.98 μm for both the CuNWs and the AgCuNWs.

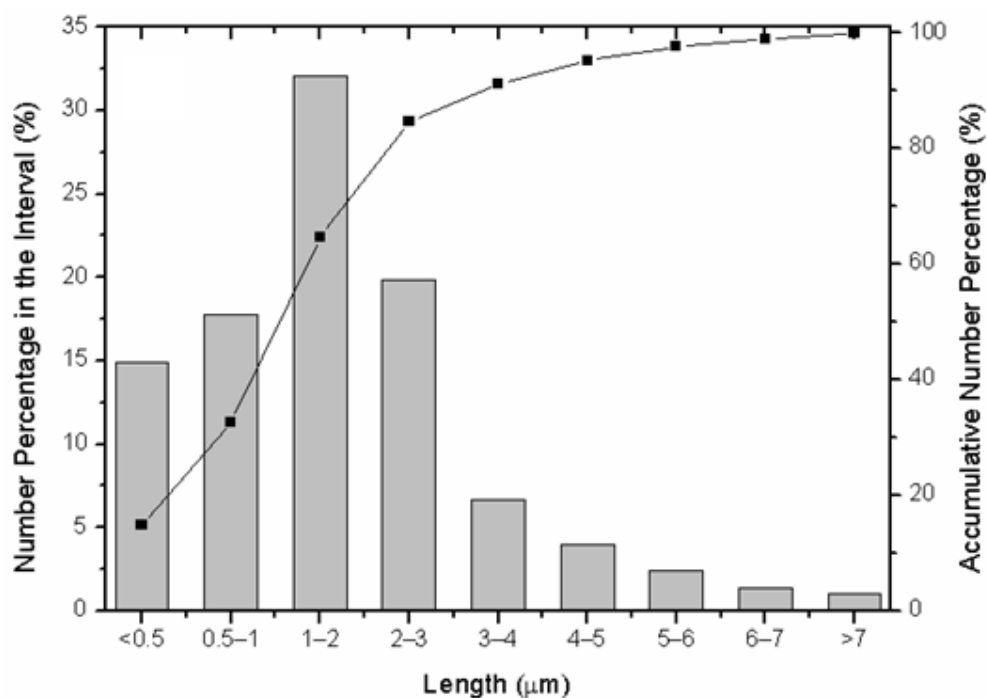


Figure 4-5. The length distribution of the AgCuNWs.

4.3.3. Anti-oxidation behavior of the CuNWs and AgCuNWs

The XRD patterns of the CuNWs and AgCuNWs are shown in Figure 4–6.

Cu and Cu_2O can be identified in the pattern of the CuNWs. However, only Cu and Ag peaks can be found in the pattern of the AgCuNWs. Since the NW samples were kept in N_2 atmosphere before the XRD test, there are two possible explanations for Cu_2O in the CuNW sample. First, the Cu_2O can be formed during the electrodeposition, liberation and cleaning process. Second, the CuNW sample was exposed to air during the XRD test. The X-ray beam heated CuNW sample during the test and this facilitated the formation of Cu_2O . The AgCuNW sample went through a similar process as the CuNW sample. However, the diffraction peaks corresponding to Cu_2O or Ag_2O were not detected in the AgCuNW sample. These XRD results indicate that the CuNWs were very sensitive to oxidation and the AgCuNWs exhibited improved anti-oxidation property compared to the CuNWs when exposed to air.

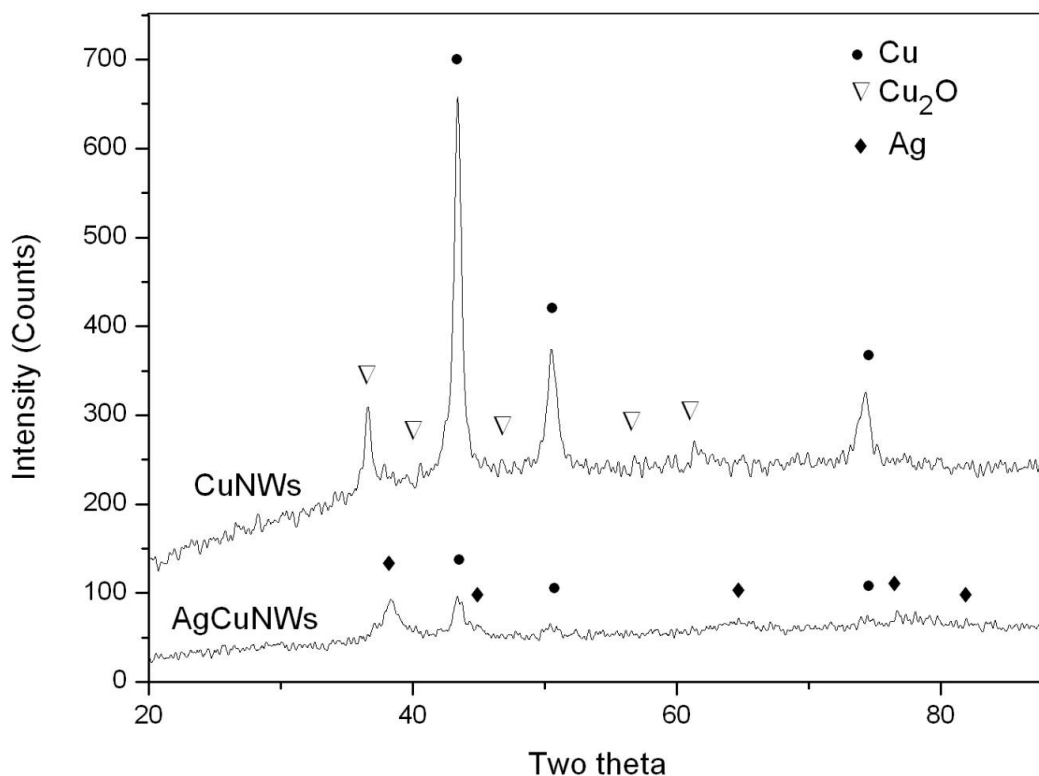


Figure 4-6. The XRD patterns of the CuNWs and AgCuNWs.

The temperature-dependent oxidation behavior of the CuNWs and AgCuNWs in air was determined by TGA as shown in Figure 4–7. The TGA curves show that the CuNWs began to gain weight at around 85 °C and the AgCuNWs began to gain weight at about 230 °C. The weight gain rate of 0.096%/°C for the CuNWs was also higher than that for the AgCuNWs, which was only 0.036%/°C. Based on the lowest weight point on the curve, the maximum percent weight gain of the CuNWs and AgCuNWs was 20.3% and 3.2%, respectively, during the oxidation process. The CuNWs reached maximum weight at 298 °C, and the AgCuNWs reached maximum weight at 320 °C. In addition, the oxidation curve

of the CuNWs exhibited a very high weight gain rate of 0.15%/°C from 85 °C to 160 °C and a relatively low weight gain rate of 0.061%/°C from 160 °C to 298 °C. The oxidation curve of the AgCuNWs showed a weight loss of 3.3% prior to gaining weight at 230 °C, which can be attributed the volatile components and the surfactant absorbed on the surface of the AgCuNWs in the silver coating process. Therefore, the AgCuNWs began to be oxidized at higher temperature with lower weight gain rate than the CuNWs.

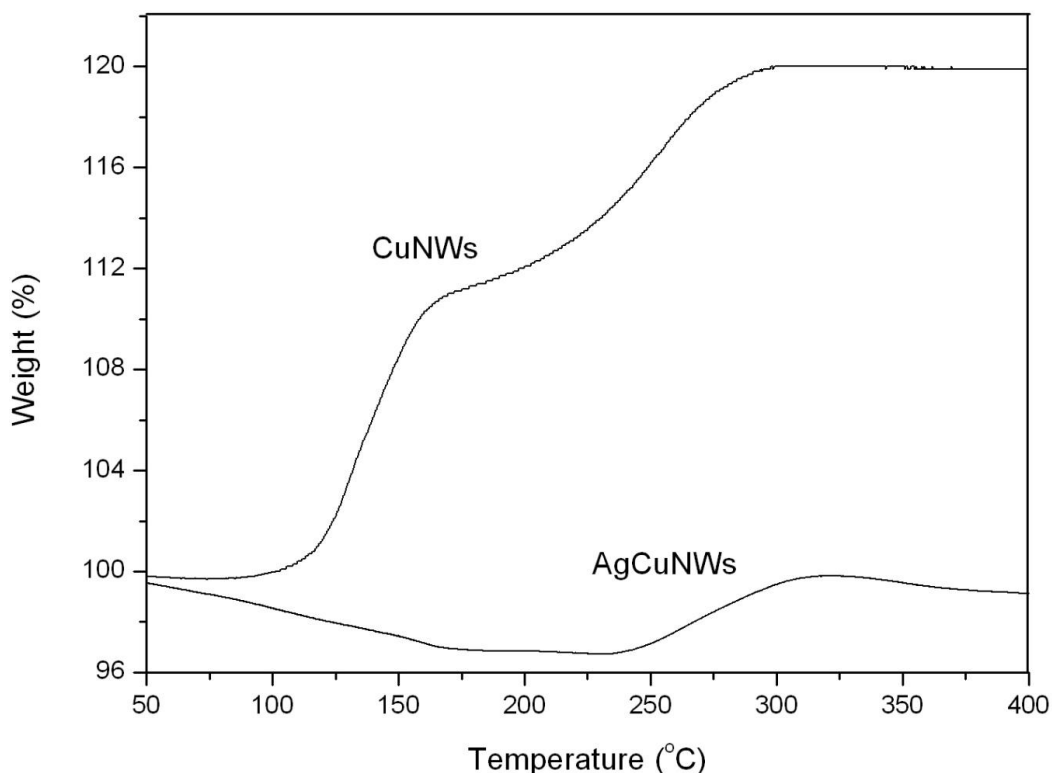


Figure 4-7. The temperature-dependent TGA curves of the CuNWs and AgCuNWs using 100 mL/min air as purge gas at 10 °C/min heating rate.

The time-dependent oxidation behavior of the CuNWs and AgCuNWs in air

at 250 °C was determined and is shown in Figure 4–8. During the first minute, the CuNWs gained over 11.0% weight, while the AgCuNWs gained almost no weight. Between 1 min and 25 min, the CuNWs gained 5.0% weight, while the AgCuNWs gained only 1.7% weight. The total weight gain of the CuNWs and AgCuNWs within 25 min under 250 °C was 16.0% and 1.7%, respectively, which translates to an average weight gain rate of 0.64%/min for the CuNWs and 0.068%/min for the AgCuNWs. Thus, the AgCuNWs exhibited one order of magnitude lower oxidation rate than the CuNWs at 250 °C, and even lower rate during the first minute.

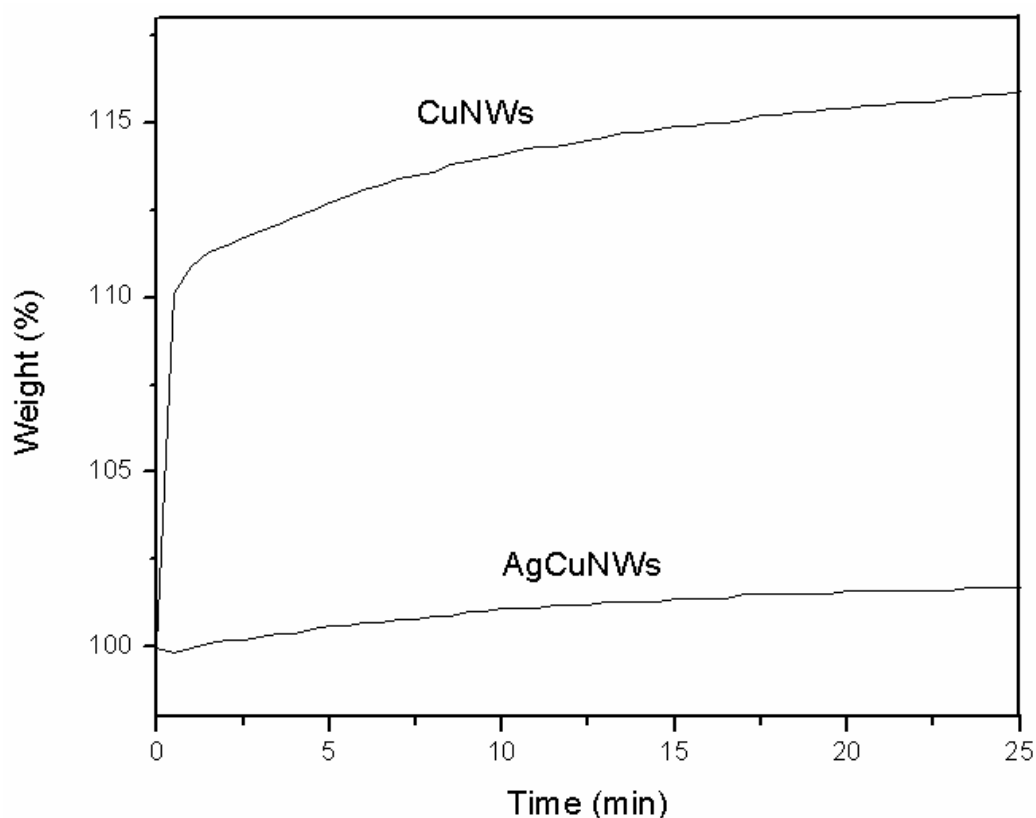


Figure 4-8. The time-dependent TGA curves of the CuNWs and AgCuNWs using 100 mL/min air as purge gas at 250 °C.

4.3.4. Electrical resistivity of NW/LDPE nanocomposites, dispersion and composition of NWs in LDPE matrix

The volume electrical resistivity of the CuNW/LDPE and AgCuNW/LDPE nanocomposites as a function of the volume concentration of the NWs is plotted in Figure 4–9. The neat polymer exhibits volume resistivity on the order of 10^{13} $\Omega\cdot\text{m}$. A plunge in the value of the volume resistivity is observed when the volume percentage of the NWs in both nanocomposites was increased from 0.5 vol. % to 0.75 vol. %, which indicates the location of the electrical percolation threshold. The electrical percolation threshold in this study is slightly higher than the value reported in our previous works [8], which is between 0.25 vol. % and 0.75 vol. % for the CuNW/PS nanocomposites. The electrical resistivity of the NW/LDPE nanocomposites decreased significantly between 0.5 vol. % and 2.0 vol. %, and reached 9.25×10^3 $\Omega\cdot\text{m}$ and 6.88×10^2 $\Omega\cdot\text{m}$ at 2.0 vol. % for the CuNW/LDPE and AgCuNW/LDPE nanocomposites, respectively. When the concentration of the NWs increased from 2.0 vol. % to 4.0 vol. %, neither nanocomposite showed significant decrease in the electrical resistivity. The difference in the shape of the percolation curves of the AgCuNW/LDPE nanocomposites and the CuNW/LDPE nanocomposites may result from the difference in the NW diameter, surface oxide and the electrical conductivity, however, the exact reason has not been determined.

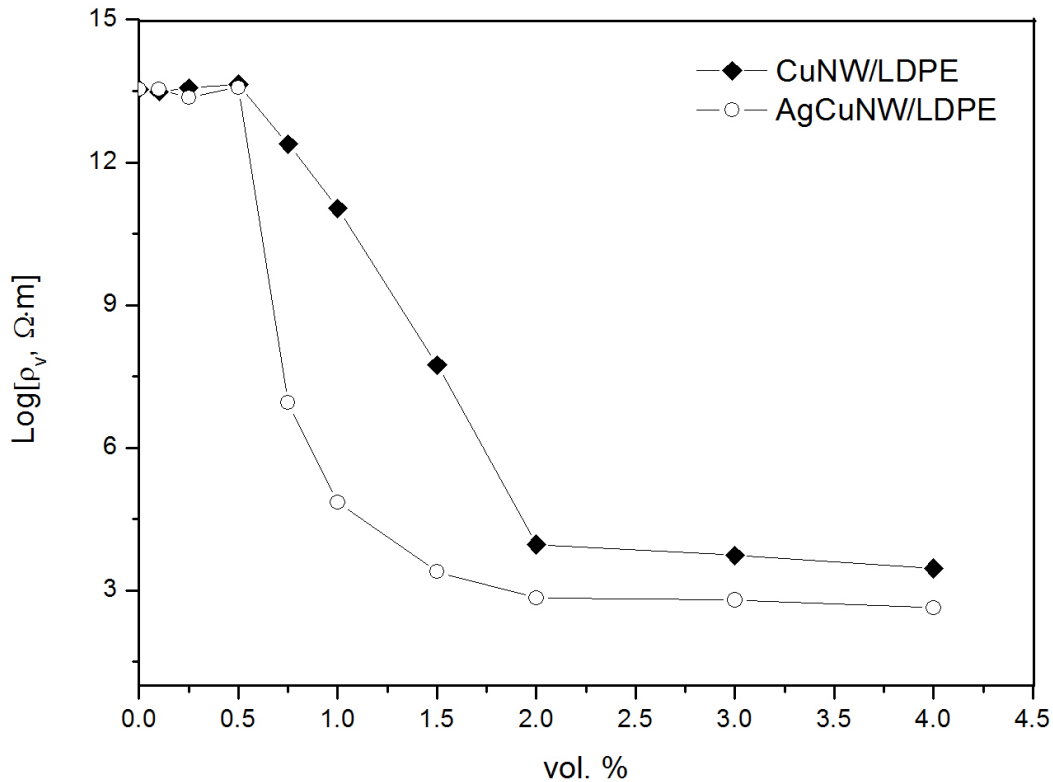


Figure 4-9. The volume electrical resistivity of the CuNW/LDPE and AgCuNW/LDPE nanocomposites as a function of the volume concentration of the NWs.

The backscattered SEM images of the freeze fractures and the TEM images of the ultramicrotomed section of the LDPE nanocomposites, containing 1 vol. % of either the CuNWs or the AgCuNWs, are shown in Figure 4-10. The bright areas in the backscattered SEM images corresponding to the large aggregates of the NWs can be observed in both nanocomposites. The poor dispersion of the NWs in the LDPE matrix in some areas can be attributed to the high surface energy of the nanowires and the low polarity of the LDPE matrix. In Figures

4–10e and f, the alignments of the NWs were particularly evident. Those areas with concentrated aligned NWs may be formed during the compression molding process which oriented the NWs in the plane. Both the poor dispersion and the alignment of the NWs in the LDPE matrix can adversely affect the formation of the electrically conductive networks in the NW/LDPE nanocomposites. The electrical resistivity of the NW/LDPE nanocomposites can be further decreased by improving the dispersion and minimizing the alignment of the NWs in the LDPE matrix.

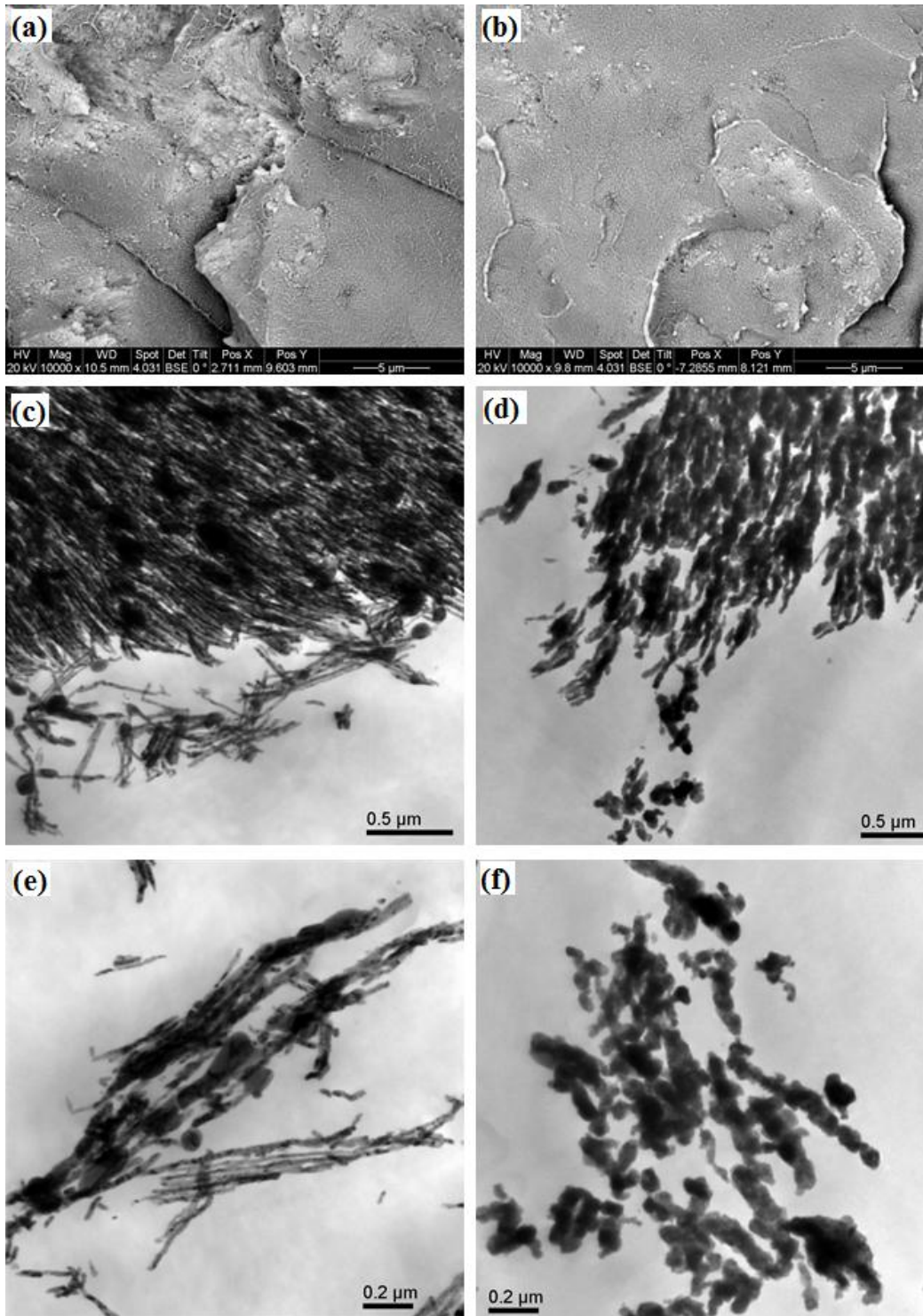


Figure 4-10. The (a, b) backscattered SEM images of the freeze fractures and (c, d, e, f) TEM images of the ultramicrotomed section of the LDPE

nanocomposites, containing 1 vol. % of either the (a, c, e) CuNWs or the (b, d, f) AgCuNWs. The (c, d) TEM images show the areas with less concentrated NWs in the nanocomposites. And the (e, f) TEM images show the concentrated NWs in the nanocomposites with alignments.

The XRD patterns of the neat LDPE and the NW/LDPE nanocomposites in Figure 4–11 reveal the composition of the NWs in the nanocomposites after compression molding. The neat LDPE exhibited two peaks at $2\theta < 25^\circ$ with the more intense peak at 22° in the XRD spectra. Both Cu and Cu_2O were detected in the CuNW/LDPE nanocomposites. However, the diffraction peaks of Cu, Ag and Cu_2O were detected in the AgCuNW/LDPE nanocomposites in addition to those of the neat LDPE. This result indicates that Cu was oxidized when exposed to air during the preparation process, but silver was not oxidized. That the Cu_2O was not detected in the AgCuNW sample, but detected in the AgCuNW/LDPE nanocomposites, indicates that the silver coating on the CuNWs can effectively protect the copper from oxidation under moderate temperature, but it cannot completely stop the outward diffusion of the Cu content in the AgCuNWs at 250°C ; this was the temperature at which the AgCuNW/LDPE nanocomposites were compression molded for 30 min. This XRD result is consistent with the TGA result indicating that the AgCuNWs began to gain weight at about 230°C . Although the copper was still partially oxidized in the AgCuNW/LDPE nanocomposites, the decreased electrical resistivity of the AgCuNW/LDPE

nanocomposites, compared to that of the CuNW/LDPE nanocomposites, can be attributed to the silver content in the AgCuNWs, considering the 66.5 wt. % of silver in the AgCuNWs.

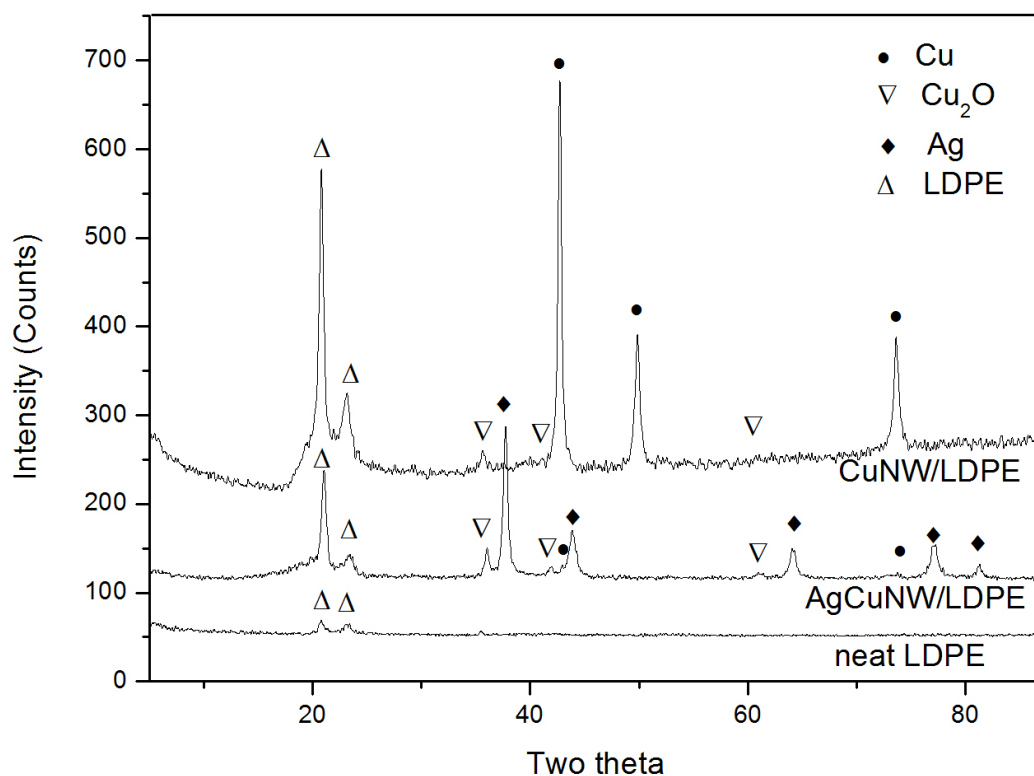


Figure 4-11. The XRD patterns of the reference neat LDPE and the compression molded CuNW/LDPE and AgCuNW/LDPE nanocomposites.

4.3.5. The Effect of NWs on the crystallinity of the LDPE matrices

Figure 4–11 shows that the intensity of the LDPE XRD peaks of the NWs/LDPE nanocomposites significantly increased compared to that of the reference LDPE sample. This indicates that the presence of the NWs in the

LDPE matrices facilitated crystallization of the LDPE matrices. A. S. Luyt et al [24] explained that metal particles prefer staying in the amorphous region of the LDPE matrix. The inherent low crystallinity of the LDPE and the metals particles in the amorphous region contribute to the epitaxial crystallization of the LDPE matrices on the surface of the metal particles.

The effect of the CuNWs and AgCuNWs on the crystallinity of LDPE matrix is shown in Figure 4–12. The crystallinity of the neat LDPE processed by the hot solution mixing and the compression molding was 34.0%. The crystallinity of the LDPE matrices was 35.3% for CuNWs/LDPE nanocomposite and 36.2% for AgCuNWs/LDPE nanocomposite with nanowire concentration of 1.0 vol. %; the percent crystallinity was 36.0% in the CuNWs/LDPE nanocomposite and 36.3% in the AgCuNWs/LDPE, respectively at nanowire concentration of 2.0 vol. %. The AgCuNWs exhibit a more noticeable effect on the crystallinity of the LDPE matrices than the CuNWs at nanowire concentration ≤ 2.0 vol. %, which can be attributed to the uneven surface of the AgCuNWs which increased the contact area with the LDPE matrices and facilitated the epitaxial crystallization of the LDPE matrices on the surface. The crystallinity of the LDPE matrices reached a maximum of around 36.4% at nanowire concentration ≥ 3.0 vol. % for both the CuNWs/LDPE and AgCuNWs/LDPE nanocomposites.

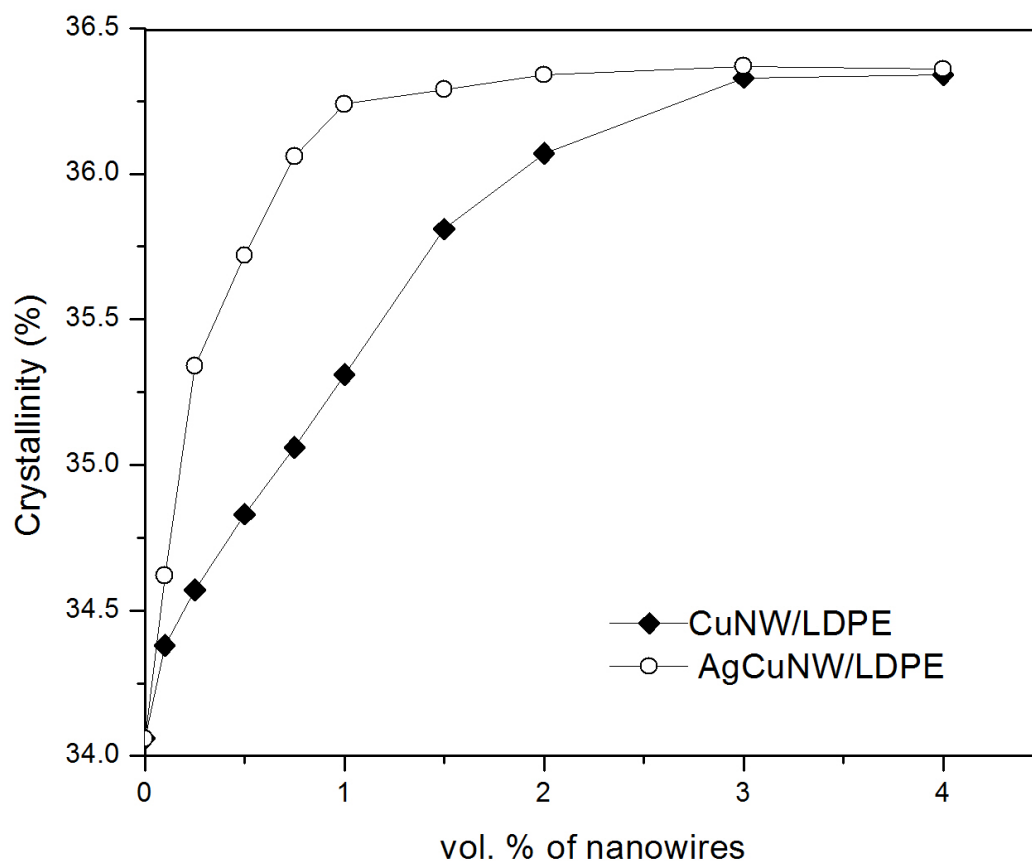


Figure 4-12. The effect of the NW concentration on the crystallinity of the LDPE matrices in the CuNW/LDPE and AgCuNW/LDPE nanocomposites.

4.3.6. Fragmentation of the AgCuNWs in PS matrices

The volume electrical resistivity of the CuNW/PS and AgCuNW/PS nanocomposites prepared by the MSMP method as a function of the volume concentration of NWs is shown in Figure 4–13. The electrical resistivity of the CuNW/PS nanocomposites in this study is very similar to the values reported by U. Sundararaj et al [20, 25]. However, the electrical resistivity of the AgCuNW/PS nanocomposites almost did not change with the increasing

concentration of the AgCuNWs up to 4.0 vol. %.

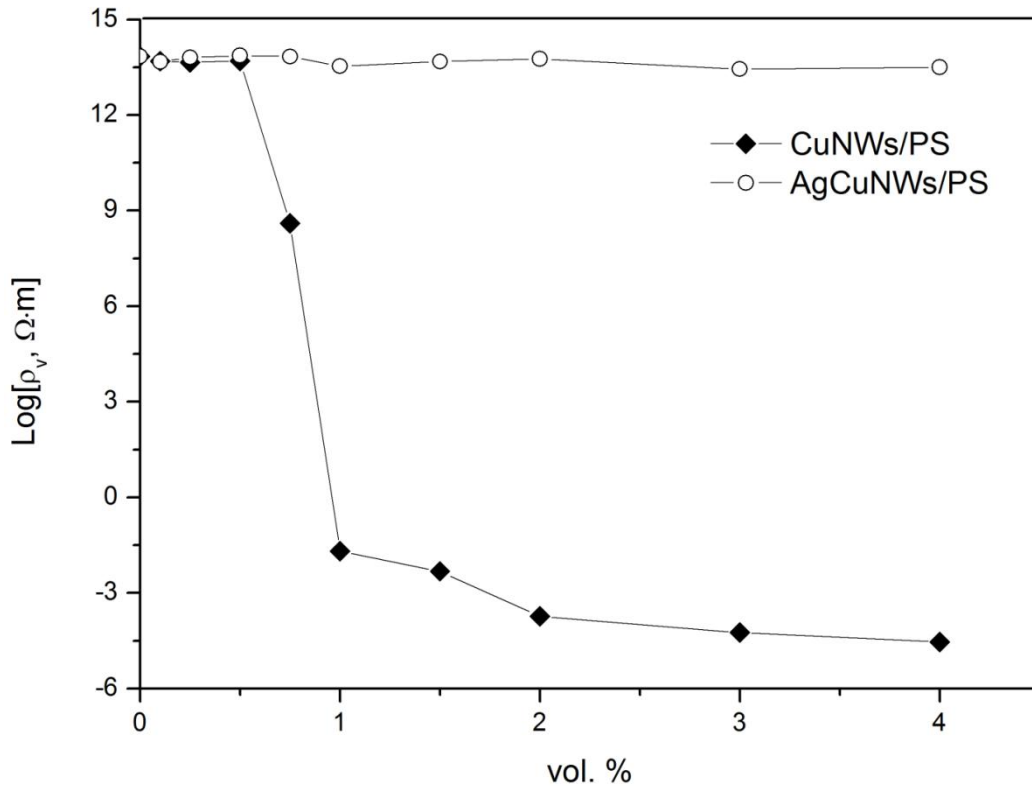


Figure 4-13. The volume electrical resistivity of the CuNW/PS and AgCuNW/PS nanocomposites as a function of the volume concentration of the NWs.

The backscattered SEM images of the freeze fractures of the AgCuNW/PS nanocomposites, containing 4.0 vol. % of AgCuNWs, before the compression molding, after the compression molding and after the removal of the PS matrices from the molded samples are shown in Figure 4-14. In Figure 4-14a, the AgCuNWs in the PS nanocomposites before the compression molding appeared as individual or agglomerated wires. However, the AgCuNWs in the PS

nanocomposites after the compression molding, and after the removal of PS from the molded sample as shown in Figures 4–14b and c, respectively looked very different from the original NWs. Instead, they appeared small particles because of the fragmentation during the compression molding, which is the reason for the high electrical resistivity of the AgCuNW/PS nanocomposites with the increasing concentration of AgCuNWs that is equivalent to the neat PS. The fragmentation of the AgCuNWs into sphere-like small particles with aspect ratio ~ 1 made it more difficult to form the networks within the PS matrices as pathways for electron travelling.

The highest temperature during the compression molding that caused the fragmentation of the AgCuNWs was around 250 °C, which is over 700 °C lower than the melting points of the bulk copper and silver. The similar phenomena of metal NW breakup from stress or irradiation were observed, studied and simulated in the literature [26–31], which can be attributed to Rayleigh instability usually seen in fluid systems [32]. The approach of Rayleigh instability was extended to solid by Nichols and Mullins [33], who developed the model by assuming the stress-free, isolated solid cylinders with isotropic surface energy. The Nichols–Mullins model has been successfully applied to interpret the breakup of copper and gold NWs and obtained good correlations between the experimental and the calculated sphere diameter and the sphere separation distances [26, 28]. In this work, it is found that the AgCuNWs fragmented in the PS matrices subjected to the stress under 250 °C during the compression molding, which is believed to arise from the combined effects of the surface tension,

Chapter 4. Silver Coated Copper Nanowires with Improved Anti-oxidation Property as Conductive Fillers in Low Density Polyethylene and Polystyrene

filler/polymer interaction, temperature, shear stress and/or pressure during the compression molding of the AgCuNW/PS nanocomposites.

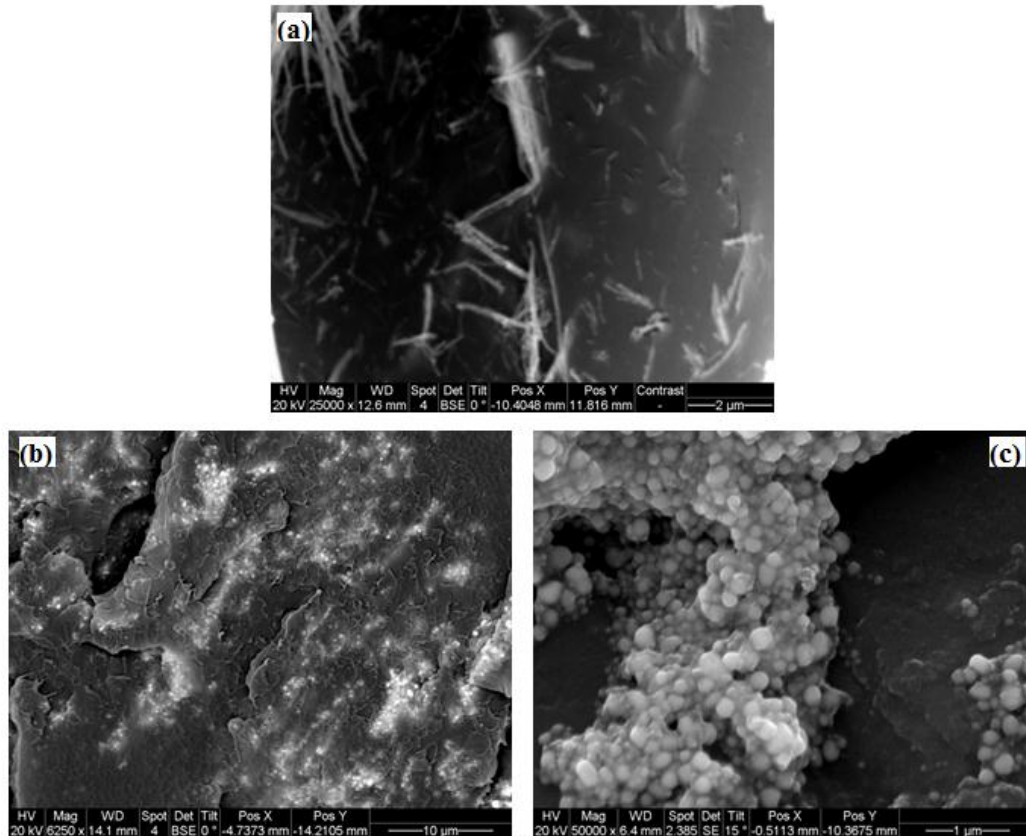


Figure 4-14. The backscattered SEM images of the freeze fractures of the AgCuNW/PS nanocomposites, containing 4.0 vol. % of the AgCuNWs, (a) before the compression molding, (b) after the compression molding and (c) after the removal of the PS matrices from the molded samples.

That the AgCuNWs were not fragmented in the LDPE matrices as they were in the PS matrices can be attributed to the different interactions between the AgCuNW/LDPE and the AgCuNW/PS. That the CuNWs were not fragmented in

the PS matrices as the AgCuNWs can also result from the different interaction between the CuNW/PS and the AgCuNW/PS. In addition, the oxides formed on the surface of the CuNWs can also contribute to the increased stability during the compression molding.

4.4. Conclusions

AgCuNWs with diameter of 28–33 nm can be synthesized by applying silver coating on 23–26 nm diameter CuNWs in Ag-amine solution. The AgCuNWs with silver content of 66.5 wt. % showed less regular surface than the pure CuNWs.

The XRD patterns of the CuNWs and AgCuNWs indicate that the silver coating on the AgCuNWs can effectively prevent the formation of copper oxide under room temperature. The TGA data reveal that the temperature at which the NWs began to gain weight can be improved from 85 °C to 230 °C and that the maximum weight gain can be decreased from 20.3% to 3.2% by applying the silver coating.

The new AgCuNWs with improved anti-oxidation properties are promising electrically conductive fillers in the LDPE. The electrical resistivity of the AgCuNW/LDPE nanocomposites was lower than that of the CuNW/LDPE nanocomposites because the silver content in the AgCuNWs was not oxidized during the compression molding. However, the silver coating cannot completely

prevent the outward diffusion and the oxidation of the copper content in the AgCuNWs at 250 °C. The morphology of the NW/LDPE nanocomposites showed that the dispersion of the NWs in the LDPE matrix was poor in certain areas.

The electrical resistivity of the AgCuNW/PS nanocomposites almost did not decrease with the increasing concentration of the AgCuNWs up to 4.0 vol. %. The backscattered SEM images showed the fragmentation of the AgCuNWs in the PS matrix during the compression molding under 250 °C and 138 MPa, which is believed to arise from the combined effects of the surface tension, filler/polymer interaction, temperature, shear stress and/or pressure during the compression molding of the AgCuNW/PS nanocomposites.

4.5. References

- [1] Salem AK, Hung CK, Kim TW, Wu TC, Searson PC, Leong, KW. Multi-component nanorods for vaccination applications. *Nanotech* 2005;16(4):484–487.
- [2] Paxton WF, Kistler KC, Olmeda CC, Sen A, St Angelo SK, Cao YY, Lammert MPE, Crespi VH. Catalytic nanomotors: autonomous movement of striped nanorods. *J Am Chem Soc* 2004;126 (41):13424–13431.
- [3] Liu J, Duan L, Toimil-Molares ME, Karim S, Cornelius TW, Dobrev D, Yao HJ, Sun YM, Hou MD, Mo D, Wang ZG, Neumann R. Electrochemical

fabrication of single-crystalline and polycrystalline Au nanowires: the influence of deposition parameters. *Nanotech* 2006; 17(8):1922–1926.

[4] Kok KY, Hangarter CM, Goldsmith B, Ng KI, Saidin NB, Myung NV. Synthesis and characterization of electrodeposited permalloy (Ni₈₀Fe₂₀)/Cu multilayered nanowires. *J Magn Magn Mater* 2010;322(24):3876–3881.

[5] Duana JL, Liu J, Yao HJ, Mo D, Hou MD, Suna YM, Chen YF, Zhang L. Controlled synthesis and diameter-dependent optical properties of Cu nanowire arrays. *Mat Sci Eng B-Solid* 2008;147(1):57–62.

[6] Zhang W, Dehghani-Sanij AA. Carbon based conductive polymer composites. *J Mater Sci* 2007;42:3408–3418.

[7] Pöllänen M, Pelz U, Suvanto M, Pakkanen TT. Effective method for dispersing SiO₂ nanoparticles into polyethylene. *J Appl Polym Sci* 2010;116(2):1218–1225.

[8] Gelves GA, Sundararaj U, Haber JA. Low Electrical percolation threshold of silver and copper nanowires in polystyrene composites. *Adv. Funct. Mater.* 2006; 16(18): 2423–2430.

[9] Lin B, Gelves GA, Haber JA, Pötschke U, Sundararaj U. Electrical, morphological and rheological study of melt-mixed polystyrene/copper nanowire nanocomposites. *Macromol. Mater. Eng.* 2008; 293: 631–640.

- [10] Lin YS, Chiu SS. Effects of oxidation and particle shape on critical volume fractions of silver-coated copper powders in conductive adhesives for microelectronic applications. *Polym Eng Sci* 2004;44(11):2075–2082.
- [11] Lin B, Gelves GA, Haber JA, Pötschke P, Sundararaj J. Electrical, morphological and rheological study of melt-mixed polystyrene/copper nanowire nanocomposites. *Macromol Mater Eng* 2008;293:631–640.
- [12] Gelves GA, Haber JA, Sundararaj U. Enhancing dispersion of copper nanowires in melt-mixed polystyrene composites. *J Polym Sci: Part B: Polym Phys* 2008;46:2064–2078.
- [13] Wu HP, Wu XJ, Ge MY, Zhang GQ, Wang YW, Jiang JZ. Properties investigation on isotropical conductive adhesives filled with silver coated carbon nanotubes. *Compos Sci Tech* 2007;67:1182–1186.
- [14] Jiang G, Gilbert M, Wilcox GD, Balasubramanian K. Preparation of nickel coated mica as a conductive filler. *Compos Part A* 2002;33(5):745–751.
- [15] Bar H, Boiteux G. The electrical behavior of thermosetting polymer composites containing metal plated ceramic filler. *Polym Compos* 2005;26(1):12–19.
- [16] Lu G, Jiang H. Electrical and shielding properties of ABS resin filled with nickel-coated carbon fibers. *Compos Sci Tech* 1996;56 (2):193–200.

[17] Talukdar MI, Baker EH. Conductivity studies on silver oxide. *Soli Stat Commu* 1969;7(2):309–310.

[18] Lin YS, Chiu SS. Electrical properties of conductive adhesives as affected by particle compositions, particle shapes, and oxidizing temperatures of copper powders in a polymer matrix. *J Appl Polym Sci* 2004;93:2045–2053.

[19] Gelves GA, Chau J, Bellehumeur C, Sundararaj U. Polymer Nanocomposites with Copper Nanowire and Carbon Nanotubes: Hybrid Materials exhibiting Low Electrical Percolation Thresholds, High Electrical Conductivity, and High EMI Shielding. *Soc Plastics Eng Technol Prog (ANTEC)* 2011.

[20] Gelves GA, Al-Saleh MH, Sundararaj U. Highly electrically conductive and high performance EMI shielding nanowire/polymer nanocomposites by miscible mixing and precipitation. *J Mater Chem* 2011; 21: 829–836.

[21] Lu JJ, Sue H, Rieker TP. Morphology and mechanical property relationship in linear low-density polyethylene blown films. *J Mater Sci* 2000; 35(20): 5169–5178.

[22] Xu X, Luo X, Zhuang H, Li W, Zhang B. Electroless silver coating on fine copper powder and its effects on oxidation resistance. *Mater Lett* 2003; 57 (24–25): 3987–3991.

[23] Hai HT, Ahn JG, Kim DJ, Lee JR, Chung HS, Kim CO. Developing process for coating copper particles with silver by electroless plating method. *Surf Coat Tech* 2006; 201 (6): 3788–3792.

[24] Luyt AS, Molefi JA, Krump H. Thermal, mechanical and electrical properties of copper powder filled low-density and linear low-density polyethylene composites. *Polym Degrad & Stab* 2006;91 (7):1629–1636.

[25] Al-Saleh MH, Gelves GA, Sundararaj U. Copper nanowire/polystyrene nanocomposites: Lower percolation threshold and higher EMI shielding. *Compos Part A-Appl S.* 2011; 42: 92–97.

[26] Karim S, Toimil-Molares ME, Balogh AG, Ensinger W, Cornelius TW, Khan EU, Neumann R. Morphological evolution of Au nanowires controlled by Rayleigh instability, *Nanotechnology* 2006; 17: 5954–5959.

[27] Wang D, Zhao J, Hu S, Yin X, Liang S, Liu Y, Deng S. Where, and how, does a nanowire break? *Nano Lett.* 2007; 7: 1208–1212.

[28] Toimil-Molares ME, Balogh AG, Cornelius TW, Neumann R, Trautmann C. Fragmentation of nanowires driven by Rayleigh instability. *Appl Phys Lett* 2004; 85: 5337–5339.

[29] Zhao K, Averback RS, Cahill DG. Patterning of metal nanowires by directed ion-induced dewetting. *Appl Phys Lett* 2006; 89: Art. No. 053103.

[30] da Silva EZ, da Silva AJR, Fazzio A. How do gold nanowires break? *Phys Rev Lett* 2001; 87: Art. No. 256102.

[31] Burki J, Goldstein RE, Stafford CA. Quantum necking in stressed metallic nanowires. *Phys Rev Lett* 2003, 91: Art. No. 254501.

[32] Rayleigh L. On the Capillary Phenomena of Jets. *Proceedings of the Royal Society of London* 1879; 29: 71–97.

[33] Nichols FA, Mullins WW. Surface (interface) and volume diffusion contributions to morphological changes driven by capillarity. *Trans Metall Soc AIME* 1965; 233: 1840–1848.

Chapter 5

Effect of Macromolecular Structure on Electrical and Rheological Properties in Copper Nanowire Polyethylene Nanocomposites: Effect of Molecular Weight and Branching

5.1. Introduction

Polymer nanocomposites are a new class of materials that have recently attracted increasing attention in industry and academia due to the wide range of applications in which they can be used such as aerospace, catalysis, optical devices, sensors, and EMI shielding [1–4]. Nanocomposites are mainly formulated by dispersing nanofillers into polymer matrices. The synergy between the macromolecules and the nanofillers provides improved mechanical, thermal or electrical properties for the desired applications [5]. For the electrically conductive polymer nanocomposites, high aspect ratio 1D nanofillers such as carbon nanotubes, vapor grown carbon nanofibers, and metal nanowires have been studied in different polymer matrices [5–11].

CuNWs with high electrical conductivity, Young's modulus, and tensile strength can be synthesized at lower cost than other metal nanowires like silver and nickel. CuNWs have been studied as conductive nanofillers for polymer nanocomposites and demonstrated outstanding performance in terms of electrical conductivity and EMI shielding [5, 12]. Polyethylene (PE) is one of the volume leader thermoplastics in industry with good processability, excellent stability and

non-toxicity. The electrically conductive polymer nanocomposites formulated with CuNWs and PE can find applications in ESD, antistatic and EMI shielding [13].

The diameter of CuNWs in the order of nanometers is comparable to the size of the radius of gyration of a polymer chain, R_g 5–20 nm [14]. Thus, the improved surficial interaction is expected between the two materials when the nanowires are well dispersed in the polymer matrices. To prepare CuNW/PE nanocomposites with desired properties, it is essential to promote the deagglomeration and dispersion of the nanowires [15–17], which will lead to the significant changes in electrical properties and rheological behaviour of the composites particularly at low concentration of nanofillers. For instance, our group recently reported a new method of mixing called MSMP, which enables good mixing of the nanowires in polymer matrices and prevent the agglomeration of nanowires resulting in the highly conductive nanocomposites [12]. Usually, three different types of percolation thresholds can be detected within polymer composites. Geometric percolation threshold appears when a pathway is formed by the filler particles in the polymer matrices [18]. The electrical percolation threshold can be reached when the electrically conductive fillers in the insulating polymer matrix provide a pathway for electrons to travel from one surface of the sample to the other. It is still possible at separation distances up to 5–10 nm between conductive fillers for electrons to hop and/or tunnel through [19]. Theoretically, the electrical percolation can be regarded as an approximation of the geometric percolation. Experimentally, a sharp increase

in the volume electrical conductivity of several orders of magnitude can be detected in the polymer composites at the electrical percolation threshold. With the increasing concentration of fillers in the polymer composites, networks begin to form between the filler particles and the macromolecular chains that lead to a significant rheological change of polymer composite melts from the liquid-like behavior to the solid-like behavior [7, 20, 21]. Oscillatory melt rheology is a highly sensitive technique used to detect the microstructural changes in the melts of polymers or polymer composites [20]. The concentration of fillers required for this transition is commonly known as the rheological percolation threshold.

Polymer matrices of different macromolecular structure, polarity, crystallinity or surface tension will have different effect on the electrical conductivity and percolation threshold of the conductive polymer composites [22–26]. PE consists of long hydrocarbon chains with $-CH_2-$ repeating units. However, PE can be classified into several categories like UHMWPE, HDPE, LDPE, LLDPE, etc, mainly based on their branching, density and molecular weight. The different macromolecular structures of each category of PE lead to the different interaction between the polymer matrices and the fillers, which affects the overall performance of the polymer composites. It is interesting to evaluate the effect of different types of PEs on the filler dispersion, and electrical and rheological properties in CuNW/PE nanocomposites in order to be able to understand the interaction between the polymer matrices and the CuNWs. This study can then be used as a guideline to prepare CuNW polymer nanocomposites with desired performance.

In this work, we studied the effect of the macromolecular structure on the morphology, the electrical and rheological properties in the CuNW/PE nanocomposites. A MSMP method was used to disperse the CuNWs in four different types of polyethylenes: (1) ultra high molecular weight polyethylene (UHMWPE), (2) high density polyethylene (HDPE), (3) LDPE and (4) linear low density polyethylene (LLDPE), which were then compression molded at 250 °C for characterization. The morphology of the CuNW/PE nanocomposites was characterized by SEM and TEM. Electrical percolation thresholds were determined by plotting electrical conductivity of different types of PE nanocomposites versus concentration of CuNWs. Oscillatory melt rheology was carried out at 200 °C to evaluate the influence of the CuNW concentration on the rheological properties of the CuNW/PE nanocomposites. Finally, the differences in the filler dispersion, electrical and rheological properties were interpreted based on molecular structure of the PEs.

5.2. Experimental

5.2.1. Preparation of CuNW/CH₃OH dispersion

CuNWs were synthesized by AC electrodeposition of copper into anodic PAO template as described in Chapter 1. CuNWs synthesized and liberated by this method were ultrasonicated for 1 h in methanol and at the end of ultrasonication have diameter of 25 ± 4 nm and average length of ca. 2 μ m. The concentration of the CuNW/CH₃OH dispersion was determined by weighing the solid content

after evaporating the CH₃OH completely in a fume hood from 2 mL of the dispersion.

5.2.2. DSC characterization of the PEs

DSC analyses were carried out with a TA DSC Q100 instrument with 50 mL/min N₂ (Praxair) as purge gas at 20 °C/min heating rate. The DSC data were analyzed with the Universal Analysis 2000 software (TA Instruments, Waters LLC) to determine the melting temperature and the crystallinity. The PE melting enthalpy used for the crystallinity determination is 293 J/g [27].

5.2.3. Preparation of CuNW/PE nanocomposites

Four types of PEs with distinct properties were kindly provided by the manufacturers (see Table 5–1). The details of the PEs used in this study are listed in Table 5–1. The DSC analyses of the PEs are plotted in Figure 5–1. Crystallinity and melting point denoted with * in Table 5–1 were determined from DSC analyses.

Table 5-1. The details of the four types of PEs used as polymer matrices

| | UHMWPE | HDPE | LDPE | LLDPE |
|------------------------------|----------|----------------|-------------------|------------|
| Manufacturer | Ticona | Nova Chemicals | Nova Chemicals | ExxonMobil |
| Commercial Name | GUR 4120 | SCLAIR 19G | NOVAPOL LA-0219-A | LL 6201.19 |
| Density (g/cm ³) | 0.93 | 0.96 | 0.918 | 0.926 |
| Melt Index (g/10 min) | --- | 1.2 | 2.3 | 50 |
| Melting Temperature (°C) | 132* | 125* | 97* | 119*, 123 |
| Crystallinity | 56.8%* | 55.6%* | 16.6%* | 24.2%* |

* Values determined by the DSC analyses, all other information are from the manufacturers' product data sheet.

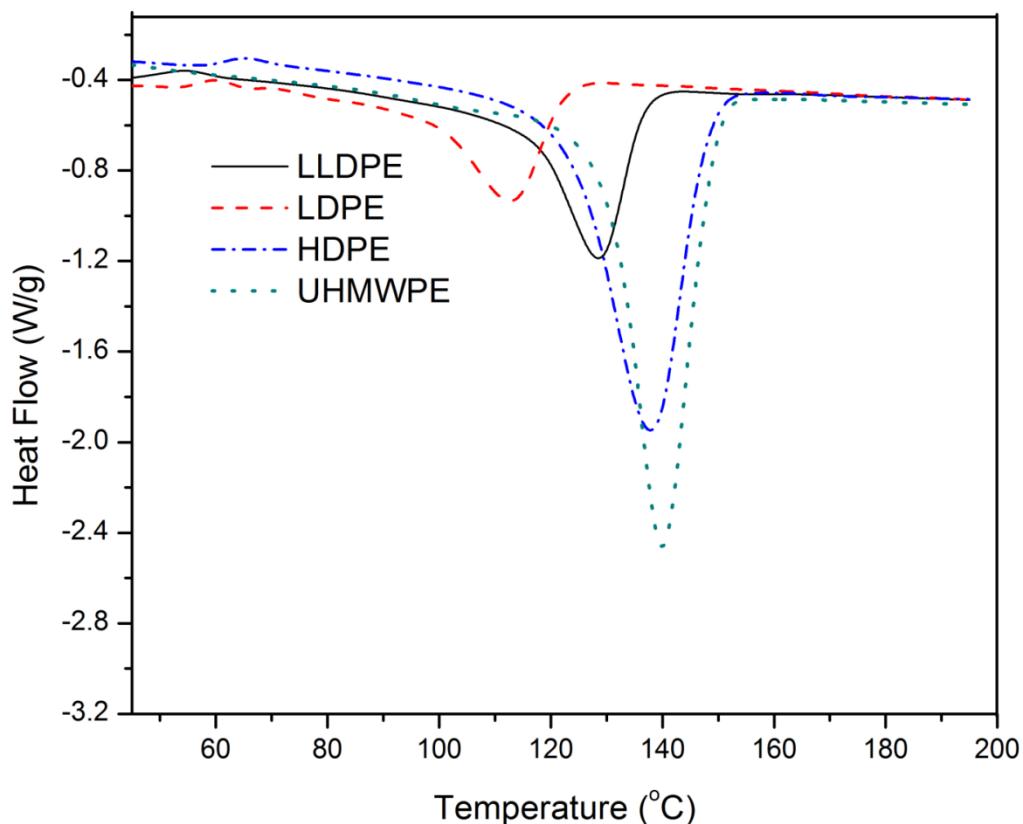


Figure 5-1. The DSC analyses of the four types of PEs used as polymer matrices.

The CuNW/PE nanocomposites with different concentrations of CuNWs were prepared by MSMP method described in ref. [12]. HDPE, LDPE and LLDPE solutions were prepared by dissolving 2.0 g polymer in 100 mL xylene (98.5% min., BDH) at 100 °C under vigorous stirring. UHMWPE solution was prepared by dissolving 0.4 g polymer powder in 100 mL xylene (98.5% min., BDH) at 100 °C. The CuNW/CH₃OH dispersion of desired volume was added to the PE/xylene hot solutions drop by drop at around 2 mL/min to evaporate the CH₃OH and leave the CuNWs dispersed in the hot solutions under vigorous

stirring. After the dispersion of CuNWs into the hot solution, 50 mL CH₃OH at room temperature was added into the mixture to precipitate the nanocomposite. The CuNW/PE precipitates were then filtered. The CuNW/PE nanocomposites were transferred to evaporation dishes for 24 h in a fume hood under ambient conditions, and then moved into a vacuum oven at room temperature for 12 h to completely remove the residual solvent.

The dry powder of the CuNW/PE nanocomposites was compression molded under 250 °C, 138 MPa for 30 min with a Carver compression molder in a 25.4 mm diameter and 0.8 mm thick stainless steel mold using PTFE sheets as release films between the mold and the top/ bottom stainless steel plates. The compression molded CuNW/PE nanocomposites were cooled down to room temperature in the compression molder with circulating tap water for 15 min under pressure and kept for 24 h under ambient conditions prior to the characterization. The experimental process for the CuNW/PE nanocomposite preparation and characterization are illustrated as the flow chart in Figure 5–2.

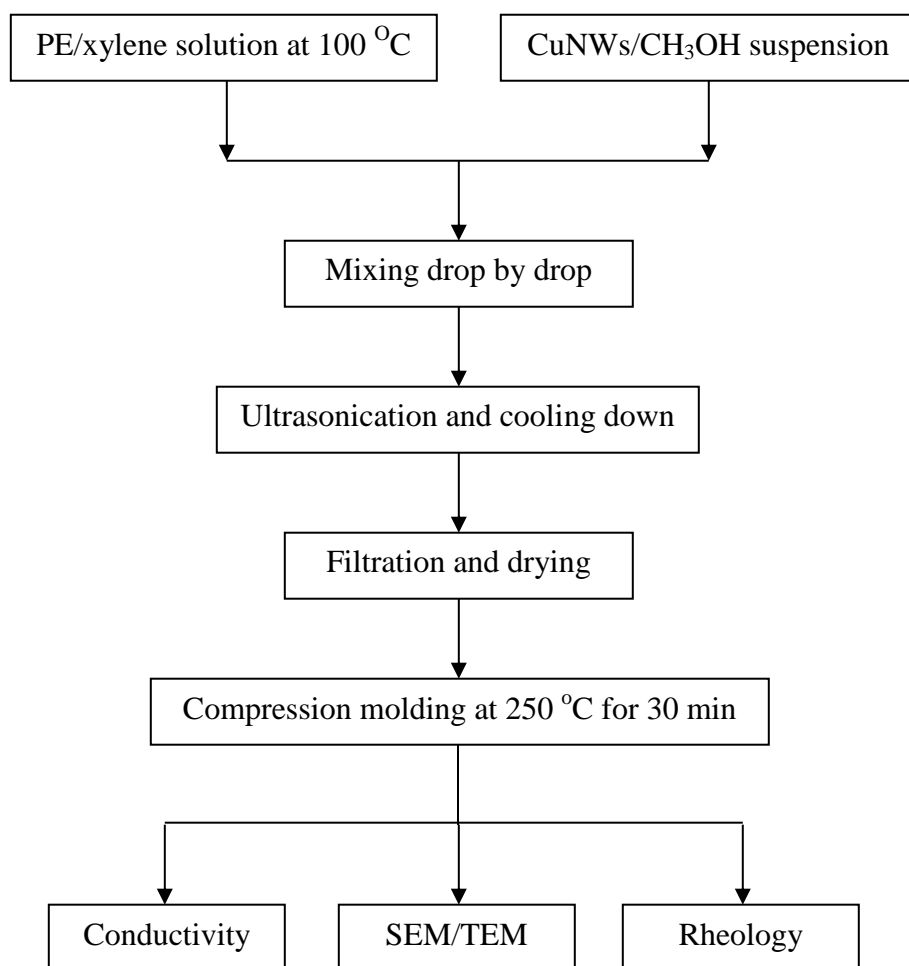


Figure 5-2. The flow chart illustrating the experimental process for the CuNW/PE nanocomposite preparation and characterization.

5.2.4. Morphological characterization of the CuNW/PE nanocomposites

The SEM images of the CuNW/PE nanocomposites were collected using a Philips XL30 scanning electron microscope. The nanocomposites were fractured in liquid nitrogen and coated with gold and palladium by cathode sputtering to collect the backscattered images under 20 kV accelerating voltage.

The TEM images were collected with a Tecnai F20 field emission gun transmission electron microscope under 200 kV accelerating voltage. The CuNW/PE nanocomposite samples were ultramicrotomed by a Leica EM UC6 with an ultracut diamond knife to obtain desired cross sections of thickness about 100 nm at -130 °C. The ultramicrotomed sections were then transferred onto a holey copper TEM grid for observation.

5.2.5. Electrical and rheological characterization of the CuNW/PE nanocomposites

The electrical resistivity of the CuNW/PE nanocomposites was measured by two different instruments as described in Section 4.2.4.

The compression molded nanocomposite samples with diameter of 25.4 mm and thick of 0.8 mm were used for the dynamic rheological characterization in a Rheometrics RMS800 rheometer with a 25 mm parallel plate fixture under 200 °C in nitrogen atmosphere. The frequency sweeps from 10^{-1} to 10^2 rad/s were performed at low strains, 0.5–4%, where all the four types of PEs exhibited linear viscoelastic behavior. The neat PEs for the dynamic rheological characterization were processed by the MSMP method as the CuNW/PE nanocomposites too.

5.3. Results and discussion

5.3.1. Electrical conductivity of the CuNW/PE nanocomposites

The electrical conductivity and electrical percolation of the polymer nanocomposites depend on several factors like the type and concentration of the conductive nanofillers, the properties of the polymer matrices and the processing conditions that affect the dispersion, distribution and aspect ratio of the nanofillers in the nanocomposites. The electrical conductivity of the four types of PEs filled with different concentrations of CuNWs is shown in Figure 5–3. There is a significant increase of several orders in the electrical conductivity with the increasing concentrations of CuNWs that can be observed in the plot for each type of PE, the concentration where the increase occurs indicates electrical percolation threshold. All the four curves exhibited the typical percolation behaviour but with different percolation threshold concentrations of 2.0 vol. %, 0.5 vol. %, 0.25 vol. % and 0.25 vol. % for the CuNW/UHMWPE, CuNW/HDPE, CuNW/LDPE and CuNW/LLDPE nanocomposites, respectively. Below the electrical percolation threshold, the electrical conductivity of the CuNW/PE nanocomposites was not improved compared to the neat polymers indicating the absence of conductive pathways to transport electrons within the insulating PE matrix. When the concentration of CuNWs in the PE matrices increased from their respective percolation thresholds, a sharp change of several orders in the electrical conductivity can be observed on the curves indicating the formation of conductive networks by CuNWs within the PE matrices.

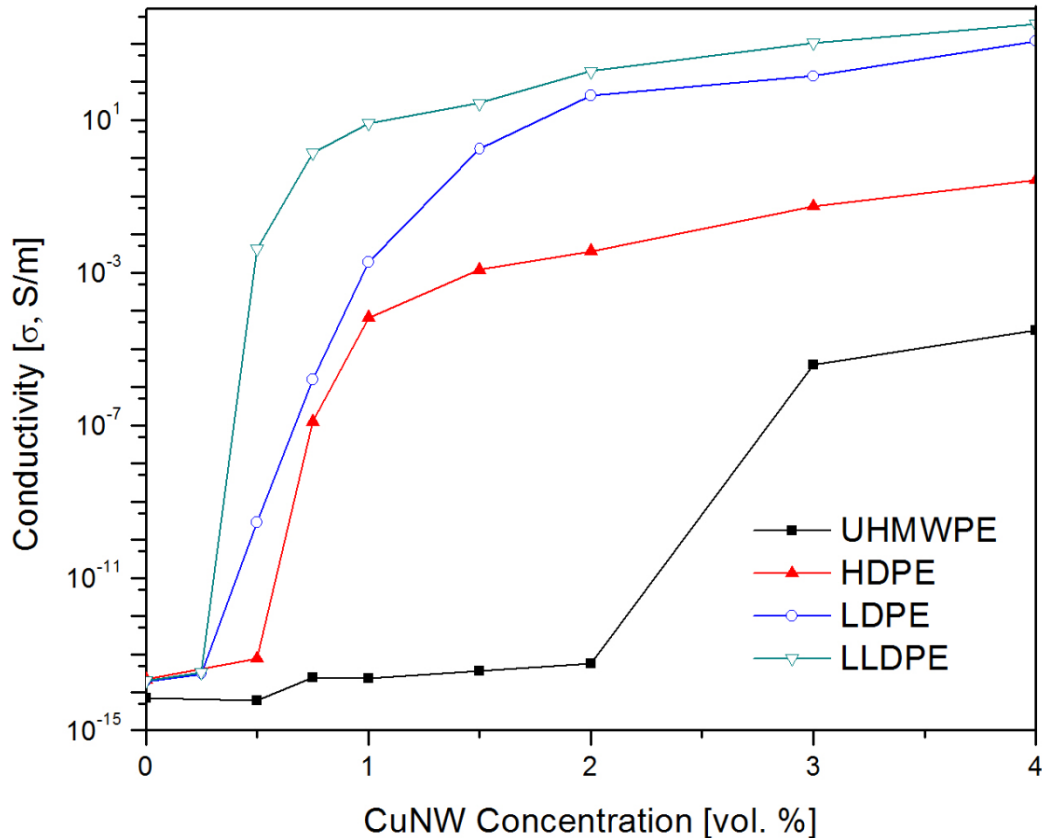


Figure 5-3. The electrical conductivity of the four types of PE nanocomposites with different concentrations of CuNWs.

The electrical conductivity and the percolation curves of the CuNWs in the four types of PEs exhibited significant differences. The CuNW/UHMWPE nanocomposites showed the highest percolation threshold (CuNW concentration of 2.0 vol. %) and the lowest electrical conductivity which was only 3.1×10^{-5} S/m at the highest concentration used in this study (4.0 vol. %). The CuNW/HDPE nanocomposites with the percolation threshold at 0.5 vol. % showed higher electrical conductivity than the CuNW/UHMWPE nanocomposites. The electrical conductivity of the CuNW/HDPE

nanocomposites was 0.27 S/m at 4.0 vol. %. Both the CuNW/LDPE and CuNW/LLDPE nanocomposites exhibited the lowest percolation threshold at CuNW concentration of 0.25 vol. %. Moreover, the CuNW/LLDPE nanocomposites showed the highest electrical conductivity of 3.3×10^2 S/m at CuNW concentration of 4.0 vol. %, which is almost three times higher than that of the CuNW/LDPE nanocomposite and 7 orders of magnitude higher than the CuNW/UHMWPE nanocomposites.

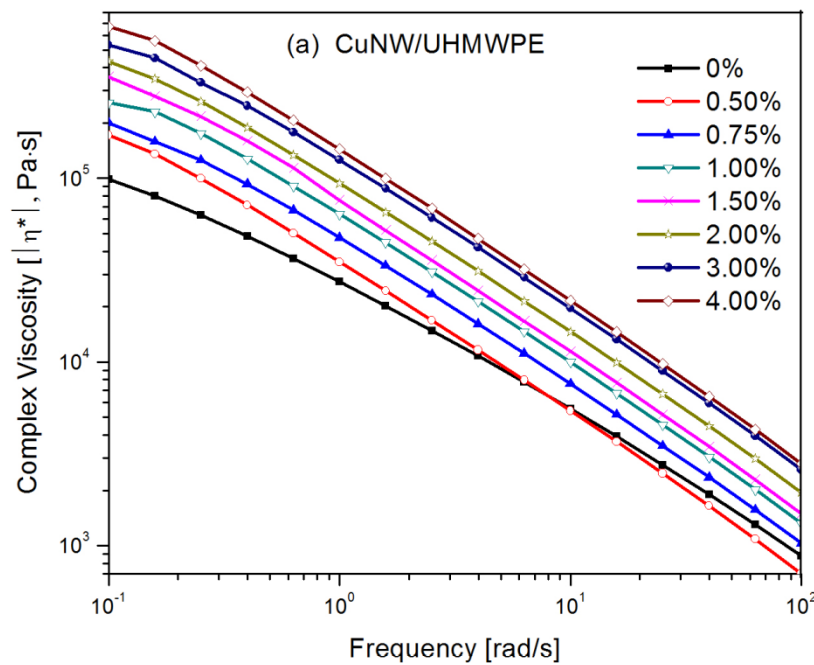
Electrical conductivity and percolation of the four types of PEs filled with CuNWs are closely related to the dispersion and distribution of the CuNWs that have significant effects on the formation of the conductive networks within the PE matrices. The CuNW/UHMWPE nanocomposites demonstrated the highest percolation threshold concentration and the lowest electrical conductivity, which implies poor dispersion of the CuNWs and difficulty to form conductive networks within the UHMWPE matrix. In comparison, the lowest percolation threshold and the highest electrical conductivity of the CuNW/LLDPE nanocomposites indicate better dispersion of the CuNWs and preference to form more conductive pathways within the LLDPE matrix at the lower concentration of CuNWs.

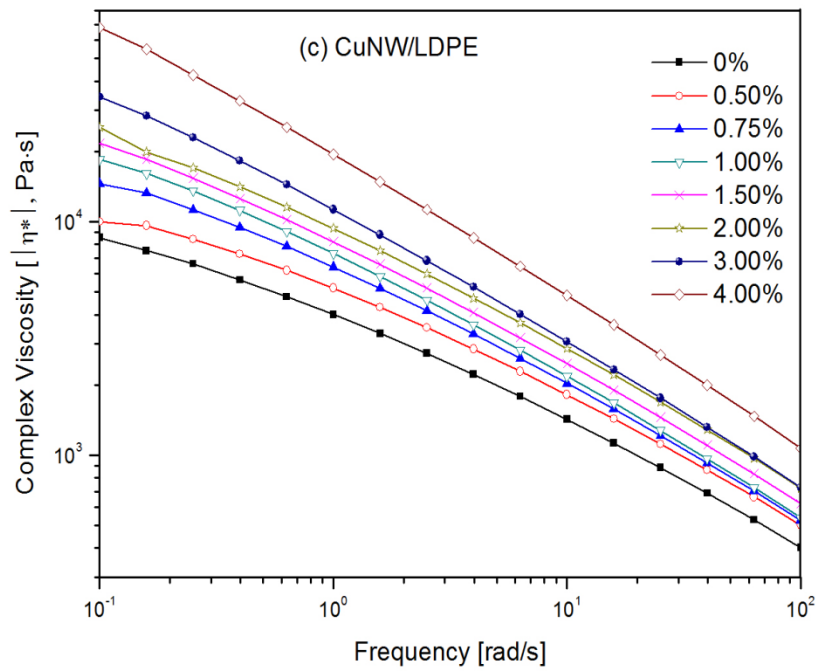
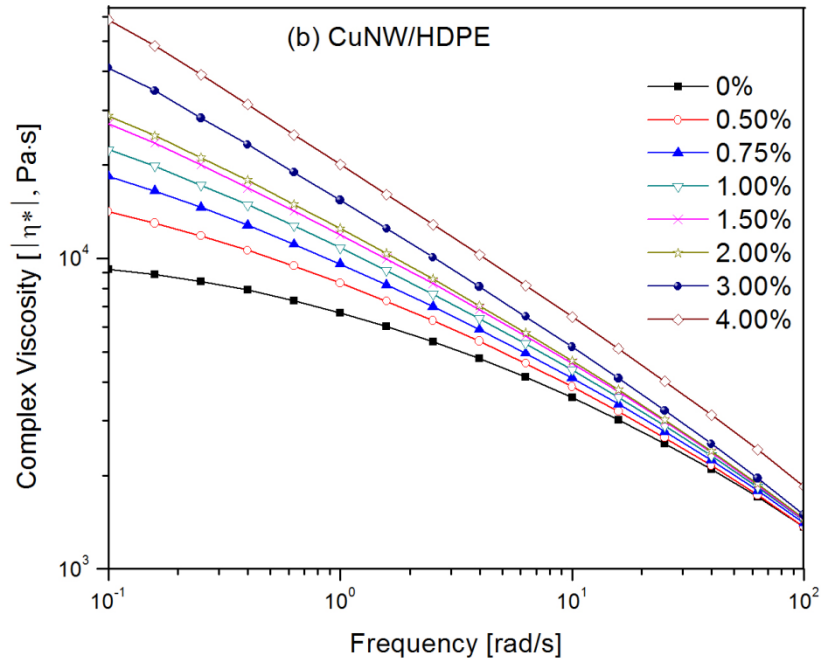
5.3.2. Melt rheology of CuNW/PE nanocomposites at 200 °C

Figures 5–4 to 5–7 show the results of rheological characterization of viscoelastic properties of the nanocomposites prepared with the four different

types of PEs with different concentrations of CuNWs. It is clearly seen in Figure 5–4 that the addition of CuNWs into PEs increased the absolute value of the complex viscosity. With 0.5 vol. % CuNWs added into the neat PEs, the absolute values of complex viscosity at 10^{-1} rad/s frequency increased 74%, 54%, 17% and 39% for the CuNW/UHMWPE, CuNW/HDPE, CuNW/LDPE and CuNW/LLDPE nanocomposites, respectively. All the CuNW/PE nanocomposites exhibited the shear thinning effect. Adding CuNWs into different neat PEs has different effects on the relationship between complex viscosity (η^*) and frequency depending on the type of PE. In CuNW/UHMWPE nanocomposites, complex viscosity (η^*) of neat UHMWPE showed a gentle increase with decrease in frequency compared to those of the CuNW/UHMWPE nanocomposites. The complex viscosity of the CuNW/UHMWPE nanocomposite with 0.5 vol. % CuNWs was lower than that of the neat UHMWPE at high frequency, which is attributed to the van der Waals force between the long chains of UHMWPE and CuNWs. This increases the relaxation time of the UHMWPE chains. The probability of the longer chains to keep interaction with the CuNWs within the experimental time frame will be higher than the shorter chains because long chains can have multiple contacts. Similar phenomenon was not observed for other three types of PE nanocomposites, in which the PE macromolecular chains are shorter than the UHMWPE. The similar deviation originating van der Waals forces was reported in the SWNT/UHMWPE nanocomposites by Zhang et al [28]. In Figure 5–4b, the neat HDPE showed a small Newtonian plateau at low frequencies. However, the

plateau was not observed for the curves of the CuNW/HDPE nanocomposites. The effect of the CuNW concentration on complex viscosity (η^*) increase was more noticeable at lower frequency and the relative difference diminished with the increasing frequency due to the shear thinning effect. In Figure 5–4c, the addition of CuNWs into the LDPE matrix did not have too much impact on the frequency dependence of complex viscosity until the CuNW concentration reached 4.0 vol. %, when the shear thinning effect became more pronounced in the CuNW/LDPE nanocomposites. The CuNW/LLDPE nanocomposites exhibited very different frequency dependence of complex viscosity from the other three types of CuNW/PE nanocomposites as shown in Figure 5–4d. The shear thinning effect of the CuNW/LLDPE nanocomposites was more pronounced at lower frequencies.





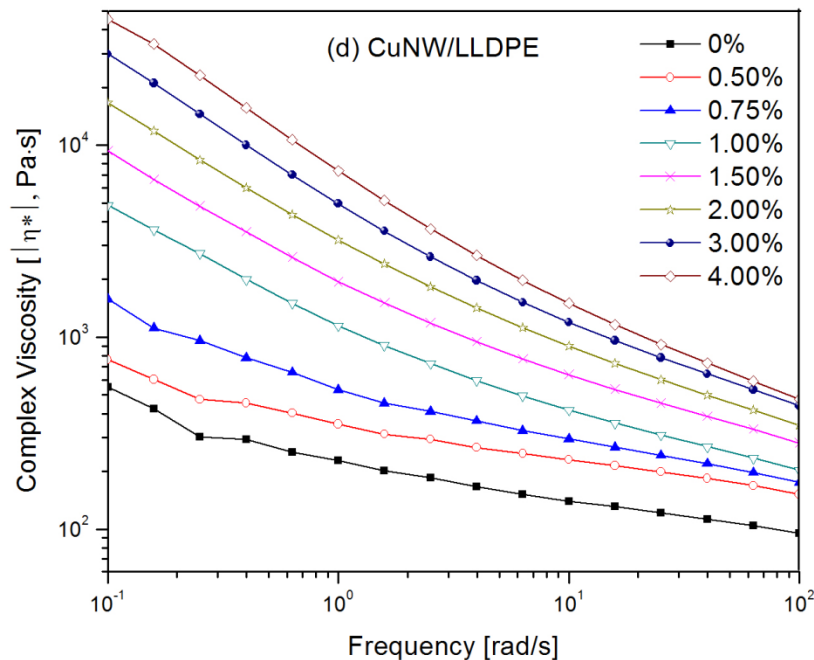
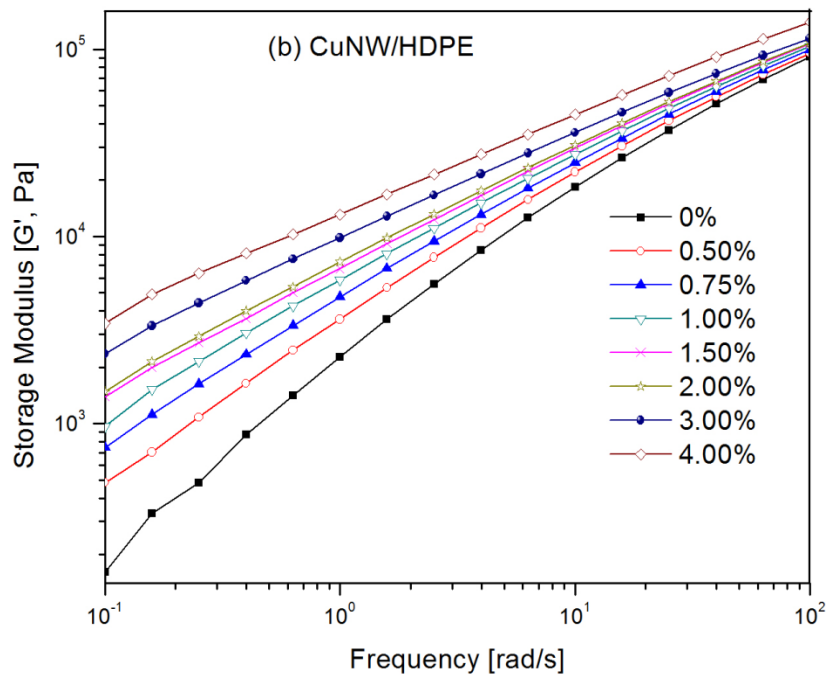
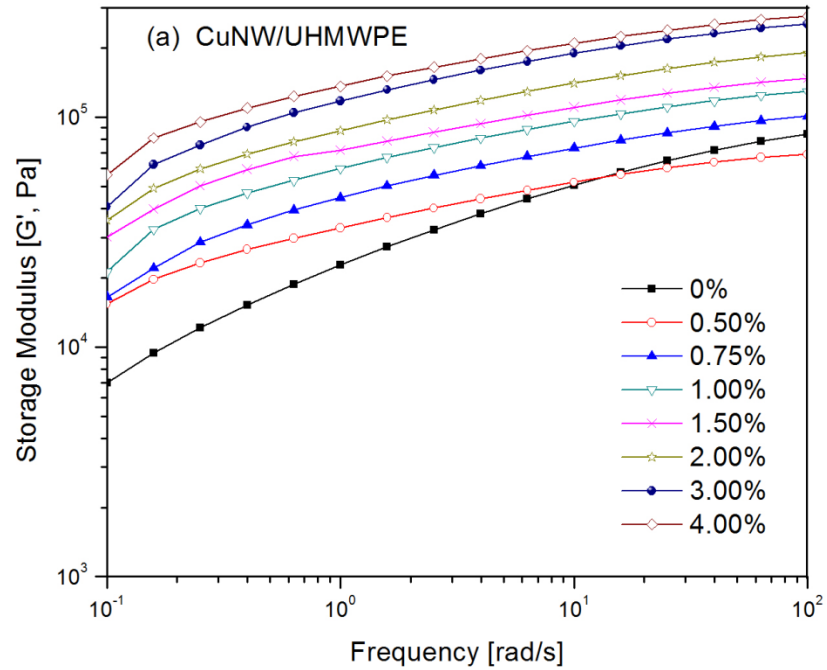


Figure 5-4. Complex viscosity (η^*) as a function of frequency at 200 °C for the (a) CuNW/UHMWPE, (b) CuNW/HDPE, (c) CuNW/LDPE and (d) CuNW/LLDPE nanocomposites.

It can be clearly observed in Figure 5–5 that the addition of CuNWs into PE matrices resulted in the storage modulus increase for all the four types of PEs. The storage modulus increase with 0.5 vol. % CuNWs addition into neat PE matrices at 10^{-1} rad/s was 120%, 200%, 29% and 34% for UHMWPE, HDPE, LDPE and LLDPE, respectively. The addition of 0.5 vol. % CuNWs into the UHMWPE matrix made the storage modulus vs. frequency curve much more flat and the impact of frequency on storage modulus less significant. The storage modulus increase with the increasing concentration of CuNWs in the HDPE

matrix was more pronounced at low frequencies than at high frequencies as shown in Figure 5–5b. The storage modulus vs. frequency plots of the CuNW/LDPE nanocomposites with different concentration of CuNWs are shown in Figure 5–5c. When the concentration of CuNWs in the LDPE matrix increased from 3.0 vol. % to 4.0 vol. %, there was a noticeable increase in the storage modulus, and the storage modulus vs. frequency curve also became more flat. The CuNW/LLDPE nanocomposites exhibited different frequency dependence of storage modulus from other three types of CuNW/PE nanocomposites in that all the curves in Figure 5–5d were more flat at low frequencies than at high frequencies. For CuNW/LLDPE nanocomposites, when CuNW concentration in LLDPE matrix increased from 0.75 vol. % to 1.0 vol. %, there was a significant change in the shape of the storage modulus curve. For concentration above 1.0 vol. % CuNWs, a plateau can be found at low frequencies on the storage modulus vs. frequency curve.

Chapter 5. Effect of Macromolecular Structure on Electrical and Rheological Properties in Copper Nanowire Polyethylene Nanocomposites:
Effect of Molecular Weight and Branching



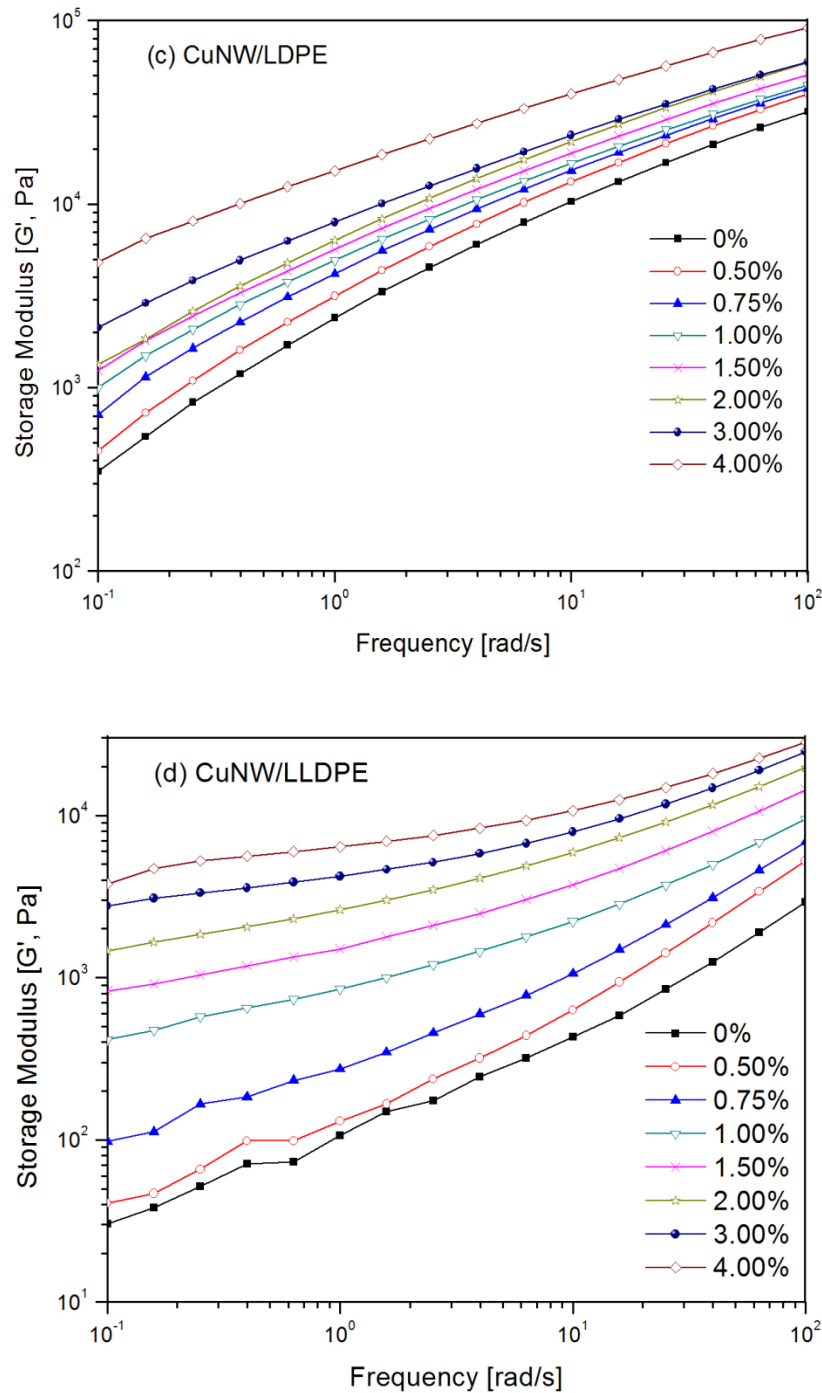


Figure 5-5. Storage Modulus (G') as a function of frequency at 200 °C for the (a) CuNW/UHMWPE, (b) CuNW/HDPE, (c) CuNW/LDPE and (d) CuNW/LLDPE nanocomposites.

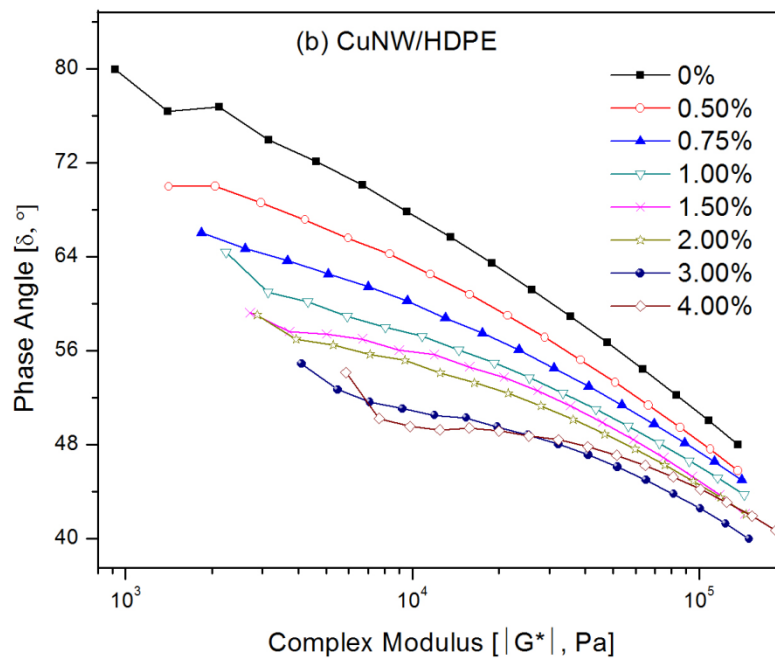
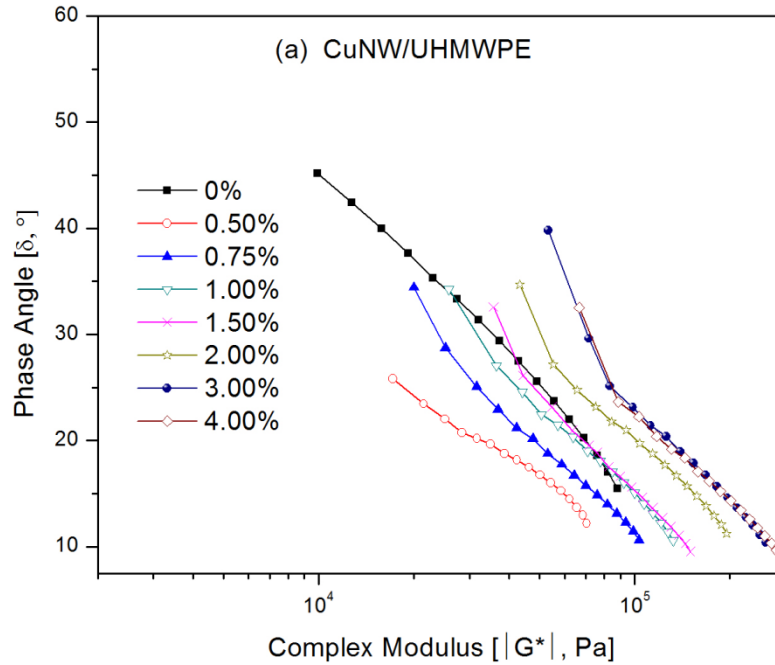
Rheological percolation thresholds of each type of CuNW/PE nanocomposites at 200 °C can be determined from the complex viscosity or storage modulus versus frequency plots for different concentrations of CuNWs. A significant change occurred in the frequency dependence of complex viscosity and storage modulus starting from CuNW concentration of 0.5 vol. % which indicated the microstructure change in the CuNW/UHMWPE nanocomposites. The polymer-CuNW networks formed effectively because of the interactions between the long macromolecular chains of the UHMWPE and CuNWs. Therefore, CuNW/UHMWPE nanocomposites behave differently from the neat UHMWPE indicating the rheological percolation threshold of the CuNW/UHMWPE nanocomposites at CuNW concentration of 0.5 vol. %. The neat HDPE exhibited a small Newtonian plateau for the plot of complex viscosity versus frequency at low frequencies, which was not observed for the CuNW/HDPE nanocomposites with CuNW concentration above 0.5 vol. %. The clear deviation of the frequency dependence of storage modulus can be observed particularly at low frequencies starting from CuNW concentration of 0.5 vol. %. Therefore, rheological percolation threshold of CuNW/HDPE nanocomposites was determined to be at CuNW concentration of 0.5 vol. %. The rheological percolation threshold of the CuNW/LDPE nanocomposites was determined at CuNW concentration of 4.0 vol. % by the noticeable increase in the complex viscosity and storage modulus at that concentration. There was significant deviation in the viscoelastic properties of CuNW/LLDPE nanocomposites with CuNW concentrations above 1.0 vol. % compared to the liquid like behavior of nanocomposites with CuNW

concentrations below 1.0 vol. % particularly at low frequencies. Thus, 1.0 vol. % is the rheological percolation threshold indicator.

Phase angle δ was plotted against the absolute value of complex modulus at 200 °C for the four types of CuNW/PE nanocomposites in Figure 5–6. This curve is also known as van Gurp Palmen plot [29] and has been previously used to identify the rheological percolation in polymer nanocomposites [20, 30–32]. In the CuNW/UHMWPE, CuNW/HDPE, CuNW/LDPE and CuNW/LLDPE nanocomposites, the phase angle decreased with the increasing absolute value of complex modulus. In Figure 5–6a, the phase angle of the neat UHMWPE without CuNWs was about 45.2° at minimum absolute value of complex modulus and decreases linearly to 15.5° at the maximum absolute value of complex modulus. However, the phase angles of CuNW/UHMWPE nanocomposites dropped significantly below 40° in the whole frequency range. The noticeable deviation of the phase angle δ of the CuNW/UHMWPE nanocomposites from the neat UHMWPE starting at CuNW concentration of 0.5 vol. % indicates that the rheological percolation was reached. The minimum and maximum phase angles of the CuNW/HDPE nanocomposites in Figure 5–6b were 40° and 80° respectively higher than those of the CuNW/UHMWPE nanocomposites, which indicated the more liquid-like behavior of the CuNW/HDPE nanocomposites. The neat HDPE curve showed a slight deviation from the other curves in Figure 5–6b, which was more pronounced at low absolute value of complex modulus. Considering the small Newtonian plateau at low frequency on the curve of complex viscosity (η^*) against frequency of the

neat HDPE and the absence of a noticeable shape change on the storage modulus vs. frequency curves of the neat HDPE and the CuNW/HDPE nanocomposites, the rheological percolation threshold would be suggested at CuNW concentration of 0.5 vol. % for the CuNW/HDPE nanocomposites. In the CuNW/LDPE nanocomposites, the phase angles were greater than 45° at low absolute value of complex modulus except the nanocomposite with CuNW concentration of 4.0 vol. % whose phase angles were $\leq 45^\circ$ in the whole frequency range. The deviation of the van Gorp Palmen plot of the CuNWs/LDPE nanocomposite with CuNW concentration of 4.0 vol. % from others indicated the rheological percolation threshold for the CuNW/LDPE nanocomposites. The van Gorp Palmen plots of the CuNW/LLDPE nanocomposites showed a different relationship from other three types of nanocomposites in that the phase angle increased with the increasing absolute value of complex modulus for the CuNW/LLDPE nanocomposites only. This can be interpreted by the disentanglement effect of the LLDPE macromolecular chains at the higher shear rates. All the phase angles of the CuNW/LLDPE nanocomposites with CuNW concentrations less than 1.0 vol. % were greater than 45° , which indicated the liquid-like behavior of the nanocomposites. However, the phase angles less than 45° of the nanocomposites with CuNW concentration ≥ 1.0 vol. % at low absolute value of complex modulus implied the solid-like behavior. Moreover, the dramatic phase angle decrease at low absolute value of complex modulus when the concentration of CuNWs increased from 0.75 vol. % to 1.0 vol. %

suggested the rheological percolation threshold of the CuNW/LLDPE nanocomposites at CuNW concentration of 1.0 vol. %.



Chapter 5. Effect of Macromolecular Structure on Electrical and Rheological Properties in Copper Nanowire Polyethylene Nanocomposites:
Effect of Molecular Weight and Branching

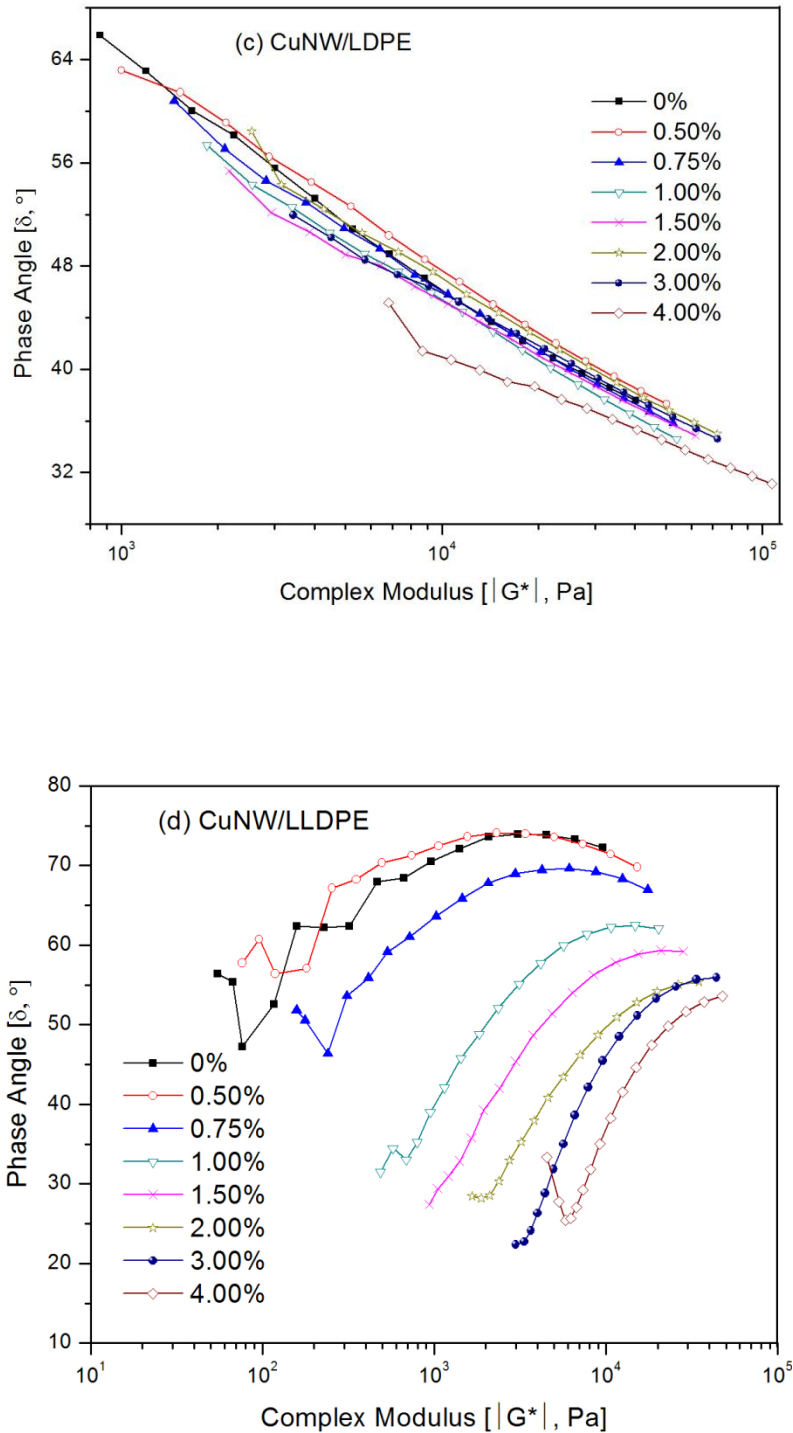
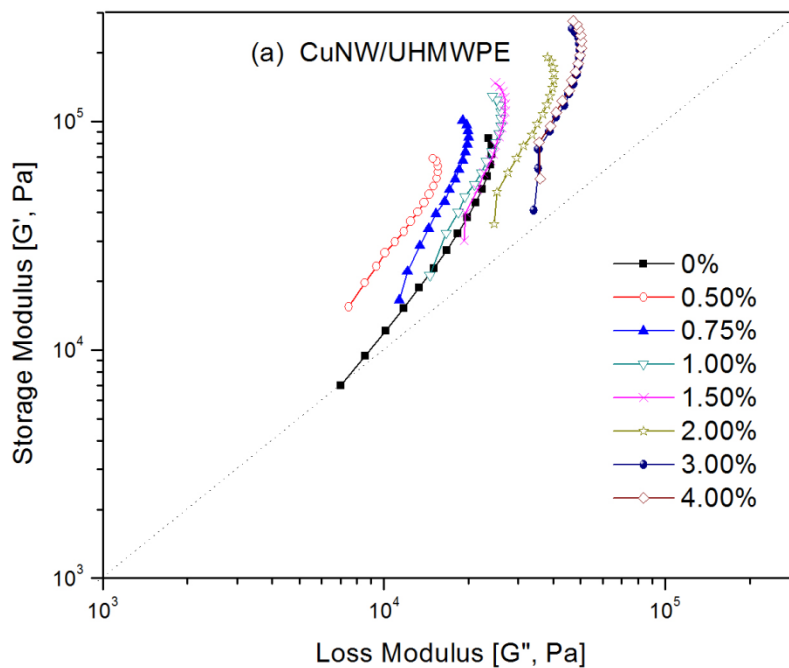


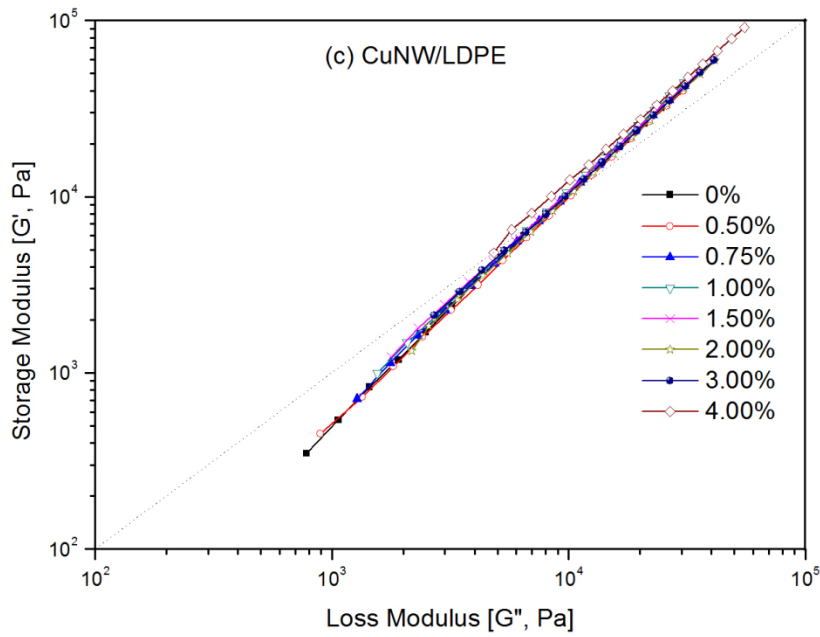
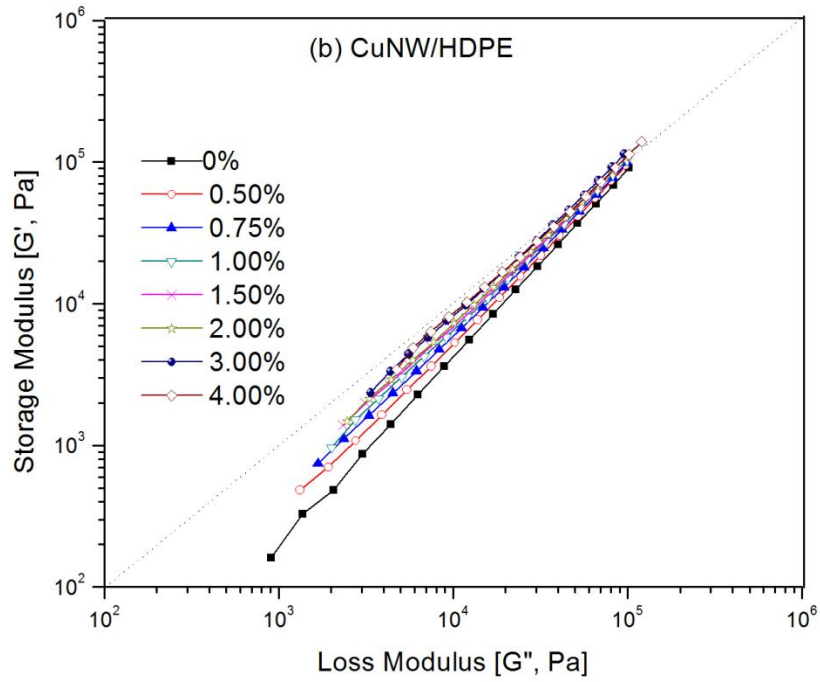
Figure 5-6. Phase angle (δ) as a function of the absolute value of the complex modulus (van Gorp Palmen plot) at 200 $^{\circ}$ C for the (a) CuNW/UHMWPE, (b) CuNW/HDPE, (c) CuNW/LDPE and (d) CuNW/LLDPE nanocomposites.

The plots of storage modulus (G') versus loss modulus (G'') have been previously used to determine the rheological percolation threshold of polymer nanocomposites under a given temperature [33]. In addition, storage modulus (G') at low frequencies was considered one of the most sensitive parameters for indicating the onset of the microstructure change of polymer nanocomposites [33, 7, 20, 34]. The plots of storage modulus (G') versus loss modulus (G'') at 200 °C for the four types of CuNW/PE nanocomposites are shown in Figure 5–7. The deviation of the neat UHMWPE from the other CuNW/UHMWPE nanocomposites in Figure 5–7a indicated the rheological percolation threshold of the CuNW/UHMWPE nanocomposites at CuNW concentration of 0.5 vol. %. In Figure 5–7b, only the plot of the neat HDPE was below the diagonal line in the whole range of frequencies, and the deviation of the neat HDPE from the CuNW/HDPE nanocomposites at low frequencies was pronounced. Both indicated the rheological percolation threshold of the CuNW/HDPE nanocomposites at CuNW concentration of 0.5 vol. %. Similar to the CuNW/HDPE nanocomposites, the CuNW/LDPE nanocomposites had only the plot of CuNW concentration of 4.0 vol. % exhibiting more noticeable deviation than the others and above the diagonal line in the whole range of frequencies, which indicated the rheological percolation threshold of the CuNW/LDPE nanocomposites at CuNW concentration of 4.0 vol. %. The deviation of the CuNW/LLDPE nanocomposites with CuNW concentration above 1.0 % from those with CuNW concentration below 1.0 % was the indicator for the rheological percolation threshold for the CuNW/LLDPE nanocomposites.

Chapter 5. Effect of Macromolecular Structure on Electrical and Rheological Properties in Copper Nanowire Polyethylene Nanocomposites: Effect of Molecular Weight and Branching

In summary, the rheological percolation thresholds of the four types of CuNW/PE nanocomposites at 200 °C determined by different methods were consistent, which appeared at CuNW concentration of 0.5 vol. %, 0.5 vol. %, 4.0 vol. % and 1.0 vol. % for the CuNW/UHMWPE, CuNW/HDPE, CuNW/LDPE and CuNW/LLDPE nanocomposites, respectively.





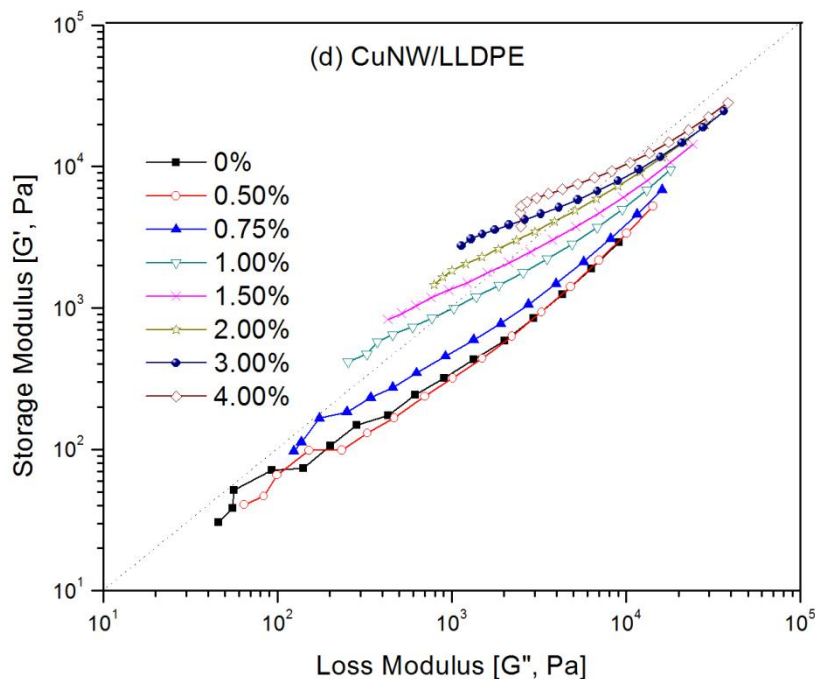
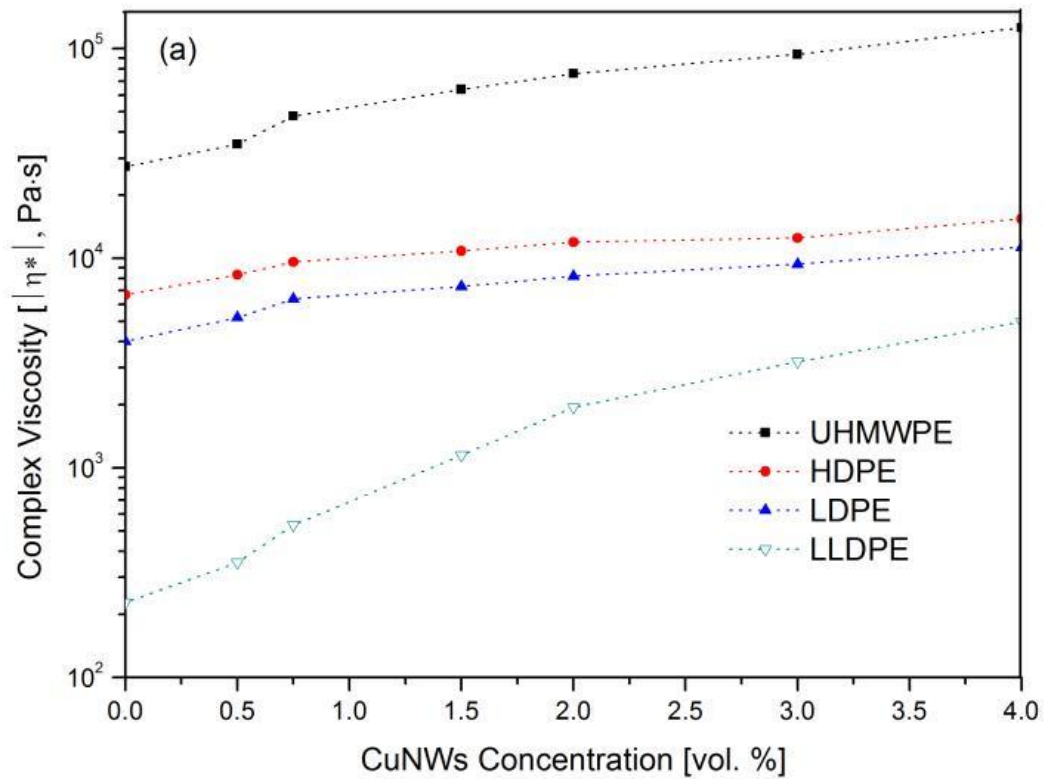


Figure 5-7. Storage modulus (G') versus loss modulus (G'') at 200 °C for the (a) CuNW/UHMWPE, (b) CuNW/HDPE, (c) CuNW/LDPE and (d) CuNW/LLDPE nanocomposites.

Complex viscosity (η^*) and storage modulus (G') versus CuNW concentration was plotted in Figure 5–8 for the four types of nanocomposites at 200 °C and 1 rad/s frequency. In Figure 5–8a, complex viscosity of the four types of CuNW/PE nanocomposites increased with the CuNW concentration. But the effect of the CuNW concentration on the complex viscosity was different for different type of PE matrices. The effect was insignificant in the CuNW/HDPE and CuNW/LDPE nanocomposites and more pronounced in the CuNW/LLDPE and CuNW/UHMWPE nanocomposites. There was a significant

increase of the complex viscosity in the CuNW/UHMWPE nanocomposites when the CuNW concentration increased from 0 vol. % to 0.5 vol. %. The complex viscosity increase was more noticeable when the CuNW concentration increased from 0.5 vol. % to 2.0 vol. % in the CuNW/LLDPE nanocomposites.



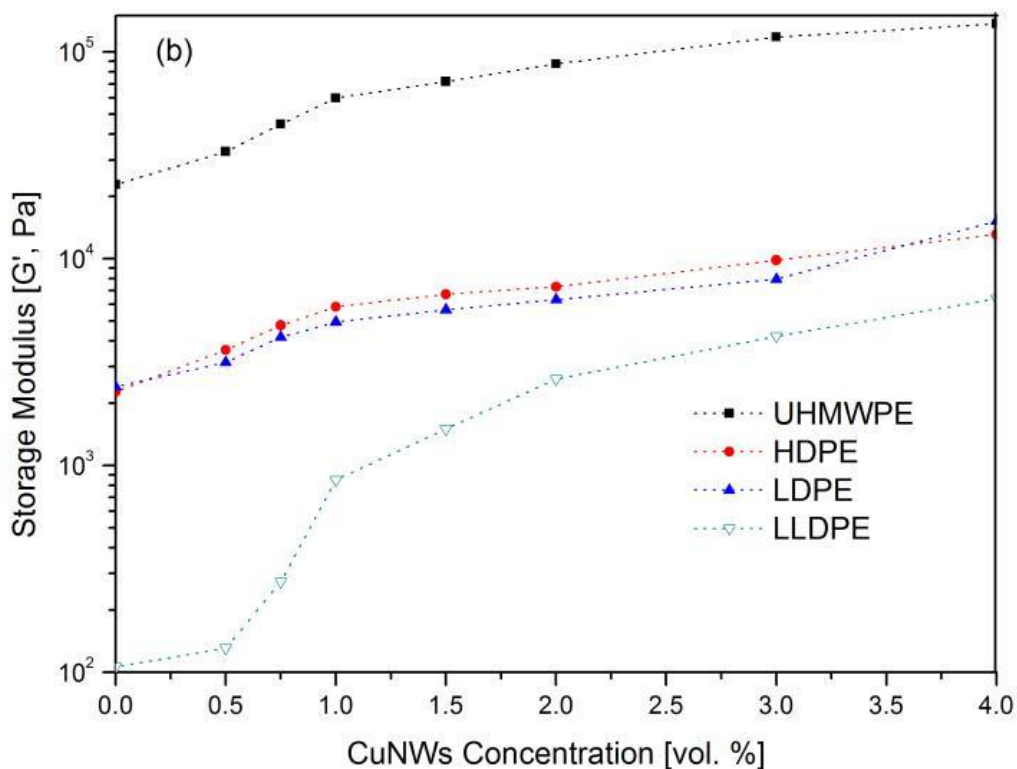


Figure 5-8. The (a) complex viscosity (η^*) and (b) storage modulus (G') at 200 °C and 1 rad/s for the CuNW/PE nanocomposites as functions of the CuNW concentration.

In Figure 5–8b, the storage modulus also increased with the increasing CuNW concentration for all the four types of PE nanocomposites. The effect of the CuNW concentration on the storage modulus was more noticeable than its effect on the complex viscosity. The storage modulus of the CuNW/LLDPE nanocomposites increased 5.5-fold when the CuNW concentration increased from 0.5 vol. % to 1.0 vol. %. The most significant increase of storage modulus in the CuNW/UHMWPE nanocomposites took place when the CuNW

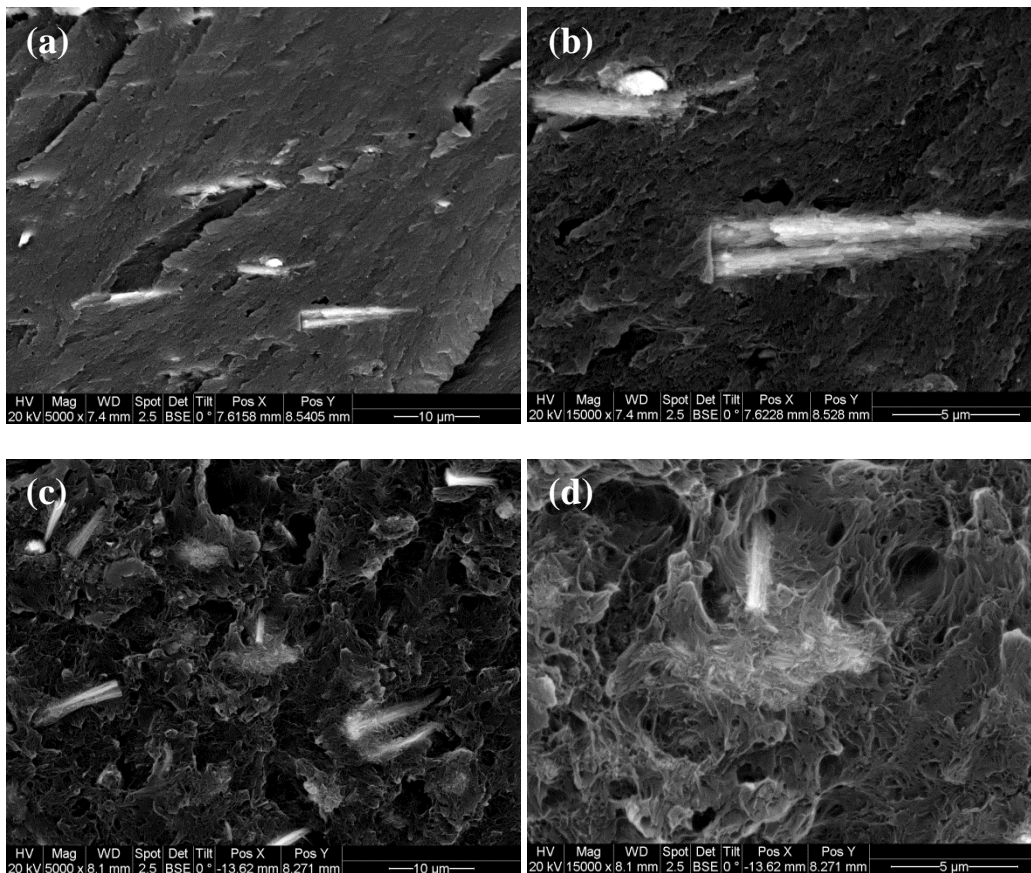
concentration increased from 0 vol. % to 0.5 vol. %. The impact of the CuNW concentration on storage modulus was also less significant in the CuNW/HDPE and CuNW/LDPE nanocomposites. However, there was a more noticeable increase in storage modulus on the curve of the CuNW/LDPE nanocomposites when the CuNW concentration increased from 3.0 vol. % to 4.0 vol. %. The storage modulus of the CuNW/LDPE nanocomposites at CuNW concentration of 4.0 vol. % was more than that of CuNW/HDPE nanocomposites, which can be attributed to the formation of the NW–NW network within the CuNW/LDPE nanocomposites.

5.3.3. Morphology of CuNW/PE nanocomposites

Figure 5–9 shows the backscattered SEM images of the freeze-fractured (a, b) UHMWPE, (c, d) HDPE, (e, f) LDPE and (g, h) LLDPE nanocomposites containing 1.0 vol. % CuNWs. The images on the left at low magnification revealed the general dispersion of CuNWs in the four different types of PE matrices. The images on the right were at high magnification. The bright spots and areas in the backscattered SEM images were single CuNWs and/or CuNW agglomerates. In the low magnification SEM images, several bundles of large agglomerates are shown in Figures 5–9a and c, only one bundle of agglomerates and many bright spots can be observed in Figure 6e, and no bright bundle is visible in Figure 5–9g. The difference in CuNW dispersion was revealed clearly in the high SEM magnification images. The bundles shown in Figure 5–9b were

Chapter 5. Effect of Macromolecular Structure on Electrical and Rheological Properties in Copper Nanowire Polyethylene Nanocomposites:
Effect of Molecular Weight and Branching

larger and brighter than the one in Figure 5–9d indicating the better dispersion of CuNWs in HDPE than in UHMWPE. A few bright stripes without bundles in Figure 5–9f indicated the improved dispersion of CuNWs in LDPE over that in HDPE. In addition, no bright spot or area can be observed in Figure 5–9h evidencing the uniform dispersion of CuNWs in LLDPE. In general, the backscattered SEM images indicated that dispersion of CuNWs in the different PE matrices is LLDPE > LDPE > HDPE > UHMWPE.



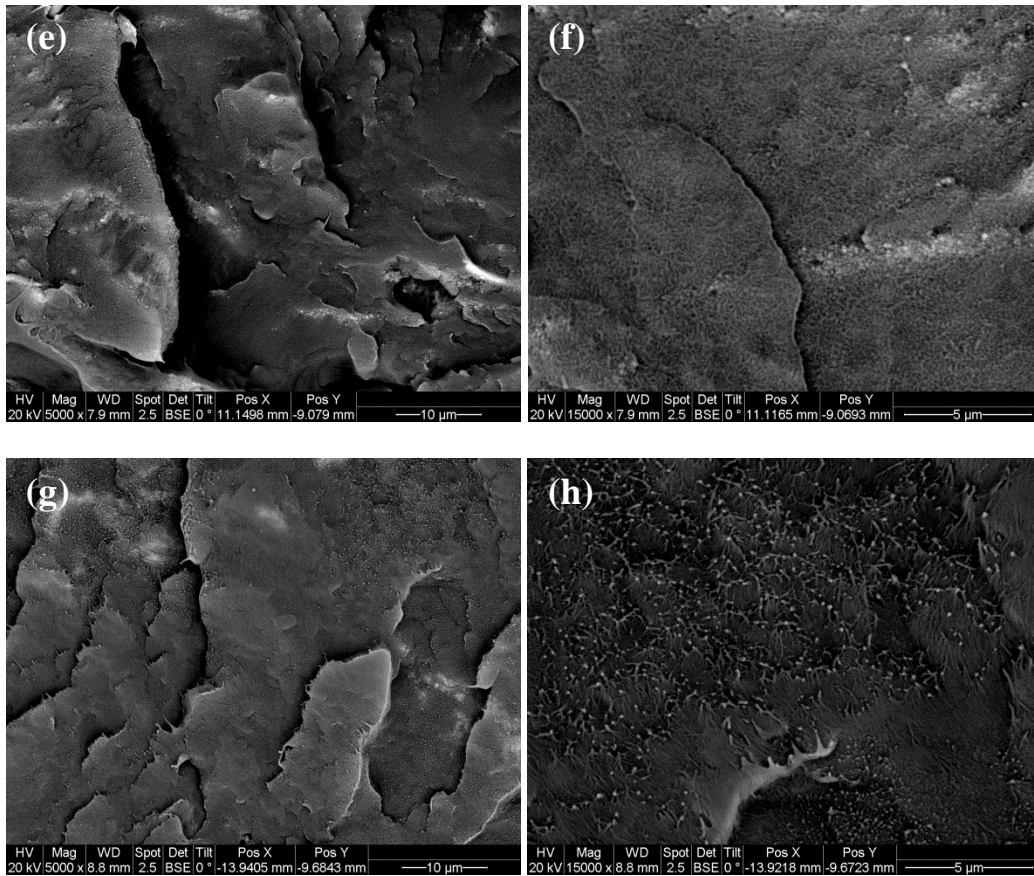
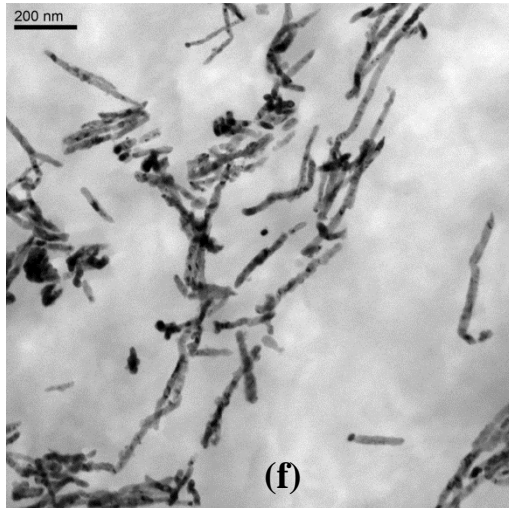
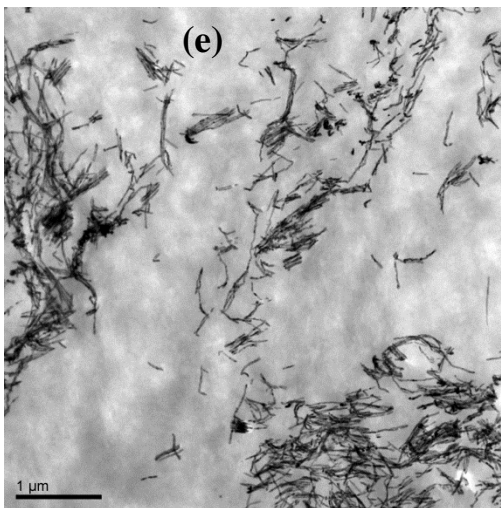
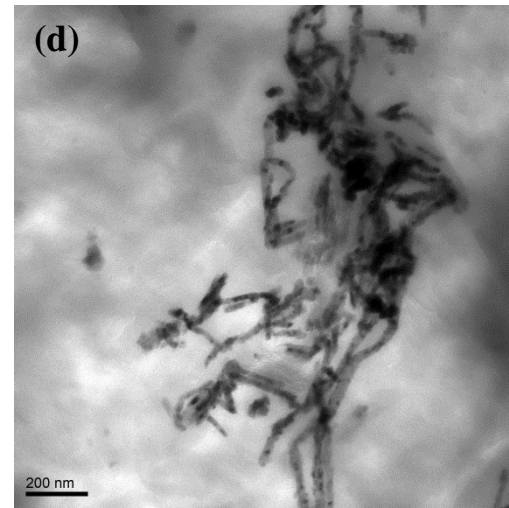
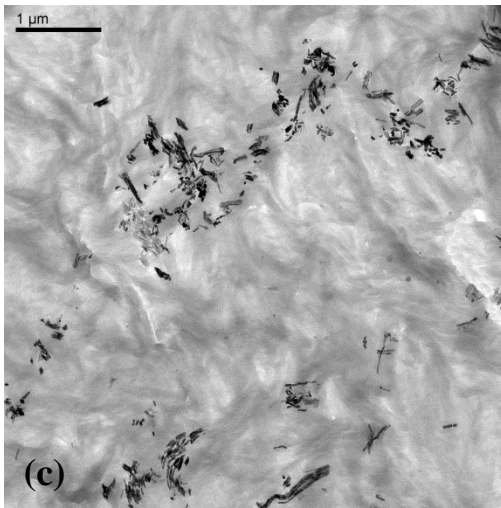
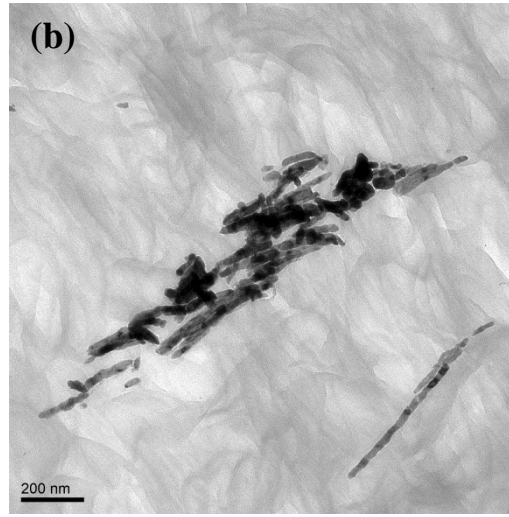
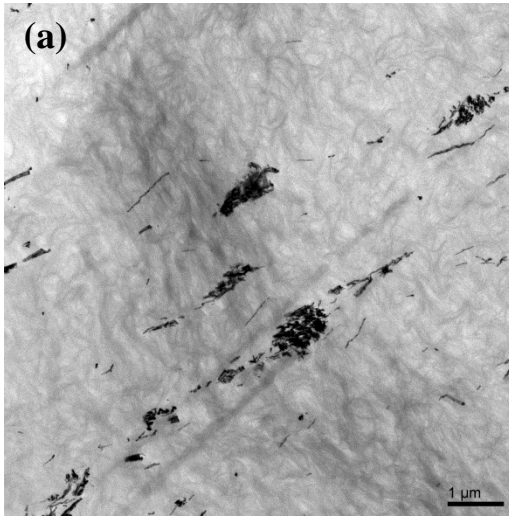


Figure 5-9. The low (left) and high (right) magnification backscattered SEM images of the freeze-fractured (a, b) UHMWPE, (c, d) HDPE, (e, f) LDPE and (g, h) LLDPE nanocomposites containing 1.0 vol. % CuNWs.

Figure 5–10 presents the TEM images of the (a, b) UHMWPE, (c, d) HDPE, (e, f) LDPE and (g, h) LLDPE nanocomposites containing 1.0 vol. % CuNWs. The low magnification TEM images on the left revealed the large agglomerates of CuNWs in UHMWPE and more scattered CuNW particles localized within the HDPE matrix. A greater amount of CuNWs were observed in the low magnification TEM images for the LDPE and LLDPE matrixes, which indicated

the much better dispersion of CuNWs in these matrices. The high magnification TEM images on the right showed that the CuNWs were more agglomerated in the case of UHMWPE and HDPE but better dispersed in the LDPE and LLDPE. The CuNWs in Figure 5–10b seemed tightly constrained by the UHMWPE matrix. CuNWs in Figure 5–10d also looked constrained by the HDPE matrix but less tightly and the polymer had intercalated between the wires. High magnification images also revealed the better dispersion of CuNWs in the LDPE and LLDPE matrices. Moreover, the CuNWs in the LLDPE matrix appeared to have a little better segregation, dispersion and network formation than in LDPE matrix. Therefore, the TEM images also corroborate the different dispersion of CuNWs in the four types of PE matrices as was observed from SEM characterization.

Electrically Conductive Metal Nanowire Polymer Nanocomposites



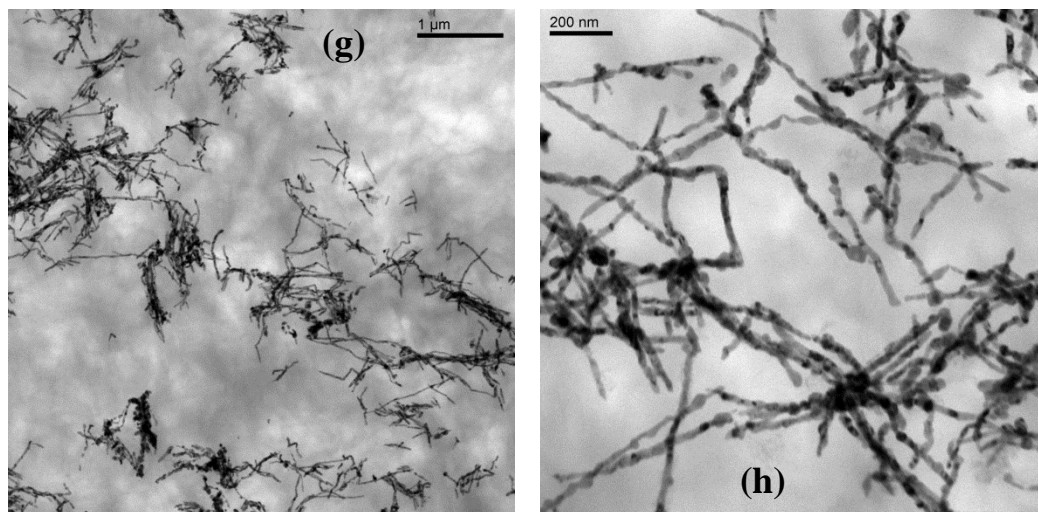


Figure 5-10. The low (left) and high (right) magnification TEM images of the (a, b) UHMWPE, (c, d) HDPE, (e, f) LDPE and (g, h) LLDPE nanocomposites containing 1.0 vol. % CuNWs.

5.3.4. Effect of macromolecular structures on filler dispersion, electrical and rheological properties

The electrical percolation thresholds and rheological percolation thresholds at 200 °C observed in this work were 2.0 vol. % and 0.5 vol. % for the CuNW/UHMWPE, 0.5 vol. % and 0.5 vol. % for the CuNW/HDPE, 0.25 vol. % and 4.0 vol. % for the CuNW/LDPE as well as 0.25 vol. % and 1.0 vol. % for the CuNW/LLDPE nanocomposites. The electrical percolation threshold was higher than the rheological percolation threshold for the CuNW/UHMWPE, the same for the CuNW/HDPE and lower for the CuNW/LDPE and CuNW/LLDPE nanocomposites. Electrical conductivity and percolation thresholds of the four types of CuNW/PE nanocomposites are highly related to the dispersion of the

CuNWs in the different PE matrices. The better dispersion of CuNWs in PE matrix typically leads to the higher electrical conductivity and the lower electrical percolation threshold. However, it has been shown that too much dispersion may be detrimental to electrical conductivity [35].

Different macromolecular structures of PEs play an important role in the dispersion of CuNWs. Both UHMWPE and HDPE are linear macromolecules with little branching that gives rise to strong intermolecular forces. However, UHMWPE has extremely long chains with molecular weight between 3 to 6 million which is almost 150~300 times higher than that of HDPE. Intermolecular force is relatively weak for each overlap of atom. Larger number of overlaps can exist along the longer linear macromolecular chains that results in stronger intermolecular force in UHMWPE than in HDPE. The longer chains of the UHMPE can also have more entanglements than the HDPE not allowing chains to intercalate between wires. Both the stronger intermolecular force and the more entanglements severely limited the dispersion of CuNWs within the UHMWPE matrix.

LDPE is highly branched and possesses short and long chains in the macromolecule; and LLDPE is essentially a linear polymer with a greater numbers of short branches. The large number of short or long chains can significantly decrease the intermolecular force by increasing the distance between the macromolecules [36], which is the main reason that the dispersion of CuNWs in LDPE and LLDPE was much better than in UHMWPE and HDPE. Moreover, the long branches of the LDPE may contribute much more to

entanglements than the short branches of the LLDPE, and thus we found better dispersion of CuNWs in the LLDPE.

It has been previously reported that the electrical percolation threshold of the carbon nanotube polymer nanocomposites was higher than the rheological percolation threshold [7, 20, 33, 37]. Lin et al also reported the higher electrical percolation threshold than the rheological percolation threshold for the CuNW/polystyrene [11] and MWNT/polycarbonate [31] nanocomposites. Gelves et al [32] reported the opposite for the functionalized CuNWs filled polystyrene nanocomposites made by solution mixing. It was also previously found [38] that the unfunctionalized CuNWs filled polystyrene nanocomposites formulated by melt mixing method showed the electrical percolation threshold between 1.0 and 2.0 vol. % of CuNWs without exhibiting rheological percolation up to CuNW concentration of 4.0 vol. %.

It has been assumed that both the poly-CNT and CNT-CNT networks contribute significantly to the rheological percolation in the carbon nanotube polymer nanocomposites [7, 20, 33], which is also the fundamental theory used to interpret the rheological percolation in CuNW/PE nanocomposites. Similarly, three types of networks can be expected in CuNW/PE nanocomposites: **Type I**: the temporary networks among polymer chains (poly-poly networks), **Type II**: the networks between polymer chains and CuNW/agglomerates (poly-NW networks) and **Type III**: the networks formed among CuNW/agglomerates (NW-NW networks). The poly-NW networks are formed by van der Waals force between PE chains and CuNWs. The strength of van der Waals force in this case

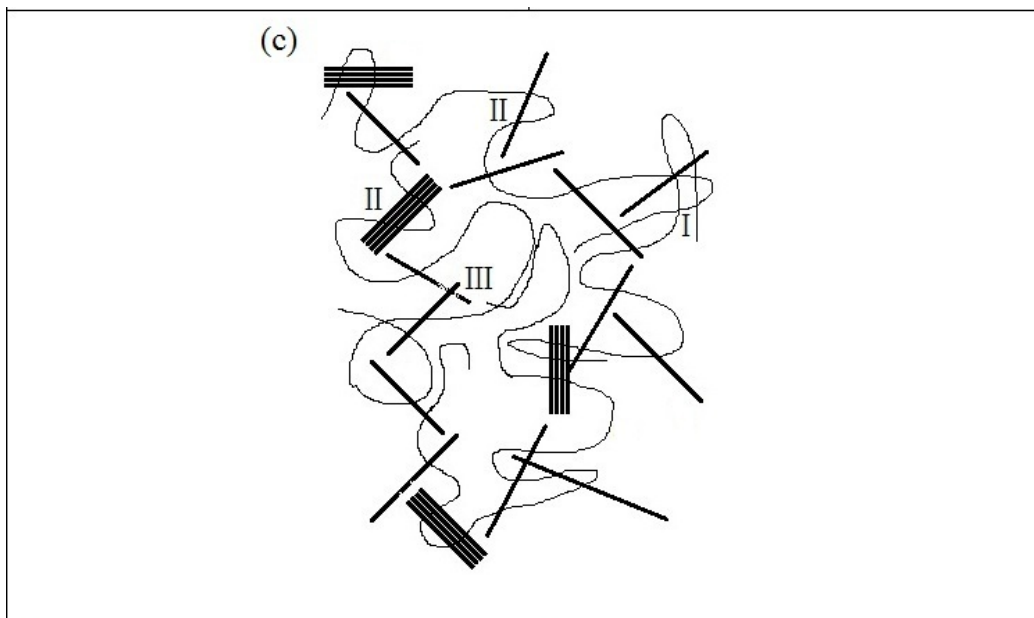
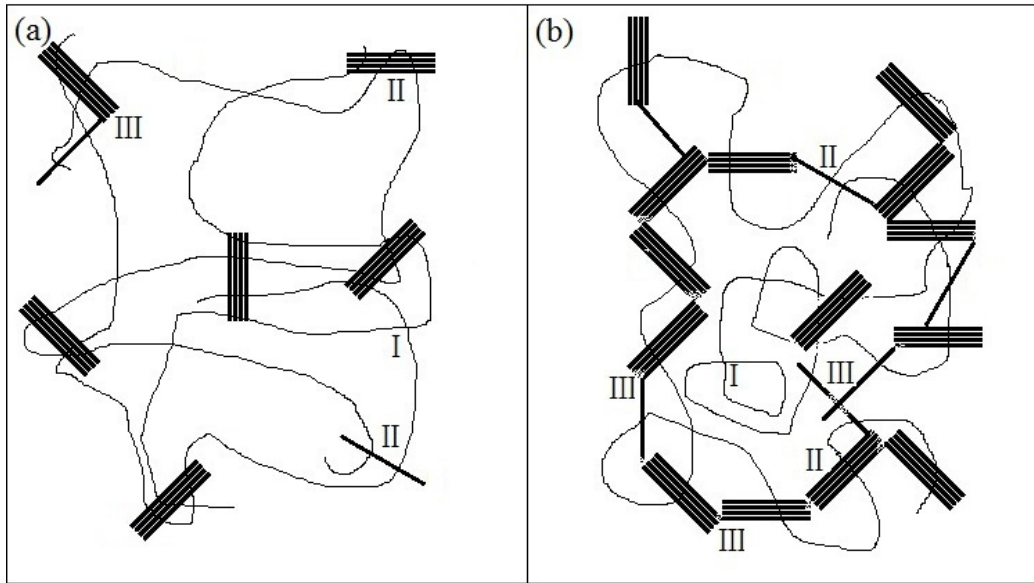
mainly depends on the distance and the number of overlapping atoms between the two components. Linear macromolecular chains without branching in both UHMWPE and HDPE allowed for the close overlapping with CuNWs to form effective poly-NW networks. However, both the LDPE and LLDPE macromolecular chains have a large number of long and/or short branches which hindered overlapping with CuNWs resulting in poor poly-NW networks within the CuNW/LDPE and CuNW/LLDPE nanocomposites.

Figure 5–11 schematically illustrates the network formation for the rheological percolation threshold and the electrical percolation threshold for the CuNW/PE nanocomposites.

The poly-NW networks within both the CuNW/UHMWPE and CuNW/HDPE nanocomposites enabled the low rheological percolation threshold at CuNW concentration of 0.5 vol. % under 200 °C. At CuNW concentration of 0.5 vol. %, the distance between the individual CuNWs (or CuNW agglomerates) in the CuNW/UHMWPE nanocomposites under room temperature was still too far for electrons to travel through. Thus, the electrical percolation threshold did not appear in the CuNW/UHMWPE nanocomposites until the distance between the individual CuNWs (or CuNW agglomerates) was small enough (5~10 nm) to allow electrons to hop and/or tunnel through [19]. This occurred at CuNW concentration of 2.0 vol. % under room temperature. Because of the better dispersion in the CuNW/HDPE nanocomposites, the distance between the individual CuNWs (or CuNW agglomerates) at CuNW concentration of 0.5 vol. %

is enough for electrons to travel through resulting in the electrical percolation threshold observed.

Due to the lack of the effective poly-NW networks, the CuNW/LDPE and CuNW/LLDPE nanocomposites cannot reach rheological percolation thresholds until the effective formation of NW-NW networks. The better dispersion resulted in the formation of NW-NW networks at lower concentration of CuNWs. Therefore, the CuNW/LDPE and CuNW/LLDPE nanocomposites reached the rheological percolation thresholds at CuNW concentrations of 4.0 vol. % and 1.0 vol. %, respectively. However, electrons can travel among individual CuNWs (or CuNW agglomerates) separated by small enough distance by the hopping and/or tunnelling mechanism before the formation of NW-NW networks. Consequently, the electrical percolation thresholds of the CuNW/LDPE and CuNW/LLDPE nanocomposites can appear at very low CuNW concentration of 0.25 vol. %.



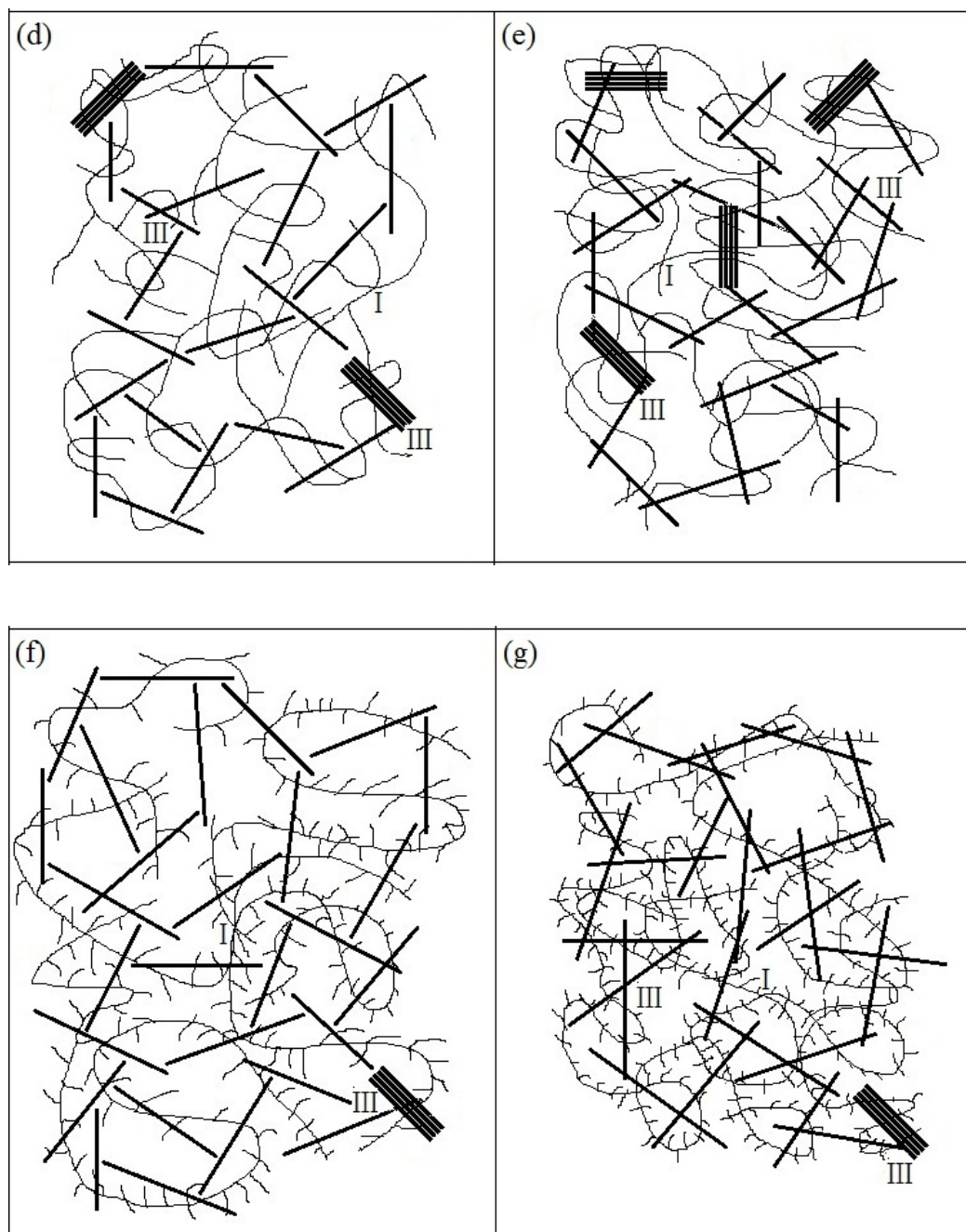


Figure 5-11. The schematic illustration of CuNW dispersion, the (a, c, e, g) rheological percolation threshold at 200 °C and (b, c, d, f) electrical percolation threshold for the (a, b) CuNW/UHMWPE, (c) CuNW/HDPE, (d, e) CuNW/LDPE and (f, g) CuNW/LLDPE nanocomposites. I represents the

networks between the polymer chains (poly-poly networks), II stands for the networks between the polymer chain and the individual CuNWs/CuNW agglomerates (poly-NW networks), III presents the networks formed among the individual CuNWs/CuNW agglomerates (NW-NW networks). II poly-NW network is absent in d, e, f and g because the branches on the chains of LDPE and LLDPE hinder its formation. The CuNW concentration in the nanocomposites increases from left to right.

5.4. Conclusions

CuNW/PE nanocomposites were prepared by the miscible solvent mixing and precipitation (MSMP) method with four different types of PEs. For CuNW/UHMWPE, CuNW/HDPE, CuNW/LDPE and CuNW/LLDPE nanocomposites, the electrical percolation thresholds were 2.0 vol. %, 0.5 vol. %, 0.25 vol. % and 0.25 vol. %, respectively, and the rheological percolation thresholds at 200 °C were 0.5 vol. %, 0.5 vol. %, 4.0 vol. % and 1.0 vol. % respectively. SEM and TEM images revealed the dispersion difference of the CuNWs in the different types of PE matrices in the order of LLDPE > LDPE > HDPE > UHMWPE, which corroborated the electrical conductivity and electrical percolation threshold difference in the four types of PE matrices

The difference in the CuNW dispersion, electrical properties and rheological properties in the four types of PE matrices resulted from the difference in the solution viscosity during the mixing, the intermolecular force, and entanglement,

which originated from the different macromolecular structures of the different types of PEs such as molecular weight and branching.

5.5. References

- [1] Sanchez C, Julian B, Belleville P, Popall M. Applications of hybrid organic–inorganic nanocomposites. *J. Mater. Chem.* 2005; 15: 3559–3592.
- [2] Njuguna J, Pielichowski K. Polymer nanocomposites for Aerospace Applications: properties. *Adv. Eng. Mater.* 2003; 5 (11): 769–778.
- [3] Caseri W. Nanocomposites of polymers and metals or semiconductors: historical background and optical properties. *Macromol. Rap. Commun.* 2000; 21 (11): 705–722.
- [4] Breuer O, Sundararaj U. Big Returns from small fibers: a review of polymer/carbon nanotube composites. *Polym. Compos.* 2004; 25 (6): 630–45.
- [5] Gelves GA, Lin B, Sundararaj U, Haber JA. Low electrical percolation threshold of silver and copper nanowires in polystyrene composites. *Adv. Funct. Mater.* 2006; 16: 2423–2430.
- [6] Yu X, Rajamani R, Stelson KA, Cui T. Carbon nanotube based transparent conductive thin films. *J. Nanosci. Nanotechnol.* 2006; 6 (7): 1939–1944.
- [7] Du F, Scogna RC, Zhou W, Brand S, Fischer JE, Winey KI. Nanotube Networks in Polymer Nanocomposites: Rheology and Electrical Conductivity. *Macromol.* 2004; 37 (24): 9048–9055.

- [8] Das NC, Maiti S. Electromagnetic interference shielding of carbon nanotube/ethylene vinyl acetate composites. *J. Mater. Sci.* 2008; 43 (6): 1920–1925.
- [9] Tibbetts GG, Lake ML, Strong KL, Rice BP. A review of the fabrication and properties of vapor-grown carbon nanofiber/polymer composites. *Compos. Sci. Technol.* 2007; 67 (7–8): 1709–1718.
- [10] Higgins BA, Brittain WJ. Polycarbonate carbon nanofiber composites. *Eur. Polym. J.* 2005; 41 (5): 889–893.
- [11] Lin B, Gelves GA, Haber JA, Sundararaj U. Electrical, rheological, and mechanical properties of polystyrene/copper nanowire nanocomposites. *Ind. Eng. Chem. Res.* 2007; 46 (8): 2481–2487.
- [12] Gelves GA, Al-Saleh MH, Sundararaj U. Highly electrically conductive and high performance EMI shielding nanowire/polymer nanocomposites by miscible mixing and precipitation. *J. Mater. Chem.* 2011; 21: 829–836.
- [13] Colbert DT. Single-wall nanotubes: a new option for conductive plastics and engineering polymers. *Plast. Addit. Compd.* 2003; 5 (1): 18–21.
- [14] Lin B, Gelves GA, Haber JA, Pötschke P, Sundararaj U. Electrical, Morphological and Rheological Study of Melt-Mixed Polystyrene/Copper Nanowire Nanocomposites. *Macromol. Mater. Eng.* 2008; 293: 631–640.
- [15] Haggenueller R, Gommans HH, Rinzler AG, Fischer JE, Winey KI. Aligned single-wall carbon nanotubes in composites by melt processing methods. *Chem. Phys. Lett.* 2000; 330: 219–225.

- [16] Pötschke P, Bhattacharyya AR, Janke A, Goering H. Melt mixing of polycarbonate/multi-wall carbon nanotube composites. *Compos. Interface* 2003; 10: 389–404.
- [17] Gojny FH, Schulte K. Functionalisation effect on the thermo-mechanical behaviour of multi-wall carbon nanotube/epoxy-composites. *Compos. Sci. Technol.* 2004; 64: 2303–2308.
- [18] Balberg I. Recent developments in continuum percolation. *Phil. Mag. B* 1987; 56(6): 991–1003.
- [19] Bunde A, Havlin S. *Fractals and Disordered Systems*, Springer, Berlin, 1996.
- [20] Pötschke P, Abdel-Goad M, Alig I, Dudkin S, Lellinger D. Rheological and dielectrical characterization of melt mixed polycarbonate-multiwalled carbon nanotube composites. *Polymer* 2004; 45 (26): 8863–8870.
- [21] Abdel-Goad M, Pötschke P. Rheological characterization of melt processed polycarbonate-multiwalled carbon nanotube composites. *J. Non-Newtonian Fluid Mech.* 2005; 128 (1): 2–6.
- [22] Valentino O, Sarno M, Rainone NG, Nobile MR, Ciambelli P, Neitzert HC, Simon GP. Influence of the polymer structure and nanotube concentration on the conductivity and rheological properties of polyethylene/CNT composites. *Physica E* 2008; 40: 2440–2445.
- [23] Miyasaka K, Watanabe K, Jojima E, Aida H, Sumita M, Ishikawa K. Electrical conductivity of carbon-polymer composites as a function of carbon content. *J. Mater. Sci.* 1982; 17 (6): 1610–1616.

[24] Sau KP, Chaki TK, Khastgir D. Carbon fibre filled conductive composites based on nitrile rubber (NBR), ethylene propylene diene rubber (EPDM) and their blend. *Polym.* 1998; 39 (25): 6461–6471.

[25] Kandasubramanian B, Gilbert M. An electroconductive filler for shielding plastics. *Macromol. Symp.* 2005; 221 (1): 185–196.

[26] F. Gubbels, R. Jerome, Ph. Teyssie, E. Vanlathem, R. Deltour, A. Calderone, V. Parente, J. L. Breads. Selective localization of carbon black in immiscible polymer blends: a useful tool To design electrical conductive composites. *Macromol.* 1994; 27: 1972–1974.

[27] Blaine RL. *Polymer Heats of Fusion*, TN 48, TA Instruments, New Castle, DE.

[28] Zhang Q, Lippits DR, Rastogi S. Dispersion and rheological aspects of SWNTs in ultrahigh molecular weight polyethylene. *Macromol.* 2006; 39: 658–666.

[29] van Gurp M, Palmen J. Time temperature superposition for polymeric blends. *Rheol. Bull.* 1998; 67: 5–8.

[30] Meincke O, Kaempfer D, Weickmann H, Friedrich C, Vathauer M, Warth H. Mechanical properties and electrical conductivity of carbon-nanotube filled polyamide-6 and its blends with acrylonitrile/butadiene/styrene. *Polymer* 2004; 45 (3): 739–748.

[31] Lin B, Sundararaj U, Pötschke P. Melt mixing of polycarbonate with multi-walled carbon nanotubes in miniature mixers. *Macromol. Mater. Eng.* 2006; 291: 227–238.

[32] Gelves GA, Lin B, Sundararaj U, Haber JA. Electrical and rheological percolation of polymer nanocomposites prepared with functionalized copper nanowires. *Nanotechnology* 2008, 19: 215712.

[33] Pötschke P, Fornes TD, Paul DR. Rheological behavior of multiwalled carbon nanotube/polycarbonate composites. *Polymer* 2002, 43 (11): 3247–3255.

[34] Meincke O, Hoffmann B, Dietrich C, Friedrich C. Viscoelastic properties of polystyrene nanocomposites based on layered silicates. *Macromol. Chem. Phys.* 2003; 204: 823–830.

[35] Lin B, Sundararaj U, Pötschke P. Melt Mixing of Polycarbonate with Multiwalled Carbon Nanotubes in Miniature Mixers. *Macromol. Mater. Eng.* 2006; 291: 227–238.

[36] Hamaker HC. The London – van der Waals attraction between spherical particles. *Physica* 1937; 4 (10): 1058–1072.

[37] Kota AK, Cipriano BH, Duesterberg MK, Gershon AL, Powell D, Raghavan SR, Bruck HA. Electrical and Rheological Percolation in Polystyrene/MWCNT Nanocomposites. *Macromolecules*, 2007, 40 (20): 7400–7406.

[38] Gelves GA, Lin B, Haber JA, Sundararaj U. Enhancing dispersion of copper nanowires in melt-mixed polystyrene composites. *J. Polym. Sci., Part B: Polym. Phys.* 2008; 46: 2064–2078.

Chapter 6

Scalable AC Electrosynthesis and Characterization of High Aspect Ratio Polycrystalline Nickel Nanowires

6.1. Introduction

NiNWs are one-dimensional nanostructures with ferromagnetic properties, which have attracted much attention in fundamental physical research decades ago [1]. Engineers are interested in the possible application of NiNWs as an ultra-high-density magnetic recording medium [1, 2].

We are very interested in the EMI shielding properties of the NiNW polymer nanocomposites. EMI shielding refers to the prevention of the electromagnetic radiation from penetration through a shield by the mechanism of reflection and adsorption [3]. The absorption loss of the electromagnetic radiation increases with the product of the electrical conductivity relative to copper (σ_r) and the relative magnetic permeability (μ_r). The electrical conductivity relative to copper (σ_r), relative magnetic permeability (μ_r) and the product of both ($\sigma_r\mu_r$) of selected metals and alloys are shown in Table 6–1 [4]. The product value ($\sigma_r\mu_r$) of Ni is 20 times higher than Cu [4]. NiNWs are both electrically conductive and ferromagnetic with high aspect ratio, which make them the promising fillers in polymer nanocomposites for EMI shielding.

Table 6-1. The electrical conductivity relative to copper (σ_r), relative magnetic permeability (μ_r) and the product of both ($\sigma_r\mu_r$) of selected metals and alloys [4].

| Materials | σ_r | μ_r | $\sigma_r\mu_r$ |
|---------------------------|------------|---------|-----------------|
| Silver | 1.05 | 1 | 1.05 |
| Copper | 1 | 1 | 1 |
| Gold | 0.7 | 1 | 0.7 |
| Aluminum | 0.61 | 1 | 0.61 |
| Brass | 0.26 | 1 | 0.26 |
| Bronze | 0.18 | 1 | 0.18 |
| Tin | 0.15 | 1 | 0.15 |
| Lead | 0.08 | 1 | 0.08 |
| Nickel | 0.2 | 100 | 20 |
| Stainless Steel 430 | 0.02 | 500 | 10 |
| Mumetal (at 1 kHz) | 0.03 | 20,000 | 600 |
| Superpermalloy (at 1 kHz) | 0.03 | 100,000 | 3,000 |

PAO template-assisted synthesis of nanoscopic materials as a versatile and less expensive approach has been discussed and applied for the CuNW synthesis in Chapters 1 and 2 respectively. The size and structural properties of the electrodeposited nanomaterials can be controlled by the templates and the electrodeposition parameters [5]. The typical conditions to obtain self-ordered pores of different dimensions in polyprotic acids are shown in Table 6–2 [6].

Table 6-2. The typical conditions to obtain self-ordered pores of different dimensions in polyprotic acids [6].

| Polyprotic acid | Electrolyte | | Anodization | | Pore diameter (nm) | Inner wall thickness (nm) | Interpore distance (nm) | Porosity |
|--------------------------------|---------------|--|----------------|--|--------------------|---------------------------|-------------------------|----------|
| | Concentration | | DC voltage (V) | | | | | |
| H ₂ SO ₄ | 0.3 mol/L | | 25 | | 24 | 7.2 | 66.3 | 12 |
| (COOH) ₂ | 0.3 mol/L | | 40 | | 31 | 9.1 | 105 | 8 |
| H ₃ PO ₄ | 0.1 mol/L | | 195 | | 158.4 | 54 | 501 | 9 |

The barrier layer formed during the anodization in certain polyprotic acid can be thinned by stepwise decreasing the DC voltage at the end of anodization as described in Chapter 1. Both the proper thickness and the rectification properties of the barrier layer facilitate the AC electrodeposition of Ni into the PAO templates to generate NiNWs.

In this work, we used a scalable AC electrodeposition method to synthesize NiNWs in PAO templates, which were then liberated, characterized and dispersed into LLDPE to prepare electrically conductive polymer nanocomposites.

6.2. Experimental

6.2.1. Preparation of PAO templates

The PAO templates used for AC electrodeposition were prepared by the two-step anodization method [7] using 0.3 mol/L oxalic acid ($\geq 97.0\%$, Sigma Aldrich) as the electrolyte under DC anodization voltage of 40 V. Five aluminum plates and six copper plates, cut into 5×11 cm pieces, were used as the anodes and cathodes respectively. All the electrodes were placed alternately in parallel with inter-plate distance of 1.5 cm into 3.0 L 0.3 mol/L oxalic acid aqueous solution, and anodized at $0\sim 4$ °C in a double walled, chilled cylindrical glass container as shown in Figure 6–1. At the end of the second anodization, the DC voltage was decreased from 40.0 V to 10.0 V at 2 V/min rate and held for 10 min at 10.0 V to thin the barrier layer between the PAO templates and the Al

substrate. All other details not described in this section are identical to those in Section 2.2.1.

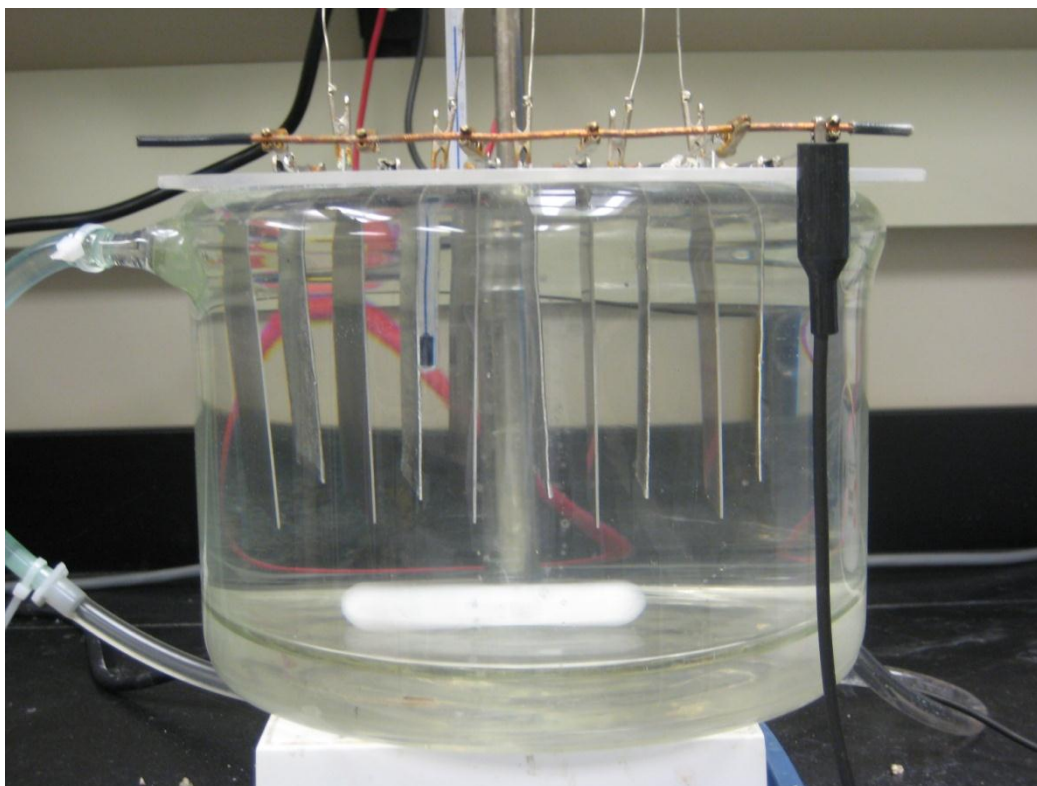


Figure 6-1. The photograph of the anodization setup in a double-walled, chilled cylindrical glass container.

6.2.2. AC electrodeposition of Ni into the PAO templates and the liberation of the deposited NiNWs

The aqueous solution for the electrodeposition was formulated with 300 g/L $\text{NiSO}_4 \cdot 6\text{H}_2\text{O}$ (98%, Alfa Aesar), 40 g/L H_3BO_3 (99.5% min., EMD Millipore) and 8 mg/L SDS. H_3BO_3 functioned as a PH buffer. The surfactant sodium dodecyl sulfate facilitated the penetration of the electrodeposition solution into

the pores in the PAO templates and the removal of the H₂ bubbles produced on the surface of the electrodes during the electrodeposition.

AC electrodeposition was carried out at 40 °C. The higher temperature can increase the electrical conductivity of the electrolyte and decrease the electrodeposition voltage. In addition, the increased temperature can prevent the components in the solution from precipitation. The edges of the Al plates with grown PAO templates were coated with nail polish to prevent the preferential deposition of Ni there. Two Ni foils (1.0 mm thick, 99.5%, Alfa Aesar) of 5 cm × 10 cm size were used as the counter electrodes. Ni was deposited into the pores in the both sides of each Al electrode by continuous 200 Hz sine wave AC of 20 V_{rms} for 7 min with a Kepco BOP 50–20 MG AC power supply. The AC electrodeposition conditions and solution composition were summarized in Table 6–3. The details not described in this section are identical to those in Sections 2.2.2 and 2.2.3.

Table 6-3. The AC electrodeposition conditions and solution composition.

| Electrodeposition Solution | | | Electrodeposition power | | |
|-------------------------------------|---------------|-------------|-------------------------|---------------------|-----------|
| Chemicals | Concentration | Temperature | Wave | Voltage | Frequency |
| NiSO ₄ 6H ₂ O | 300 g/L | | | | |
| H ₃ BO ₃ | 40 g/L | 40 °C | Sine | 20 V _{rms} | 200 Hz |
| SDS | 8 mg/L | | | | |

6.2.3. Preparation of NiNW/LLDPE nanocomposites

The NiNW/LLDPE nanocomposites with different concentrations of NiNWs were prepared by the MSMP method as described in Section 5.2.3. LLDPE (LL 6201.19) were kindly provided by ExxonMobil with the technical details listed in Table 5–1. The density of bulk nickel (8.91 g/cm^3) was used to determine the volume percentages of the NiNWs in the LLDPE matrix. The dry powder of the NiNW/LLDPE nanocomposites was compression molded under $250 \text{ }^\circ\text{C}$ and 138 MPa for 30 min in a 10.5 mm diameter and 1.2 mm thick stainless steel mold as described in Section 5.2.3 before characterization.

6.2.4. SEM characterization of the aluminum plates, the liberated NiNWs and the NiNW/LLDPE nanocomposites

The aluminum plates before and after anodized in oxalic acid and the preparation of the NiNW samples for SEM imaging were detailed in Section 2.2.6.

The length distribution of the NiNWs dispersed in methanol was determined from the SEM images collected from the areas of the glass cover with well-dispersed NiNWs. The lengths of over 1000 individual NiNWs were measured with ImageJ 1.44p software (National Institute of Health, USA).

The NiNW/LLDPE nanocomposites were fractured in liquid nitrogen and coated with gold and palladium to collect the backscattered SEM images. All the

SEM images were collected using a Philips XL30 scanning electron microscope under 20 kV accelerating voltage.

6.2.5. TEM/EDX/SAED characterization of the liberated NiNWs and the NiNW/LLDPE nanocomposites

The TEM images, selected area electron diffraction (SAED) pattern and EDX spectra of the liberated NiNWs were collected with a Tecnai F20 field emission gun TEM under 200 kV accelerating voltage. The sample of the liberated NiNWs was prepared by dropping the NiNW/CH₃OH dispersion very dilute onto a holey carbon coated Cu TEM grid. The NiNW/LLDPE nanocomposite samples were ultramicrotomed under -130 °C with an ultracut diamond knife to obtain desired cross sections with thickness about 100 nm. The ultramicrotomed slice was then transferred onto a holey copper TEM grid for observation.

6.2.6. XRD and XPS characterization of the NiNW powder

The XRD patterns of the NiNW powder were collected by a Rigaku Multiflex Diffraction System with Cu K α radiation operating at 40 kV and 20 mA. The NiNW powder was prepared by drying the NiNW/CH₃OH dispersion in a vacuum oven under room temperature.

The XPS were collected with a PHI VersaProbe 5000-XPS spectrometer with the K α X-rays from an Al source operating at 25 mV. The base pressure of the

XPS spectrometer was around 8×10^{-8} Pa. The NiNW sample for XPS characterization was prepared by sticking the NiNW powder onto an aluminum stub with a double-sided carbon tape on the surface.

6.2.7. TGA of the NiNW powder

The TGA plots of the NiNW powder were obtained with a TA Q500 TGA instrument using a standard Pt pan. The balance gas for the test was always 40 mL/min N₂ (Praxair). 60 mL/min air (Praxair) was used as the purge gas to acquire the TGA plot in air at 20 °C/min heating rate. 60 mL/min 4% H₂ balance N₂ (Praxair) was used as the purge gas to obtain the TGA plot in H₂ at 20 °C/min heating rate.

6.2.8. Ferromagnetic properties of the NiNW powder

The same TA Q500 TGA instrument was used to determine the Curie temperature (T_C) of the NiNW powder. The balance gas and purge gas were 40 mL/min N₂ and 60 mL/min N₂, respectively. A bar permanent magnet was positioned under the furnace to apply a magnetism to attract the NiNW sample in the Pt pan during the test. The instrument temperature was programmed to heat up to 700 °C and cool down to 100 °C at 10 °C/min rate.

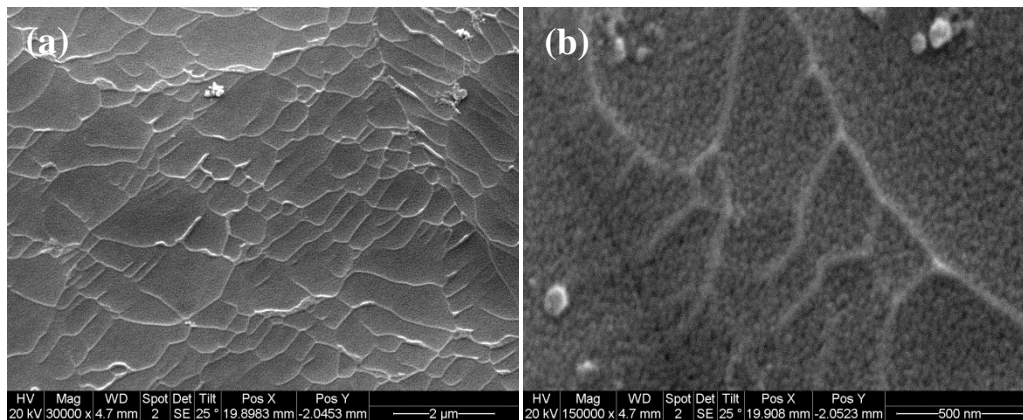
6.2.9. Electrical characterization of the NiNW/LLDPE nanocomposites

The electrical resistivity of the CuNW/LLDPE nanocomposites was measured by two different instruments as described in Section 4.2.4. A QPP four pin probe (MCP-TPQPP model, Mitsubishi Chemical Co., Japan) with inter-pin distance 1.5 mm was connected to the Loresta GP resistivity meter (MCP-T610 model, Mitsubishi Chemical Co., Japan) to measure the nanocomposites with resistivity lower than $10^4 \Omega \cdot \text{m}$.

6.3. Results and discussion

6.3.1. Surface morphology evolvement of the aluminum plate during the anodization in oxalic acid solution

The surface morphology evolvement of the aluminum plate during the anodization in oxalic acid solution is shown in Figure 6–2. The surface morphology of the bare aluminum plate after fully cleaning with acetone and 1 mol/L NaOH aqueous solution is shown in Figures 2–8a and b.



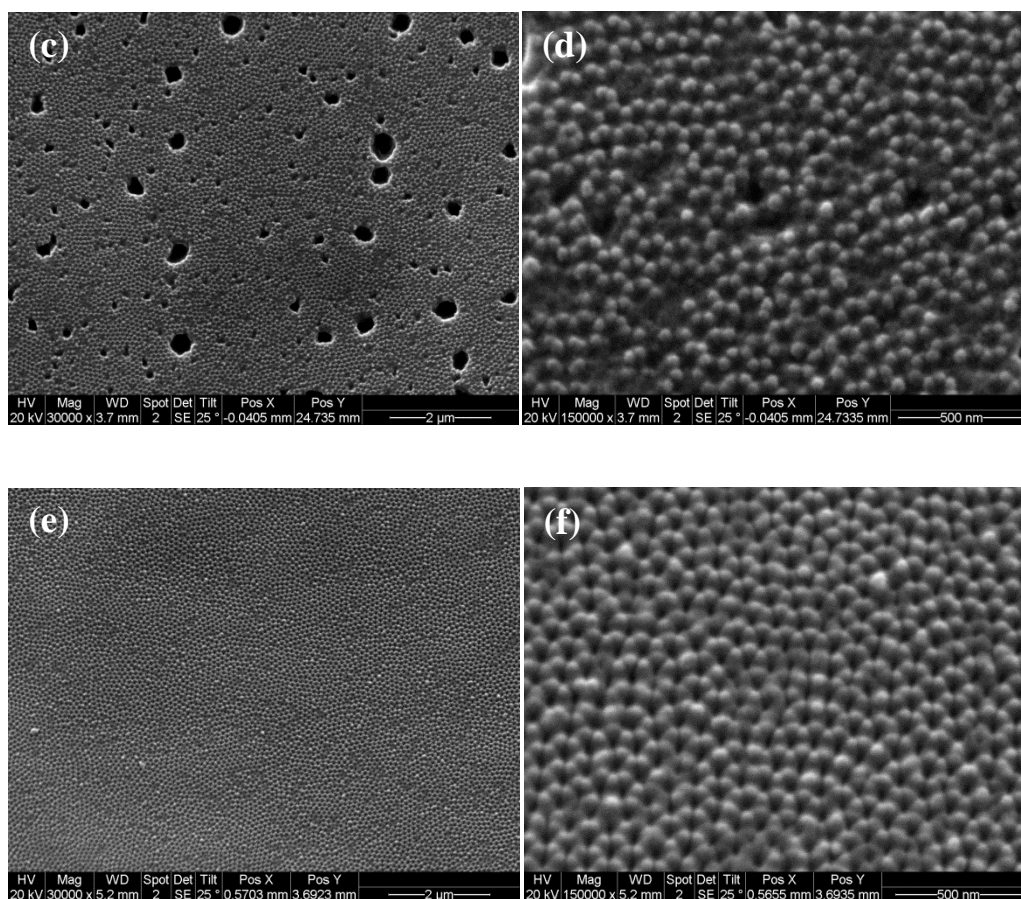


Figure 6-2. Surface morphology development of the aluminum plate during the anodization: (a, b) after anodized in 0.3 mol/L oxalic acid for 2 h, (c, d) after etched in the solution of 0.1 mol/L H_2CrO_4 and 0.3 mol/L H_3PO_4 under 60 °C for 30 min, (e, f) after anodized in 0.3 mol/L oxalic acid for 8 h.

After the anodization in 0.3 mol/L oxalic acid solution for 2 h, some loose floccule can be observed in the SEM images (Figures 6–2a and b). The surface of the aluminum plate looked clean with some shallow patterns of pores as well as a few scattered bigger and deeper holes (Figures 6–2c and d) formed by the

corrosive effect of the etching solution after etched in the solution of 0.1 mol/L H_2CrO_4 and 0.3 mol/L H_3PO_4 under 60 °C for 30 min. The clear self-ordered pores formed after the second anodization for 8 h are shown in Figures 6–2e and f. The surface morphology evolution of the aluminum plate during the anodization in oxalic acid solution is very similar to that in H_2SO_4 solution as described in Section 2.3.1

6.3.2. Morphology and aspect ratio of the liberated NiNWs

The low magnification and high magnification SEM images of the liberated NiNWs are shown in Figure 6–3. The NiNWs exhibited very uniform diameter of ca. 38 nm, the estimated length of most of the individual NiNWs ranged from 1 to 4 μm . Some aggregates of the NiNWs were also observed, which can be attributed to the high surface area of the NiNWs. In both images, the surface of the cylindrical NiNWs looked clean and smooth.

The SEM image with well-dispersed NiNWs used for the length distribution determination is shown in Figure 6–4a, and the length distribution of the NiNWs is shown in Figure 6–4b. The length of over 96% of the NiNWs ranged from 0.6 to 6 μm . The NiNWs with length between 2–3 μm accounted for over 30%. The average length of the NiNWs after liberation in NaOH and ultrasonication in methanol was 2.68 μm .

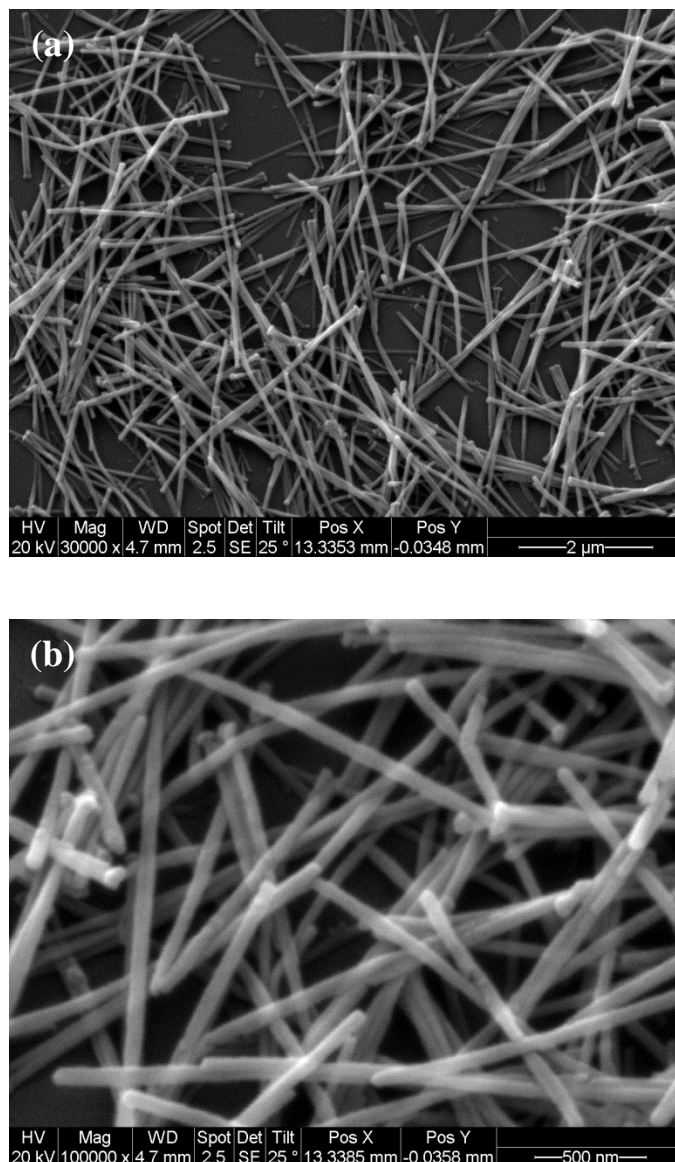


Figure 6-3. The (a) low magnification and (b) high magnification (b) SEM images of the liberated NiNWs.

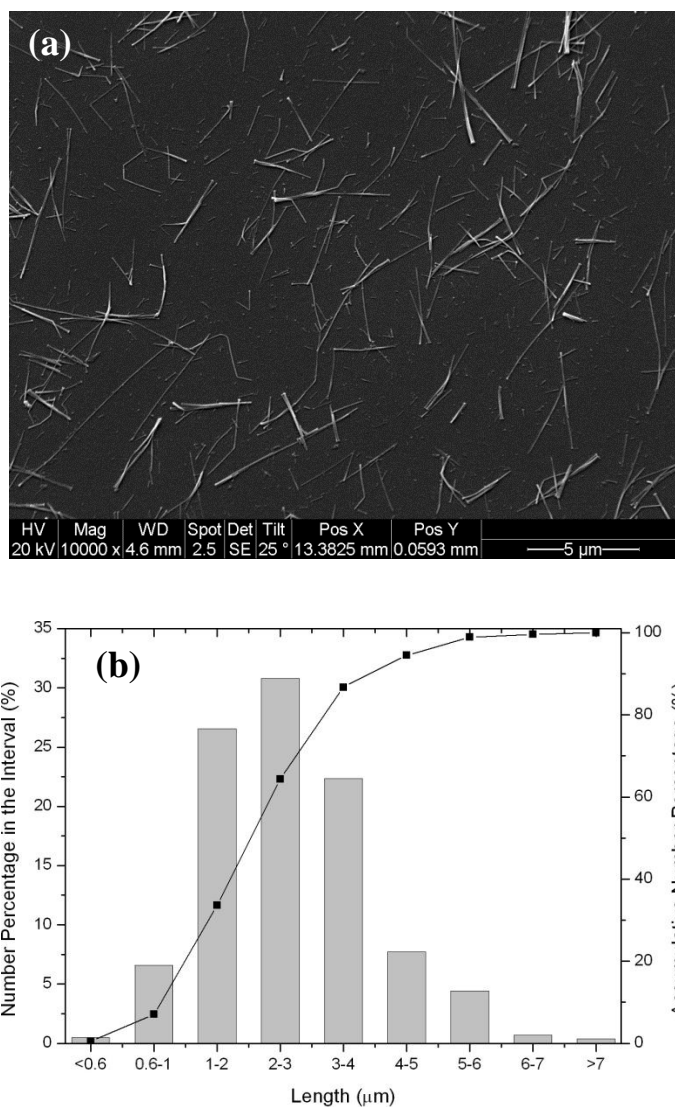


Figure 6-4. The (a) SEM image with well-dispersed NiNWs used for length distribution determination and the (b) length distribution of the NiNWs.

The low magnification and high magnification TEM images of the liberated NiNWs are shown in Figures 6–5a and b, respectively. In the low magnification image, the NiNWs appeared uniform in diameter, but a little fluctuation in diameter can be observed in the high magnification image. The measured

diameter of the NiNWs in both TEM images was 38 ± 4 nm which was consistent with the diameter measured in the SEM image. Based on the average length $2.68 \mu\text{m}$ and the diameter measured in the TEM images, the average aspect ratio of the NiNWs after liberation and ultrasonication was around 70.

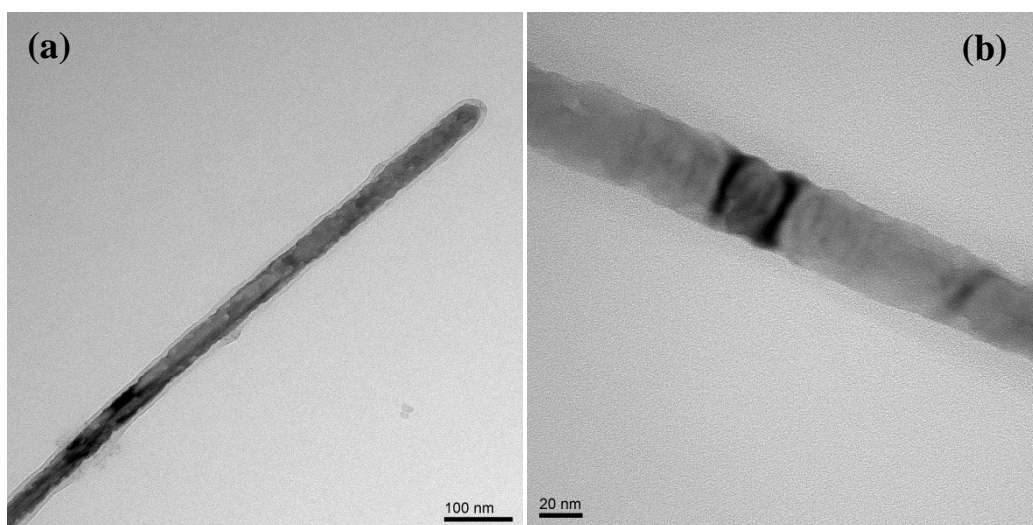


Figure 6-5. The low magnification (a) and high magnification (b) TEM images of liberated NiNWs.

6.3.3. Chemistry and crystal structure of liberated NiNWs

The EDX spectra and the SAED pattern collected with the TEM are shown in Figures 6–6 and 6–7, respectively. The C and Cu peaks in the EDX spectra originated from the holey carbon coated Cu TEM grid. Four Ni peaks can be identified in the EDX spectra. Specifically, they were Ni-L α , Ni-L β , Ni-K α and Ni-K β with increasing bonding energies.

The polycrystalline property of the AC electrosynthesized NiNWs is revealed in the SAED pattern. The smallest 3 rings in the SAED pattern have diameters of 9.86 1/nm, 11.35 1/nm and 16.13 1/nm, respectively, corresponding to plane distances of 0.203 nm, 0.176 nm and 0.124 nm that is consistent with the indices 111, 200 and 220 of fcc nickel [8].

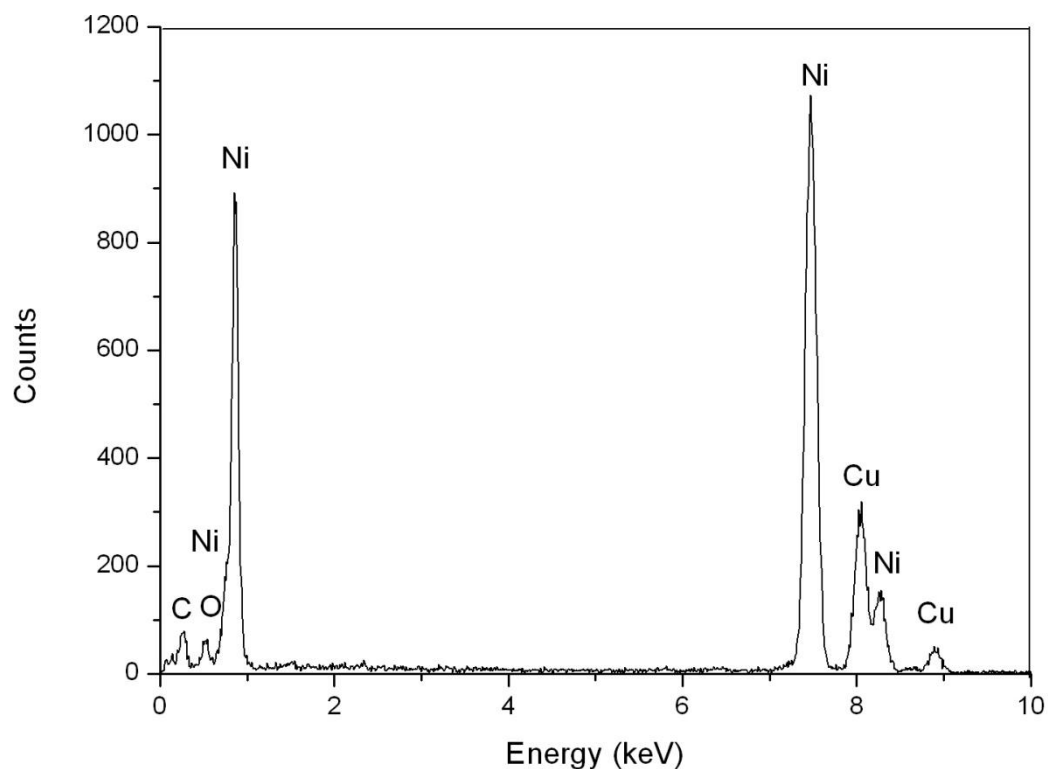


Figure 6-6. The EDX spectra of the NiNW powder collected with TEM.

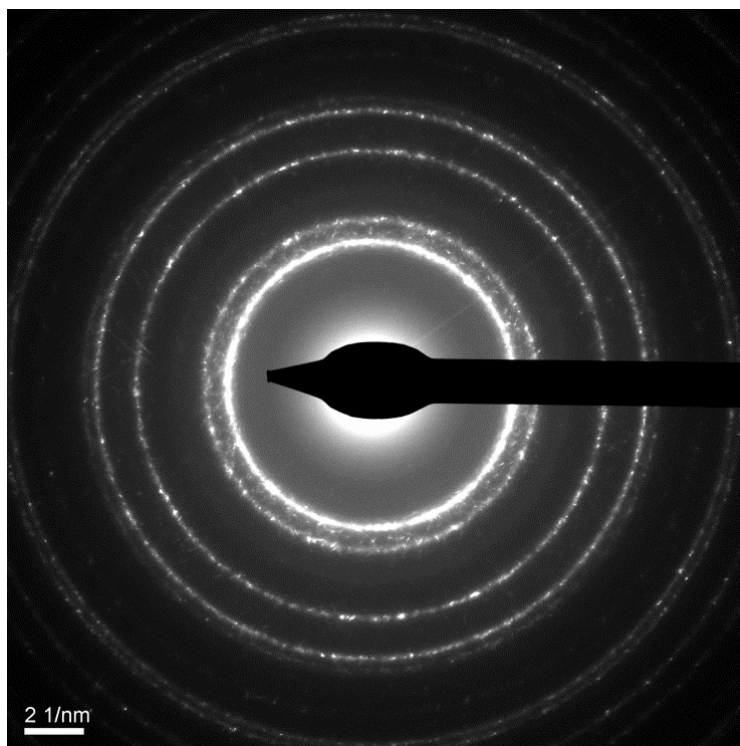


Figure 6-7. The SAED pattern of the NiNW powder collected with TEM.

The XRD pattern of the NiNW powder is shown in Figure 6–8. The three sharp peaks of the fcc crystal structure of metal nickel can be clearly identified at two theta of 44.49, 51.85 and 76.38 corresponding to the planes of (111), (200) and (220), respectively (PDF# 65-2865) as labeled in Figure 6–8. The small peaks of NiO can also be identified as marked on the XRD pattern (PDF# 47-1049). Ni₂O₃ was not detected by XRD. The d-spacings of the corresponding planes of fcc metal nickel determined from the SAED and XRD patterns are shown in Table 6–4 for comparison. The d-spacings of the corresponding planes of fcc nickel determined from both test methods are consistent.

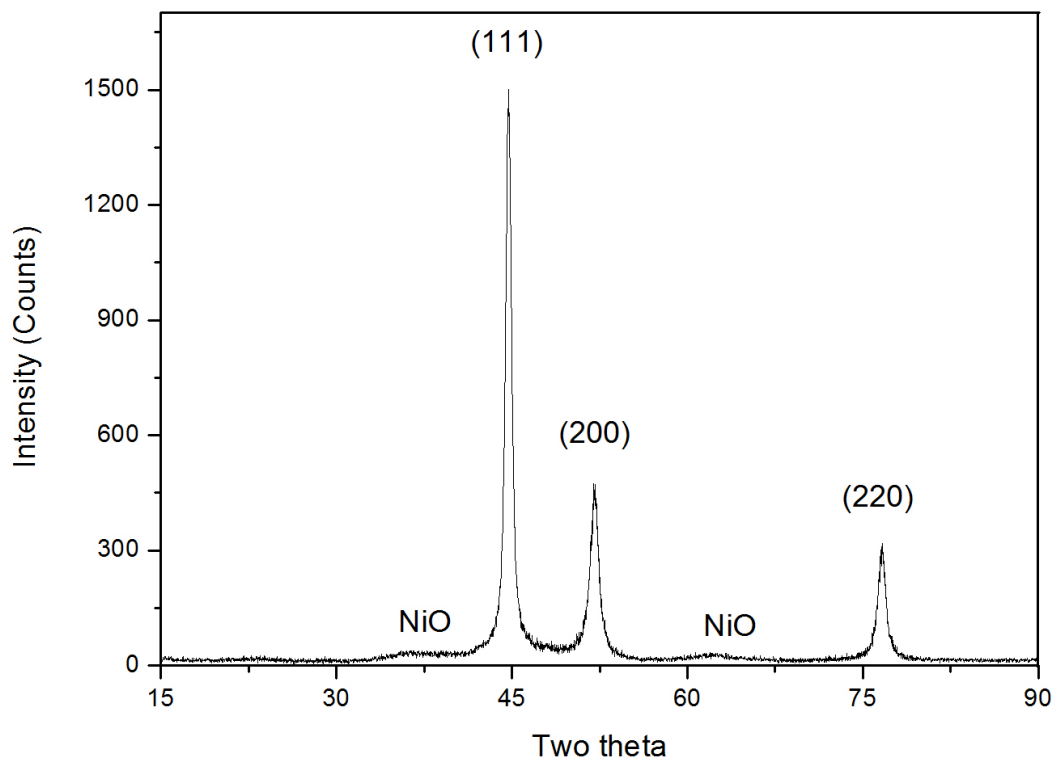


Figure 6-8. The XRD pattern of the NiNW powder.

Table 6-4. The d-spacings of the corresponding planes of fcc metal nickel determined from the SAED and XRD patterns.

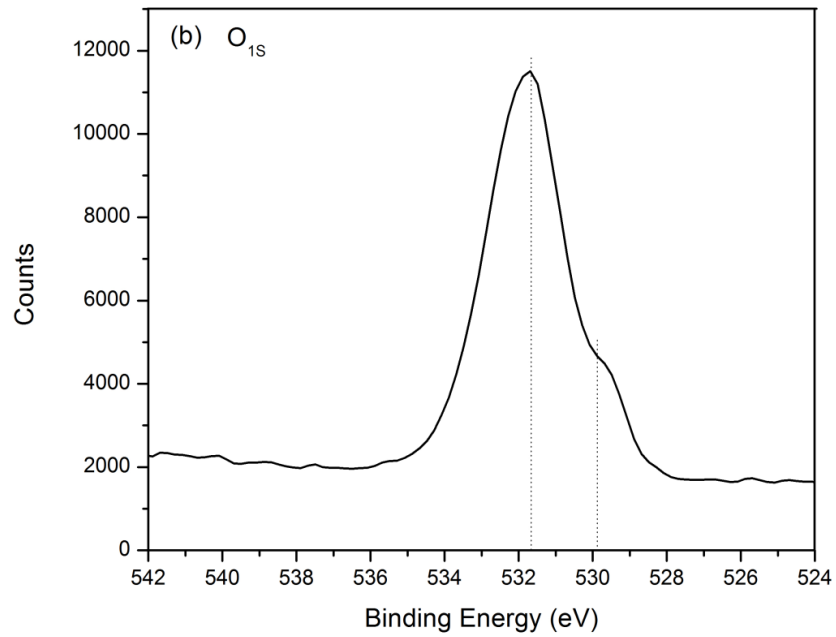
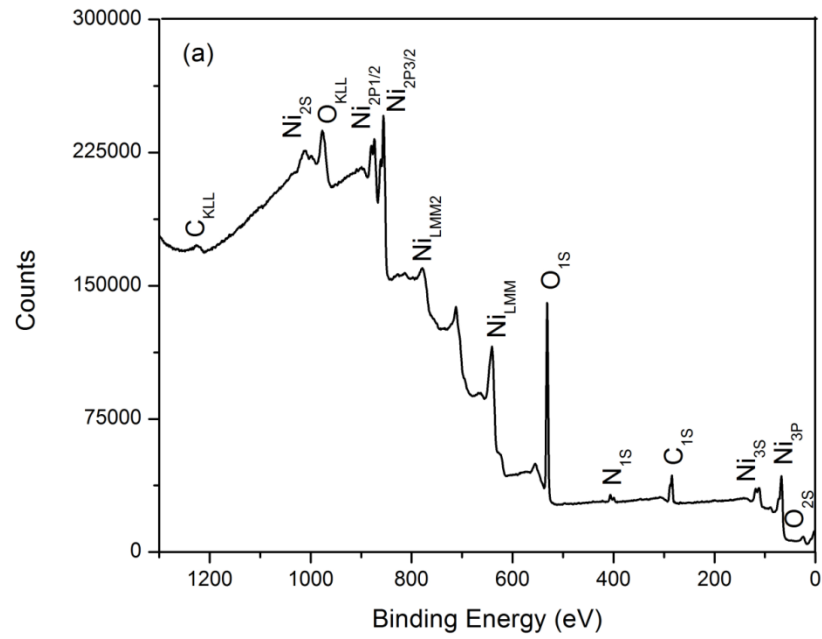
| (hkl) | SAED | | XRD | |
|-------|----------------------|-------|-----------|-------|
| | Ring diameter (1/nm) | d (Å) | Two theta | d (Å) |
| (111) | 9.86 | 2.03 | 44.49 | 2.03 |
| (200) | 11.35 | 1.76 | 51.85 | 1.76 |
| (220) | 16.13 | 1.24 | 76.38 | 1.25 |

Figure 6–9 shows the X-ray photoelectron spectra of the NiNW powder. The survey spectra, high resolution spectra of O 1S and Ni 2P peaks are shown in Figures 6–9a, b and c, respectively. Table 6–5 shows the X-ray photoelectron binding energies of metal nickel and oxides [9], which can help to identify the different nickel species in the XP spectra.

The peaks of Ni, O and C can be identified on the survey spectra. The O peaks may originate from the oxide species in the sample or the O₂ absorbed on the surface. The C signals can be attributed to the carbon tape used to stick the NiNW powder on the aluminum stub. The survey spectra showed that the NiNW powder was pretty clean with no impurity above the detection limit of XPS.

The X-ray photoelectron spectra binding energies of O 1S are 529.9 eV and 531.7 eV for NiO and Ni₂O₃, respectively, which can be readily used to identify the oxide species in the NiNW sample. As shown in Figure 6–9b, the main peak at 531.7 eV and a shoulder at 529.9 eV indicated the presence of both Ni₂O₃ and NiO species.

The X-ray photoelectron spectra of Ni 2P_{3/2} can be used to distinguish metal Ni from its oxides. The peak with bonding energy of 852.9 eV in Figure 6–9c indicated the presence of metal Ni in the sample. However, it is impossible to distinguish the oxide species in the high resolution spectra of Ni 2P_{3/2}. The peaks at 856.1 eV and 861.5 eV may originate from either or both of NiO and Ni₂O₃ species.



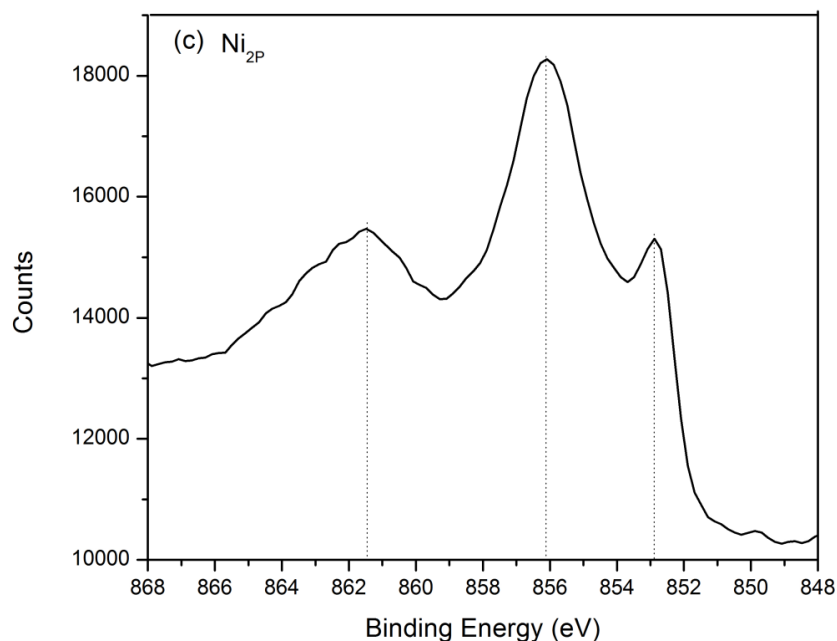


Figure 6-9. The X-ray photoelectron spectra of the NiNW powder. (a) The surveys, (b) the high resolution XP spectra of O 1S peak and (c) the high resolution XP spectra of Ni 2P_{3/2} peak.

That Ni₂O₃ was not detected by XRD but identified on the XP high resolution spectra of O 1S may result from the low concentration of Ni₂O₃ below the detect limit of XRD and/or its amorphous existence in the powder sample.

Table 6-5. The X-ray photoelectron binding energies (eV) of metal nickel and its oxides [9].

| Species | Ni 2P _{3/2} | O 1S |
|--------------------------------|----------------------|-------|
| Ni | 852.9 | |
| | 858.8 | |
| NiO | 854.5 | 529.9 |
| | 856.3 | |
| | 861.7 | |
| Ni ₂ O ₃ | 855.8 | 531.7 |
| | 861.4 | |

6.3.4. TGA of the NiNW powder

Figure 6–10 shows the TGA plot of the NiNW powder heated up to 600 °C in air. The weight gain onset point of the NiNWs powder was about 320 °C. The maximum rate of weight gain appeared at 374 °C. The overall weight gain till 600 °C based on the lowest weight point 97.5% on the plot was 17.76%.

The TGA plot of the NiNW powder reduced in H₂ is shown in Figure 6–11. The onset point of the reduction reaction of the NiNW powder in 4% H₂ was 144.4 °C. The maximum rate of weight loss appeared at 151.7 °C. The total weight loss excluding the volatile components during the reduction was 7.32%.

It can be determined that the NiNW powder comprised around 92.7 wt. % Ni and 7.3 wt. % O elements, assuming the oxidation product at 600 °C was stoichiometrical NiO (Ni_2O_3 is not stable at this temperature) and the reduction product at 700 °C was metal nickel. The high weight percentage of O in the sample resulted from the high specific surface area and the high oxidation reactivity of the NiNWs.

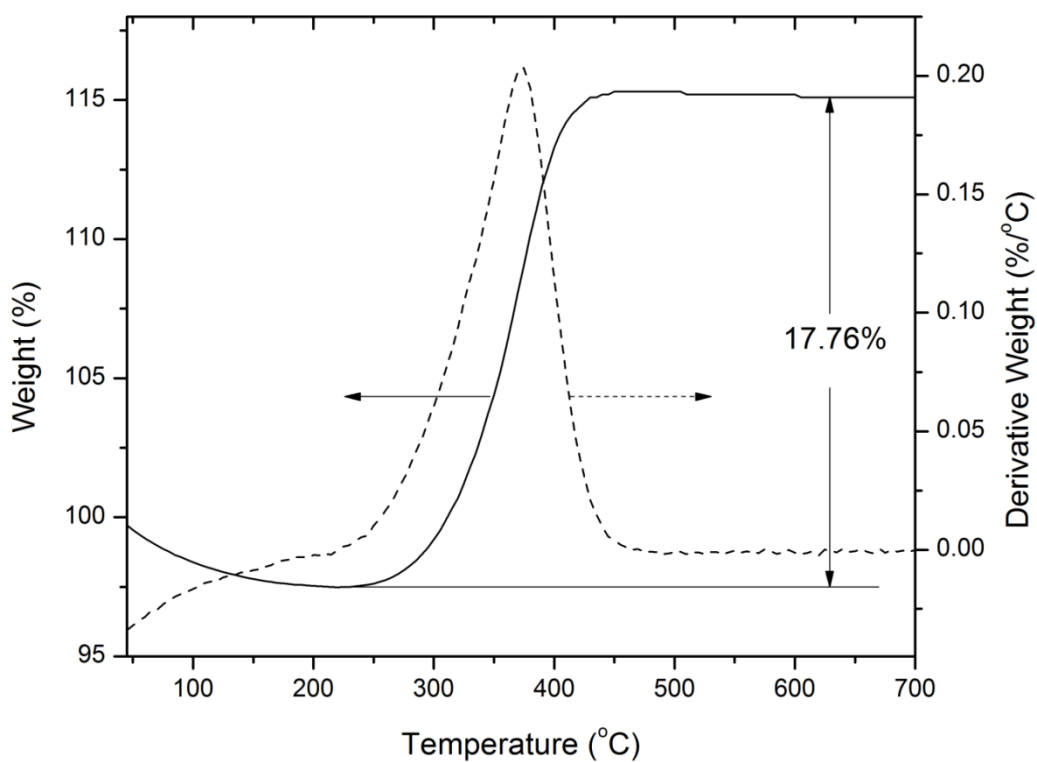


Figure 6-10. The TGA plot of the NiNW powder heated up to 600 °C at 10 °C/min rate in air.

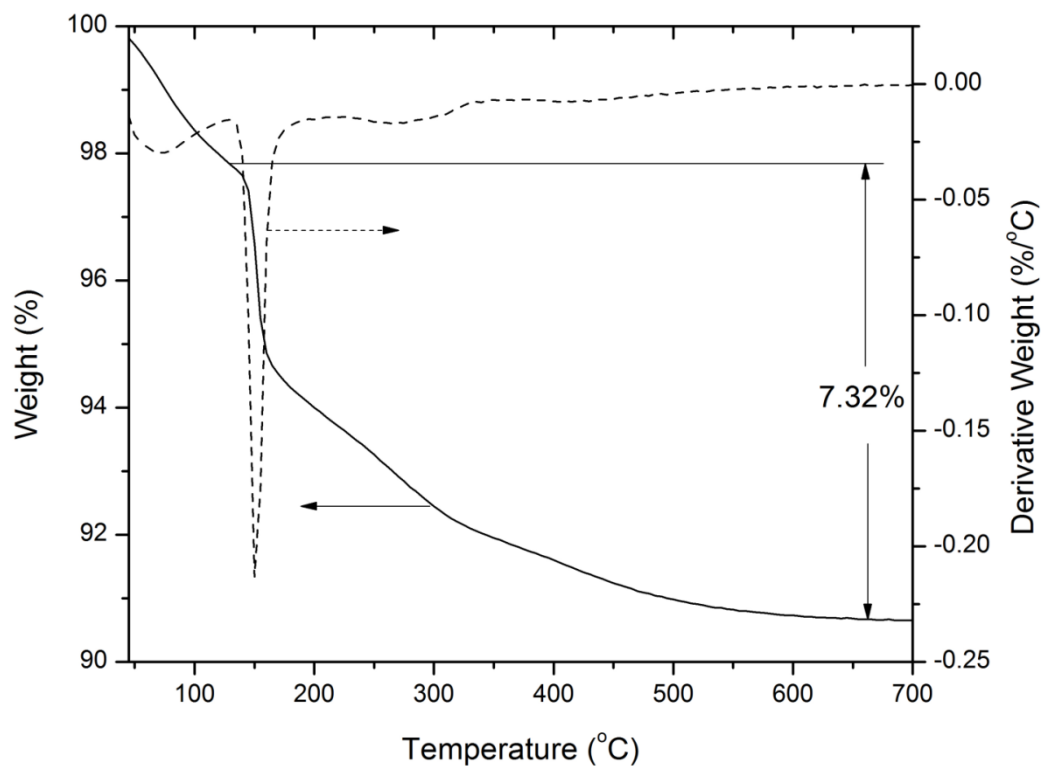


Figure 6-11. The TGA plot of the NiNW powder heated up to 800 °C at 10 °C/min rate in 4% H₂.

6.3.5. Ferromagnetic properties of the NiNW powder

The NiNWs dispersed in methanol can be manipulated by a magnetic field. Figure 6–12 shows the photograph of the NiNWs dispersed in methanol attracted to one side of the vial by a bar permanent magnet.

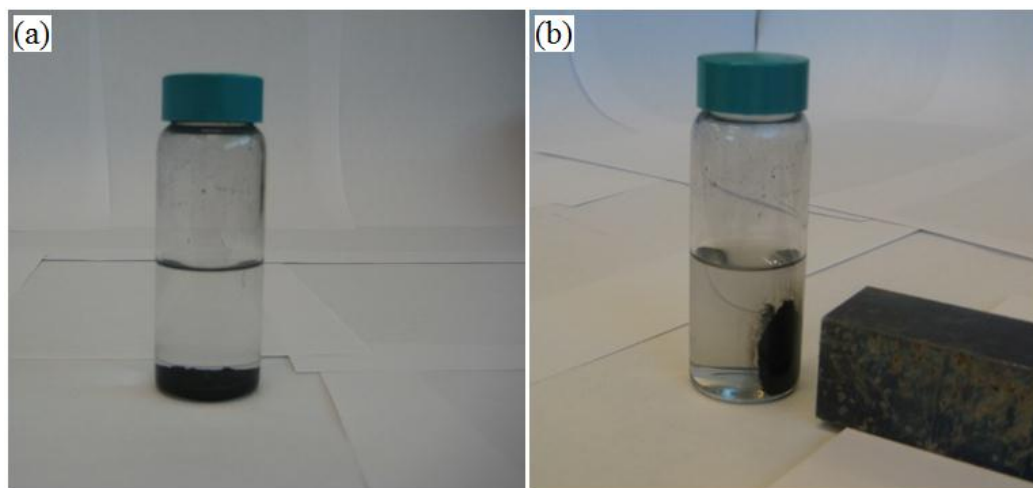


Figure 6-12. The photographs of (a) the NiNWs staying on the bottom in methanol and (b) the NiNWs attracted to one side of the vial by a bar permanent magnet.

The TGA plot used for determination of the Curie temperature and ferromagnetism reversibility of the NiNW powder is shown in Figure 6–13. The Curie temperature of the NiNW powder appeared at 343.6 °C. There was a sharp peak just before the Curie temperature in the plot with a vertex at 330.3 °C which was explained by C. Kittel that the magnetic susceptibility approaches infinity as the temperature approaches T_C [10]. The NiNWs transformed its ferromagnetism to paramagnetism at the Curie temperature of 343.6 °C during the heating cycle and regained its ferromagnetism at 345.2 °C during the cooling cycle. The Curie temperature of bulk Ni with purity ≥ 99.99 mol % at 358.28 ± 0.4 °C has been reported [11]. In this study, the Curie temperature of the NiNWs powder was around 14 °C lower than the reported value of the bulk nickel, which can be

attributed to the impurity in the NiNWs and the sub-micron grained nature of the NiNWs [11, 12]. R. Z. Valiev et al [12] interpreted that ferromagnetic materials with grain size smaller than a certain critical value at temperature below the Curie temperature of the bulk material actually include two phases: one is the ferromagnetic grain phase with bulk material Curie temperature, the other one is the paramagnetic grain boundary phase with a considerably lower Curie temperature. If the grain size is small enough, the transformation from the ferromagnetic grain phase to the paramagnetic grain boundary phase can take place at temperature much lower than the Curie temperature of the bulk material, which leads to the lower Curie temperature of the given sub-micron grained material than the same bulk material.

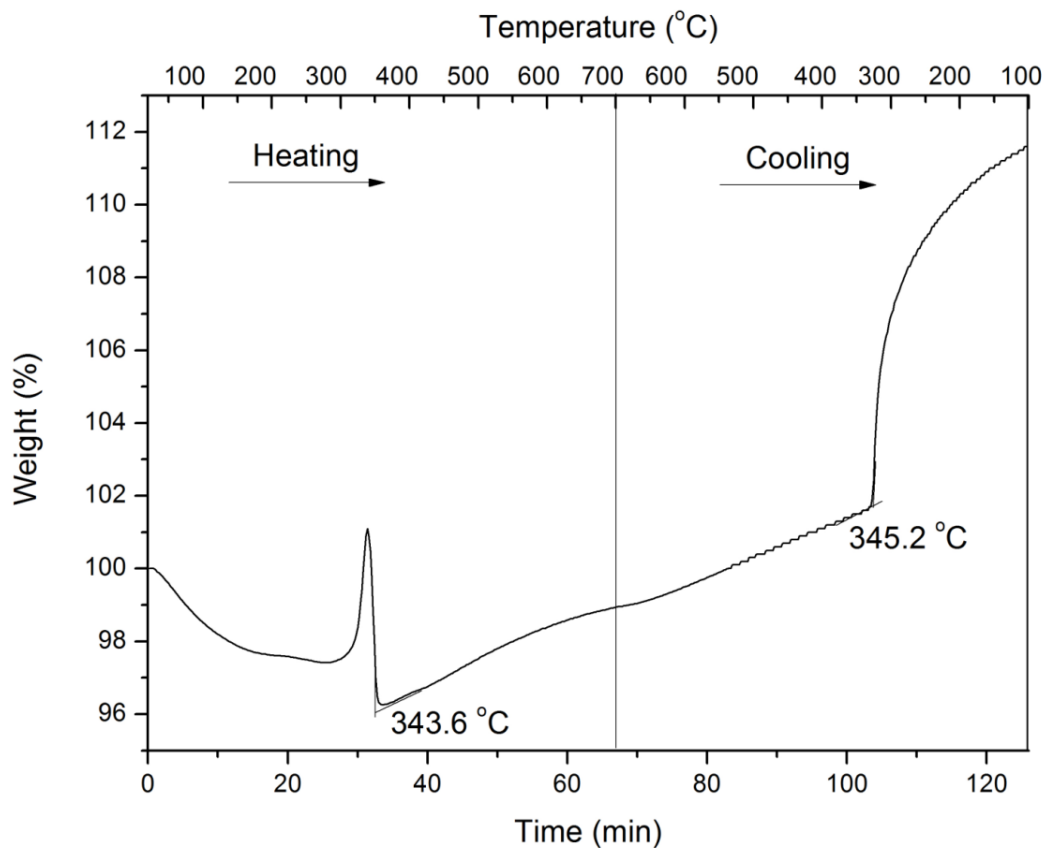


Figure 6-13. The TGA plot for the determination of the Curie temperature and ferromagnetism reversibility of the NiNW powder.

6.3.6. Electrical resistivity of the NiNW/LLDPE nanocomposites and the dispersion of NiNWs

Electrical conductivity of polymer nanocomposites mainly depends on the type and volume fraction, distribution, dispersion, aspect ratio and surface properties of the conductive nanofillers, polymer matrix as well as the conditions of processing. Figure 6–14a shows the electrical conductivity of the NiNW/LLDPE nanocomposites as a function of the volume fraction of the

NiNWs, which exhibited the typical percolation behavior. The electrical conductivity of the NiNW/LLDPE nanocomposites with NiNW volume fraction below 0.005 was close to that of the neat LLDPE matrix. However, a remarkable increase of over 12 orders of magnitude in the electrical conductivity can be observed when the volume fraction of NiNWs in the nanocomposites increased from 0.005 to 0.0075, which indicated the formation of the pathway for electrical conduction in the NiNW/LLDPE nanocomposites. Based on the electrical conductivity change with the volume fraction of the NiNWs in the nanocomposites, the electrical percolation threshold of the NiNW/LLDPE nanocomposites was at NiNW volume fraction of 0.005. An increase in the NiNW volume fraction from 0.0075 to 0.03 led to a gradual increase in the electrical conductivity of the NiNW/LLDPE nanocomposites from 6×10^{-2} S/m to 28.3 S/m.

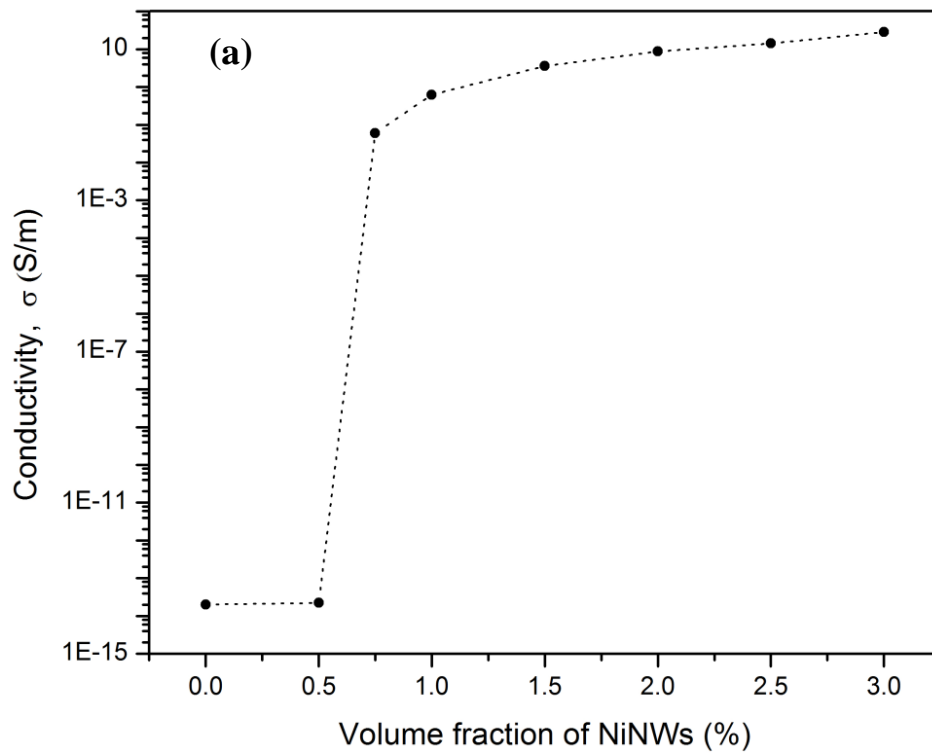
The percolation theory can be applied to interpret the behavior of the composites with non-conducting matrix and conductive fillers [13–15]. A power law (equation 6–1) based on the classical statistical percolation model was developed to relate the composite conductivity to the volume fraction of the conducting fillers in the vicinity of the percolation threshold.

$$\sigma = \sigma_0(\phi - \phi_c)^t \quad (6-1)$$

Where, σ is the electrical conductivity of the composites; σ_0 is the electrical conductivity of the conductive fillers; ϕ is the volume fraction of the conductive fillers in the composites; ϕ_c is the percolation threshold; and t is the critical

exponent revealing the lattice dimensionality.

The linear fitting of the electrical conductivity data to the power law for the electrical conductivity with percolation threshold $\phi_c = 0.005$ is shown in Figure 6-14b, where the dot line represents the best fit. The fitting results are $\sigma_0 = 4.34 \times 10^5$ S/m and $t = 2.59 \pm 0.12$.



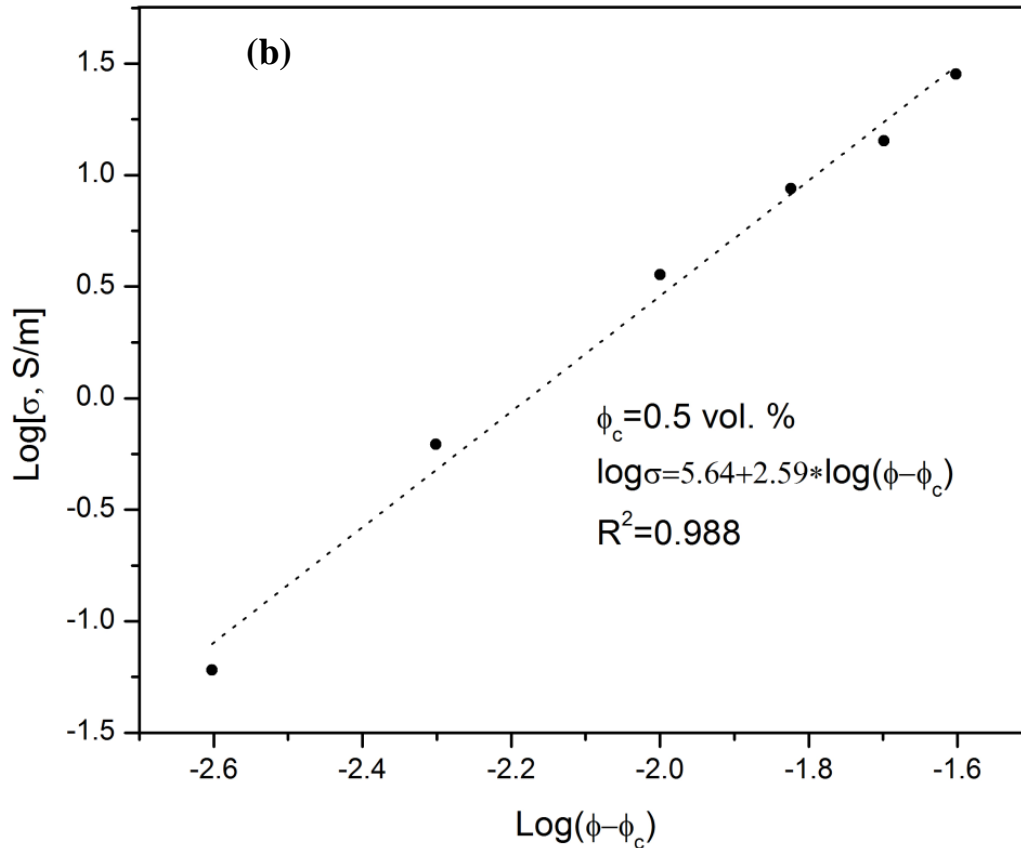


Figure 6-14. (a) The electrical conductivity of the NiNW/LLDPE nanocomposites as a function of the volume fraction of the NiNWs, and (b) the linear fitting of the data to the power law for the electrical conductivity with percolation threshold $\phi_c = 0.005$.

The low percolation threshold $\phi_c = 0.005$ of the NiNW/LLDPE nanocomposites can be attributed to the high aspect ratio of the NiNWs that facilitated the formation of networks for electrical conduction. The critical exponent $t = 2.59 \pm 0.12$ (close to 3) indicated that the electrical conductivity in the NiNW/LLDPE nanocomposites mainly originated from the contact among

individual fibers. It has been reported that t is around 1.9 for the systems with spherical conducting particles, but higher than 2 for the systems with fiber-filled conducting particles [14]. And t of around 3 has been reported for the systems with 1D conducting nanofillers [16, 17]. The electrical conductivity of the conductive fillers $\sigma_0 = 4.34 \times 10^5$ S/m by fitting to the power law was much lower than that of the bulk nickel ($\sigma_{Ni} = 1.44 \times 10^7$ S/m), which may result from the oxides and the macromolecules absorbed on the surface of the NiNWs that decreased the electrical conductivity of the conductive fillers in the polymer nanocomposites.

Lonjon A et al [18] also synthesized NiNWs of around 200 ~ 250 nm in diameter by DC electrodeposition using the commercial PAO membrane with average pore diameter of 200 nm and thickness of 50 μm as templates. The NiNWs were mixed with poly(vinylidene difluoride)-trifluoroethylene (P(VDF-TrFE)) by the solvent casting method. The dry NiNW/P(VDF-TrFE) nanocomposites were then compression molded at 200 $^\circ\text{C}$ under a pressure of about 0.3 MPa for electrical measurements.

They reported the percolation threshold $\phi_c = 0.0075$, the electrical conductivity around 5 S/m for the NiNW/P(VDF-TrFE) nanocomposite with NiNW volume fraction of 0.03 that was only equivalent to 16.7% of the conductivity of the NiNW/LLDPE nanocomposites with NiNW volume fraction of 0.03 in this our work. Moreover, the electrical conductivity of the neat P(VDF-TrFE) reported by Lonjon A et al was over 2 orders of magnitude higher

than that of the neat LLDPE tested by us in this study. The power law fitting results reported for the NiNW/P(VDF-TrFE) nanocomposites [18] were $t = 1.57$, and $\sigma_0 = 3.55 \times 10^{-3}$ S/m. The improved electrical conductivity, decreased percolation threshold and improved power law fitting results of the NiNW/LLDPE nanocomposites in our study may result from the nanoscale diameter of the NiNWs, the formation of conducting networks facilitated by the MSMP method, the decreased alignment and the improved dispersion of the NiNWs in the nanocomposites.

Figure 6–15 shows the backscattered SEM images of the freeze fractures and the TEM images of the ultramicrotomed section of the NiNW/LLDPE nanocomposites, containing 1 vol. % of NiNWs. All the images showed good dispersion of the NiNWs in the LLDPE matrix. Particularly, the good segregation and network formation of the NiNWs in the nanocomposites can be observed in both TEM images.

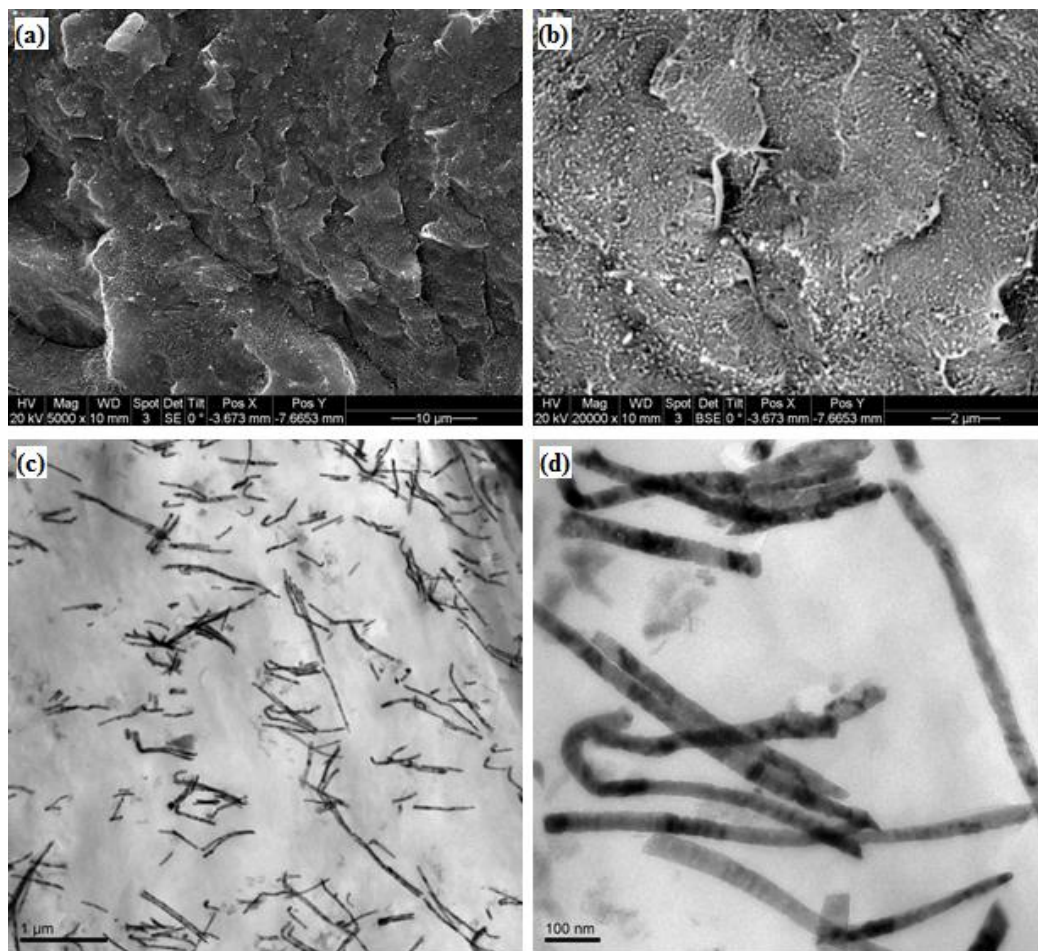


Figure 6-15. The (a, b) backscattered SEM images of the freeze fractures and (c, d) TEM images of the ultramicrotomed section of the NiNW/LLDPE nanocomposites, containing 1 vol. % of NiNWs.

6.4. Conclusions

NiNWs were synthesized by a scalable method of AC electrodeposition of nickel into the in-house prepared PAO templates.

The synthesized NiNWs after liberation and ultrasonication exhibited very uniform diameter of ca. 38 nm and an average length of 2.68 μm , which translates to an average aspect ratio of 70. The SAED revealed the polycrystalline property of the NiNWs. Both the SAED and XRD patterns indicated the fcc nickel crystal structure. The XPS results showed that the NiNW dry powder consisted of metal Ni, NiO and Ni₂O₃. Both the TGA plots acquired in air and H₂ revealed that the NiNW powder comprised around 92.7 wt. % Ni and 7.3 wt. % O elements. The NiNWs dispersed in methanol can be manipulated by a permanent magnet. The Curie temperature of the NiNW powder determined by TGA was 343.6 °C, and its ferromagnetism can be regained at 345.2 °C during the cooling cycle.

NiNW/LLDPE nanocomposites with different volume fractions of NiNWs were prepared by the MSMP method and compression molded at 250 °C and 138 MPa. A remarkable increase of over 12 orders of magnitude in the electrical conductivity of the NiNW/LLDPE nanocomposites with increasing volume fractions of NiNWs indicated the percolation threshold at NiNW volume fraction of 0.005. The electrical conductivity of the NiNW/LLDPE nanocomposite with NiNW volume fraction of 0.03 was up to 28.3 S/m. The power law fitting results implied that the electrical conductivity of the NiNW/LLDPE nanocomposites in this study mainly originated from the contact among individual nanowires.

The backscattered SEM images of the freeze fractures revealed the good dispersion of the NiNWs. The TEM images of the ultramicrotomed section of

the NiNW/LLDPE nanocomposite, containing 1 vol. % of NiNWs, showed the good segregation and network formation of the NiNWs in the LLDPE matrix.

6.5. References

- [1] Paulus PM, Luis F, Kröll M, Schmid G, de Jongh LJ, Low-temperature study of the magnetization reversal and magnetic anisotropy of Fe, Ni, and Co nanowires. *J. Magn. Magn. Mater.* 2001; 224: 180–196.
- [2] Tsuya N, Saito Y, Nakamura H, Hayano S, Furugohri A, Ohta K, Wakui Y, Tokushima T. A perpendicular magnetic recording medium by alumite. *J. Magn. Magn. Mater.* 1986; 54–57: 1681–1682.
- [3] Huang JC. EMI shielding plastics: A review. *Adv. Polym. Tech.* 1995; 14 (2): 137–150.
- [4] Chung DDL. Materials for electromagnetic interference shielding. *J. Mater. Eng. Perf.* 2000; 9 (3): 350–354.
- [5] Bao JC, Tie CY, Xu Z, Zhou QF, Shen D, Ma Q. Template synthesis of an array of nickel nanotubules and its magnetic behavior. *Adv. Mater.*, 2001, 13 (21): 1631–1633.
- [6] Nielsch K, Choi J, Schwirn K, Wehrspohn RB, Gösele U. Self-ordering regimes of porous alumina: the 10 porosity rule. *Nano Lett.* 2002; 2 (7): 677–680.
- [7] Masuda H, Hasegawa F, Ono S. Self-ordering of cell arrangement of anodic porous alumina formed in sulfuric acid solution. *J. Electrochem. Soc.* 1997; 144 (5): L127–L130.

- [8] Q. Liu, H. J. Liu, M. Han, J. M. Zhu, Y. Y. Liang, Z. Xu, Y. Song, *Adv. Mater.*, 2005, 17: 1995–1999.
- [9] Kim KS, Winograd N. X-ray photoelectron spectroscopic studies of nickel-oxygen surfaces using oxygen and argon ion-bombardment. *Surf. Sci.* 1974; 43: 625–643.
- [10] Kittel C. *Intro. Sol. Stat. Phy.* (6 ed.), John Wiley & Sons. 1986; ISBN 0471874744.
- [11] Legendre B, Sghaier M. Curie temperature of nickel. *J. Therm. Anal. Calorim.* 2011; 105 (1): 141–143.
- [12] Valiev RZ, Vishnyakov AD, Mulyukov RR, Fainshtein GS. On the decrease of Curie temperature in submicron-grained nickel. *Phys. Stat. Sol. (A)* 1990; 117: 549–553.
- [13] Genaro GA, Al-Saleh MH, Sundararaj U. Highly electrically conductive and high performance EMI shielding nanowire/polymer nanocomposites by miscible mixing and precipitation. *J. Mater. Chem.* 2011; 21: 829–836.
- [14] Weber M, Kamal MR. Estimation of the volume resistivity of electrically conductive composites. *Polym. Compos.* 1997; 18: 711–725.
- [15] Lux F. Models proposed to explain the electrical conductivity of mixtures made of conductive and insulating materials. *J. Mater. Sci.* 1993; 28: 285–301.
- [16] Bryning MB, Islam MF, Kikkawa JM, Yodh AG. Very low conductivity threshold in bulk isotropic single-walled carbon nanotube–epoxy composites. *Adv. Mater.* 2005; 17: 1186–1191.

[17] Li N, Huang Y, Du F, He XB, Lin X, Gao HJ, Ma HF, Li FF, Chen YS, Eklund PC. Electromagnetic interference (EMI) shielding of single-walled carbon nanotube epoxy composites. *Nano Lett.* 2006; 6: 1141–1145.

[18] Lonjon A, Laffont L, Demont P, Dantras E, Lacabanne C. New highly conductive nickel nanowire-filled P(VDF-TrFE) copolymer nanocomposites: elaboration and structural study. *J. Phys. Chem. C* 2009; 113: 12002–12006.

Chapter 7

General Discussion and Future Work

7.1. General discussion

This thesis focuses on the preparation and characterization of ECPNC formulated with metal nanowires for ESD and EMI shielding, which were synthesized in our lab with the PAO template.

Both DC and AC electrodeposition of various metals into PAO templates have been widely investigated [1–7]. The DC electrodeposition requires multi procedures to process the PAO templates grown on the Al substrate beforehand: dissolving the Al substrate by HgCl_2 , removing the barrier layer by acid, and depositing a metallic layer on the bottom of the pretty fragile free-standing PAO membranes [8]. The expensive high purity Al plates can be used as the templates for once only. The complicated process and the high cost limit the application of the DC electrodeposition in bench scale (up to grams) synthesis of nanomaterials. There is an oxide barrier layer with numerous defects between the PAO template and the Al substrate after the anodization of hours in polyprotic acid solution for several hours which hinders tunnelling electrons through the barrier layer during AC electrodeposition [9].

To prepare the PAO templates suitable for AC electrodeposition of CuNWs, the high purity (99.99+%, Alfa Aesar) aluminum plates were cleaned, and then

anodized under 25 V DC in 0.3 mol/L H_2SO_4 solution by Masuda's two-step process [10, 11] with an etching process in between. After the second anodization for 8 h at 0~4 °C, the barrier layer between the PAO layer and the aluminum substrate can be thinned by stepwise decreasing of the anodization DC voltage from 25 V to 9 V and keeping at 9 V for 5 min. The left barrier layer aluminum oxide of proper thickness is a semiconductor material with low electrical conductivity because of the O^{2-} deficit in its lattice at the interface between the barrier layer and the Al substrate as well as the Al^{3+} deficit at the interface between the barrier layer and the electrolyte [12]. Both the proper thickness and the rectification properties of the barrier layer facilitate the AC electrodeposition of copper into the PAO template to generate uniform CuNWs.

The AC electrodeposition of copper into the PAO template was carried out with 200 Hz sine wave of 10 V_{rms} in 0.5 mol/L $\text{CuSO}_4 \cdot 5\text{H}_2\text{O}$ solution under room temperature for 10.5 min. The CuNW yield of per unit area of PAO template was proportional to the hours of the second anodization. The CuNWs after liberation and ultrasonication had an average length of 1.98 μm . The diameter of the CuNWs measured in TEM images was 25 ± 4 nm. Therefore, the average aspect ratio of the CuNWs was around 80. Metal Cu and Cu_2O can be identified in the CuNW dry powder by XRD pattern and XPS spectra.

The CuNWs synthesized by this method with diameter less than 100 nm have large surface area and high crystalline strain, which lead to the much higher oxidation rate in air than the bulk copper. Therefore, studying the oxidation

kinetics of the CuNWs can know the corrosion and activity loss, and understand the long term performance and durability of the ECPNC formulated with the CuNWs.

The CuNW dry powder before oxidation with oxygen content of 2.997 wt. % determined by the TGA in H_2 is equivalent to 73.2 wt. % Cu and 26.8 wt. % Cu_2O . The oxidation reaction of the CuNWs in air can be divided into two stages at the weight of 111.2% based on the TGA and DTG plots of different heating rates. The oxidized CuNWs after the stage 1 consisted of Cu_2O and CuO as identified by XRD and looked loose and rough with diameter of 25 ± 6 nm. The oxidized CuNWs after the stage 2 comprised CuO only as identified by XRD and looked dense and smooth with larger diameter of 32 ± 6 nm. The CuNWs oxidized after the stage 2 became denser and thicker can be attributed to the merge of two or more individual CuNWs into one during the oxidation.

Kissinger method [13] and other five model-free isoconversional methods: FWO [14], Starink [15], KAS [16], Boswell [17] and Friedman differential methods [18] were utilized to determine the oxidation activation energies of both stages in ignorance of the oxidation mechanism. The activation energies of the stage 2 were much lower than those of the stage 1. Among the activation energies determined by different methods, Kissinger and Boswell methods obtained the greater values, the values by Friedman method exhibited the maximum fluctuation, Starink and KAS methods obtained very close values that fell among the values determined by other methods.

Starink activation energies were selected to fit the different master plots [19]. JMA equation [19] gave the best fit for both stages. The surface atoms of the CuNWs are the sites for the random nucleation and the crystallite strain in the CuNWs is the driving force for the growth of nuclei mechanism during the oxidation.

To improve the anti-oxidation properties of the CuNWs, chemical plating method was applied to coat silver on the surface of the CuNWs in Ag-amine solution. The synthesized AgCuNWs of 28–33 nm in diameter with silver content of 66.52 wt. % showed less regular surface than the CuNWs.

It is evident that the silver coating on AgCuNWs can effectively prevent the copper oxide from forming under room temperature by comparing the XRD patterns of the CuNWs and the AgCuNWs. The TGA plots obtained in air showed that the silver coating on the AgCuNWs increased the weight gain onset temperature from 85 °C to 230 °C and decreased the maximum weight gain from 20.3% to 3.2%.

AgCuNW/LDPE nanocomposites were prepared by the hot solution mixing method. The electrical resistivity of the AgCuNW/LDPE nanocomposites measured after the compression molding of the dry powder of the nanocomposites under 250 °C and 138 MPa for 30 min was lower than that of the CuNW/LDPE nanocomposites because the silver content in AgCuNWs was not oxidized during the compression molding as evidenced by the XRD pattern. At the same time, the XRD pattern indicated that the silver coating cannot

completely prevent the outward diffusion and the oxidation of the copper content in the AgCuNWs at 250 °C.

To evaluate the influence of the different polymer matrices on the electrical properties of the nanocomposites, AgCuNW/PS nanocomposites were prepared by the MSMP method [20]. The electrical resistivity of the AgCuNW/PS nanocomposites showed no noticeable decrease with the increasing concentrations of the AgCuNWs up to 4.0 vol. %. The backscattered SEM images indicated that the AgCuNWs in the PS matrix during the compression molding fragmented into particles due to the combined effects of Rayleigh instability [21–24], surface tension, filler/polymer interaction, temperature, shear stress and/or pressure.

The macromolecular structure, polarity, crystallinity and surface tension of the different polymer matrices can significantly impact the electrical conductivity and the percolation threshold of conductive polymer composites [25–27]. PE can be classified into UHMWPE, HDPE, LDPE, LLDPE, etc, based on their branching, density and molecular weight. Each type of PE with different macromolecular structure can have different interaction with the fillers. Regarding the CuNW/PE nanocomposites, the different interaction between the CuNWs and the different types of PE matrices can lead to the difference in filler dispersion, the electrical and rheological properties.

To study the different interaction between the CuNWs and the different types of PE matrices, the nanocomposites formulated with the CuNWs and the four

different types of PEs were formulated with the MSMP method and compression molded before characterization. The electrical percolation thresholds were 2.0 vol. %, 0.5 vol. %, 0.25 vol. % and 0.25 vol. %, and the rheological percolation thresholds under 200 °C were 0.5 vol. %, 0.5 vol. %, 4.0 vol. % and 1.0 vol. % for the CuNW/UHMWPE, CuNW/HDPE, CuNW/LDPE and CuNW/LLDPE nanocomposites, respectively. The dispersion of the CuNWs in the different types of PE matrices corroborated the electrical conductivity and the electrical percolation thresholds difference in the four types of PE matrices.

The difference in the solution viscosity during the mixing, intermolecular force, and entanglement of the four types of PE matrices leads to the difference in the filler dispersion, the electrical properties and the rheological properties at 200 °C of the nanocomposites. And the different macromolecular structures such as molecular weight and branching of the four types of PEs were the root cause for the difference in the solution viscosity, intermolecular force, and entanglement.

Both the poly-NW and the NW-NW networks contribute to the rheological percolation in the CuNW/polymer nanocomposites. The formation of the poly-NW networks depends on the van der Waals force between the PE chains and the CuNWs. And the strength of the van der Waals force mainly depends on the distance and the number of overlapped atoms between the both parties involved. The linear macromolecular chains without branching like UHMWPE and HDPE allow the close overlapping with the CuNWs to form the poly-NW networks

effectively within the nanocomposites. On the contrary, the macromolecular chains of both the LDPE and LLDPE have large number of long and/or short branches that hinder the close overlapping with the CuNWs. Therefore, it is difficult to form the poly-NW networks effectively within the CuNW/LDPE and CuNW/LLDPE nanocomposites.

Since the absorption loss of electromagnetic radiations increases with the product of the electrical conductivity relative to copper (σ_r) and the relative magnetic permeability (μ_r) [28], The ECPNCs formulated with ferromagnetic nanowires are more interesting than those formulated with CuNWs. Ferromagnetic NiNWs were synthesized successfully by a scalable method of AC electrodeposition of nickel into the PAO templates anodized in 0.3 mol/L oxalic acid solution of 0~4 °C under 40 V DC.

The NiNWs after liberation from the PAO templates and ultrasonication exhibited uniform diameter of ca. 38 nm and an average length of 2.68 μm equivalent to an average aspect ratio of 70. Both the SAED and XRD patterns revealed the fcc nickel crystal structure of the NiNWs. And the polycrystalline property of the synthesized NiNWs was revealed by the SAED pattern too. The dry powder of the NiNWs comprised metal Ni, NiO and Ni₂O₃ as evidenced by the XP spectra. The TGA data obtained both in air and in H₂ indicated that the dry powder of the NiNWs included around 92.7 wt. % Ni and 7.3 wt. % O elements.

The NiNWs dispersed in methanol can be manipulated, and attracted to one side of the vial by a permanent magnet. The NiNWs transformed its ferromagnetism to paramagnetism at Curie temperature of 343.6 °C during the heating cycle and regained its ferromagnetism at 345.2 °C during the cooling cycle. The Curie temperature of the NiNWs in this study was over 14 °C lower than the reported value of the bulk nickel, which may result from the impurity in the NiNWs and the sub-micron grained nature of the NiNWs [29, 30].

NiNW/LLDPE nanocomposites were prepared by the MSMP method and compression molded at 250 °C and 138 MPa before characterization. The electrical percolation threshold of the NiNW/LLDPE nanocomposites appeared at the NiNW volume fraction of 0.005 as indicated by the significant increase of over 12 orders of magnitude in the electrical conductivity with the increasing volume fractions of the NiNWs. The electrical conductivity of the NiNW/LLDPE nanocomposites reached 28.3 S/m at the NiNW volume fraction of 0.03. The electrical conductivity of the nanocomposites with different NiNW volume fractions can be fitted to the power law based on the classical statistical percolation model [31]. The fitting results were the electrical conductivity of the conductive fillers $\sigma_0 = 4.34 \times 10^5$ S/m and the critical exponent $t = 2.59 \pm 0.12$, which imply that the electrical conductivity of the NiNW/LLDPE nanocomposites mainly originated from the contact among individual nanowires. Both the backscattered SEM images of the freeze fractures and the TEM images of the ultramicrotomed sections of the NiNW/LLDPE nanocomposites showed

the good dispersion and good segregation of the NiNWs and the formation of networks within the LLDPE matrix.

7.2. Future work

7.2.1. *Enhancing dispersion of CuNWs in polymer matrix by melt mixing*

The conventional melt processes such as extrusion and injection molding that need no solvent handling are more widely used and also more desirable in the polymer industry than the solution mixing processes [32–34]. However, the previous studies by our group have shown the poor dispersion and low electrical conductivity of the CuNW polymer nanocomposites prepared by melt mixing method [33, 34]. The work by Gelves GA et al in our group [33] somewhat enhanced the dispersion of the CuNWs in the PS matrix, but not up to the requirement of large-scale processing yet. And the functionalization of CuNWs by thiols remarkably decreased the electrical conductivity of the nanocomposites [33].

Moreover, we also tried to functionalize CuNWs with silanes of different functional groups: (3-mercaptopropyl)trimethoxysilane $\text{HS}(\text{CH}_2)_3\text{Si}(\text{OCH}_3)_3$, (3-aminopropyl)trimethoxysilane $\text{H}_2\text{N}(\text{CH}_2)_3\text{Si}(\text{OCH}_3)_3$, trimethoxy(propyl)silane, $\text{CH}_3\text{CH}_2\text{CH}_2\text{Si}(\text{OCH}_3)_3$ and trimethoxy(octyl)silane $\text{CH}_3(\text{CH}_2)_7\text{Si}(\text{OCH}_3)_3$. All these silanes can help improve the dispersion of the functionalized CuNWs in the LDPE matrix. However, the functionalization of CuNWs with silanes lowered

the electrical conductivity of the CuNW/LDPE nanocomposites of over 3 orders of magnitude.

Base on all these previous works of our group, the functionalization of CuNWs with chemicals can enhance the dispersion of the functionalized CuNWs in the polymer matrices. However, the chemicals absorbed on the surface of the CuNWs hinder the electrical conduction. Alternative approaches were also attempted in our group by coating CuNWs with functional polymers, diamine terminated poly(ethylene oxide) or the block copolymer of styrene and 2-vinyl pyridine, for instance, prior to the melt mixing with the matrix polymer. The preliminary results are promising in that these approaches can increase the electrical conductivity of the nanocomposites while enhancing the dispersion of the CuNWs within the polymer matrices. We will carry through these alternative approaches by optimizing the dosage of the functional polymers, the processing concentration, time and temperature, and evaluate the electrical conductivity, the CuNW dispersion, and the rheological and mechanical properties of the functional polymer coated CuNW polymer nanocomposites. All these results will be instrumental for us to realize the formulation of the CuNW polymer nanocomposites of desired performances by extrusion or injection molding.

7.2.2. Quantitation of the structure-property relationships in CuNW/LLDPE nanocomposites

We have shown in Chapter 5 that the macromolecular structures of PEs, specifically, the length and branching of the macromolecular chains, have significant effects on the electrical conductivity, dispersion of CuNWs, and rheological properties of the CuNW/PE nanocomposites. However, all the structure-property relationships discussed in Chapter 5 based on the four different types of PEs (UHMWPE, HDPE, LDPE and LLDPE) are qualitative only.

To quantitate the effects of the branch length on the properties of the CuNW/LLDPE nanocomposites, the LLDPEs synthesized from ethylene and monoalkenes of different numbers of carbon can be utilized as the polymer matrices. The LLDPEs synthesized by different ratios of ethylene and monoalkene have different number and density of braches, which can be used as the matrices to quantitatively determine the impact of number and density of braches on the properties of the CuNW/LLDPE nanocomposites. The LLDPEs of different macromolecular weights synthesized from ethylene and the same monoalkene in the same ratio can be used as the matrices to quantitate the effect of the macromolecular weights on the properties of the CuNW/LLDPE nanocomposites. The quantitative structure-property relationships will be very useful for the computational simulation of the properties of the CuNW/LLDPE nanocomposites.

7.2.3. Evaluation of the EMI shielding and mechanical properties of the NiNW/PE nanocomposites

We are highly interested in the EMI shielding properties of the NiNW polymer nanocomposites in that the high magnetic permeability of the NiNWs in the nanocomposites can significantly increase the absorption loss of the electromagnetic radiations travelling through the NiNW polymer nanocomposites [35]. The samples for EMI shielding test should be compression molded into the size of 42 mm × 25 mm first, which is much bigger than the sample of 10.5 mm diameter used for the electrical conductivity evaluation in Chapter 6, and thus requires much more NiNWs. Regarding the determination of Young's modulus, tensile strength and elongation at break of the NiNW/PE nanocomposites with different NiNW contents, NiNWs of grams are required for the sample preparation. Unfortunately, we can only synthesized around 50 mg NiNWs with five pieces of aluminum plates of 5 cm × 10 cm anodized in the double-walled cylindrical glass container as shown in Figure 6–1. Therefore, we need to increase the capacity of the NiNW synthesis from milligrams to grams by scaling up of the anodization and electrodeposition setup, increasing the pore-filling percentage through the process/ recipe optimization.

7.2.4. Polymer nanocomposites of hybrid conductive nanofillers

NiNWs of high magnetic permeability can increase the absorption loss of electromagnetic radiations while decrease the reflection loss [35]. So the polymer nanocomposites formulated with hybrid conductive nanofillers of

NiNWs and other non-ferromagnetic nanofillers such as CNTs, CuNWs and graphenes are promising in that the ferromagnetic NiNWs should be able to increase the absorption loss of the electromagnetic radiations while the non-ferromagnetic nanofillers can provide sufficient EMI shielding by the reflection mechanism.

An alternative approach to improve the EMI shielding effect of the conductive hybrid polymer nanocomposites without increasing the concentration of the nanofillers can be attempted by the manipulation of the ferromagnetic NiNWs with a magnetic field. For instance, a hybrid ECPNC system using NiNWs and CNTs as the conductive fillers can be manipulated by a magnetic field during the compression molding to preferentially distribute the ferromagnetic NiNWs at the bottom layer of the hybrid ECPNC sample. Thus, the compression molded samples can have two layers: one is the CNT rich layer which can mitigate the electromagnetic radiations by reflection; the other one is the NiNW rich layer which can shield the EMI effectively by absorption.

7.3. References

- [1] Salem AK, Hung CF, Kim TW, Wu TC, Searson PC, Leong KW. Multi-component nanorods for vaccination applications. *Nanotechnology* 2005; 16 (4): 484–487.

- [2] Salem AK, Chao J, Leong KW, Searson PC. Receptor-mediated self-assembly of multi-component magnetic nanowires. *Adv. Mater.* 2004; 16 (3): 268–271.
- [3] Molares MET, Buschmann V, Dobrev D, Neumann R, Scholz R, Schuchert IU, Vetter J. Single-crystalline copper nanowires produced by electrochemical deposition in polymeric ion track membranes. *Adv. Mater.* 2001; 13 (1): 62–65.
- [4] Keating CD, Natan MJ. Striped metal nanowires as building blocks and optical tags. *Adv. Mater.* 2003; 15 (5): 451–454.
- [5] Sauer G, Brehm G, Schneider S, Nielsch K, Wherspohn RB, Choi J, Hofmeister H, Gösele U. Highly ordered monocrystalline silver nanowire arrays. *J. Appl. Phys.* 2002; 91: 3243–3247.
- [6] Nielsch K, Muller F, Li AP, Gösele U. Uniform nickel deposition into ordered alumina pores by pulsed electrodeposition. *Adv. Mater.* 2000; 12 (8): 582–586.
- [7] Xu JX, Wang KY, Xu Y. Structural and magnetic properties of Co–Ni nanowire array prepared by alternating current electrodeposition. *Chem. Lett.* 2007; 36: 868–869.
- [8] Xu DS, YXu YJ, Chen DP, Guo GL, Gui LL, Tang YQ. Preparation and characterization of CdS nanowire arrays by dc electrodeposit in porous anodic aluminum oxide templates. *Chem. Phys. Lett.*, 2000, 325 (4): 340–344.
- [9] Schmid G. Materials in nanoporous alumina. *J. Mater. Chem.* 2002; 12: 1231–1238.

- [10] Masuda H, Satoh M. Fabrication of gold nanodot array using anodic porous alumina as an evaporation mask. *Jpn. J. Appl. Phys.* 1996; 35: L126–L129.
- [11] Masuda H, Hasegawa F, Ono S. Self-ordering of cell arrangement of anodic porous alumina formed in sulfuric acid solution. *J. Electrochem. Soc.* 1997; 144 (5): L127–L130.
- [12] Saedi A, Ghorbani M, Electrodeposition of Ni-Fe-Co alloy nanowire in modified AAO template. *Mater. Chem. Phys.* 2005; 91 (2–3): 417–423.
- [13] Kissinger HE. Reaction kinetics in differential thermal analysis. *Anal. Chem.* 1957; 29: 1702–1706.
- [14] Flynn JH, Wall LA. A quick, direct method for the determination of activation energy from thermogravimetric data. *J. Polymer Sci. B Polymer Lett.* 1966; 4 (5): 323–328.
- [15] Starink MJ. A new method for the derivation of activation energies from experiments performed at constant heating rate. *Thermochim. Acta.* 1996; 288 (1–2): 97–104.
- [16] Robinson PP, Arun V, Manju S, Aniz CU, Yusuff KKM. Oxidation kinetics of nickel nano crystallites obtained by controlled thermolysis of diaquabis(ethylenediamine)nickel(II) nitrate. *J. Therm. Anal. Calorim.* 2010; 100 (2): 733–740.
- [17] Boswell PG. On the calculation of activation energies using a modified Kissinger method. *J. Thermal. Acta.*, 1980; 18 (2): 353–358.

[18] Friedman HL. New methods for evaluating kinetic parameters from thermal analysis data. *J. Polymer Sci. B Polymer Lett.* 1969; 7 (1): 41–46.

[19] Gotor FJ, Criado JM, Malek J, Koga N. Kinetic Analysis of Solid-State Reactions: The Universality of Master Plots for Analyzing Isothermal and Nonisothermal Experiments. *J. Phys. Chem. A* 2000; 104 (46): 10777–10782.

[20] Gelves GA, Al-Saleh MH, Sundararaj U. Highly electrically conductive and high performance EMI shielding nanowire/polymer nanocomposites by miscible mixing and precipitation. *J. Mater. Chem.* 2011; 21: 829–836.

[21] Karim S, Toimil-Molares ME, Balogh AG, Ensinger W, Cornelius TW, Khan EU, Neumann R. Morphological evolution of Au nanowires controlled by Rayleigh instability, *Nanotechnology* 2006; 17: 5954–5959.

[22] Toimil-Molares ME, Balogh AG, Cornelius TW, Neumann R, Trautmann C. Fragmentation of nanowires driven by Rayleigh instability. *Appl Phys Lett* 2004; 85: 5337–5339.

[23] Rayleigh L. On the Capillary Phenomena of Jets. *Proceedings of the Royal Society of London* 1879; 29: 71–97.

[24] Nichols FA, Mullins WW. Surface (interface) and volume diffusion contributions to morphological changes driven by capillarity. *Trans Metall Soc AIME* 1965; 233: 1840–1848.

- [25] Valentino O, Sarno M, Rainone NG, Nobile MR, Ciambelli P, Neitzert HC, Simon GP. Influence of the polymer structure and nanotube concentration on the conductivity and rheological properties of polyethylene/CNT composites. *Physica E* 2008; 40: 2440–2445.
- [26] Sau KP, Chaki TK, Khastgir D. Carbon fibre filled conductive composites based on nitrile rubber (NBR), ethylene propylene diene rubber (EPDM) and their blend. *Polym.* 1998; 39 (25): 6461–6471.
- [27] F. Gubbels, R. Jerome, Ph. Teyssie, E. Vanlathem, R. Deltour, A. Calderone, V. Parente, J. L. Breads. Selective localization of carbon black in immiscible polymer blends: a useful tool to design electrical conductive composites. *Macromol.* 1994; 27: 1972–1974.
- [28] Chung DDL. Materials for electromagnetic interference shielding. *J. Mater. Eng. Perf.* 2000; 9 (3): 350–354.
- [29] Legendre B, Sghaier M. Curie temperature of nickel. *J. Therm. Anal. Calorim.* 2011; 105 (1): 141–143.
- [30] Valiev RZ, Vishnyakov AD, Mulyukov RR, Fainshtein GS. On the decrease of Curie temperature in submicron-grained nickel. *Phys. Stat. Sol. (A)* 1990; 117: 549–553.
- [31] Lux F. Models proposed to explain the electrical conductivity of mixtures made of conductive and insulating materials. *J. Mater. Sci.* 1993; 28: 285–301.
- [32] Breuer O, Sundararaj U. Big returns from small fibers: A review of polymer/carbon nanotube composites. *Polym. Composite.* 2004; 25 (6): 630–645.

[33] Gelves GA, Lin B, Haber JA, Sundararaj U. Enhancing dispersion of copper nanowires in melt-mixed polystyrene composites. *J. Polym. Sci., Part B: Polym. Phys.* 2008; 46: 2064–2078.

[34] Lin B, Gelves GA, Haber JA, Pötschke P, Sundararaj U. Electrical, Morphological and Rheological Study of Melt-Mixed Polystyrene/Copper Nanowire Nanocomposites. *Macromol. Mater. Eng.* 2008; 293: 631–640.

[35] Huang JC. EMI shielding plastics: A review. *Adv. Polym. Tech.* 1995; 14 (2): 137–150.